UNIVERSITY OF CALIFORNIA

Los Angeles

Thermodynamic Characterization and Heat Generation of Fast-Charging Wadsley-Roth Shear Phase Materials for Battery Application

A dissertation submitted in partial satisfaction
of the requirements for the degree
Doctor of Philosophy in Mechanical Engineering

by

Sun Woong Baek

2022

Abstract of the Dissertation

Thermodynamic Characterization and Heat Generation
of Fast-Charging Wadsley-Roth Shear Phase Materials
for Battery Application

by

Sun Woong Baek
Doctor of Philosophy in Mechanical Engineering
University of California, Los Angeles, 2022
Professor Laurent G Pilon, Chair

This dissertation reviews and clarifies the fundamental thermodynamic relationships relevant to the interpretation of potentiometric entropy measurements on lithium-ion batteries (LIBs) to gain insight into the physicochemical phenomena occurring during cycling. First, contributions from configurational, vibrational, and electronic excitations to the entropy of an *ideal* intercalation compound used as a cathode in a battery system were analyzed. The results of this analysis were used to provide an interpretative guide of open circuit voltage $U_{ocv}(x,T)$ and entropic potential $\partial U_{ocv}(x,T)/\partial T$ measurements to identify different mechanisms of intercalation, including (i) lithium intercalation as a homogeneous solid solution, (ii) ion ordering reactions from a homogeneous solid solution, (iii) first-order phase transitions involving a two-phase coexistence, and/or (iv) first-order phase transitions passing through a stable intermediate phase. These interpretations were illustrated with experimental data for different battery electrode materials including TiS_2, $LiCoO_2$, $Li_{4/3}Ti_{5/3}O_4$, $LiFePO_4$, and graphite electrodes with metallic lithium as the counter electrode. The systematic interpretation of $U_{ocv}(x,T)$ and $\partial U_{ocv}(x,T)/\partial T$ can enhance other structural analysis techniques such as X-ray diffraction, electron energy-loss spectroscopy, and Raman spectroscopy.

Thermal signatures associated with electrochemical and transport phenomena occurring in LIB systems were investigated by performing potentiometric entropy measurement and

isothermal *operando* calorimetry on LIB systems. Here, LIB system consisting of electrodes made of $TiNb_2O_7$ and PNb_9O_{25} were investigated. The potentiometric entropy measurements of $TiNb_2O_7$ and PNb_9O_{25} featured signatures of intralayer ion ordering upon lithiation that could not be observed with *in situ* X-ray diffraction. Furthermore, entropy measurements also confirmed the semiconductor-to-metal transition taking place at PNb_9O_{25} upon lithiation. Furthermore, isothermal *operando* calorimetry measurements indicated that the nature of heat generation was dominated by Joule heating, which sensitively changed as the conductivity of the electrode increased with increasing lithiation. The heat generation rate decreased at the $TiNb_2O_7$ and PNb_9O_{25} electrode upon lithiation due to the decrease in electrical resistivity caused by the semiconductor-to-metal transition also observed in potentiometric entropy measurements. In addition, the time-averaged irreversible heat generation rate indicated that the electrical resistance of the lithium metal electrode was constant and independent of the state of charge while the electrical resistance of the PNb_9O_{25} changed significantly with the state of charge. Moreover, calorimetry measurements have shown that the electrical energy losses were dissipated entirely in the form of heat. Furthermore, the enthalpy of mixing, obtained from *operando* calorimetry, is found to be small across the different degrees of lithiation, pointing to the high rate of lithium-ion diffusion at the origin of rapid rate performance of $TiNb_2O_7$ and PNb_9O_{25}.

Moreover, the effect of particle size on the electrochemical performance and heat generation in LIB systems were investigated using two LIBs consisting of electrodes made of either $(W_{0.2}V_{0.8})_3O_7$ *nanoparticles* synthesized by sol-gel method combined with freeze-drying or $(W_{0.2}V_{0.8})_3O_7$ *microparticles* synthesized by solid-state method. Galvanostatic cycling confirmed that the electrode made of $(W_{0.2}V_{0.8})_3O_7$ *nanoparticles* featured larger capacity and better retention at high C-rates than that made of the $(W_{0.2}V_{0.8})_3O_7$ *microparticles*. Entropic potential measurements performed at slow C-rate indicated that both *nanoparticles* and *microparticles* underwent a semiconductor to metal transition, and *nanoparticles* underwent a two-phase coexistence region over a narrower range of composition. *Operando* calorimetry measurements at high C-rate established that the heat generation rate increased at the $(W_{0.2}V_{0.8})_3O_7$ electrode upon lithiation due to an increase in charge transfer resistance

regardless of particle size. Moreover, the time-averaged irreversible heat generation rate was slightly but systematically smaller at the electrode made of *nanoparticles*. Furthermore, the specific dissipated energy and the contribution from enthalpy of mixing caused by lithium concentration gradient was notably smaller for $(W_{0.2}V_{0.8})_3O_7$ *nanoparticles*. These observations were attributed to the fact that *nanoparticles* were less electrically resistive and able to accommodate more lithium while lithium ion intercalation therein was more kinetically favorable.

The dissertation of Sun Woong Baek is approved.

Anton Van der Ven

Sarah H Tolbert

Bruce S Dunn

Laurent G Pilon, Committee Chair

University of California, Los Angeles

2022

This dissertation is dedicated to my wife

Table of Contents

List of Figures

NOMENCLATURE

A	Surface area, m^2
C	Specific capacity, mAh/g
c	Concentration, mol/m^3
D	Apparent diffusion coefficient of ion into electrode, cm^2/s
E	Energy dissipated, J
F	Faraday constant, 96,485 C/mol
G	Gibbs free energy, J
g	Molar Gibbs free energy, J/mol
$\bar{g}$	Partial molar Gibbs free energy, J/mol
H	Enthalpy, J
h	Molar enthalpy, J/mol
$\bar{h}$	Partial molar enthalpy, J/mol
I	Current, mA
M	Molecular weight, g/mol
N	Number of moles, mol
n	Valency of material
p	Pressure, Pa
Q	Dissipated heat, J
$\dot{Q}$	Instantaneous heat generation rate, W
q''	Heat flux, W/m^2
R_I	Internal resistance, Ω
$\dot{r}$	Reaction rate, mol/s
S	Entropy, J/K
s	Molar entropy, J/mol·K
$\bar{s}$	Partial molar entropy, J/mol·K
T	Temperature, K
t	Time, t

U_{ocv}	Open circuit voltage, V
V	Operating voltage, V
V_e	Volume of electrode, m^3
x	Ion composition in the host material
ΔE_e	Electrical energy losses due to voltage hysteresis, J
ΔU_{ocv}	Change in open circuit voltage between two consecutive current pulses, V
ΔV	Voltage difference generated in the heat flux sensor, μV
ΔV_t	Change in cell potential due to current pulses excluding the IR drop, V

Greek symbols

η	Overpotential, V
μ	Chemical potential, J/mol
ν	Scan rate, mV/s
τ	Duration of current pulse, sec

Superscripts and subscripts

avg	Refers to volume-averaged
de	Refers to delithiation
e	Refers to electron charge
irr	Refers to irreversible process
J	Refers to Joule heating
Li	Refers to lithium metal
Li^+	Refers to lithium ion
li	Refers to lithiation
$measured$	Refers to measured
mix	Refers to enthalpy of mixing
rev	Refers to reversible process
rxn	Refers to reaction
sr	Refers to side reaction

T	Refers to total
theo	Refers to theoretical
cathode	Refers to cathode
anode	Refers to anode

Acknowledgments

Firstly, I would like to thank my advisor, Prof. Laurent Pilon, for his mentorship throughout my Ph.D. study. His guidance, motivation, and excitement helped me to complete my doctoral work. I honestly believe that I would not be able to complete my degree without his help.

Secondly, I would like to thank my Ph.D. committee members Prof. Anton Van der Ven, Prof. Sarah Tolbert, and Prof. Bruce Dunn for serving on my thesis committee. I would also like I would also like to acknowledge all my current and former lab members Dr. Tiphaine Galy, Jack Hoeniges, Sara Vallejo-Castano, Dr. Michal Marszewski, Matevž Frajnkovič, Ali Dashti, Dr. Ampol Likitchatchawankun, Dr. Obaidallah Mohammad Munteshari. Finally, I would like to thank my family for their patience and unconditional support.

Vita

2012-2018 B.S. Mechanical and Aerospace Engineering Department, University of California, Los Angeles, U.S.

2018-2019 M.S, Mechanical and Aerospace Engineering Department, University of California, Los Angeles, U.S.

Publications

SW. Baek, K.E. Wyckoff, D.M. Butts, J. Bienz, A. Likitchatchawankun, M.B. Preefer, M. Frajnkovič, B.S. Dunn, R. Seshadri, L. Pilon, 2021, *Operando* calorimetry informs the origin of rapid rate performance in microwave-prepared $TiNb_2O_7$ electrodes, Journal of Power Sources, Vol. 490, pp. 229537.

SW. Baek, M.B. Preefer, M. Saber, K. Zhai, M. Frajnkovič, Y. Zhou, B.S. Dunn, A. Van der Ven, R. Seshadri, L. Pilon, 2022, Potentiometric entropy and *operando* calorimetric measurements reveal fast cahrging mechanisms in PNb_9O_{25}, Journal of Power Sources, Vol. 520, pp. 230776.

K.E. Wyckoff, J.L. Kaufman, **SW. Baek**, C. Dolle, J.J. Zak, J. Bienz, L. Kautzsch, R.C. Vincent, A. Zohar, K.A. See, Y.M. Eggeler, L. Pilon, A. Van der Ven, R. Seshadri, 2022, Metal-metal bonding as an electrode design principle in the low-strain cluster compound $LiScMo_3O_8$, Journal of the Americal Chemical Society, Vol. 144, No. 13, pp. 5841-5854.

SW. Baek, M. Saber, A. Van der Ven, L. Pilon, 2022, Thermodynamic analysis and interpretative guide to entropic potential measurements of lithium-ion battery electrodes, Journal

of Physical Chemistry C, Vol. 126, No. 14, pp. 6096-6110.

Y. Zhou, E. Le Calvez, **SW. Baek**, M. Frajnkovič, C. Douard, E. Gautron, O. Crosnier, T. Brousse, L. Pilon, 2022, Effect of particle size on thermodynamics and lithium ion transport in electrodes made of $Ti_2Nb_2O_9$ micropatricles or nanoparticles, Energy Storage Materials, Vol. 52 (Print in progress).

M. Frajnkovič, A. Likitchatchawankun, C. Douard, Y. Zhou, **SW. Baek**, I. Catton, O. Crosnier, T. Brousse, L. Pilon, 2022, Calorimetry can detect the early onset of hydrolysis in hybrid supercapacitors with aqueous electrolytes, SSRN 4139099 (Print in progress).

SW. Baek, K.E. Wyckoff, D.D. Robertson, M. Frajnkovič, Y. Zhou, S.H. Tolbert, R. Seshadri, and L. Pilon, 2022, Probing the effect of particle size in the heat generation of Wadsley-Roth shear phase $(W_{0.2}V_{0.8})_3O_7$ with *operando* calorimetry, (writing in progress).

CHAPTER 1

Introduction

Batteries are electrical energy storage devices that can provide power by converting chemical energy directly into electrical energy. This chapter provides introductory information about batteries and presents the motivations and objectives of this Ph.D. thesis.

1.1 Lithium ion batteries

1.1.1 introduction

Batteries with high energy density, compact size, and long-life have received significant interest driven by the remarkable increase in demand for portable consumer electronics and electric vehicles (EV) [3–7]. Batteries, first developed by Alessandro Volta in 1799 [8, 9], can be categorized into (i) primary batteries, and (ii) secondary batteries [10–12]. Primary batteries can be used only once and cannot be recharged due to irreversible electrochemical reduction/oxidation (redox) reactions [12]. For example, zinc–carbon batteries are some of the most studied primary batteries [13]. On the other hand, secondary batteries are rechargeable thanks to reversible redox reactions [12]. Primary batteries hold the major share of the commercial battery market including for small electronic devices. However, they generate toxic waste and are environmentally unfriendly. By contrast, secondary batteries, such as (i) nickel-metal hydride, (ii) lithium-ion batteries (LIBs), and (iii) sodium-ion batteries (SIBs), have received significant attention with the increasing use of portable electronics (e.g., cell phones) and EVs, and the desire to use more environmental friendly technology [14–18]. Out of many types of secondary batteries, LIBs are the most widely used secondary batteries owing to their high energy density and high reversibility compared to other secondary

batteries [19, 20]. In the following subsection, the components of the LIBs are discussed to understand overall geometry of LIBs.

1.1.2 Lithium-ion battery constituents

LIBs typically consist of two electrodes separated by a separator imbibed with an electrolyte. This subsection reviews the different electrode materials and electrolytes.

Electrodes

Electrodes used in batteries include (i) a cathode or positive electrode, (ii) an anode or negative electrode. The cathode corresponds to the oxidizing electrode and accepts electrons from the external circuit during discharging. It is reduced during the discharging process. The anode is the reducing electrode and gives up electrons to the external circuit during discharging. It is oxidized during the discharging process.

An ideal cathode materials should be (i) an efficient oxidizing agent, (ii) able to operate under high working voltage, and (iii) stable when in contact with the electrolyte [12, 21, 22]. For LIBs, the earliest cathode material that satisfied all these conditions was titanium disulfide (TiS_2) proposed by Whittingham [23]. The layered crystal structure of TiS_2 allows lithium ions to intercalate and be stored between layers. However, the operating voltage of the TiS_2 was relatively low ($\simeq$ 2 V vs. Li/Li^+) [23]. Thus, many researchers have been investigating several alternative materials with a similar layered structure. In 1980s, Goodenough's group [24] discovered that layered oxides such as $LiCoO_2$ have the same layered structure as TiS_2 and lithium ion can be electrochemically and reversibly inserted and extracted at relatively high operating voltage ($\simeq$ 4 V vs. Li/Li^+). Since then, oxides with layered structure have become the most common cathode material for LIBs.

An ideal anode should (i) be an efficient reducing agent, (ii) have a high specific capacity, and (iii) be stable in contact with the electrolyte [12, 21, 22]. For LIBs, the earliest anode material that satisfied all these conditions was graphite proposed by Besenhard [25] in 1970. Graphite electrodes are still widely used in many commercial devices since they

are inexpensive to fabricate and feature a large theoretical capacity (= 370 mAh/g) [26]. However, graphite anodes suffer from performance degradation associated with formation of solid-electrolyte interface (SEI) layer due to its low operation voltage($\simeq$ 0.2 V vs. Li/Li^+). Moreover, the poor performance of graphite anodes at high C-rates limits the application of graphite anode for fast-charging LIB. Recently many conducting oxide, such as TiO_2 [27], $LiCrTiO_4$ [28], and $Li_4Ti_5O_{12}$ [29] were investigated as promising alternatives. In fact, conducting oxide based electrodes operate at higher voltage and cause less SEI formation than graphite electrodes [30]. For example, $TiNb_2O_7$ proposed by Goodenough [31], has replaced graphite anodes in many commercial devices not only due to its high theoretical capacity (= 370 mAh/g) and high operating voltage ($\simeq$ 1.5 V vs. Li/Li^+) but also due to its ability to maintain large capacity at high C-rates [32].

Electrolytes

The electrolytes enable ion transport between the anode and the cathode to match the electrical current in the external circuits. The main key of the ideal electrolyte is that it should have a good ionic conductivity yet it should not be electrically conductive to avoid internal short-circuiting. In addition, suitable electrolytes may be (i) nonreactive with the electrode materials, (ii) stable over a wide range of temperature and potential, (iii) inexpensive, (iv) non-toxic, and (vi) non flammable.

There exist mainly five different types of electrolytes namely (i) aqueous electrolytes, (ii) organic electrolytes, (iii) ionic liquids, (iv) polymer/solid electrolytes, and (v) hybrid electrolytes. Aqueous electrolytes are made by dissolving salt into deionized water. They are inexpensive and environmental friendly. However, they cannot operate below 0 °C since H_2O freezes and limits ion transfer. Also, they cannot operate above 1.23 V since H_2O undergoes electrolysis and creates H_2 and O_2 bubbles that pose safety concerns [33]. Organic electrolytes are made by dissolving salt, such as lithium hexafluorophosphate ($LiPF_6$) into an organic solvent, such as ethylene carbonate (EC) or dimethyl carbonate (DMC). They can operate over the wider range of potential window and are commonly used in many LIBs.

However, organic electrolytes have high volatility and flammability that pose serious safety concerns [34]. Ionic liquids are salts in the liquid state at room temperature. They are electrochemically and thermally stable and exhibit high ionic conductivity. However, they are currently used only for research purposes due to their high cost. Polymer electrolytes also known as solid electrolytes were developed to overcome the low mechanical strength of liquid electrolytes. Polymer electrolytes can be further divided into (i) solid-state polymer electrolytes such as polyethylene oxides, and (ii) gel polymer electrolytes such as polyvinylidene fluoride. They are thermally stable and exhibit low volatility. However, polymer electrolytes are not widely used in commercial devices due to their low ionic conductivity [35]. Hybrid electrolytes are mixtures of two or more different types of the previously mentioned electrolytes. They are developed to overcome the disadvantages of each type of electrolytes. Ionogel, a composite material consisting of an ionic liquids immobilized by a polymer matrix, is one example of hybrid electrolytes that combined ionic liquids and polymer electrolyte. A recent study shows that ionogels can achieve both high mechanical strength and high ionic conductivity [36]. However, their adoption is limited by complicated preparation compared to other types of electrolytes.

1.2 Lithium-ion battery cycling and characteristics

This section presents physicochemical phenomena occurring at the cathode and the anode upon operation of battery. In addition, important LIB characteristics, such as open circuit voltage, entropic potential and theoretical specific capacitiy, are discussed to.

1.2.1 Lithium-ion battery cycling

Figures 1.1(a) and 1.1(b) show a typical LIB consisting of a metallic intercalation compound MA serving as the cathode, a lithium metal electrode serving as the anode, and a Li-ion based electrolyte. The intercalation compound MA consists of a transition metal M and an anion unit referred to as A. Figure 1.1(a) schematically shows the direction of ion and electron transport in a LIB during *discharging*. Then, the Li^+ ions intercalate into the MA

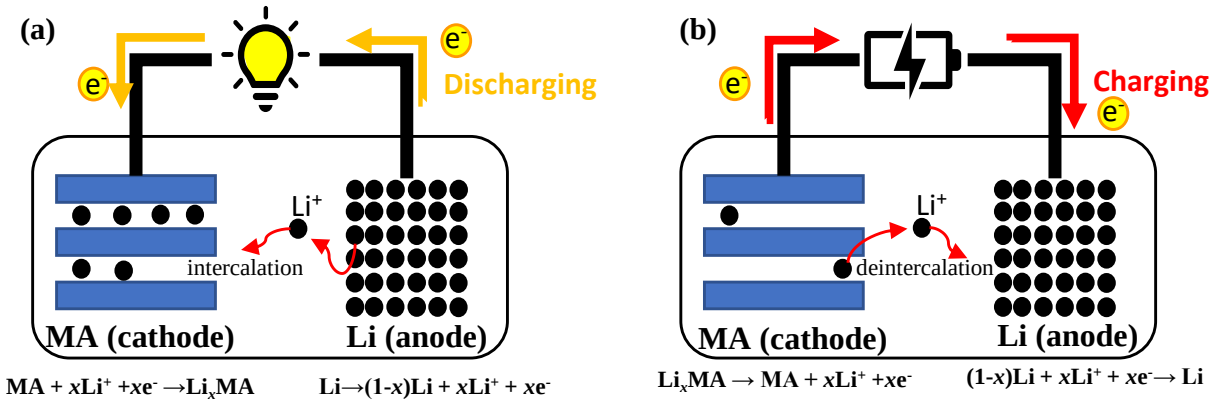

Figure 1.1: Schematic of the ionic and electronic transport processes in a lithium-ion battery and redox reactions associated with the (a) *discharging* and (b) *charging* processes.

cathode to balance the charge of electrons coming from the oxidation of the metallic lithium anode according to [21, 37]

$$\mathrm{Li} \rightarrow (1-x)\mathrm{Li} + x\mathrm{Li}^{+} + xe^{-}. \tag{1.1}$$

Upon insertion of Li^{+} ions in the cathode, MA transforms into a lithiated compound $\mathrm{Li}_x\mathrm{MA}$ according to [21, 37],

$$\mathrm{MA} + x\mathrm{Li}^{+} + xe^{-} \rightarrow \mathrm{Li}_x\mathrm{MA}. \tag{1.2}$$

The lithium composition x is defined as the fraction of the number of intercalated lithium N_{Li} per number of host MA units N_{MA}, i.e.,

$$x = \frac{N_{\mathrm{Li}}}{N_{\mathrm{MA}}}. \tag{1.3}$$

Combining Eqs.(1.1) and (1.2) yields the overall reaction of the battery system during *discharging* [21, 37]

$$\mathrm{MA} + \mathrm{Li} \rightarrow \mathrm{Li}_x\mathrm{MA} + (1-x)\mathrm{Li}. \tag{1.4}$$

The arrows in the above reactions are reversed during *charging*, as schematically illustrated in Figure 1.1(b).

1.2.2 Open circuit voltage and entropic potential

Variations in the lithium composition x of the cathode material during *charging/discharging* leads to a change in the open circuit voltage of the battery. The open circuit voltage $U_{ocv}(x,T)$ of a Li^+ ion battery is related to fundamental thermodynamic quantities of the electrodes according to the Nernst equation expressed as [38]

$$U_{ocv}(x,T) = -\frac{\mu_{\mathrm{Li}}^{\mathrm{Li}_x\mathrm{MA}}(x,T) - \mu_{\mathrm{Li}}^{\mathrm{o}}(T)}{e} \tag{1.5}$$

where e is the elementary charge while $\mu_{\mathrm{Li}}^{\mathrm{Li}_x\mathrm{MA}}(x,T)$ and $\mu_{\mathrm{Li}}^{\mathrm{o}}(T)$ are respectively the Li chemical potentials of $\mathrm{Li}_x\mathrm{MA}$ in the cathode and of metallic Li in the anode. The lithium chemical potential $\mu_{\mathrm{Li}}^{\mathrm{Li}_x\mathrm{MA}}(x,T)$ of $\mathrm{Li}_x\mathrm{MA}$ is related to the Gibbs free energy of $\mathrm{Li}_x\mathrm{MA}$ according to

$$\mu_{\mathrm{Li}}^{\mathrm{Li}_x\mathrm{MA}}(x,T) = \frac{\partial G_{\mathrm{Li}_x\mathrm{MA}}(x,T)}{\partial N_{\mathrm{Li}}} = \left(\frac{\partial g_{\mathrm{Li}_x\mathrm{MA}}(x,T) N_{\mathrm{MA}}}{\partial x}\right)\left(\frac{\partial x}{\partial N_{\mathrm{Li}}}\right) = \frac{\partial g_{\mathrm{Li}_x\mathrm{MA}}(x,T)}{\partial x} \tag{1.6}$$

where $g_{\mathrm{Li}_x\mathrm{MA}}(x,T)$ is the Gibbs free energy of $\mathrm{Li}_x\mathrm{MA}$ normalized by the number N_{MA} of MA units. Furthermore, the chemical potential of Li in the anode can be expressed as

$$\mu_{\mathrm{Li}}^{\mathrm{o}}(T) = \frac{\partial G_{\mathrm{Li}}(T)}{\partial N_{\mathrm{Li}}} = \frac{G_{\mathrm{Li}}(T)}{N_{\mathrm{Li}}} = g_{\mathrm{Li}}^{\mathrm{o}}(T) \tag{1.7}$$

where the middle equality holds because the anode is a pure Li metal, i.e., a single component solid. Here, Eq.(1.7) assumes that the metallic Li electrode has macroscopic dimensions and that contributions from surface energy can be neglected [39]. In this thermodynamic limit, the Li chemical potential of the anode is a constant under isothermal and isobaric conditions.

By substituting Eqs.(1.6) and (1.7) into Eq.(1.5), the open circuit voltage $U_{ocv}(x,T)$ of the battery can be related to the Gibbs free energies of the two electrodes as

$$U_{ocv}(x,T) = -\frac{1}{e}\left[\frac{\partial g_{\mathrm{Li}_x\mathrm{MA}}(x,T)}{\partial x} - g_{\mathrm{Li}}^{\mathrm{o}}(T)\right]. \tag{1.8}$$

Based on the Clairaut's theorem, taking the derivative of both sides of Eq.(1.8) with respect to temperature T yields

$$\frac{\partial U_{ocv}(x,T)}{\partial T} = -\frac{1}{e}\left[\frac{\partial}{\partial x}\left(\frac{\partial g_{\mathrm{Li}_x\mathrm{MA}}(x,T)}{\partial T}\right) - \frac{\partial g_{\mathrm{Li}}^{\mathrm{o}}(T)}{\partial T}\right]. \tag{1.9}$$

The temperature derivative of the Gibbs free energy, under isobaric conditions, is related to the entropy $s(x,T)$ according to [40]

$$s(x,T) = -\frac{\partial g(x,T)}{\partial T} \tag{1.10}$$

where both $s(x,T)$ and $g(x,T)$ are normalized per unit of MA or metallic Li. Thus, it is possible to relate the temperature derivative of the open circuit voltage to the entropies of the cathode material and the Li anode according to

$$\frac{\partial U_{ocv}(x,T)}{\partial T} = \frac{1}{e}\left[\frac{\partial s_{\mathrm{Li}_x\mathrm{MA}}(x,T)}{\partial x} - s^{\mathrm{o}}_{\mathrm{Li}}(T)\right]. \tag{1.11}$$

Here, $\partial U_{ocv}(x,T)/\partial T$ is also known as the entropic potential. The partial derivative with respect to lithium composition x of the entropy of the cathode $s_{\mathrm{Li}_x\mathrm{MA}}(x,T)$ per unit MA of $\mathrm{Li}_x\mathrm{MA}$ is referred to as the partial entropy. Note that $s^{\mathrm{o}}_{\mathrm{Li}}(T)$ is the entropy of the metallic lithium electrode which is always positive and depends only on temperature; at room temperature $s^{\mathrm{o}}_{\mathrm{Li}}(298K)$ was reported to be 29 J/mol·K [41].

1.2.3 Theoretical specific capacity

The capacity of an electrode expresses the total amount of charge stored by the electrode and is expressed in mAh. Since more active materials in the electrodes result in a greater capacity, specific capacity, typically expressed in mAh/g, is used to characterize the charge stored in the electrode. The theoretical specific capacity C_{theo} of the electrode can be calculated based on the molecular weight of active electrode material M, i.e. [21],

$$C_{theo} = \frac{nF}{3600M} \tag{1.12}$$

where n is the valency of the active electrode material. For example, the molecular weight of graphite C_6 is 72 g/mol, and the valency of graphite is 1 since the theoretically fully lithiated state is LiC_6. Therefore, the C_{theo} of graphite is 370 mAh/g. Furthermore, lithium composition x in a battery electrode can be calculated based on the theoretical capacity C_{theo} such that

$$x = \frac{C_{measured}}{C_{theo}} \tag{1.13}$$

where $C_{measured}$ is experimentally measured specific capacity upon cycling.

1.3 Electrochemical testing methods

In this section, useful electrochemical testing methods, such as galvanostatic cycling, cyclic voltammetry, and galvanostatic intermittent titration, and potentiometric entropy measurement technique are presented.

1.3.1 Galvanostatic cycling

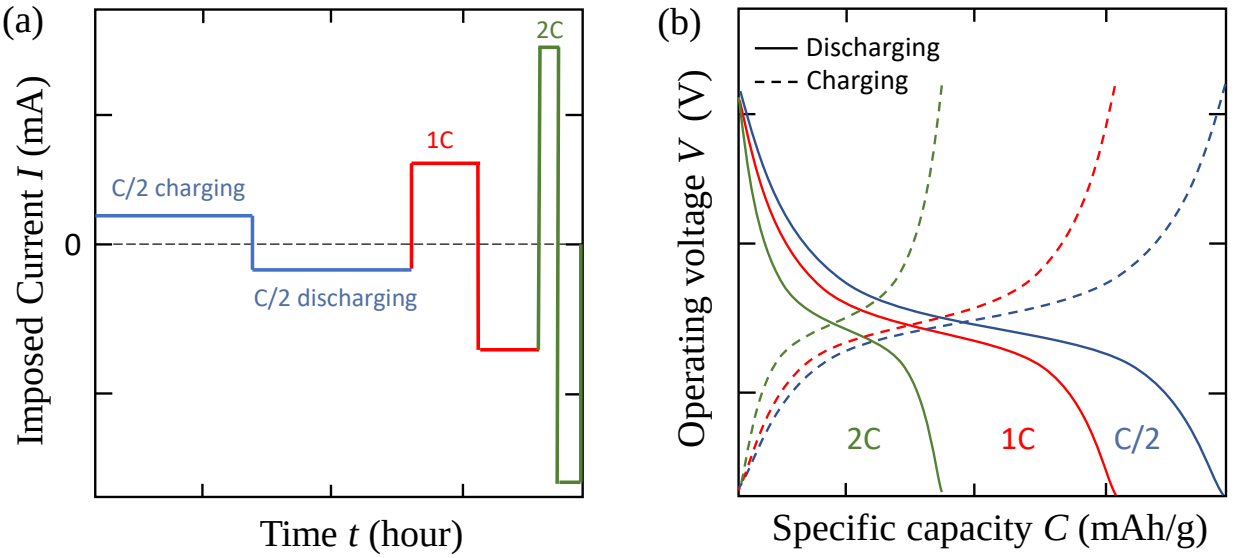

Figure 1.2: (a) Schematic of applied current I as a function of time t and (b) operating voltage $V(x,T)$ as a function of specific capacity C during galvanostatic cycling at three different C-rates.

Galvanostatic cycling also known as constant current cycling is one of the fundamental electrochemical testing methods for batteries. Figure 1.2(a) shows the imposed current I as a function of time t. During galvanostatic cycling, a constant current is applied until the desired cell voltage is reached. The operating voltage of the device is measured during cycling. In battery systems, the charge and discharge current in galvanostatic cycling are often expressed as a C-rate. The C-rate is a measure of the rate at which the battery is charged or discharged based on its theoretical specific capacity. For instance, 1C means that the current applied during galvanostatic cycling can completely charge or discharge the

theoretical specific capacity of the battery in one hour. Figure 1.2(b) illustrates how the specific capacity of the device decreases with increasing C-rate due to the increase in the overpotential $\eta(x,T) = U_{ocv}(x,T) - V(x,T)$ [42, 43].

1.3.2 Cyclic voltammetry

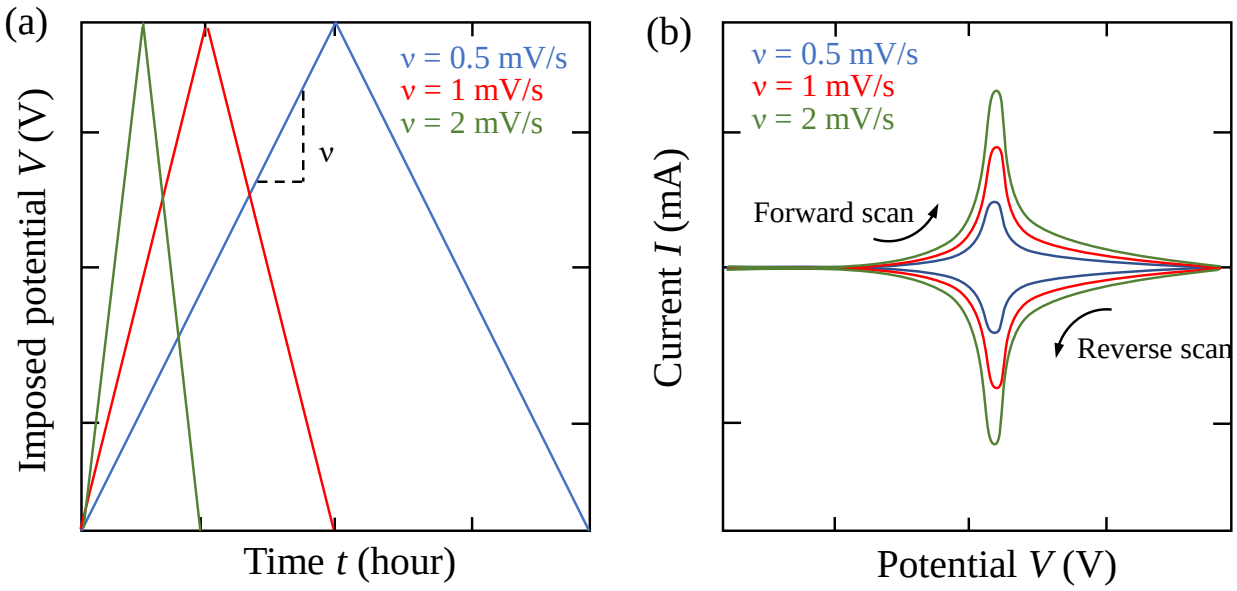

Figure 1.3: (a) Schematic of imposed potential $V(x,T)$ as a function of time t and (b) measured current I as a function of imposed potential $V(x,T)$ during cyclic voltammetry at three different scan rates ν.

Cyclic voltammetry (CV) is another electrochemical characterization method imposing a triangular potential as a function of time [Figure 1.3(a)] while the resulting current is measured simultaneously. The scan rate ν represents the rate of voltage change with time, as illustrated in Figure 1.3(a). During the forward scan, the imposed potential increases with time and lithium-ions deintercalate from active materials in the electrode. In the beginning of the forward scan, the measured current increases over time until the reduction potential of active material in the electrode is reached. After the reduction potential is reached, the measured current decreases and forms an oxidation peak in cyclic voltammogram as lithium-ions in the active material are depleted [Figure 1.3(b)] [42]. On the other hands, during the

reverse scan, the imposed potential decreases with time and the active materials undergo lithiation. If the active materials are reversible, the reduction peak is located at the same potential as the oxidation peak. Figure 1.3(b) shows that the measured current increases with increasing scan rate. This is because larger current is needed to force the redox reaction to occur at a required rate [44].

1.3.3 Galvanostatic intermittent titration technique

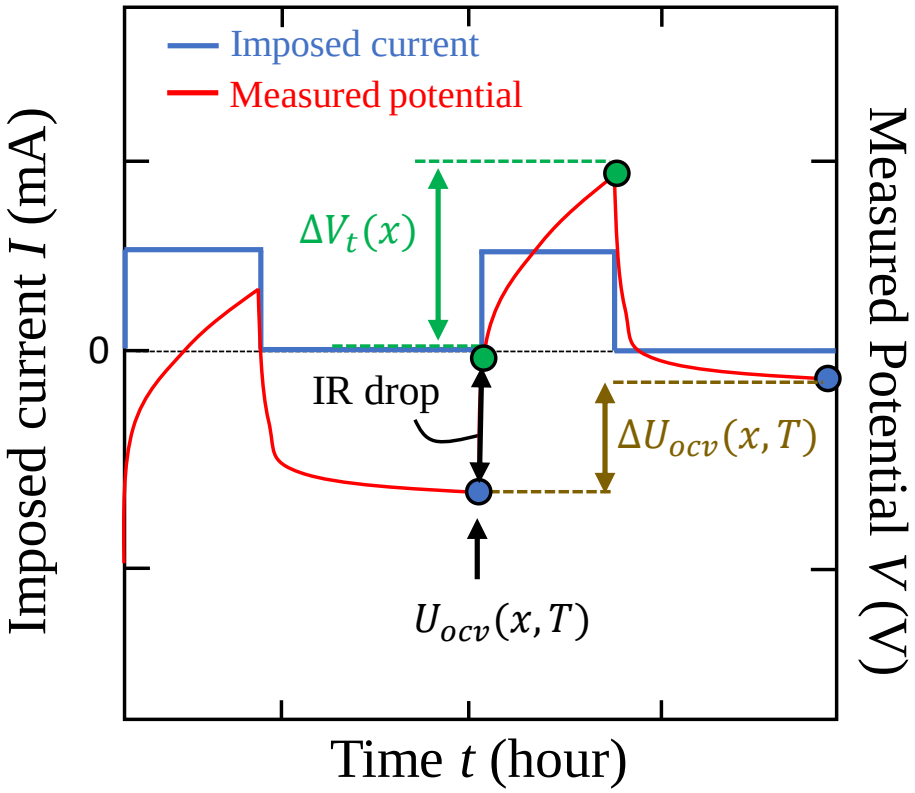

Figure 1.4: Schematic of imposed current I and measured potential $V(x,T)$ as a function of time t during Galvanostatic intermittent titration technique.

Galvanostatic intermittent titration technique (GITT) is another electrochemical characterization method to measure the open circuit voltage $U_{ocv}(x,T)$ of the device as well as the apparent diffusion coefficient of the ion $D(x,T)$ into the electrode. Figure 1.4 shows the imposed current and measured potential during GITT. The procedure of GITT consists of

a series of constant current pulses followed by a period of relaxation. The $U_{ocv}(x,T)$ of the battery is the potential after relaxation when thermodynamic equilibrium has been reached as shown as blue dots in the Figure 1.4. The key in the GITT is that long enough relaxation time is needed for the device to reach its thermodynamic equilibrium. Typically, when the change in voltage is less than 5 mV/hour, thermodynamic equilibrium is considered to be reached and the corresponding cell potential is $U_{ocv}(x,T)$ [45].

In addition, the apparent diffusion coefficient $D(x,T)$ of ions into the electrode can be estimated by combining GITT and Fick's second law of diffusion given by [45],

$$D(x,T) = \frac{4}{\pi\tau}\left(\frac{V_e}{A_e}\right)^2\left(\frac{\Delta U_{ocv}(x,T)}{\Delta V_t(x,T)}\right)^2. \tag{1.14}$$

Here, τ is the duration of the GITT current pulse, A_e and V_e are the surface area and the volume of the electrode, respectively. In addition, $\Delta V_t(x,T)$ is the change in the cell potential as a result of the imposed current pulses excluding the IR drop at the beginning of the current pulse, and $\Delta U_{ocv}(x,T)$ is the change in the open circuit voltage between two consecutive current pulses [Figure 1.4]. Here, IR drop is typically considered as the sharp change in the potential for the first one millisecond from the beginning of the current pulse [46].

1.3.4 Potentiometric entropy measurement technique

The entropic potential $\partial U_{ocv}(x,T)/\partial T$ of the coin cells is measured as functions of lithium composition x using the potentiometric entropy measurement technique. In brief, the overall process is very similar to GITT discussed previously. The potentiometric entropy measurement technique consists of imposing a series of constant current pulses followed by a period of relaxation. During the relaxation period, the temperature of the coin cell is varied typically from 15 °C to 25 °C in 5 °C increments using a thermoelectric cold plate in contact with the coin cell. The corresponding coin cell voltage evolution is recorded with a high accuracy potentiostat (Figure 1.5). The key in the potentiometric measurement is that the coin cell needs to be in thermodynamic equilibrium before imposing the next temperature step during the relaxation period. To do so, two conditions are simultaneously checked that

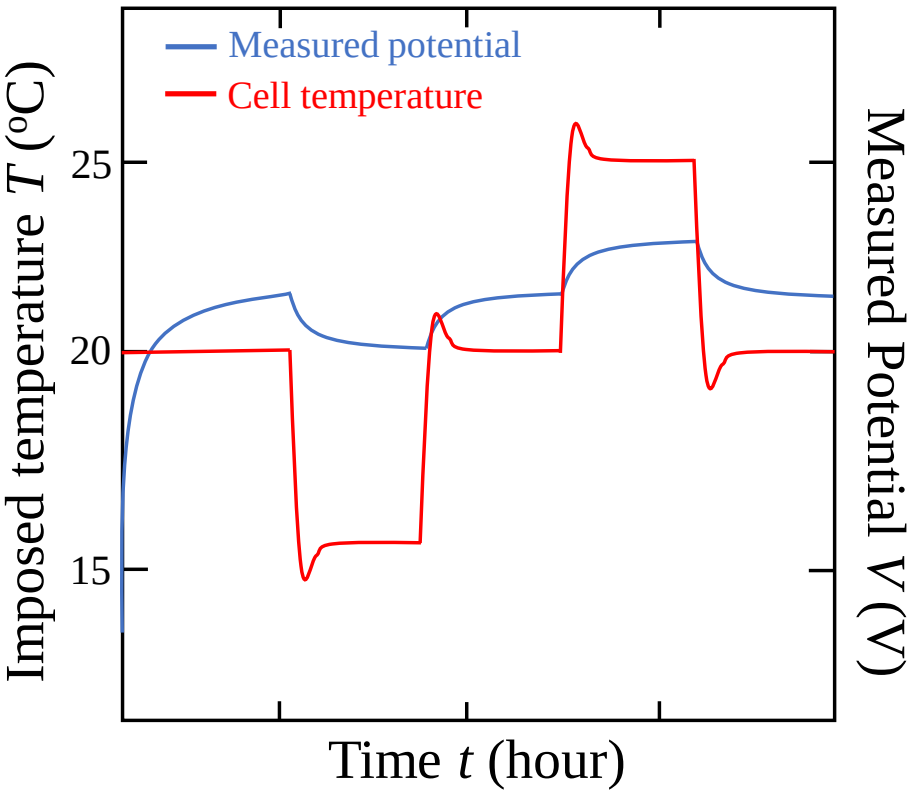

Figure 1.5: Schematic of cell temperature T and measured open circuit voltage $U_{ocv}(x,T)$ as a function of time t during potentiometric entropy measurement technique.

(i) the temperature difference between the cold plate and the top of the coin cell surface is less than 0.1 °C and (ii) the time rate of change of the open circuit voltage $\partial U_{ocv}(x,T)/\partial t$ is less than 5 mV/h.

1.4 Calorimetry

In this section, different contributions of heat generation of a battery system is discussed. In addition, this section presents the energy balance of a battery system upon cycling.

1.4.1 Heat generation in battery system

The total instantaneous heat generation rate $\dot{Q}_T(x,T)$ (in W) in a two-electrode cell can be divided into four contributions namely (1) Joule heating $\dot{Q}_J(x,T)$, (2) reversible entropic heat generation $\dot{Q}_{rev}(x,T)$, (3) enthalpy of mixing $\dot{Q}_{mix}(x,T)$, and (4) heat generation due to side reactions $\dot{Q}_{sr}(x,T)$. Thus, $\dot{Q}_T(x,T)$ can be expressed as [47–50],

$$\dot{Q}_T(x,T) = \dot{Q}_J(x,T) + \dot{Q}_{rev}(x,T) + \dot{Q}_{mix}(x,T) + \dot{Q}_{sr}(x,T) \tag{1.15}$$

where $\dot{Q}_T(x,T)$ is negative when the electrode absorbs heat and positive when it releases heat.

Under isothermal conditions, the exothermic Joule heating $\dot{Q}_J(x,T)$ associated with irreversible resistive losses can be written as [47–50],

$$\dot{Q}_J(x,T) = I[V(x,T) - U^{avg}(x,T)]. \tag{1.16}$$

Here, I is the applied current and $U^{avg}(x,T)$ is the open circuit voltage evaluated at the volume-averaged concentration of lithium ion in the cell considering a single electrochemical reaction [51]. Specifically, $U^{avg}(x,T)$ is "the potential to which the cell would relax if the current was interrupted [49]." In practice, $U^{avg}(x,T)$ can be measured using GITT at the same C-rate as that used for the calorimetric measurements provided that the materials can cycle sufficiently fast. In addition, $[V(x,T)$ - $U^{avg}(x,T)]$ is the so-called battery overpotential corresponding to the voltage drop due to internal resistance.

In addition, the reversible entropic heat generation rate $\dot{Q}_{rev}(x,T)$ associated with the changes in the entropy of the battery upon cycling can be expressed as [47–49]

$$\dot{Q}_{rev}(x,T) = IT\frac{\partial U^{avg}(x,T)}{\partial T}. \tag{1.17}$$

Under extremely small current, Li is uniformly distributed within the cell and the operating voltage $V(x,T)$ is equal to the open circuit voltage $U_{ocv}(x,T)$, i.e., $V(x,T) = U^{avg}(x,T) = U_{ocv}(x,T)$. Then, $\dot{Q}_J(x,T) \simeq 0$ and heat generation is solely due to $\dot{Q}_{rev}(x,T)$ [52]. However, under high current, $\dot{Q}_J(x,T)$ dominates [52] and Li concentration gradients form within the working electrode and electrolyte due to mass transport resistance.

The heat generation rate from enthalpy of mixing $\dot{Q}_{mix}(x,T)$ due to the ion concentration gradients in the working electrode and electrolyte caused by diffusion limitation in the LIB can be written as [47–49]

$$\dot{Q}_{mix}(x,T) = -\int_{V_\infty} \sum_i [\bar{h}_i(x,T) - \bar{h}_i^{avg}(x,T)] \frac{\partial c_i}{\partial t} dV. \tag{1.18}$$

Here, V_∞ is the volume of the cell, c_i is the local concentration of ion species i. In addition, $\bar{h}_i(x,T)$ and $\bar{h}_i^{avg}(x,T)$ are the local and the volume-averaged partial molar enthalpy of ion species i, respectively. The enthalpy of mixing is mainly caused by four different ionic concentration gradients (i) across the electrolyte due to mass transfer resistance, (ii) across the electrode caused by non-uniform current distribution, (iii) within vacancies of the electrode, and (iv) within intercalated Li in the electrode due to electrochemical reactions [51, 53]. In general, the ionic concentration gradient of the intercalated Li in the electrode is the dominant contribution to the enthalpy of mixing in LIBs [49]. Thus, if the transport of Li^+ ion in the electrode is fast, $\dot{Q}_{mix}(x,T)$ should remain small.

Most calorimetry studies on LIBs have neglected the heat generation caused by side reaction $\dot{Q}_{sr}(x,T)$ [47–49]. Indeed, undesirable side reactions are prevented by cycling the device in an appropriate potential range [54]. Then, the aging process of LIBs occurs at relatively slow rates [47] and the associated $\dot{Q}_{sr}(x,T)$ is negligible compare to $\dot{Q}_J(x,T)$, $\dot{Q}_{rev}(x,T)$, and $\dot{Q}_{mix}(x,T)$ early in the LIB's life [48].

Moreover, the total thermal energy Q_T (in J) dissipated over a charging/discharging cycle as well as the heat released in the form of Joule heating Q_J and enthalpy of mixing Q_{mix} can be calculated as [48]

$$Q_i = \oint_{cycle} \dot{Q}_i(x,T)\mathrm{d}t \quad \text{with } i = \ T,\ J,\ rev, \text{ or } mix \tag{1.19}$$

Note that integrating the reversible heat generation rate $\dot{Q}_{rev}(x,T)$ with respect to time over a cycle yields zero, i.e., Q_{rev}=0.

Finally, the net electrical energy losses ΔE_e (in J) over a charging/discharging cycle is the difference between the electrical energy delivered during charging and that recovered during discharging. Graphically, ΔE_e is the area enclosed by the hysteric voltage $V(x,T)$

vs. the charge transferred q and can be written as [48, 50]

$$\Delta E_e = \oint_{cycle} V(x,T)\mathrm{d}q = \oint_{cycle} V(x,T)I\mathrm{d}t. \tag{1.20}$$

Here, I is the current such that I=dq/dt. Based on the first law of thermodynamics, the total thermal energy Q_T dissipated during a cycle is equal to the net electrical energy loss ΔE_e, i.e.,

$$\Delta E_e = Q_J + Q_{mix} = Q_T. \tag{1.21}$$

This relationship has been validated experimentally with LIBs with electrodes made of $TiNb_2O_7$ [50], PNb_9O_{25} [55], and $Ti_2Nb_2O_9$ [56].

1.4.2 Energy balance

The total thermal energy Q_T (in J) released during a cycle as well as the irreversible heat dissipated in the form of Joule heating Q_J and enthalpy of mixing Q_{mix} can be expressed as [48]

$$Q_i = \oint_{cycle} \dot{Q}_i(x,T)\mathrm{d}t \quad \text{with } i = \ T,\ J,\ rev \text{ or } mix \tag{1.22}$$

By definition, integrating the reversible heat generation rate $\dot{Q}_{rev}(x,T)$ with respect to time over an entire cycle should vanish, i.e., Q_{rev}=0.

On the other hand, the net electrical energy losses ΔE_e (in J) corresponds to the difference between the electrical energy provided during charging and that recovered during discharging and is illustrated by the hysteric voltage $V(x,T)$ profile [48, 50]. Thus, ΔE_e is expressed as [48]

$$\Delta E_e = \oint_{cycle} V(x,T)\mathrm{d}q = \oint_{cycle} V(x,T)I\mathrm{d}t \tag{1.23}$$

where q is the charge transferred upon electrochemical reaction so that I=dq/dt. Thermodynamically, the total thermal energy Q_T dissipated during a full cycle should be equal to ΔE_e, i.e., ΔE_e=$Q_J + Q_{mix} = Q_T$ [50].

1.5 Motivation of the present study

As previously mentioned, LIBs are the most widely used secondary batteries. While significant progress has been made in characterization of LIBs, the importance of entropic potential $\partial U_{ocv}(x,T)/\partial T$ has been underestimated. As previously discussed, understanding how $\partial U_{ocv}(x,T)/\partial T$ varies with respect to x upon cycling can inform how the entropy of the active material in the electrode change with lithiation/delithiation [Eq.(1.11)]. However, interpretation of $\partial U_{ocv}(x,T)/\partial T$ remains ambiguous in many literature [57–63]. In particular, it remains unclear as to how characteristic features in the $\partial U_{ocv}(x,T)/\partial T$ curve as a function of x are to be correlated with the occurrence of structural changes occurring in the electrode. There is, therefore, a scientific need to revisit the interpretation of entropic potential measurements to deepen our understanding of physicochemical phenomena occurring in a battery system. In fact, the entropy of a solid arises from a variety of electronic and atomic excitations. There are three important sources of the entropy in an intercalation compound [64, 65]. One emerges from configurational degrees of freedom associated with all possible ways of arranging Li ions and vacancies over the interstitial sites of the intercalation compound [66]. A second contribution arises from vibrational excitations involving both the host ions and the Li ions [67]. A third is due to electronic excitations, assuming a variety of forms of density of states. Thus, analyzing these different contributions can shed light on the behavior of the entropic potential $\partial U_{ocv}(x,T)/\partial T$ of the battery.

Furthermore, heat generation in LIBs during cycling can be used to identify thermal signatures associated with various phenomena. In fact, previous *operando* isothermal calorimetry studies on supercapacitors have revealed thermal signatures associated with a variety of physicochemical phenomena including ion adsorption/desorption [68–71], electrolyte decomposition at high voltages and/or high temperatures [69, 72], ion intercalation [69], overscreening effect [72, 73], Thus, performing *operando* isothermal calorimetry measurements on LIBs can also reveal many thermal signatures associated with different physicochemical phenomena that cannot be detected with conventional electrochemical characterization method. Moreover, excessive heat generation can result in temperature rise in LIBs. Such tempera-

ture rise can accelerate ageing and degrade the battery capacity as it enhances irreversible intercalation in the electrode [74]. Temperature rise can also cause thermal expansion of the battery components leading to short-circuit due to the resulting electric contact between electrodes [75]. Therefore, entropic and calorimetric characterization in the battery material is needed to not only gain more insight about the physicochemical phenomena occurring in the battery but also design thermal management system for batteries.

1.6 Objectives of the present study

The present study aims to design, assemble, validate, and operate a potentiometric entropy measurement setup to measure the open circuit voltage U_{ocv} and the entropic potential $\partial U_{ocv}(x,T)/\partial T$ of LIBs. In addition, this study plans to develop an interpretative guide of U_{ocv} and $\partial U_{ocv}(x,T)/\partial T$ measurements for different charging/discharging mechanisms by reviewing and clarifying the associated fundamental thermodynamic relationships and properties of LIB systems. To do so, different contributions to Gibbs free energy and entropy, such as configurational, vibrational, and electronic contributions, were accounted for in a physical model developed to deepen our understanding. Furthermore, U_{ocv} and $\partial U_{ocv}(x,T)/\partial T$ of different LIB systems were investigated to experimentally validate the interpretative guide.

The present study pursues to identify the entropic and calorimetric signatures of the different physicochemical phenomena taking place during charging/discharging at the working electrode consisting of the selected Wadsley-Roth shear phase materials and at the lithium metal counter electrode. Potentiometric entropy and calorimetry measurements were combined with XRD measurements to understand the structural changes in the selected Wadsley-Roth shear phase materials upon lithiation/delithiation. Furthermore, the instantaneous heat generation rate measurements at each electrodes during cycling was used to deepen our understanding into electrochemical phenomena resulting in heat dissipation. Moreover, this study aims to investigate the effect of particle size of selected Wadsley-Roth shear phase battery materials on the heat generation in LIB systems.

1.7 Organization of the document

Chapter 2 reviews and clarifies the fundamental thermodynamic relationships and properties of lithium-ion battery systems having intercalation compounds and presents an interpretative guide to open circuit voltage and entropic potential measurements. Chapter 3 presents the potentiometric entropy measurements as well as *operando* calorimetry measurements to gain insight about the origins of rapid rate performance of the Wadsley-Roth shear phase compound $TiNb_2O_7$. Chapter 4 and Chapter 5 extend the investigation of Chapter 3 to other Wadsley-Roth shear phase materials namely PNb_9O_{25} and $(W_{0.2}V_{0.8})_3O_7$, respectively. Finally, Chapter 6 summarizes the finding of this PhD thesis and provides recommendations for future research.

CHAPTER 2

Thermodynamic analysis and interpretative guide to entropic potential measurements of lithium-ion battery electrodes

This chapter aims to review and clarify fundamental thermodynamic relationships in order to develop an interpretative guide to $U_{ocv}(x,T)$ and $\partial U_{ocv}(x,T)/\partial T$ *operando* measurements so as to gain insights into the different physicochemical phenomena occurring in LIBs under different charging/discharging scenarios. Phenomena of interest include intercalation in homogeneous solid solutions, cation ordering, first-order phase transitions accompanied by two-phase coexistence, and first-order transitions with an intermediate phase. The thermodynamic relationships are rigorously derived and systematically illustrated with experimental data for various LIB materials. The analysis starts with a rigorous treatment of *ideal* intercalation compounds, which capture the first-order contributions to $U_{ocv}(x,T)$ and $\partial U_{ocv}(x,T)/\partial T$ due to configurational, vibrational and electronic excitations. Deviations from ideality are then discussed in the context of experimentally measured $U_{ocv}(x,T)$ and $\partial U_{ocv}(x,T)/\partial T$ curves of important intercalation compounds.

2.1 Analysis

2.1.1 Intercalation in homogeneous solid solution

Layered materials such as TiS_2 [76] and $LiCoO_2$ [77,78] have been widely investigated as Li-ion battery electrode materials. They form homogeneous solid solutions and maintain their crystal structure over large intervals of Li concentration. These layered materials consist of

a stacking of two-dimensional transition metal sulfide or oxide sheets that are held together by van der Waals forces in the absence of Li [79,80]. Li^+ ions can intercalate into the vacant sites between the two-dimensional sheets of the host. The Gibbs free energy $g_{Li_xMA}(x,T)$ of an intercalation compound Li_xMA that forms a homogeneous solid solution upon lithiation is a convex function with respect to the lithium composition x as schematically illustrated in Figure 2.1(a). In addition, Figure 2.1(b) illustrates that the lithium chemical potential $\mu_{Li}^{Li_xMA}(x,T)$ of Li_xMA monotonically decreases with increasing lithium composition x for a homogeneous solid solution. Figure 2.1(c) schematically plots the entropy $s_{Li_xMA}(x,T)$ of Li_xMA as a function of the Li composition. For a solid solution, $s_{Li_xMA}(x,T)$ is a concave function with respect to the lithium composition x. Finally, Figure 2.1(d) plots the open circuit voltage $U_{ocv}(x,T)$ and the entropic potential $\partial U_{ocv}(x,T)/\partial T$ of the battery for a host material MA that forms a homogeneous solid solution during Li insertion. Overall, lithium intercalation in a homogeneous solid solution is characterized by a monotonically decreasing $U_{ocv}(x,T)$ and $\partial U_{ocv}(x,T)/\partial T$ with lithium composition x.

The insertion of Li into Li_xMA alters a variety of properties of the host material, including its lattice parameters, electronic structure, and vibrational frequencies. In general, Li ions within the host also interact with other Li ions, with the strength and nature of these interactions determining whether the intercalation compound favors a solid solution, a series of ordered phases or a state of two-phase coexistence. Before considering real intercalation compounds where such interactions are present, important insights can be generated by studying the electrochemical properties of *ideal* intercalation compounds, defined as compounds in which interactions among Li ions and between Li and the host can be neglected. An *ideal* intercalation compound serves as a useful model to obtain bounds and to identify first-order trends of various thermodynamic quantities.

The Gibbs free energy of a solid arises from a variety of electronic and atomic excitations. There are three important sources of the Gibbs free energy in an intercalation compound [64, 65]. One emerges from configurational degrees of freedom associated with all possible ways of arranging Li ions and vacancies over the interstitial sites of the intercalation compound [66]. A second contribution arises from vibrational excitations involving both the host ions and

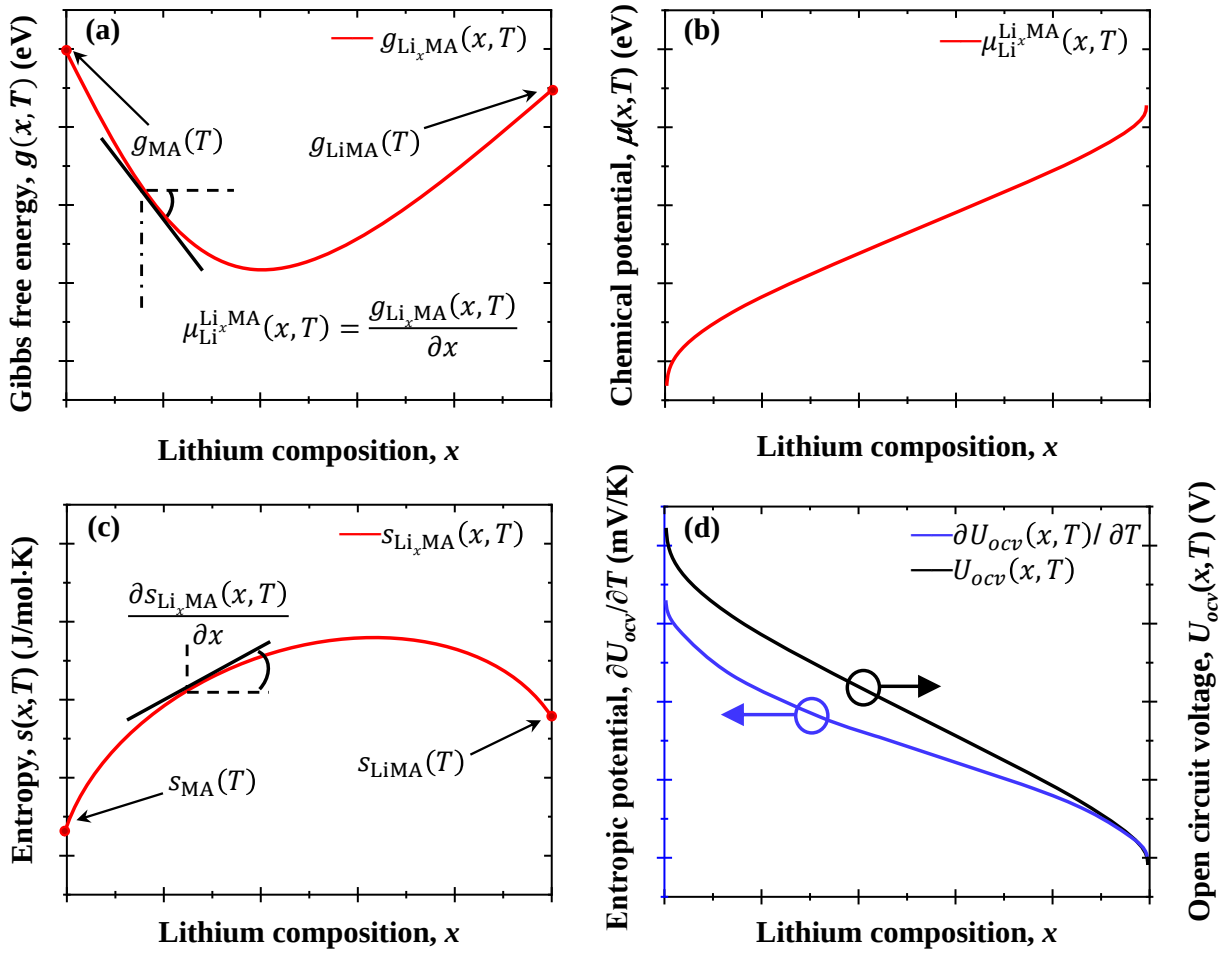

Figure 2.1: (a) Schematic plots of Gibbs free energy $g_{\mathrm{Li}_x\mathrm{MA}}(x,T)$, (b) chemical potential $\mu_{\mathrm{Li}}^{\mathrm{Li}_x\mathrm{MA}}(x,T)$, (c) entropy $s_{\mathrm{Li}_x\mathrm{MA}}(x,T)$ of $\mathrm{Li}_x\mathrm{MA}$, and (d) open circuit voltage $U_{ocv}(x,T)$ and entropic potential $\partial U_{ocv}(x,T)/\partial T$ of the battery cell as functions of lithium composition x at temperature T when MA forms a homogeneous solid solution upon lithiation.

the Li ions [67]. A third is due to electronic excitations, assuming a variety of forms, as described later. While it is generally not possible to disentangle these contributions for real solids, for *ideal* intercalation compounds, it is possible to express the total Gibbs free energy of an *ideal* intercalation compound as a simple sum of these three contributions, i.e.,

$$g(x,T) = g^{conf}(x,T) + g^{vib}(x,T) + g^{elec}(x,T) \tag{2.1}$$

where $g^{conf}(x,T)$, $g^{vib}(x,T)$ and $g^{elec}(x,T)$ are the configurational, vibrational, and electronic Gibbs free energies, respectively, of the compound. Based on Eq.(1.10), the entropy can also

be expressed as the sum of individual contributions according to

$$s(x,T) = s^{conf}(x,T) + s^{vib}(x,T) + s^{elec}(x,T). \tag{2.2}$$

The following sections derive expressions for the entropy of an ideal intercalation compound associated with configurational $s^{conf}(x,T)$, vibrational $s^{vib}(x,T)$, and electronic $s^{elec}(x,T)$ excitations. These expressions are then used to shed light on the behavior of the entropic potential $\partial U_{ocv}(x,T)/\partial T$ of the battery.

2.1.1.1 Configurational entropy, $s^{conf}_{\mathbf{Li}_x\mathbf{MA}}(x,T)$

The configurational entropy of an intercalation compound, $\mathrm{Li}_x\mathrm{MA}$, exhibiting a solid solution is bounded by the *ideal* solution configurational entropy expressed as [81]

$$s^{conf}_{\mathrm{Li}_x\mathrm{MA}}(x,T) = -k_B \left[x\ln(x) + (1-x)\ln(1-x)\right]. \tag{2.3}$$

The configurational entropies of stoichiometric LiMA and MA are equal to zero (i.e., s^{conf}_{LiMA}=0 and s^{conf}_{MA}=0) since no disorder exists among Li ions and vacancies when all Li sites are fully filled ($x=1$) or completely empty ($x=0$). It is also interesting to note that this contribution is independent of the material MA. Figure 2.2(a) plots $s^{conf}_{\mathrm{Li}_x\mathrm{MA}}(x,T)$ of $\mathrm{Li}_x\mathrm{MA}$ predicted by Eq.(2.3) as a function of lithium composition x, and featuring a maximum at half filling or $x=0.5$.

The configurational entropy of a real intercalation compound is always smaller than the *ideal* solution entropy since interactions among Li ions lead to some degree of short-range order and therefore a lowering of the entropy. There are also instances when the Li ions and vacancies adopt a long-range ordered pattern at a specific stoichiometric composition characterized by a supercell periodicity [82]. Then, the configurational entropy for an ordered phase exhibits a minimum in the form of a cusp at the stoichiometric ordering concentration, as discussed later.

Finally, since the configurational entropy of the metallic Li anode vanishes, the contribution to the entropic potential from configurational excitations for an *ideal* solid solution

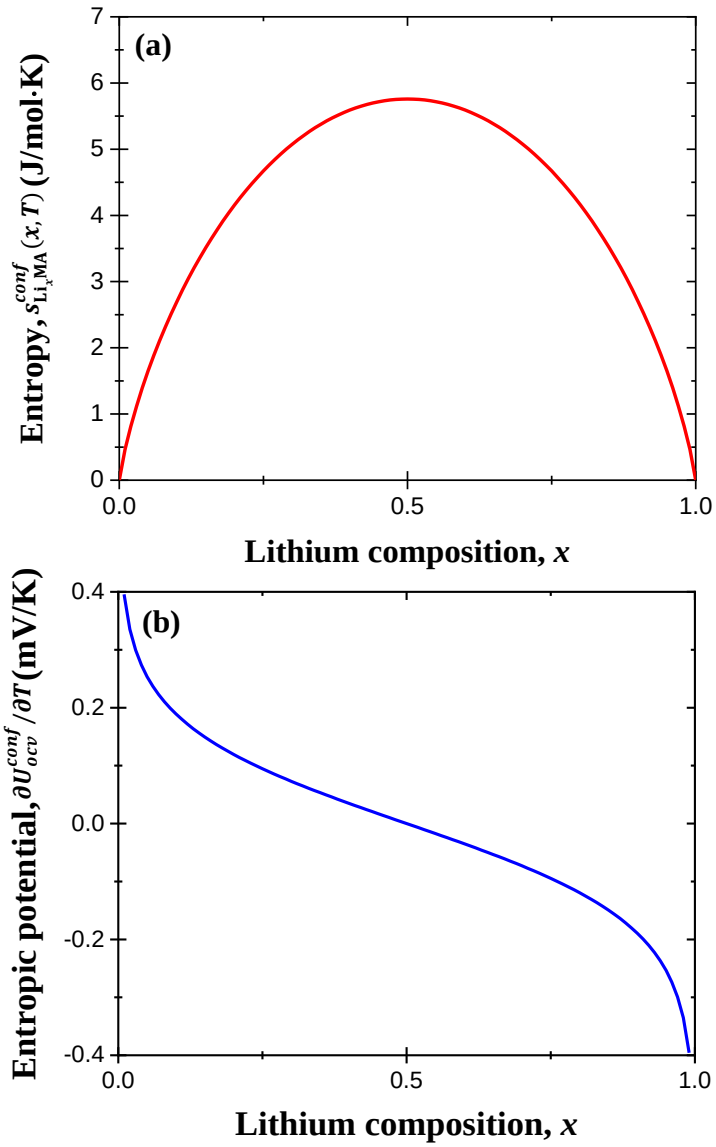

Figure 2.2: (a) Calculated configurational entropy $s^{conf}_{\mathrm{Li}_x\mathrm{MA}}(x,T)$ of Li_xMA [Eq.(2.3)], and (b) configurational entropic potential $\partial U^{conf}_{ocv}(x,T)/\partial T$ of the battery cell [Eq.(2.4)] as functions of lithium composition x for an *ideal* homogeneous solid solution Li_xMA.

simplifies to

$$\frac{\partial U^{conf}_{ocv}(x,T)}{\partial T} = \frac{1}{e}\frac{\partial s^{conf}_{\mathrm{Li}_x\mathrm{MA}}(x,T)}{\partial x} = -\frac{k_B}{e}\ln\left(\frac{x}{1-x}\right). \tag{2.4}$$

Figure 2.2(b) shows that the configurational entropic potential $\partial U^{conf}_{ocv}(x,T)/\partial T$ decreases monotonically for an *ideal* homogeneous solid solution Li_xMA upon lithiation.

2.1.1.2 Vibrational entropy, $s^{vib}(x,T)$

In general, the vibrational entropy is a function of the lithium composition x due to the change in the number of Li ions and to changes in the nature and strength of bonds between the host ions as Li intercalates into the crystal. It can be quantified using the harmonic approximation and depends on the stiffness of interatomic bonds within the compound [67].

The vibrational Helmholtz free energy $f^{vib}_{\mathrm{MA}}(T)$ of the host intercalation compound MA at constant volume v can be expressed as an integral over all phonon-mode frequencies according to [83]

$$f^{vib}_{\mathrm{MA}}(T) = k_B T \int_0^\infty \left[\frac{\hbar\omega}{2k_B T} + \ln\left(1 - e^{\hbar\omega/k_B T}\right)\right] \mathcal{D}^{vib}(\omega) d\omega. \tag{2.5}$$

Here, $\hbar$ is the reduced Planck constant and $\mathcal{D}^{vib}(\omega)$ is the phonon density of states corresponding to the number of vibrational normal modes per unit cell of the intercalation compound with a frequency ω. It is determined from the phonon dispersion relationship and, in general, depends on volume. By definition, the Gibbs free energy $g^{vib}_{\mathrm{MA}}(T)$ is the characteristic potential at constant pressure of compound MA and is related to the Helmholtz free energy $f^{vib}_{\mathrm{MA}}(T)$ according to

$$g^{vib}_{\mathrm{MA}}(T) = f^{vib}_{\mathrm{MA}}(T) + Pv(T) \tag{2.6}$$

where $v(T)$ is the equilibrium volume per unit cell at the imposed pressure P. Then, the vibrational entropy $s^{vib}_{\mathrm{MA}}(T)$ can be extracted from the vibrational Gibbs free energy using Eq.(1.10).

A change in the lithium composition of the intercalation compound MA can affect its vibrational free energy in two ways. First, the insertion of Li ions into MA introduces additional vibrational modes, three for each inserted Li ion. Second, a change in the lithium composition x affects the stiffness of the bonds of the host intercalation compound. For example, the redox processes on the transition metals that accompany variations in x often lead to some degree of rehybridization between the transition metals and the anions [84,85], which in turn affects the stiffness of their bonds.

As with configurational entropy, it is useful to consider the vibrational entropy for an ideal intercalation compounds. With respect to vibrational excitations, we define an *ideal* intercalation compound as one that accommodates Li without changing the vibrational spectrum and the phonon density of states $\mathcal{D}^{vib}(\omega)$ of the host MA. Furthermore, we assume that the vibrational spectrum of the Li ions can be approximated by the Einstein model with a characteristic frequency ω_{Li} independent of the overall lithium composition and volume of the host. Under these assumptions, the vibrational Gibbs free energy $g^{vib}_{\mathrm{Li}_x\mathrm{MA}}(x,T)$ of $\mathrm{Li}_x\mathrm{MA}$ can be expressed as

$$g^{vib}_{\mathrm{Li}_x\mathrm{MA}}(x,T) = g^{vib}_{\mathrm{MA}}(T) + g^{vib}_{\mathrm{Li}}(x,T) \tag{2.7}$$

where $g^{vib}_{\mathrm{MA}}(T)$ is the vibrational free energy of the host without Li [Eq.(2.6)] and $g^{vib}_{\mathrm{Li}}(x,T)$ captures the contributions to the vibrational free energy from Li vibrations in interstitial sites of the MA host. Assuming a constant characteristic vibrational frequency ω_{Li} for Li, $g^{vib}_{\mathrm{Li}}(x,T)$ can be written as

$$g^{vib}_{\mathrm{Li}}(x,T) = 3\left[\frac{\hbar\omega_{\mathrm{Li}}}{2} + k_BT\ln\left(1-e^{-\hbar\omega_{\mathrm{Li}}/k_BT}\right)\right]x. \tag{2.8}$$

This expression emerges when imposing the approximations of ideality as previously defined in the evaluation of the vibrational partition function, as shown in Appendix A Combining Eqs.(1.10), (2.7), and (6.11) yields the expression of the vibrational entropy

$$s^{vib}_{\mathrm{Li}_x\mathrm{MA}}(x,T) = s^{vib}_{\mathrm{MA}}(T) - 3k_B\left[\ln\left(1-e^{-\Theta_{\mathrm{Li}}/T}\right) - \frac{\Theta_{\mathrm{Li}}}{T}\frac{e^{-\Theta_{\mathrm{Li}}/T}}{1-e^{-\Theta_{\mathrm{Li}}/T}}\right]x \tag{2.9}$$

where $\Theta_{\mathrm{Li}} = \hbar\omega_{\mathrm{Li}}/k_B$. This expression shows that the vibrational entropy of an *ideal* intercalation compound is a linear function of the lithium composition x, as plotted in Figure 2.3(a). Figure 2.3(a) also shows that both the magnitude and the slope of $s^{vib}_{\mathrm{Li}_x\mathrm{MA}}(x,T)$ decreases with increasing ω_{Li}.

The contribution from vibrational excitations to the entropic potential for an *ideal* intercalation compound can be written, using Eq.(1.11), as

$$\frac{\partial U^{vib}_{ocv}(x,T)}{\partial T} = -\frac{1}{e}\left[3k_B\left(\ln\left(1-e^{-\Theta_{\mathrm{Li}}/T}\right) - \frac{\Theta_{\mathrm{Li}}}{T}\frac{e^{-\Theta_{\mathrm{Li}}/T}}{1-e^{-\Theta_{\mathrm{Li}}/T}}\right) + s^{\mathrm{o},vib}_{\mathrm{Li}}(T)\right] \tag{2.10}$$

where $s^{\mathrm{o},vib}_{\mathrm{Li}}(T)$ is the vibrational entropy of metallic Li. Here, $s^{vib}_{\mathrm{MA}}(T)$ disappeared upon differentiation with respect to the lithium composition x. Experimentally, the average vi-

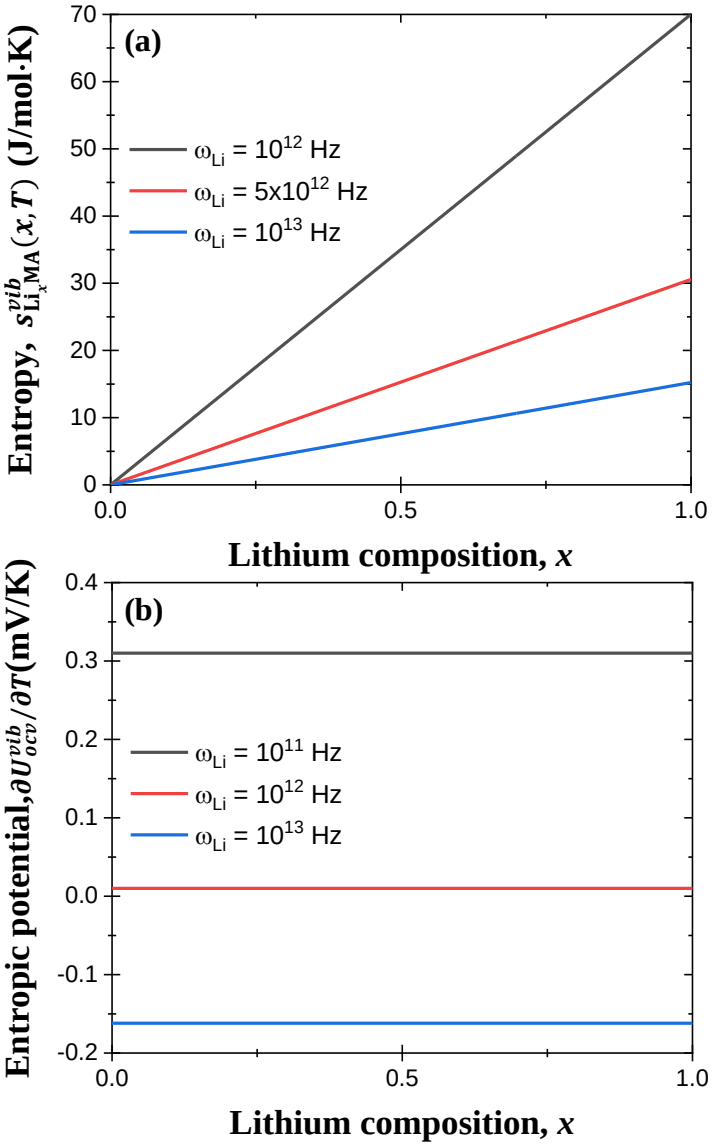

Figure 2.3: (a) Vibrational entropy $s^{vib}_{\mathrm{Li}_x\mathrm{MA}}(x,T)$ of $\mathrm{Li}_x\mathrm{MA}$ [Eq.(2.9)], and (b) vibrational entropic potential $\partial U^{vib}_{ocv}(x,T)/\partial T$ of the battery cell [Eq.(2.10)] as functions of lithium composition x for an *ideal* solid solution $\mathrm{Li}_x\mathrm{MA}$.

brational frequency ω_{Li} of metallic Li was measured to be on the order of 10^{12} Hz from slow-neutron scattering [86]. An effective vibrational frequency for metallic Li can also be estimated when assuming that the entropy of metallic Li is dominated by the vibrational entropy. This leads to an effective frequency ω_{Li} of 5.8×10^{12} Hz [41]. Figure 2.3(a) shows that the vibrational entropy $s^{vib}_{\mathrm{Li}_x\mathrm{MA}}(x,T)$ of $\mathrm{Li}_x\mathrm{MA}$ linearly increases with lithium composi-

tion x. Thus, the entropic potential $\partial U_{ocv}^{vib}(x,T)/\partial T$ of the battery cell is independent of x [Figure 2.3(b)]. In real intercalation compounds, the insertion of Li into the host introduces a composition dependence to the host vibrational entropy $s_{\mathrm{MA}}^{vib}(x,T)$ that does not cancel upon differentiation with respect to x. Furthermore, even when applying a simple Einsten model for the vibrational excitations of the intercalated Li ions, it is unlikely that the Li vibrational frequency ω_{Li} remains independent of x. Hence, in real intercalation compounds, the contribution from vibrational excitations to $\partial U_{ocv}^{vib}(x,T)/\partial T$ features a composition dependence. In binary systems, the variation of the vibrational entropy with composition x is generally assumed to be linear [64, 87, 88]. However, to the best of our knowledge, detailed studies to quantify the extent with which $s_{\mathrm{MA}}^{vib}(T)$ differs from zero in intercalation compounds have not yet been performed. Overall, the vibrational entropy $s_{\mathrm{Li}_x\mathrm{MA}}^{vib}(x,T)$ of an *ideal* homogeneous solid solution was shown to increase linearly with lithium composition x, leading to a vibrational entropic potential $\partial U_{ocv}^{vib}(x,T)/\partial T$ that is independent of x.

2.1.1.3 Electronic entropy, $s^{elec}(x,T)$

The entropy contribution $s^{elec}(x,T)$ due to electronic excitations can have a variety of forms. The entropy of itinerant electrons is generally small and negligible [81]. However, the entropy of intercalation compounds that exhibit distinct redox states that are localized on the transition metals can be sizable and is a type of configurational entropy that emerges from the many different ways of arranging distinct oxidation states over the transition metal cations [89]. If transition metals are magnetic, an additional configurational entropy may exist in association with the many possible ways of ordering local magnetic moments over the transition metal sites [90–92]. These configurational degrees of freedom associated with localized electronic states can exhibit a lithium composition dependence.

For itinerant electrons, the electronic entropy can be expressed as [83]

$$s^{elec}(x,T) = -k_B \int \left[\mathcal{F}(\epsilon)\ln\left[\mathcal{F}(\epsilon)\right] + \left[1-\mathcal{F}(\epsilon)\right]\ln\left[1-\mathcal{F}(\epsilon)\right]\right]\mathcal{D}^{elec}(\epsilon)d\epsilon \tag{2.11}$$

where $\mathcal{F}(\epsilon)$ is the Fermi-Dirac distribution and $\mathcal{D}^{elec}(\epsilon)$ is the electronic density of states per unit cell. The electronic entropy depends on the shape of the electronic density of states

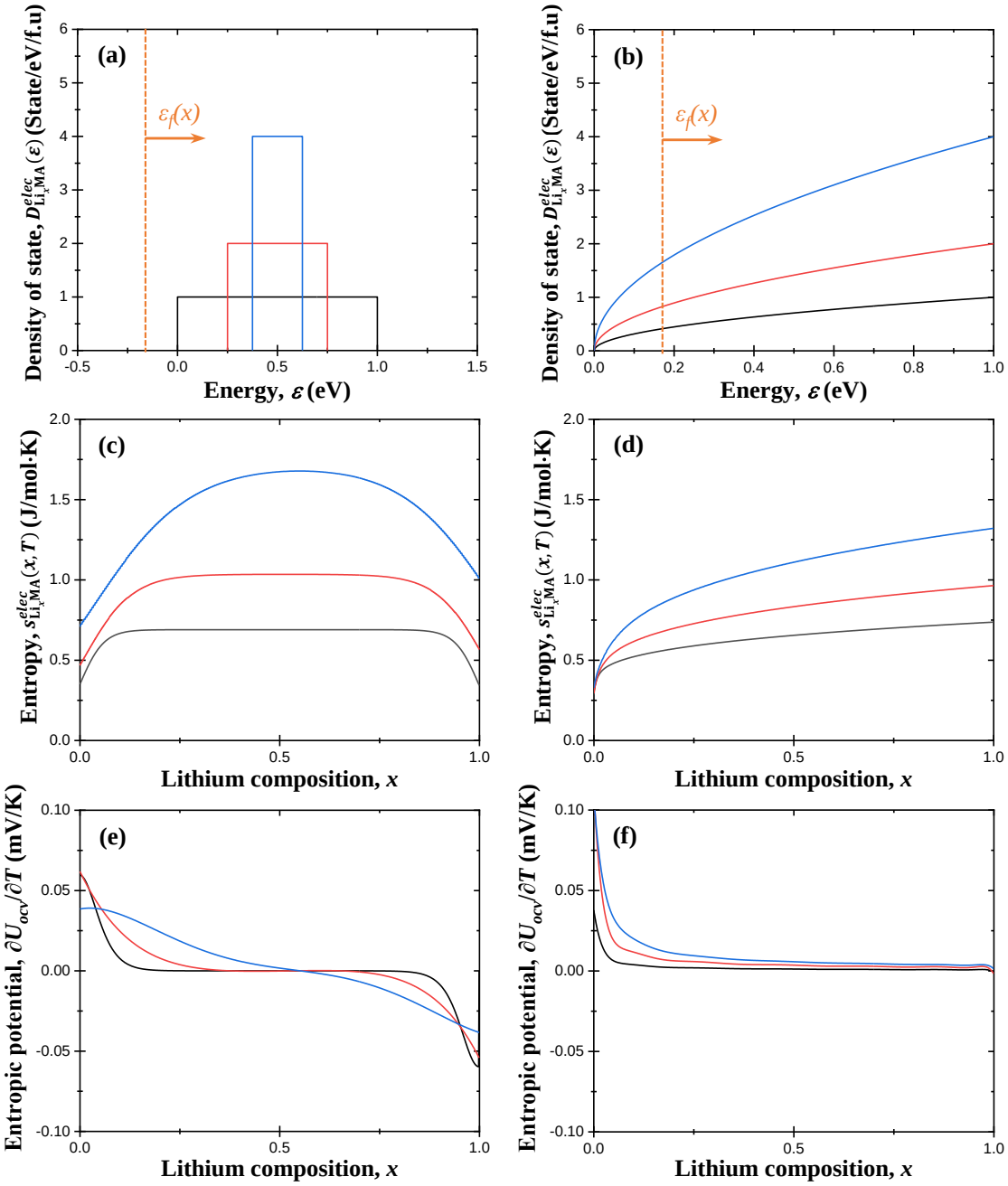

Figure 2.4: (a) Box-shaped and (b) square-root-shaped density of state $\mathcal{D}^{elec}_{\mathrm{Li}_x\mathrm{MA}}(\epsilon)$ of $\mathrm{Li}_x\mathrm{MA}$ as functions of electric energy ϵ. Electronic entropy $s^{elec}_{\mathrm{Li}_x\mathrm{MA}}(x,T)$ of $\mathrm{Li}_x\mathrm{MA}$ corresponding to (c) a box-shaped $\mathcal{D}^{elec}_{\mathrm{Li}_x\mathrm{MA}}(\epsilon)$ and (d) a square-root-shaped $\mathcal{D}^{elec}_{\mathrm{Li}_x\mathrm{MA}}(\epsilon)$, and electronic entropic potential $\partial U^{elec}_{ocv}(x,T)/\partial T$ of a battery cell for (e) a box-shaped $\mathcal{D}^{elec}_{\mathrm{Li}_x\mathrm{MA}}(\epsilon)$ and (f) a square-root-shaped $\mathcal{D}^{elec}_{\mathrm{Li}_x\mathrm{MA}}(\epsilon)$ as functions of lithium composition x.

$\mathcal{D}^{elec}(\epsilon)$ and the position of the Fermi level ϵ_F. The Li ions that intercalate into the compound generally donate their electrons to the host, thereby affecting the position of the Fermi level. The presence of Li and the donation of electrons to the host also modifies the band structure and therefore affect the electronic density of states. Thus, Li ion intercalation introduces a composition dependence to the electronic entropy of the intercalation compound.

Based on Eq.(1.11), the electronic entropic potential $\partial U_{ocv}^{elec}(x,T)/\partial T$ can be expressed as

$$\frac{\partial U_{ocv}^{elec}(x,T)}{\partial T} = \frac{1}{e}\left[\frac{\partial s_{\mathrm{Li}_x\mathrm{MA}}^{elec}(x,T)}{\partial T} - s_{\mathrm{Li}}^{\mathrm{o},elec}(T)\right] \tag{2.12}$$

where $s_{\mathrm{Li}}^{\mathrm{o},elec}(T)$ is the electronic entropy of the metallic Li anode. When the density of states of body centered cubic Li is calculated from density functional theory, $s_{\mathrm{Li}}^{\mathrm{o},elec}(T)$ evaluates to 0.16 J/mol·K (see Appendix A). In order to further investigate the shape of $\partial s_{\mathrm{Li}_x\mathrm{MA}}^{elec}(x,T)/\partial T$, it is again convenient to introduce the concept of ideality with respect to electronic excitations. We define an *ideal* intercalation compound as one whose electronic density of states are unaffected by the intercalation of Li. The only effect of Li insertion is to raise the Fermi level ϵ_f. This is equivalent to assuming a rigid band model [93]. While this assumption of ideality simplifies the analysis considerably, some degrees of freedom still remain with respect to the shape of the electronic density of states.

The electronic density of states $\mathcal{D}_{\mathrm{Li}_x\mathrm{MA}}^{elec}(\epsilon)$ could be constant as a function of the electronic energy ϵ. In this scenario, the electronic entropy $s_{\mathrm{Li}_x\mathrm{MA}}^{elec}(x,T)$ of $\mathrm{Li}_x\mathrm{MA}$ and the electronic entropic potential $\partial U_{ocv}^{elec}(x,T)/\partial T$ would be independent of the lithium composition x (See Appendix A). Other simple shapes for $\mathcal{D}^{elec}(\epsilon)$ are also possible such as a box shape and a square-root dependence on ϵ, as schematically illustrated in Figures 2.4(a) and 2.4(b), respectively. The composition dependence of the electronic entropy $s_{\mathrm{Li}_x\mathrm{MA}}^{elec}(x,T)$ for these density of states curves are shown in Figures 2.4(c) and 2.4(d). Note that for a box-shaped density of states, the area under the differently proportioned boxes are all equal to one electron per unit cell of host material. Figure 2.4(c) shows that the magnitude of the electronic entropy for the differently proportioned box-shaped $\mathcal{D}^{elec}(\epsilon)$ increases when the width of the boxes become narrower. Likewise, the magnitude of the electronic entropy for $\mathcal{D}^{elec}(\epsilon)$ with a square-root dependence on ϵ having different constant prefactors increases with increas-

ing magnitude of $\mathcal{D}^{elec}(\epsilon)$ [Figure 2.4(d)]. These results show that the electronic entropy is sensitive to the shape of the electronic density of states. Figures 2.4(e) and 2.4(f) show the electronic entropic potential $\partial U_{ocv}^{elec}(x,T)/\partial T$ corresponding to box-shaped and square-root-shaped density of states, respectively. In both cases, the magnitude of $\partial U_{ocv}^{elec}(x,T)/\partial T$ is negligible compared to that of the vibrational and configurational entropic potentials modeled in the previous sections.

2.1.1.4 Summary

For an *ideal* intercalation compound, the entropy can be expressed as the sum of individual contributions derived in previous subsections [Eq.(13)]. Figure 2.5(a) shows the calculated entropy associated with configurational $s_{\mathrm{Li}_x\mathrm{MA}}^{conf}(x,T)$, vibrational $s_{\mathrm{Li}_x\mathrm{MA}}^{vib}(x,T)$, and electronic $s_{\mathrm{Li}_x\mathrm{MA}}^{elec}(x,T)$ excitations predicted respectively by Eqs.(2.3), (2.9), and (5.7), as well as the partial entropy of the Li_xMA electrode, i.e., $s_{\mathrm{Li}_x\mathrm{MA}}(x,T) = s_{\mathrm{Li}_x\mathrm{MA}}^{conf}(x,T) + s_{\mathrm{Li}_x\mathrm{MA}}^{vib}(x,T) + s_{\mathrm{Li}_x\mathrm{MA}}^{elec}(x,T)$. Here, the vibrational frequency ω_{Li} was taken as 10^{13} Hz. The Einstein model and the square–root–shaped electronic density of state $\mathcal{D}^{elec}(\epsilon)$ were used in estimated $s_{\mathrm{Li}_x\mathrm{MA}}^{vib}(x,T)$, and $s_{\mathrm{Li}_x\mathrm{MA}}^{elec}(x,T)$, respectively. Figure 2.5(a) illustrates that $s_{\mathrm{Li}_x\mathrm{MA}}^{elec}(x,T)$ was relatively small compared to $s_{\mathrm{Li}_x\mathrm{MA}}^{conf}(x,T)$ and $s_{\mathrm{Li}_x\mathrm{MA}}^{vib}(x,T)$. Furthermore, the trend of $s_{\mathrm{Li}_x\mathrm{MA}}(x,T)$ was mostly governed by $s^{vib}(x,T)$ so that it increased with increasing lithium composition x.

Moreover, Figure 2.5(b) shows the calculated entropic potential associated with configurational $\partial U_{ocv}^{conf}(x,T)/\partial T$, vibrational $\partial U_{ocv}^{vib}(x,T)/\partial T$, and electronic $\partial U_{ocv}^{elec}(x,T)/\partial T$ excitations predicted respectively by Eqs.(2.4), (2.10), and (2.12) as well as the battery entropic potential $\partial U_{ocv}(x,T)/\partial T$. Here, $\partial U_{ocv}^{vib}(x,T)/\partial T$ was independent of lithium composition x and was negative due to the Li metal counter electrode. Likewise, $\partial U_{ocv}^{elec}(x,T)/\partial T$ was approximately constant and its magnitude was negligible compared to that of $\partial U_{ocv}^{conf}(x,T)/\partial T$ and $\partial U_{ocv}^{vib}(x,T)/\partial T$. The trend of the $\partial U_{ocv}(x,T)/\partial T$ curve was dominated by $\partial U_{ocv}^{conf}(x,T)/\partial T$. Overall, an *ideal* intercalation compound forming a homogeneous solid solution is characterized by monotonically decreasing $\partial U_{ocv}(x,T)/\partial T$ with increasing lithium composition x.

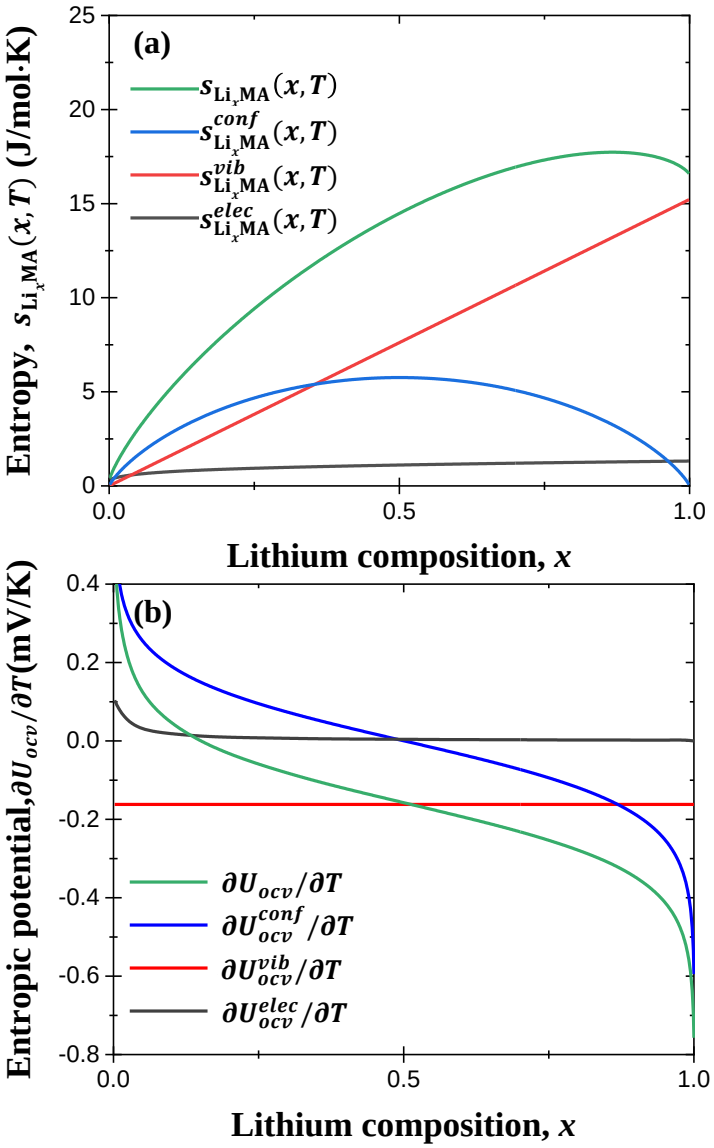

Figure 2.5: (a) Calculated entropy associated with configurational $s^{conf}_{\mathrm{Li}_x\mathrm{MA}}(x,T)$, vibrational $s^{vib}_{\mathrm{Li}_x\mathrm{MA}}(x,T)$, and electronic $s^{elec}_{\mathrm{Li}_x\mathrm{MA}}(x,T)$ excitations as well as the partial entropy of the $\mathrm{Li}_x\mathrm{MA}$ electrode, i.e., $s_{\mathrm{Li}_x\mathrm{MA}}(x,T) = s^{conf}_{\mathrm{Li}_x\mathrm{MA}}(x,T) + s^{vib}_{\mathrm{Li}_x\mathrm{MA}}(x,T) + s^{elec}_{\mathrm{Li}_x\mathrm{MA}}(x,T)$. (b) Calculated entropic potential associated with configurational $\partial U^{conf}_{ocv}(x,T)/\partial T$, vibrational $\partial U^{vib}_{ocv}(x,T)/\partial T$, and electronic $\partial U^{elec}_{ocv}(x,T)/\partial T$ excitations as well as the entropic potential of the battery, i.e., $\partial U_{ocv}(x,T)/\partial T = \partial U^{conf}_{ocv}(x,T)/\partial T + \partial U^{vib}_{ocv}(x,T)/\partial T + \partial U^{elec}_{ocv}(x,T)/\partial T$.

2.1.2 Ion ordering from a homogeneous solid solution

It is common for the guest cations of an intercalation compound to order at specific stoichiometric compositions. For example, the Li ions and vacancies of layered $\mathrm{Li}_x\mathrm{CoO}_2$ adopt

an ordered arrangement at x=0.5 [77,84] while the Na ions of Na_xCoO_2 form a devil's staircase of orderings over a range of compositions [94]. Guest cation ordering generally leads to spontaneous symmetry breaking and the emergence of a superlattice with some sublattices preferentially occupied by the guest cation and the others remaining vacant [82]. For most ordering reactions, the symmetry breaking can be detected with diffraction [77]. In this section, we explore how an ordering reaction manifests itself in the entropic potential $\partial U_{ocv}(x,T)/\partial T$.

While the emergence of an ordered phase arises from interactions among the guest cations, the entropy of an ordering reaction can also be explored with a simplified model that neglects such interactions. By introducing sublattices with different guest ion site energies, it is possible to extend the ideal solution model to one that exhibits features of common ordering reactions. The intercalated Li will then selectively fill the more favorable sublattice sites first, before filling the less favorable sites. We consider a model where interactions between Li ions are neglected, but where half the sites form a sublattice that hosts Li at a lower energy (sublattice 1) than the other half of available sites (sublattice 2). It is convenient to introduce sublattice concentrations x_1 and x_2 tracking the fraction of occupied sites on sublattice 1 and 2, respectively [65,82]. The overall Li concentration is related to the sublattice concentrations according to $x = (x_1 + x_2)/2$ when the number of sites on the two sublattices are equal.

The free energy of an ideal intercalation compound with two sublattices can be expressed as

$$\begin{aligned} g_{\mathrm{Li}_x\mathrm{MA}}(x,T) = g_{\mathrm{MA}}(T) + \epsilon_1 x_1 + \epsilon_2 x_2 + k_B T\left[x_1 \ln(x_1) + (1-x_1)\ln(1-x_1)\right] \\ + k_B T\left[x_2 \ln(x_2) + (1-x_2)\ln(1-x_2)\right] \end{aligned} \tag{2.13}$$

where ϵ_1 and ϵ_2 are sublattice site energies such that $\epsilon_1 \geq \epsilon_2$. These energies may be temperature-dependent if vibrational excitations are accounted for. The ideal solution entropy measure the configurational entropy of non-interacting Li ions on each sublattice. The free energy model has one independent variable at fixed Li concentration x. Since Li can freely distribute between the two sublattices, one of the sublattice concentrations, e.g., x_1, is an independent variable while x_2 is a dependent variable such that $x_2 = 2x - x_1$. Under thermodynamic equilibrium, x_1 adopts the value that minimizes the free energy [Eq.(2.13)].

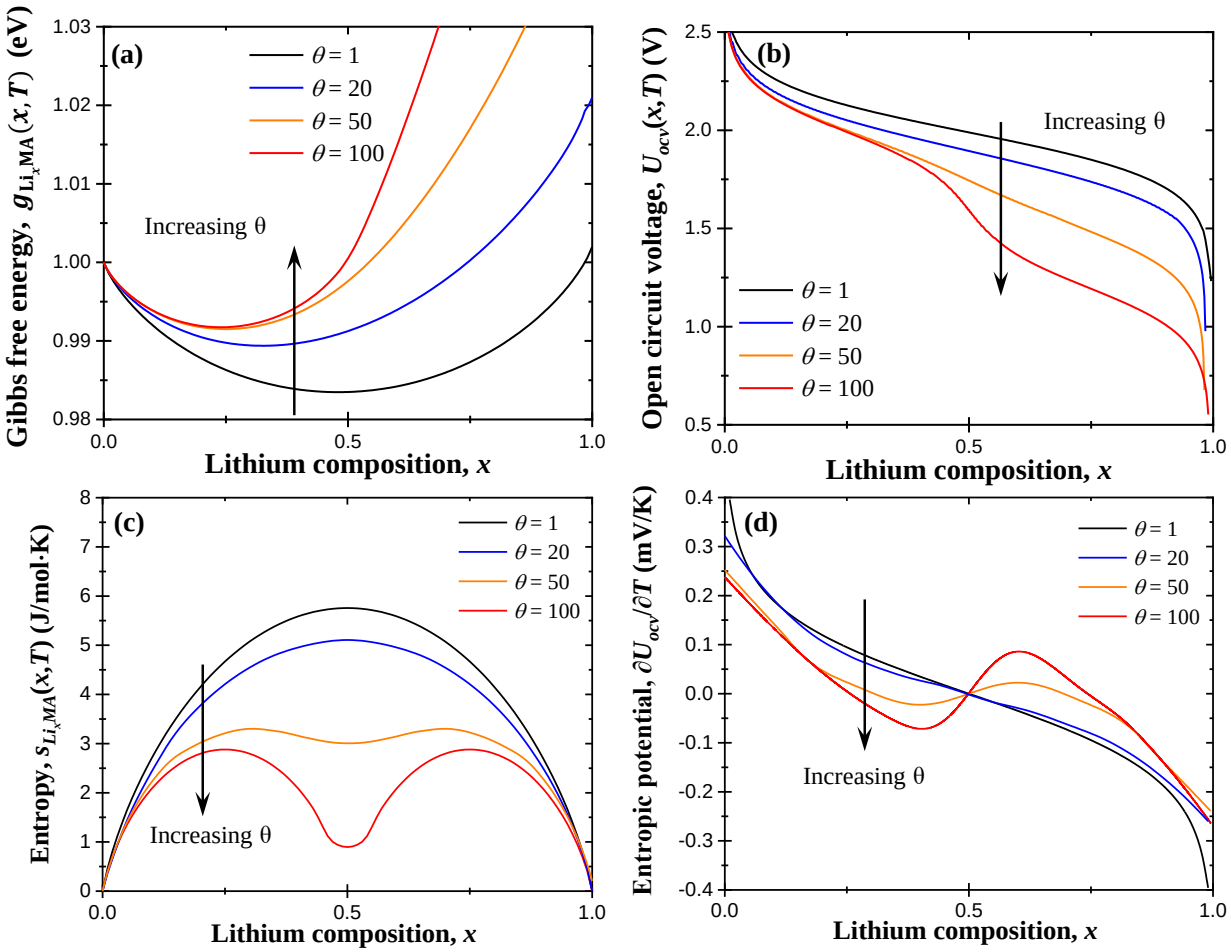

Figure 2.6: (a) The Gibbs free energy $g_{\mathrm{Li}_x\mathrm{MA}}(x,T)$ of Li_xMA, (b) the open circuit voltage $U_{ocv}(x,T)$ of the battery cell, (c) the entropy $s_{\mathrm{Li}_x\mathrm{MA}}(x,T)$ of Li_xMA, and (d) the entropic potential $\partial U_{ocv}(x,T)/\partial T$ of the battery cell as functions of lithium composition x at temperature T with varying $\theta = \epsilon_1/\epsilon_2$.

It is the equilibrium value of x_1 that must be inserted into Eq.(2.13) to obtain the equilibrium free energy and all its derived properties, including the Li chemical potential and the entropy (See Appendix A). The thermodynamic properties of this model is sensitive to the relative values of ϵ_1 and ϵ_2. The parameter $\theta = \epsilon_1/\epsilon_2$ can be used to model different scenarios. Figure 2.6(a) shows the lowest Gibbs free energy $g_{\mathrm{Li}_x\mathrm{MA}}(x,T)$ as only a function of x for different values of $\theta = \epsilon_1/\epsilon_2$. When θ=1, we recover the *ideal* solution model without any sublattice site preference. Then, the minimum free energy as a function of x occurs for x_1=x_2=x such

that the equilibrium free energy of Eq.(2.13) reduces to that of an ideal solution. A value of $\theta = \epsilon_1/\epsilon_2 > 1$ leads to a Li preference for sublattice 2 when ϵ_1 and ϵ_2 are both positive. Increasing θ leads to an increased degree of segregation to the more favorable sublattice and to a step in the open circuit voltage $U_{ocv}(x,T)$ at x=0.5, as illustrated in Figure 2.6(b). The step occurs when the more favorable site becomes fully saturated and additional Li ions are required to fill energetically less favorable sites. The resulting ordering around x=0.5 leads to a dip in the entropy $s_{\mathrm{Li}_x\mathrm{MA}}(x,T)$, as evident in Figure 2.6(c). Figure 2.6(d) shows that the battery entropic potential $\partial U_{ocv}(x,T)/\partial T$ exhibits an inflection point at $x = 0.5$ in the models that undergo a strong ordering reaction.

Although we have considered an idealized model to elucidate the effect of ion ordering on the entropy and the entropic potential, similar features are evident in real intercalation compounds that undergo order/disorder reactions. Both $\mathrm{Li}_x\mathrm{TiS}_2$ and $\mathrm{Li}_x\mathrm{CoO}_2$ are examples of intercalation compounds that exhibit ordered phases. Layered $\mathrm{Li}_x\mathrm{TiS}_2$ forms a solid solution for most values of x but undergoes a staging reaction around $x \approx 0.2$, whereby Li segregates to every other Li layer [76, 95]. Figure 2.7(a) shows experimental measurements of $U_{ocv}(x,T)$ and $\partial U_{ocv}(x,T)/\partial T$ for a battery system with a TiS_2 working electrode and a lithium metal counter electrode during lithiation. The electrolyte consisted of a mixture of 1 M of LiPF_6 with ethylene carbonate (EC) and dimethyl carbonate (DMC). The open circuit voltage $U_{ocv}(x,T)$ exhibited the characteristic shape of a solid solution above $x \approx 0.4$. While a pronounced step at $x \approx 0.2$ was not directly evident in $U_{ocv}(x,T)$, the entropic potential $\partial U_{ocv}(x,T)/\partial T$ featured a fluctuation in the form of a tilde due to the occurrence of stage ordering analogous to that of Figure 2.6(d) for the ideal model.

$\mathrm{Li}_x\mathrm{CoO}_2$ is another intercalation compound that exhibits an ordered phase [77,84]. Here, the Li ions of $\mathrm{Li}_x\mathrm{CoO}_2$ can occupy octahedrally coordinated interstitial sites that form two-dimensional triangular lattices. At $x = 0.5$ the Li ions adopt an ordered arrangement in which they line up into rows separated by rows of vacancies within each layer [77]. Figure 2.7(b) shows $U_{ocv}(x,T)$ and $\partial U_{ocv}(x,T)/\partial T$ measured for a battery system consisting of a LiCoO_2 working electrode and a lithium metal counter electrode with 1M of LiPF_6 in an EC/DMC mixture as electrolyte during delithiation [81]. Here also, $\partial U_{ocv}(x,T)/\partial T$ featured

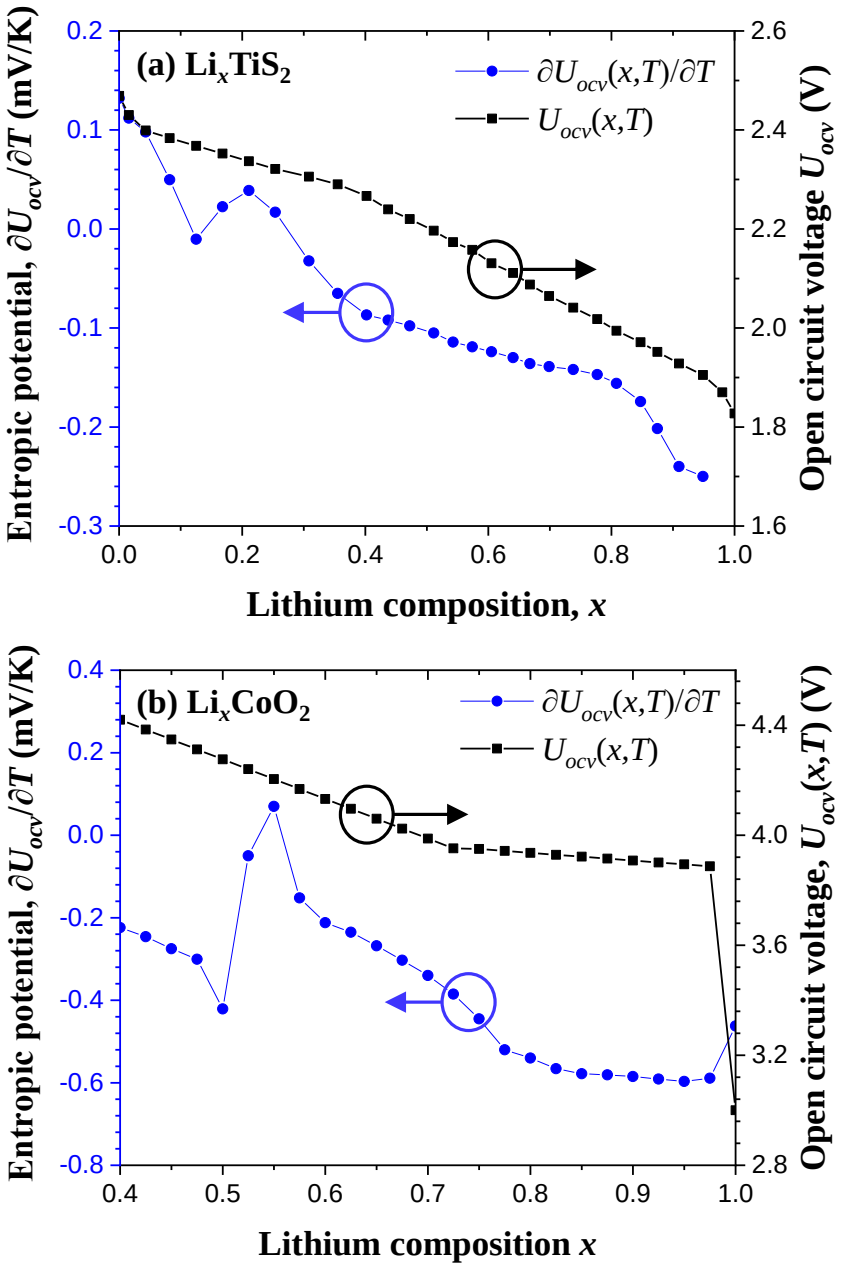

Figure 2.7: Measured open circuit voltage $U_{ocv}(x,T)$ and entropic potential $\partial U_{ocv}(x,T)/\partial T$ as functions of lithium composition x in (a) Li_xTiS_2 during lithiation, and (b) Li_xCoO_2 during delithiation.

a tilde-shaped fluctuation similar to that observed in the TiS_2 electrode [Figure 2.7(a)] due to the intralayer ion ordering in the range of $0.45 \leq x \leq 0.55$ [81,96]. In addition to an ordering reaction, Li_xCoO_2 also underwent a first-order phase transformation from a metallic solid

solution at x=0.75 to a semiconducting solid solution at x=0.93, as confirmed with *in situ* XRD measurements [77]. This was also evident in both the $\partial U_{ocv}(x,T)/\partial T$ and $U_{ocv}(x,T)$ curves, which were almost constant for $0.75 < x < 0.93$. The next section analyzes the behavior of $\partial U_{ocv}(x,T)/\partial T$ during a first-order phase transformation.

2.1.3 Phase transition accompanied by a two-phase coexistence region

An intercalation compound MA may undergo a first-order phase transition, as observed at the high lithium compositions in Li_xCoO_2, from a lithium-poor α-phase to a lithium-rich β-phase upon the insertion of Li. During such phase transition, both the α- and β-phases coexist. Figure 2.8(a) schematically shows the Gibbs free energies $g_{\mathrm{Li}_\alpha\mathrm{MA}}(T)$ and $g_{\mathrm{Li}_\beta\mathrm{MA}}(T)$ of these two phases. The common tangent construction determines the equilibrium concentrations of the two coexisting phases. The free energy of the two-phase mixture resides on the common tangent between the lithium poor phase Li_αMA with composition α and the lithium rich phase Li_βMA with composition β. Thus, the Gibbs free energy $g_{\mathrm{Li}_x\mathrm{MA}}(\alpha \le x \le \beta, T)$ in the two-phase coexistence region can be written as,

$$g_{\mathrm{Li}_x\mathrm{MA}}(\alpha \le x \le \beta, T) = g_{\mathrm{Li}_\alpha\mathrm{MA}}(T) + \frac{g_{\mathrm{Li}_\beta\mathrm{MA}}(T) - g_{\mathrm{Li}_\alpha\mathrm{MA}}(T)}{\beta - \alpha}(x - \alpha). \tag{2.14}$$

The Li chemical potential $\mu_{\mathrm{Li}}^{\mathrm{Li}_x\mathrm{MA}}(\alpha \le x \le \beta, T)$ of the host material Li_xMA in the two-phase coexistence region is then given by

$$\mu_{\mathrm{Li}}^{\mathrm{Li}_x\mathrm{MA}}(\alpha \le x \le \beta, T) = \frac{\partial g_{\mathrm{Li}_x\mathrm{MA}}(\alpha \le x \le \beta, T)}{\partial x} = \frac{g_{\mathrm{Li}_\beta\mathrm{MA}}(T) - g_{\mathrm{Li}_\alpha\mathrm{MA}}(T)}{\beta - \alpha}. \tag{2.15}$$

Thus, $\mu_{\mathrm{Li}}^{\mathrm{Li}_x\mathrm{MA}}(\alpha \le x \le \beta, T)$ remains constant in the two-phase coexistence region, as illustrated in Figure 2.8(b).

Figure 2.8(c) shows the entropy $s_{\mathrm{Li}_x\mathrm{MA}}(x,T)$ of the host material as a function of lithium composition x. The coexisting α- and β- phases are treated as solid solutions such that their entropies exhibit the characteristic dome-shaped curves of a solid solution. Here, the entropy of the α-phase was arbitrarily chosen to be smaller than that of the β-phase. Here also, the entropy of the two-phase mixture resides on the chord connecting $s_{\mathrm{Li}_\alpha\mathrm{MA}}$ and $s_{\mathrm{Li}_\beta\mathrm{MA}}$.

The open circuit voltage $U_{ocv}(\alpha \le x \le \beta, T)$ in the two-phase coexistence region can be

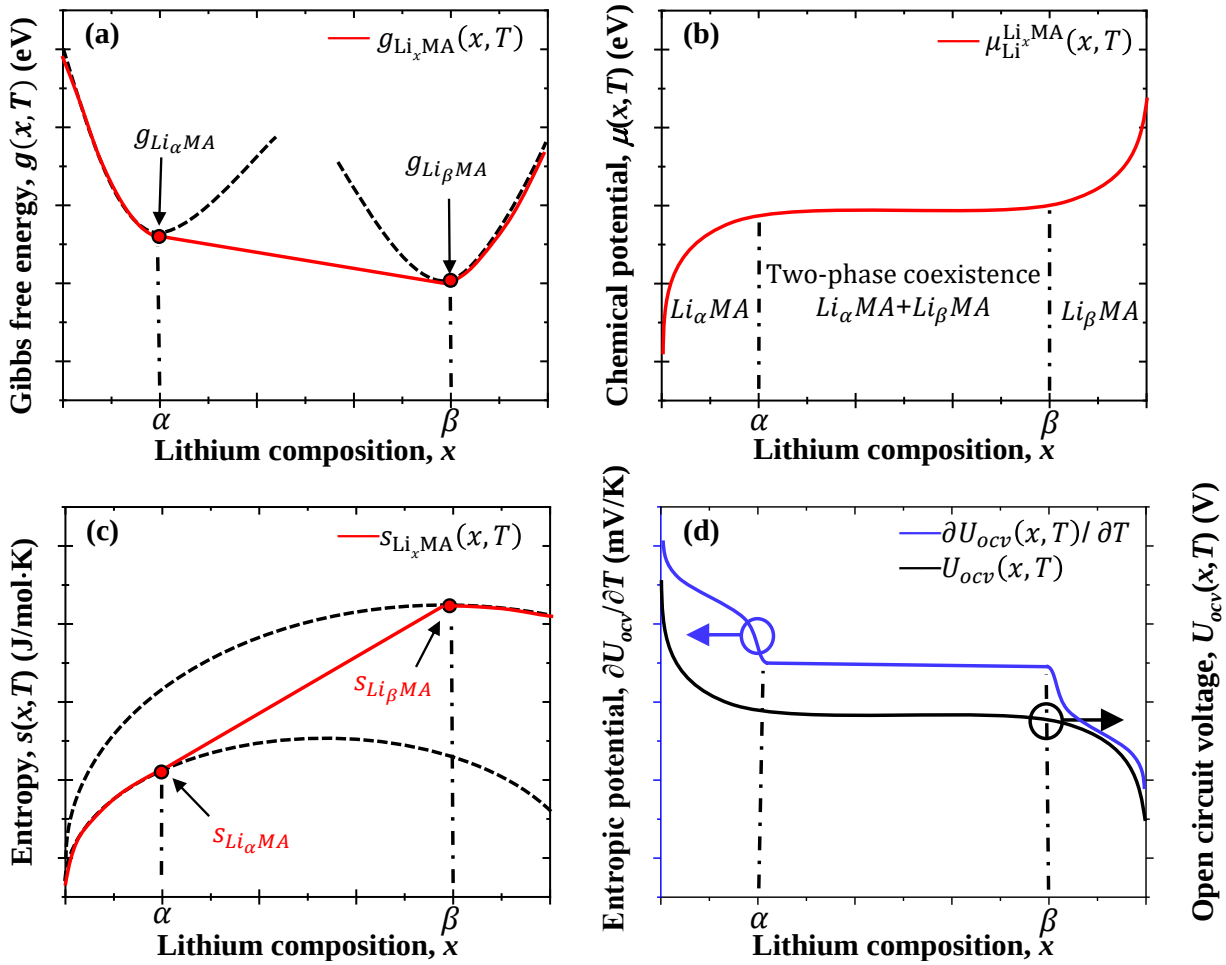

Figure 2.8: (a) Schematic plots of Gibbs free energy $g_{\mathrm{Li}_x\mathrm{MA}}(x,T)$, (b) chemical potential $\mu_{\mathrm{Li}}^{\mathrm{Li}_x\mathrm{MA}}(x,T)$, (c) entropy $s_{\mathrm{Li}_x\mathrm{MA}}(x,T)$ of $\mathrm{Li}_x\mathrm{MA}$, and (d) Open circuit voltage $U_{ocv}(x,T)$ and entropic potential $\partial U_{ocv}(x,T)/\partial T$ of the battery cell as functions of lithium composition x at temperature T during a first order phase transition accompanied by a lithium poor phase $\mathrm{Li}_\alpha\mathrm{MA}$ coexisting with a lithium rich phase $\mathrm{Li}_\beta\mathrm{MA}$.

expressed as

$$U_{ocv}(\alpha \le x \le \beta, T) = -\frac{1}{e}\left[\frac{g_{\mathrm{Li}_\beta\mathrm{MA}}(T) - g_{\mathrm{Li}_\alpha\mathrm{MA}}(T)}{\beta - \alpha} - g^o_{\mathrm{Li}}(T)\right]. \tag{2.16}$$

Thus, the corresponding entropic potential in the two-phase coexistence region is given by

$$\frac{\partial U_{ocv}}{\partial T}(\alpha \le x \le \beta, T) = \frac{1}{e}\left[\frac{s_{\mathrm{Li}_\beta\mathrm{MA}}(T) - s_{\mathrm{Li}_\alpha\mathrm{MA}}(T)}{\beta - \alpha} - s^o_{\mathrm{Li}}(T)\right]. \tag{2.17}$$

Overall, these results indicate that both $U_{ocv}(x,T)$ and $\partial U_{ocv}(x,T)/\partial T$ are constant and independent of x in the two-phase coexistence region, as illustrated in Figure 2.8(d).

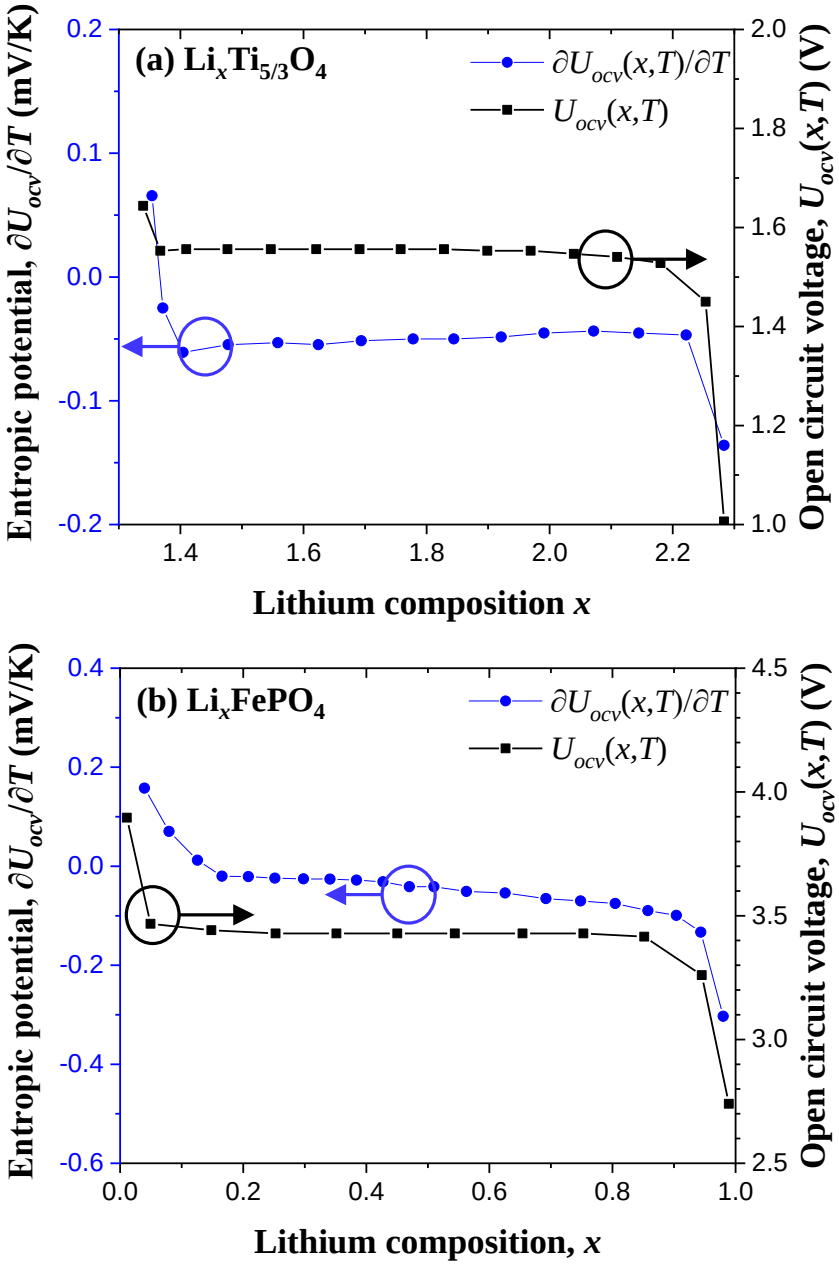

Figure 2.9: Open circuit voltage $U_{ocv}(x,T)$, and entropic potential $\partial U_{ocv}(x,T)/\partial T$ as functions of lithium composition x in (a) $Li_xTi_{5/3}O_4$ [1], and (b) Li_xFePO_4 [2] during lithiation.

To illustrate the predicted behavior of $U_{ocv}(x,T)$ and $\partial U_{ocv}(x,T)/\partial T$ given by Eqs.(2.16) and (2.17) in a two-phase coexistence region, Figure 2.9(a) shows experimental measurements for a battery system consisting of a $Li_{4/3}Ti_{5/3}O_4$ working electrode and a lithium metal counter electrode with 1.2 M of $LiPF_6$ in an EC/DMC electrolyte as a function of the lithium

composition x during lithiation [1]. EELS and *in situ* XRD measurements indicated a first order phase transition from spinel $Li_{4/3}Ti_{5/3}O_4$ to rock salt $Li_{7/3}Ti_{5/3}O_4$ during lithiation [1,97,98]. In fact, Figure 2.9(a) shows that both $U_{ocv}(x,T)$ and $\partial U_{ocv}(x,T)/\partial T$ were constant for $\alpha = 4/3 \leq x \leq 7/3 = \beta$ indicating the coexistence of the two phases $Li_{4/3}Ti_{5/3}O_4$ and $Li_{7/3}Ti_{5/3}O_4$.

Similarly, Figure 2.9(b) shows $U_{ocv}(x,T)$ and $\partial U_{ocv}(x,T)/\partial T$ for a battery system consisting of a $FePO_4$ working electrode and a lithium metal counter electrode in 1 M $LiPF_6$ in an EC/DMC electrolyte during lithiation [2]. Here also, electron energy-loss spectroscopy and *in situ* XRD measurements indicated a first order phase transition from $FePO_4$ to olivine $LiFePO_4$ during lithiation [99–101]. Figure 2.8(b) shows that both $U_{ocv}(x,T)$ and $\partial U_{ocv}(x,T)/\partial T$ were constant for $0 \leq x \leq 1$. This observation was consistent with Eqs.(2.16) and (2.17) for the coexistence of $FePO_4$ and $LiFePO_4$ phases. In summary, a first-order phase transition accompanied by two-phase coexistence is characterized by constant $U_{ocv}(x,T)$ and $\partial U_{ocv}(x,T)/\partial T$, as illustrated experimentally for $Li_{4/3}Ti_{5/3}O_4$ and $LiFePO_4$.

2.1.4 Two-phase coexistence with a stable intermediate phase

Some intercalation compounds, such as graphite, pass through a stable intermediate phase by means of first-order phase transitions upon Li insertion. Figure 2.10(a) shows schematic Gibbs free energy curves for an intercalation compound MA that has a stable intermediate γ-phase with a composition between that of the dilute α-phase and the lithiated β-phase. The stability of the intermediate γ-phase leads to two two-phase regions as shown in Figure 2.10(a) by the common tangents between α- and γ- and between γ- and β- phases. The two common tangents result in two plateaus separated by a step in the Li chemical potential curve as schematically shown in Figure 2.10(b).

Figure 2.10(c) schematically shows the entropy as a function of Li concentration for the different phases that can form upon Li insertion into MA. Two distinct scenarios are possible based on the value of the entropy of the intermediate γ-phase relative to that of the α- and β-phases. In Case I, $s_{\mathrm{Li}_\gamma\mathrm{MA}}$ lies above the chord connecting $s_{\mathrm{Li}_\alpha\mathrm{MA}}$ and

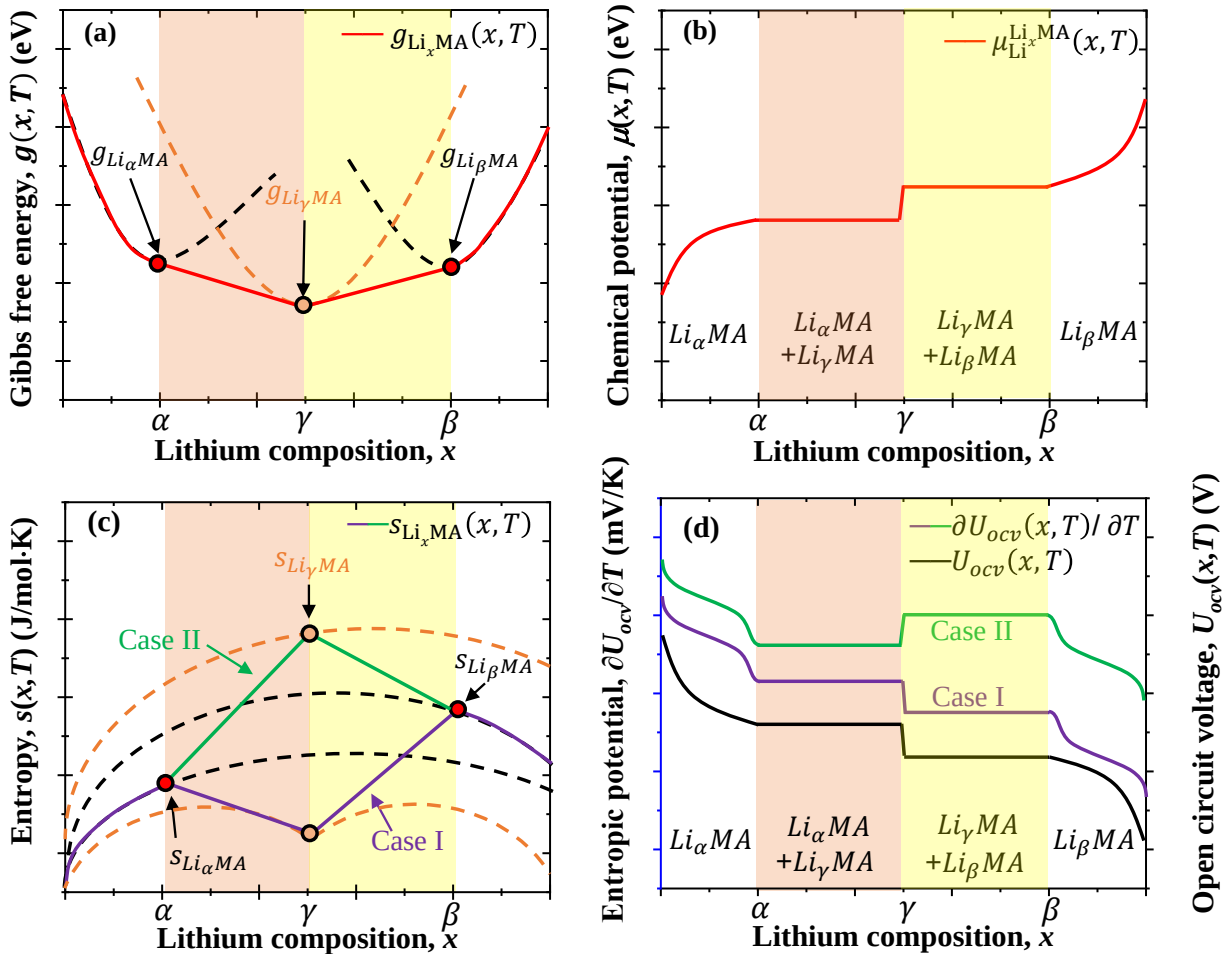

Figure 2.10: (a) Schematic plots of Gibbs free energy $g_{\mathrm{Li}_x\mathrm{MA}}(x,T)$, (b) chemical potential $\mu_{\mathrm{Li}}^{\mathrm{Li}_x\mathrm{MA}}(x,T)$, (c) entropy $s_{\mathrm{Li}_x\mathrm{MA}}(x,T)$ of the $\mathrm{Li}_x\mathrm{MA}$, and (d) Open circuit voltage $U_{ocv}(x,T)$ and entropic potential $\partial U_{ocv}(x,T)/\partial T$ of the battery cell as functions of lithium composition x at temperature T for two coexisting phases $\mathrm{Li}_\alpha\mathrm{MA}$ and $\mathrm{Li}_\beta\mathrm{MA}$ with a stable intermediate phase $\mathrm{Li}_\gamma\mathrm{MA}$.

$s_{\mathrm{Li}_\beta\mathrm{MA}}$, as illustrated in Figure 2.10(c). This scenario can be expected when the intermediate phase is a solid solution, which generally exhibits its highest configurational entropy at intermediate concentrations. In Case II, the entropy $s_{\mathrm{Li}_\gamma\mathrm{MA}}$ of the intermediate γ-phase falls below the chord connecting $s_{\mathrm{Li}_\alpha\mathrm{MA}}$ and $s_{\mathrm{Li}_\beta\mathrm{MA}}$. This is more likely to occur if the intermediate phase corresponds to an ordered phase exhibiting a minimum at the stoichiometric ordering concentration. Figure 2.10(d) shows the associated open circuit voltage $U_{ocv}(x,T)$ and the entropic potential $\partial U_{ocv}(x,T)/\partial T$ as functions of the lithium composition x. In both cases,

$U_{ocv}(x,T)$ and $\partial U_{ocv}(x,T)/\partial T$ feature two plateaus for $\alpha \leq x \leq \gamma$ and $\gamma \leq x \leq \beta$ and a step around $x = \gamma$, as observed previously for $\mu_{MA}(x)$ [Figure 2.10(b)]. However, in Case I, $\partial U_{ocv}(x,T)/\partial T$ is larger in the coexistence region of Li$_\alpha$MA and LiγMA ($\alpha \leq x \leq \gamma$) than in the coexistence region of Li$_\beta$MA and LiγMA ($\gamma \leq x \leq \beta$). By contrast, in Case II, $\partial U_{ocv}(x,T)/\partial T$ is smaller for $\alpha \leq x \leq \gamma$ than for $\gamma \leq x \leq \beta$.

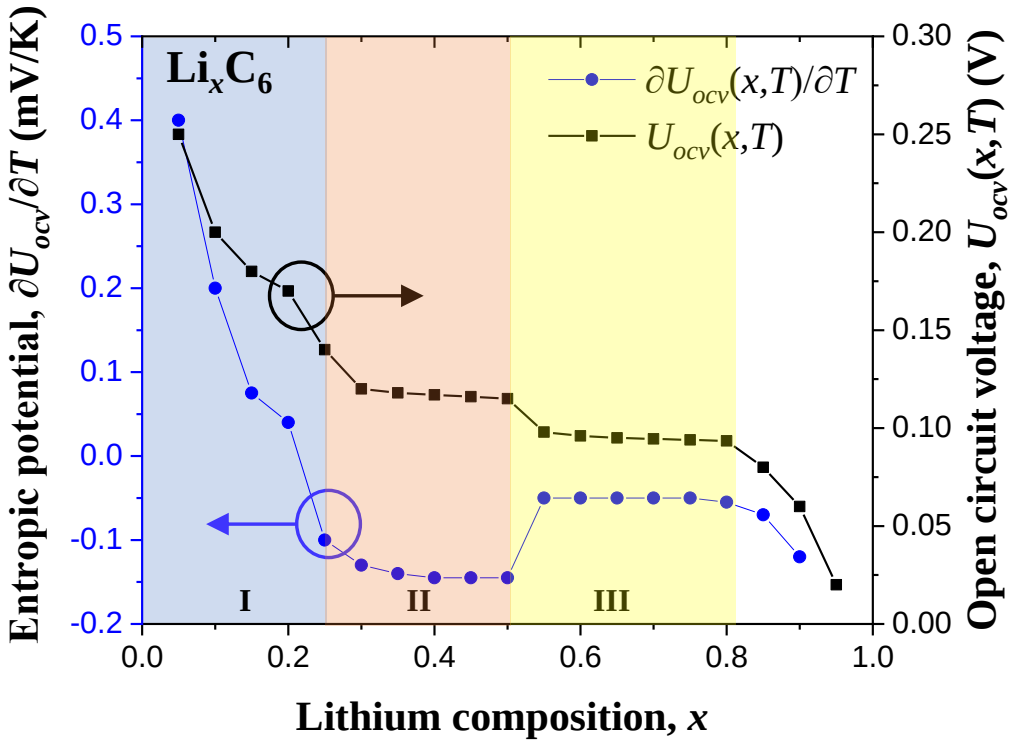

Figure 2.11: Open circuit voltage $U_{ocv}(x,T)$, and entropic potential $\partial U_{ocv}(x,T)/\partial T$ as functions of lithium composition x in Li$_x$C$_6$ during lithiation.

Figure 2.11 shows $U_{ocv}(x,T)$ and $\partial U_{ocv}(x,T)/\partial T$ measured for a battery system consisting of a graphite working electrode and a lithium metal counter electrode in 1 M of $LiPF_6$ in an EC/DMC during lithiation. Three regions can be identified from the measured $U_{ocv}(x,T)$ and $\partial U_{ocv}(x,T)/\partial T$: (I) a homogeneous solid solution in the range of $0 \leq x \leq 0.25$ with monotonically decreasing $U_{ocv}(x,T)$ and $\partial U_{ocv}(x,T)/\partial T$, (II) a two-phase coexistence of LiC_{24} and LiC_{12} in the composition range $0.25 \leq x \leq 0.5$ with constant $U_{ocv}(x,T)$ and $\partial U_{ocv}(x,T)/\partial T$, and (III) a two-phase coexistence of LiC_{12} and LiC_6 in the range of $0.5 \leq x$

≤ 0.8 with constant $U_{ocv}(x,T)$ and $\partial U_{ocv}(x,T)/\partial T$. These three regions were also identified with *in situ* XRD measurements [102,103]. The entropic potential measurements for graphite are consistent with Case II described above. The result indicates that the intermediate LiC_{12} phase has an entropy that falls below the chord that connects the entropies of LiC_{24} and LiC_6.

2.2 Conclusion

This study reviewed and clarified the fundamental thermodynamic relationships and properties of lithium-ion battery systems having intercalation compounds as their electrochemically active cathode material. Expressions for the open circuit voltage $U_{ocv}(x,T)$ and entropic potential $\partial U_{ocv}(x,T)/\partial T$ of LIB cells were rigorously derived for *ideal* intercalation compounds. They were used to develop an interpretative guide to potentiometric entropy measurements of $U_{ocv}(x,T)$ and $\partial U_{ocv}(x,T)/\partial T$ as functions of lithium composition x for different charging/discharging mechanisms. For an ideal homogeneous solid solution, contributions from configurational, vibrational, and electronic excitations to the entropy of an ideal intercalation compound were numerically calculated to estimate the first-order behavior of $\partial U_{ocv}(x,T)/\partial T$ of a battery consisting of an intercalation compound as its cathode. The analysis suggests that general trends of $\partial U_{ocv}(x,T)/\partial T$ of a homogeneous solid solution are dominated by configurational entropy, which leads to a monotonically decreasing $U_{ocv}(x,T)$ and $\partial U_{ocv}(x,T)/\partial T$ with increasing lithium composition x. An ion ordering reaction over a subset of energetically favorable interstitial sites is characterized by a tilde-shaped fluctuation in $\partial U_{ocv}(x,T)/\partial T$ versus x. Furthermore, a first order phase transition accompanied by two-phase coexistence manifests itself as a constant $U_{ocv}(x,T)$ and $\partial U_{ocv}(x,T)/\partial T$. Finally, a two-phase coexistence with a stable intermediate phase leads to a monotonically decreasing $U_{ocv}(x,T)$ curve upon lithiation that is characterized by two plateaus separated by a step. The $\partial U_{ocv}(x,T)/\partial T$ curve for this scenario also exhibits two plateaus. However, depending on the entropy of the intermediate phase, the second plateau can either be higher or lower than the first plateau. These interpretations were systematically illustrated using experi-

mental data for various cathode materials. The present interpretative guide can enhance other structural analysis techniques and can prove valuable in the characterization of new battery materials.

CHAPTER 3

Operando Calorimetry Informs the Origin of Rapid Rate Performance in Microwave-Prepared $TiNb_2O_7$ Electrodes

This chapter presents a fast, simple, and cost-effective synthesis method of $TiNb_2O_7$ for LIB anode electrodes developed in Prof. Seshadri's group at University of California Santa Barbara (UCSB). The materials synthesized and the associated electrodes were characterized by high-resolution synchrotron X-ray diffraction (XRD), conventional electrochemical methods, and potentiometric entropy measurement technique. Finally, potentiometric entropy and *operando* calorimetric measurements were used to deepen our understanding of the lithiation/delithiation process in $TiNb_2O_7$ electrodes and to investigate the associated heat generation upon cycling at high C-rates.

3.1 Materials and methods

3.1.1 Microwave synthesis of $TiNb_2O_7$

In this study, $TiNb_2O_7$ particles were synthesized using a fast and simple method consisting of a single heating step in a microwave oven under ambient atmosphere. First, the precursor powders TiO_2 (Aldrich Chemical Company, 99%) and Nb_2O_5 (Materion, 99.95%) were thoroughly ground together in stoichiometric quantities (1:1) using an agate mortar and pestle. The ground powder was then pressed into 250 mg to 300 mg pellets using a hand-operated arbor press. The pellets were placed on a small sacrificial powder layer of the same material inside of a 10 mL alumina crucible. This crucible was then nestled into a larger 20

mL alumina crucible filled with approximately 7 g of activated charcoal covered in alumina fiberboard insulation, and placed off-center in a 1250 W microwave oven (Panasonic). This stack was heated at 90% of the total microwave power (i.e., 1125 W) for 7 to 8 minutes reaching temperatures around 1200 °C, as observed with a laser thermometer, immediately upon reaction completion. The insulation was removed and the pellets were allowed to cool to room temperature. The produced crystalline $TiNb_2O_7$ particles required no additional processing prior to fabricating the electrode. Additional background on general microwave sample preparation can be found in Ref. [104].

3.1.2 Structural characterization

High resolution synchrotron X-ray diffraction measurements of the synthesized $TiNb_2O_7$ powder were collected at room temperature at the Advanced Photon Source at Argonne National Laboratories on beamline 11-BM-B using an average wavelength of 0.457856 $\mathring{A}$. The $TiNb_2O_7$ powder sample was loaded into a Kapton capillary and both ends were sealed with clay. Rietveld refinement was performed with TOPAS [105] while VESTA [106] was used for crystal structure visualization.

3.1.3 Electrochemical testing

The electrodes were cast on copper foil using an 80:10:10 (wt%) ratio of active material ($TiNb_2O_7$), conductive carbon (TIMCAL SuperP), and polyvinylidene fluoride (Sigma Aldrich). The active material was ball-milled for 30 minutes in a 2 cm^3 canister with SuperP. This mixture was added to PVDF dissolved in 1-methyl-2-pyrrolidinone (Sigma Aldrich) to form a slurry and was mixed in a FlackTek speed mixer at 2000 rpm for 30 minutes. The slurry was cast onto a copper foil using a doctor blade set for 150 μm. Then, the film was dried overnight at 110 °C in a vacuum oven. The fabricated electrode was then punched into 10 mm diameter discs resulting in an active material loading of 5.6 mg/cm^2 and assembled into a coin cell configuration (MTI parts, 2032 SS casings) with 1 M of $LiPF_6$ in EC:DMC 1:1 v/v (Sigma Aldrich) as electrolyte and polished lithium metal (Sigma Aldrich) as the

counter electrode with a 50 μm thick polypropylene/polyethylene separator (Celgard C380). Cyclic voltammetry (CV), galvanostatic cycling (GC), and galvanostatic intermittent titration technique (GITT) were performed on the coin cell in the voltage range of 1.0−3.0 V using a high accuracy potentiostat (Biologic, VSP-300). During GITT, each current pulse was applied for 1 minute followed by a relaxation period of 30 minutes to measure the open circuit voltage $U_{ocv}(x,T)$ as a function of composition x in $Li_xTiNb_2O_7$ at constant temperature T = 20 °C. All potentials in this study are reported relative to Li^+/Li, and C-rates are defined with respect to the reduction of one electron per transition metal, e.g., 1C = 233 mAh/g.

3.1.4 Potentiometric entropy measurement

The entropic potential $\partial U_{ocv}(x,T)/\partial T$ of the $TiNb_2O_7$ half-cell was measured as a function of lithium composition x using a potentiometric entropy measurement technique performed on a coin cell. The lithium metal counter electrode was considered as an infinite Li^+ reservoir with no lattice rearrangement upon lithiation/delithiation [107]. Therefore, the contribution of the lithium metal electrode to the entropic potential was assumed to be constant throughout the cycle [60, 108].

Figure 3.1 shows the schematic of the custom-made experimental setup assembled for potentiometric entropy measurements. The experimental setup consisted of a thermoelectric cold plate (TE technology, CP-121) whose temperature was measured by a type-K thermocouple (Omega, GG-KI-24S-200) via a data acquisition system (Keysight, Agilent 34972A). The temperature of the cold plate was controlled by a proportional-integral-derivative (PID) temperature controller (TE technology, TC-720). The coin cell and current collectors were wrapped with Kapton tape to prevent electrical contact with the thermoelectric cold plate. Thermal paste (Omega, OT-201-16) was applied between the thermoelectric cold plate and the wrapped coin cell to ensure good thermal contact. The type-K thermocouple was secured on top of the coin cell assembly with the thermal paste and covered by a copper tape for accurate temperature measurements. The entire setup was thermally insulated with Styro-

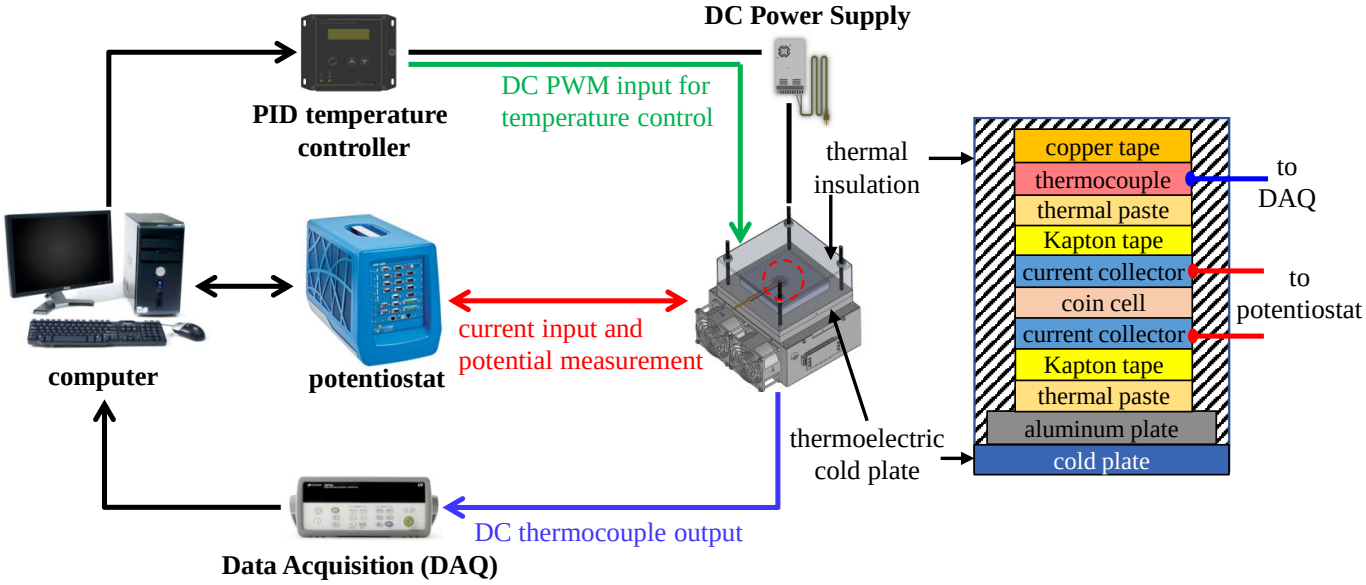

Figure 3.1: Schematic of the experimental setup used for the potentiometric entropy measurement.

foam to reduce heat losses to the surrounding and achieve precise control of the coin cell temperature.

The potentiometric entropy measurements consisted of imposing a series of constant current pulses at a C-rate of 2C for one minute at 20 °C each followed by a relaxation period of 90 minutes. During the relaxation, a step-like temperature profile was applied to the coin cell from 15 °C to 25 °C in 5 °C increments. The resulting voltage profile was recorded with the potentiostat (Biologic, VSP-300). Before recording the open circuit voltage $U_{ocv}(x,T)$ and imposing the next temperature step, we verified that the cell was in thermodynamic equilibrium by making sure that (i) the temperature difference between the cold plate and the top of the coin cell was less than 0.1 °C and (ii) the time rate of change of the open circuit voltage $\partial U_{ocv}/\partial t$ was less than 1 mV/h.

3.1.5 *Operando* isothermal calorimetry

The instantaneous heat generation rate in the $TiNb_2O_7$ half-cell was measured under galvanostatic cycling using a custom-made isothermal calorimeter previously described [109]. The $TiNb_2O_7$ electrode was cut into a 1 x 1 cm^2 square and assembled into a calorimetric cell with 1 M $LiPF_6$ in EC:DMC 1:1 v/v (Sigma Aldrich) as the electrolyte and polished lithium metal ribbon (Sigma Aldrich) as the counter electrode with a 50 μm thick Celgard C380 polypropylene/polyethylene separator. Based on the thermal analysis of a single electrode described in Supplementary Materials of Ref. [109], the heat generation rate $\dot{Q}_i(t)$ (in mW) at each electrode was equal to the heat transfer rate $q_i''(t)$ passing through the 1×1 cm^2 thermoelectric heat flux sensor (greenTEG, gSKIN-XP) such that [109],

$$\dot{Q}_i(t) = q_i''(t)A_i = \frac{\Delta V_i(t)}{S_i}A_i \qquad \text{with } i = + \text{ or } - \tag{3.1}$$

where A_i denotes the footprint area of the electrode (in cm^2) while S_i is the temperature-dependent sensitivity of the heat flux sensor provided by the manufacturer (in $\mu V/(W/m^2)$) while subscript "i" refers to either the cathode "+" or anode "−". Here, ΔV_i is the voltage difference measured in each heat flux sensor in thermal contact with electrode "i". The total instantaneous heat generation rate in the entire device was the sum of the heat generation rate measured at each electrode, i.e., $\dot{Q}_T(t) = \dot{Q}_+(t) + \dot{Q}_-(t)$.

3.2 Results and discussion

3.2.1 Structural characterization

Figure 3.2(a) shows a high resolution synchrotron X-ray diffraction (XRD) diagram of $TiNb_2O_7$ prepared using the previously described synthesis method. The XRD pattern was consistent with those prepared by conventional methods [110]. The pristine $TiNb_2O_7$ particles formed an electrically insulating white powder [111]. Figure 3.2(b) shows a SEM image of the synthesized $TiNb_2O_7$ particles typically less than 5 μm (see also Appendix B) and smaller than the average particle size of 20 μm synthesized by solid state method [110]. Figure 3.2(c) illustrates the crystallographic structure of pure $TiNb_2O_7$ featuring a Wadsley-

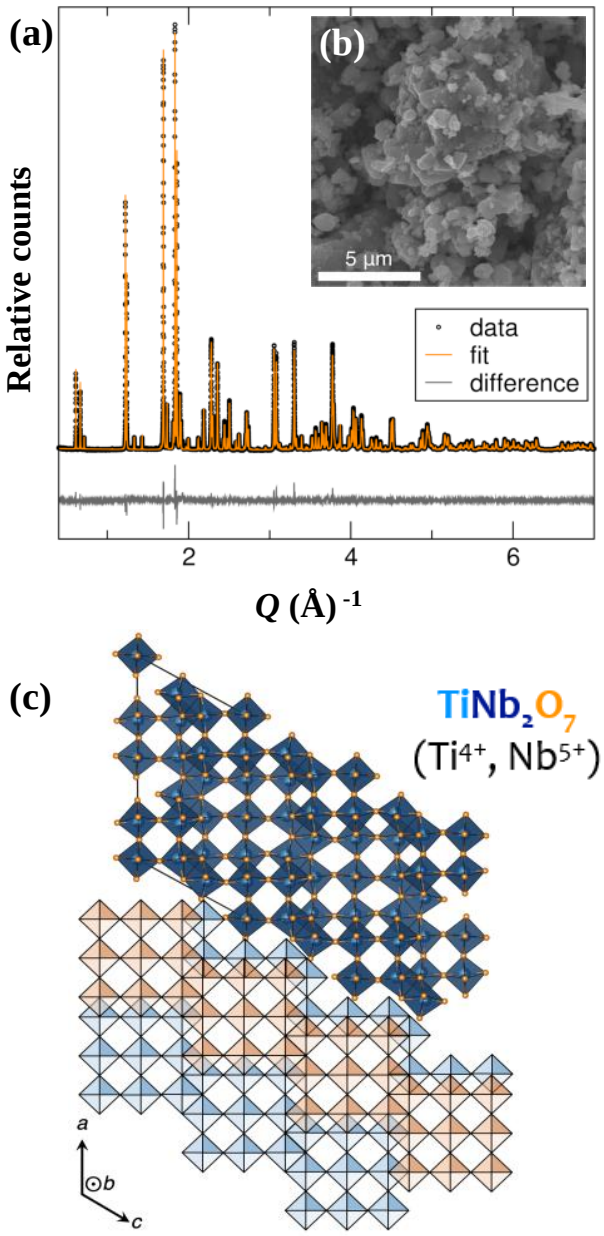

Figure 3.2: (a) Synchrotron X-ray diffraction pattern and (b) SEM image of the $TiNb_2O_7$ particles synthesized by the proposed microwave method, (c) crystallographic structure of pure $TiNb_2O_7$.

Roth crystallographic shear structure similar to those of ReO_3 and PNb_9O_{25} [111]. Overall, in stark contrast to the more conventional synthesis methods of transition metal oxide $TiNb_2O_7$ [32, 110, 112], the proposed method offers a much faster alternative. In fact, in less than 10 minutes in a standard microwave oven, the same compound was synthesized

without necessitating any additional purification or annealing steps. An additional benefit of the present microwave preparation method was that the shorter heating time resulted in smaller $TiNb_2O_7$ particles.

3.2.2 Electrochemical properties

Figure 3.3(a) shows the cyclic voltammogram of a $TiNb_2O_7$ based electrode at different scan rates between 1.0 V and 3.0 V (vs. Li/Li^+). A sharp cathodic peak at 1.58 V and an anodic peak at 1.7 V were observed at scan rate of 0.1 mV/s. These two major peaks corresponded to the conversion of Nb^{5+}/Nb^{4+} and were consistent with previous reports [31, 110, 113, 114]. In addition, one pair of shoulder peaks at 1.5 V for the cathodic sweep and at 1.62 V for the anodic sweep might be caused by different niobium states which are edge-shared octahedral and corner shared octahedral [110, 113, 114]. The pair of broad peaks in the potential range of 1.0 to 1.4 V may be caused by the Nb^{4+}/Nb^{3+} redox couple [110, 113, 114]. Another pair of a broad peaks in the potential range of 1.75 to 2.0 V was associated with the conversion of Ti^{4+}/Ti^{3+} [113, 114]. In addition, Figures 3.3(b) and 3.3(c) show the peak current I_{peak} values measured at differnt scan rates ν for the cathodic peak, and anodic peak respectively. The b-value of the cathodic and anodic peaks were obtained by calculating the index of the power law fit of the I_{peak} versus scan rate ν, i.e., $I_{peak} = a\nu^b$. The b-value of the cathodic peak was found to be 0.78 and that of the anodic peak was 0.7. The b-values in the range of 0.7-0.8 suggest that the $TiNb_2O_7$ goes through a fast redox reaction with relatively low diffusion limitations.

Figure 3.3(d) shows the capacity retention of $TiNb_2O_7$ at various C-rates also for a potential window between 1.0 V and 3.0 V (vs. Li/Li^+). The theoretical capacity of $TiNb_2O_7$ is estimated to be 388 mAh/g upon 5 lithium ion insertion [112]. Here, the measured reversible capacity of the $TiNb_2O_7$ electrode was around 255 mAh/g at C-rate of 1C. At C-rate of 2C, the $TiNb_2O_7$ electrode provided up to 60 % of its theoretical capacity while graphite anode can only provide 22 % of its theoretical capacity for the same C-rate [115]. Furthermore, even at rate of 10 C, the $TiNb_2O_7$ electrode maintained 40 % of its theoretical

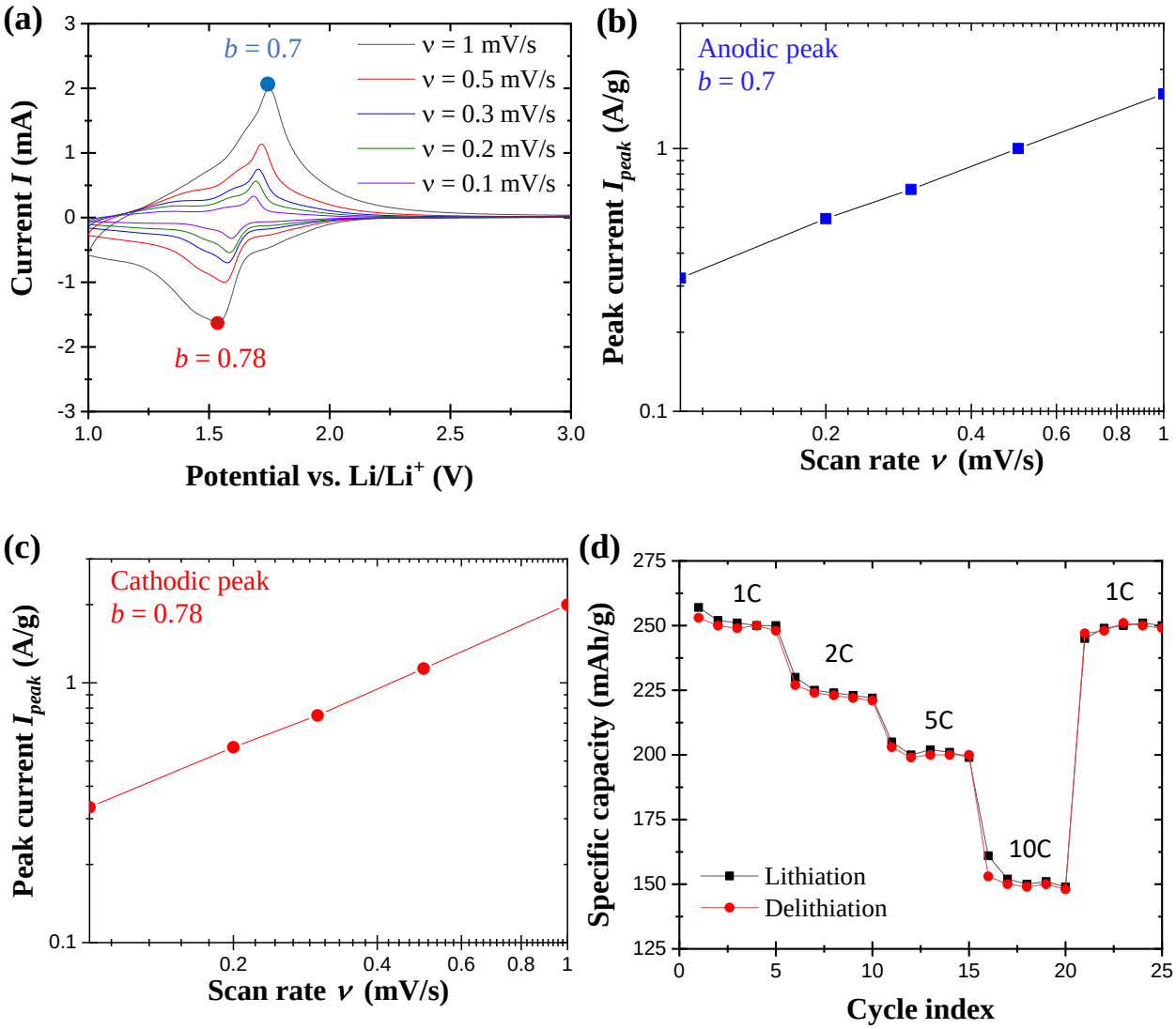

Figure 3.3: (a) Cyclic voltammogram of $TiNb_2O_7$ half-cell cycled with a potential window ranging from 1.0 to 3.0 V vs. Li/Li^+ at different scan rates ν, (b) measured peak current I_{peak} as a function of ν for the anodic peak, and (c) for the cathodic peak, (d) specific capacity retention of the $TiNb_2O_7$ at various C-rates in the voltage range of 1.0−3.0 V.

capacity and showed impressive reversibility over a number of cycles.

3.2.3 entropic potential of $TiNb_2O_7$

Figure 3.4(a) plots the cell voltage $V(x,t)$ and open circuit voltage $U_{ocv}(x,T)$ as functions of x composition in $Li_xTiNb_2O_7$ measured by GITT at C-rate of 2C and temperature $T = 20$ °C. It features three distinct regions apparent in the slope of the open circuit voltage curve during the incorporation process of Li^+ in $Li_xTiNb_2O_7$. The first sharp drop in $U_{ocv}(x,T)$ in the range $0.0 \leq x \leq 0.75$ was indicative of a homogeneous solid solution [31]. Then, the voltage plateau in the range $0.75 \leq x \leq 1.5$ corresponded to a two phase coexistence region, as discussed in the literature [31, 112]. Finally, the shallow slope for $1.5 \leq x \leq 3.0$ corresponded to another homogeneous solid solution [31, 112].

Figure 3.4(b) shows the measured entropic potential $\partial U_{ocv}(x,T)/\partial T$ and open circuit voltage $U_{ocv}(x,T)$ of the $TiNb_2O_7$ half-cell as functions of lithium composition x in $Li_xTiNb_2O_7$ during lithiation at 20 °C. The measurements were found to be in a good agreement with previous studies [116]. Indeed, $\partial U_{ocv}(x,T)/\partial T$ was negative throughout the entire lithium composition upon lithium insertion. Therefore, the reversible entropic heat generation was expected to be strictly exothermic ($\dot{Q}_{rev} \geq 0$) during lithiation and endothermic ($\dot{Q}_{rev} \leq 0$) during delithiation. For $x < 0.75$, the entropic potential $\partial U_{ocv}(x,T)/\partial T$ decreased rapidly upon insertion of lithium in the homogeneous solid solution forming a more ordered structure [116]. However, $\partial U_{ocv}(x,T)/\partial T$ started to increase around $x = 0.75$ due to the transition from a homogeneous solid solution to a two-phase coexistence region. The *in situ* XRD data reported in literature [31, 117] shows that all the $TiNb_2O_7$ reflections were maintained upon lithiation/delithiation for all values of x. Therefore, the structure of both homogeneous solid solution phases was in the monoclinic phase with the identical C/2m space group and $TiNb_2O_7$ did not experience crystallographic phase transition [117]. However, $\partial U_{ocv}(x,T)/\partial T$ experienced fluctuation in the composition range $0.75 \leq x \leq 1.5$ corresponding to a two-phase coexistence region. Since a crystallographic phase change did not occur, the observed fluctuation in entropic potential $\partial U_{ocv}(x,T)/\partial T$ was influenced by the intralayer lithium ordering rather than by a first order phase transition. This type of tilde shape entropy change was first observed by Dahn and Haering [118] upon lithiation of TiS_2.

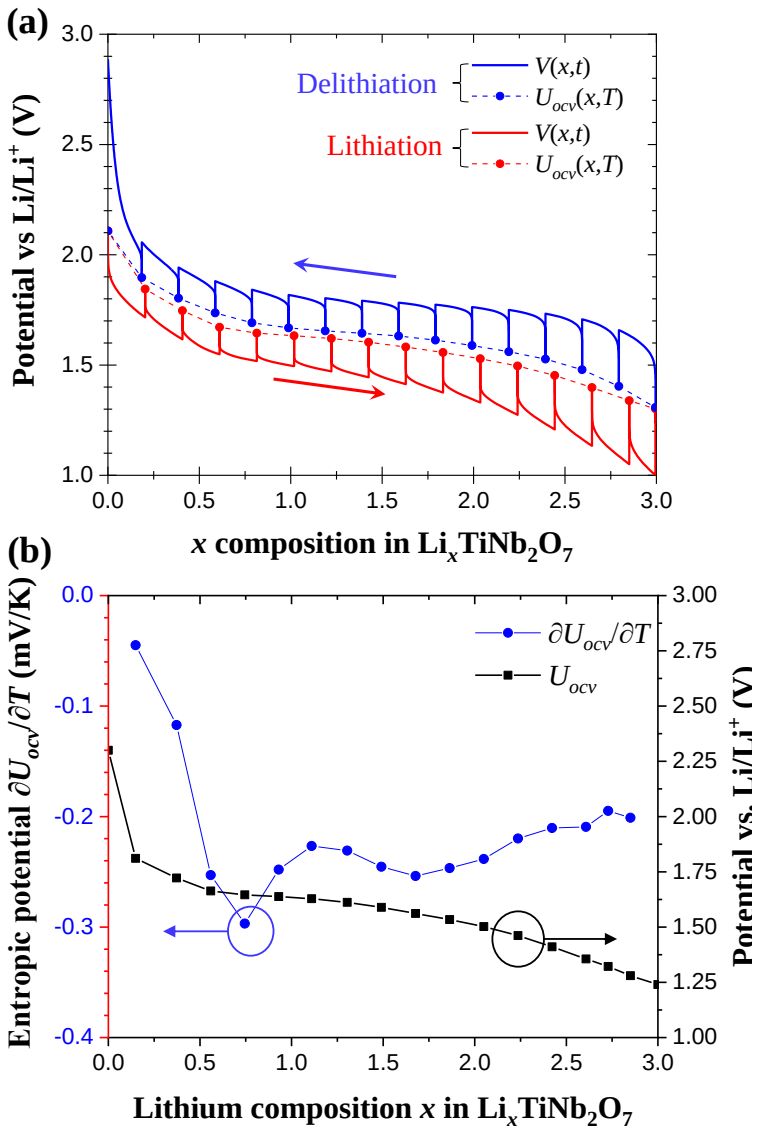

Figure 3.4: Galvanostatic intermittent titration technique (GITT) curve plotting (a) cell potential $V(x,t)$ and open circuit voltage $U_{ocv}(x,T)$ during delithiation and lithiation as functions of lithium composition x in $Li_xTiNb_2O_7$; (b) entropic potential $\partial U_{ocv}(x,T)/\partial T$ and open circuit voltage $U_{ocv}(x,T)$ as functions of x during lithiation. Both measurements were taken at C-rate of 2C and temperature $T = 20$ °C.

It occurs when it is energetically favorable for the inserted lithium ions in the lattice to arrange themselves in the vacancies in a more ordered fashion than being randomly inserted

for further insertion of lithium ions [59]. This intralayer lithium reordering corresponds to rapid lithium mobility within the Wadsley-Roth block motifs down the tunnels along the b-axis and also between the lithium vacancy sites with higher activation energy and that with lower activation energy along the intrablock tunnels as reported in a previous density functional theory (DFT) study [111]. For $x > 1.5$, entropic potential $\partial U_{ocv}(x,T)/\partial T$ was nearly constant within a range of -20 to -25 J/mol·K indicating the filling of leftover vacancy sites in the shear structure of the homogeneous solid solution [116].

3.2.4 Heat generation of $TiNb_2O_7$

Figure 3.5(a) plots the irreversible Joule heat generation rate $\dot{Q}_{J,}(x,t)$ during lithiation and delithiation calculated from Eq.3(1) based on the imposed current I, the cell voltage $V(x,t)$ measured in the calorimeter under galvanostatic cycling at C-rate of 2C, and the open circuit voltage $U_{ocv}(x,T)$ measured by GITT at 20 °C. The change observed in $\dot{Q}_J(x,t)$ could be attributed to changes in the electrical resistivity of $TiNb_2O_7$ upon lithiation. Indeed, $TiNb_2O_7$ is an insulator in its unlithiated state, and exhibits very large electrical resistivity $\sim 10^9$ Ω cm [119]. However, upon lithiation to $Li_{0.25}TiNb_2O_7$, the electrical resistivity decreases by seven orders of magnitude to ~ 50 Ω cm [119]. This change in electrical resistivity was well captured by the sharp drop in $\dot{Q}_J(x,t)$ in the composition range $0 \leq x \leq 0.9$. Furthermore, the electrical resistivity slightly increased again upon further lithium ion insertion. In fact, the electrical resistivity was measured to be ~ 700 Ω cm for $LiTiNb_2O_7$ and ~ 2000 Ω cm for $Li_{2.5}TiNb_2O_7$ [119]. This increase in the electrical resistivity of $Li_xTiNb_2O_7$ was also captured by $\dot{Q}_J(x,t)$ for composition x in the range $0.9 \leq x \leq 3$. However, $\dot{Q}_J(x,t)$ during delithiation differed from that during lithiation possibly due to the difference in mass transfer resistance associated with Li^+ diffusion in the electrode.

Moreover, Figure 3.5(b) shows the reversible heat generation rate $\dot{Q}_{rev}(x,t)$ during lithiation, and delithiation estimated using Eq.3(2) based on the measured entropic potential $\partial U_{ocv}(x,T)/\partial T$. Here, $\dot{Q}_{rev}(x,t)$ was exothermic (i.e., positive) upon lithiation and endothermic (i.e., negative) upon delithiation. The effect of $\dot{Q}_{rev}(x,t)$ became significant as

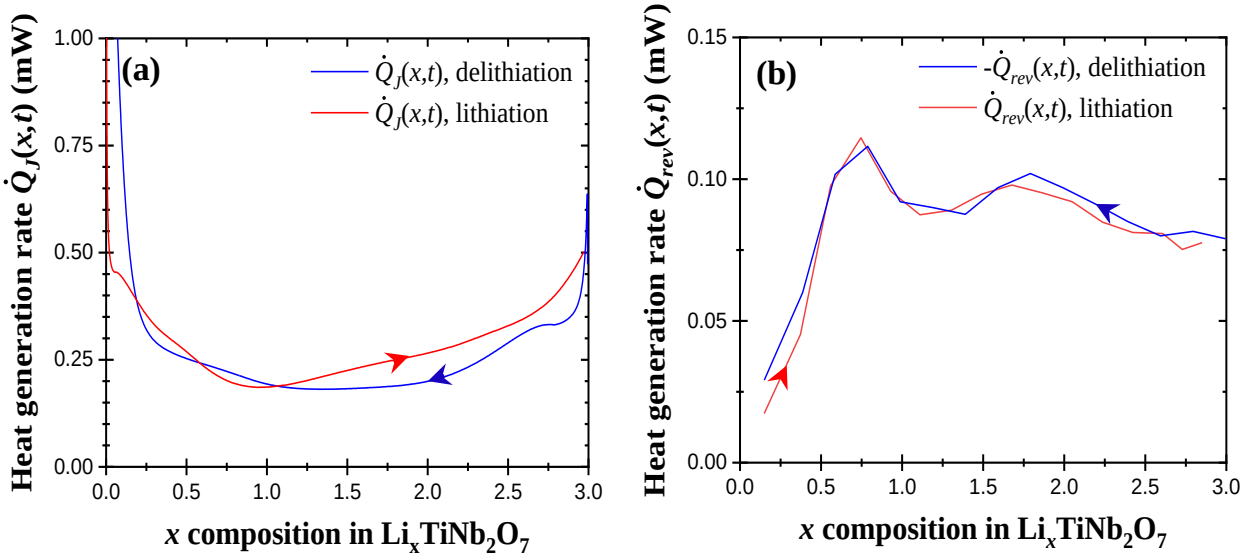

Figure 3.5: (a) Irreversible Joule heat generation rate $\dot{Q}_{J,}(x,t)$ during lithiation, and delithiation [Eqs.3(1)], and (b) reversible heat generation rate $\dot{Q}_{rev}(x,t)$ during lithiation and delithiation [Eqs.3(2)] as functions of lithium composition x in $Li_xTiNb_2O_7$ at temperature T = 20 °C.

$Li_xTiNb_2O_7$ transitioned from a homogeneous solid solution to two coexisting solid phases around $x \simeq 0.75$. After the sharp change, $\dot{Q}_{rev}(x,t)$ remained fairly constant for the rest of the lithiation process. Note also that integrating $\dot{Q}_{rev}(x,t)$ over an entire cycle yielded nearly zero, confirming the reversible nature of this heat generation mechanism.

Figures 3.6(a) and 3.6(b) plot the instantaneous heat generation rate $\dot{Q}_T(x,t)$ measured in the calorimeter cell at C-rate of 2C and $T = 20$ °C as a function of x in $Li_xTiNb_2O_7$. The sum of $\dot{Q}_J(x,t)+\dot{Q}_{rev}(x,t)$ was in relatively good agreement with the measured total heat generation rate $\dot{Q}_T(x,t)$. Assuming that the effect of heat generation due to side reactions $\dot{Q}_{sr}(x,t)$ was negligible [47–49], the difference between $\dot{Q}_T(x,t)$, and the sum $\dot{Q}_J(x,t) + \dot{Q}_{rev}(x,t)$ corresponded to the enthalpy of mixing, i.e., $\dot{Q}_{mix}(x,t) = \dot{Q}_T(x,t) - \dot{Q}_J(x,t) - \dot{Q}_{rev}(x,t)$ [Eq.3(4)]. The heat dissipated due to enthalpy of mixing upon relaxation of quasi-steady state concentration gradients formed upon cycling was reported to be inversely proportional

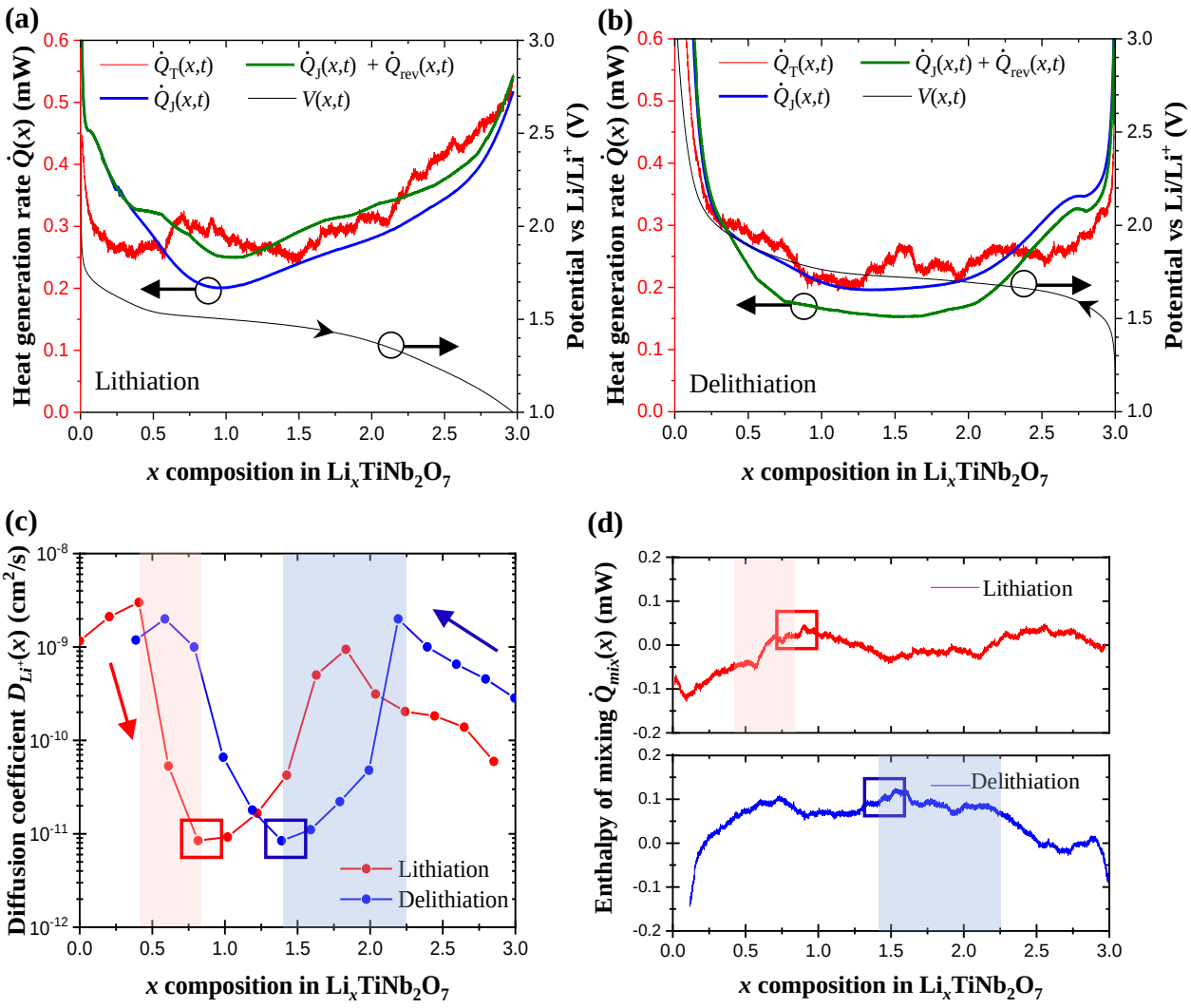

Figure 3.6: Heat generation rates $\dot{Q}_T(x,t)$, $\dot{Q}_J(x,t)$, $\dot{Q}_J(x,t) + \dot{Q}_{rev}(x,t)$ [Eqs.3(1),(2),(5)] and cell voltage $V(x,t)$ measured upon (a) lithiation, (b) delithiation at C-rate of 2C at 20 °C. (c) Apparent diffusion coefficient D_{Li^+} of lithium ion in $Li_xTiNb_2O_7$ and (d) enthalpy of mixing $\dot{Q}_{mix}(x,t) = \dot{Q}_T(x,t) - [\dot{Q}_J(x,t) + \dot{Q}_{rev}(x,t)]$ as functions of lithium composition x in $Li_xTiNb_2O_7$ at temperature $T = 20$ °C.

to the square of the apparent diffusion coefficient [51]. In fact, the apparent diffusion coefficient of lithium into the electrode, $D_{Li^+}(x)$ can be estimated by combining GITT and Fick's

second law according to [120]

$$D_{Li^+}(x,T) = \frac{4}{\pi\tau}\left(\frac{V}{A}\right)^2\left(\frac{\Delta U_{ocv}(x,T)}{\Delta V_t(x)}\right)^2. \tag{3.2}$$

Here, τ is the duration of the GITT current pulse, A and V are the surface area and the volume of the electrode, $\Delta V_t(x)$ is the change in the cell potential as a result of the imposed current pulses excluding the IR drop at the beginning of the current pulse, and $\Delta U_{ocv}(x,T)$ is the change in the open circuit voltage between two consecutive current pulses. Figure 3.6(c) shows the apparent diffusion coefficient of Li^+ in the electrode $D_{Li^+}(x)$ measured as a function of x in $Li_xTiNb_2O_7$ at 20 °C. It reached a minimum of $8{\times}10^{-12}$ cm^2/s at $x_{min} \simeq 0.8$ during lithiation and at $x_{min} \simeq 1.4$ during delithiation. Interestingly, these values of x_{min} corresponded closely to the bounds of the voltage plateau (at $U_{ocv} = 1.6$ V) observed in the GITT curve (Fig. 4). This indicates that the very sharp decrease in $D_{Li^+}(x)$ was caused by the transition from a homogeneous solid solution phase reaction to a two-phase coexistence region [121]. In addition, this change in the apparent diffusion coefficient was also observed with the enthalpy of mixing $\dot{Q}_{mix}$. During the lithiation process, a significant drop in $D_{Li^+}(x,T)$ was observed for $0.4 \leq x \leq 0.8$. This contributed to an increase in the enthalpy of mixing $\dot{Q}_{mix}(x,t)$ and to its local maximum highlighted in Figure 3.6(d). Similarly, the sharp decrease in $D_{Li^+}(x,T)$ during delithiation between $2.25 \geq x \geq 1.4$ correlated with an increase in the enthalpy of mixing and the local maximum highlighted in Figure 3.6(d).

A recent experimental study demonstrated that the net electrical energy losses due to the hysteretic voltage profile upon cycling were dissipated as Joule heating at a low C-rate [48]. By operating at a C-rate of C/10, the authors were able to neglect the effect of enthalpy of mixing [48]. However, the latter can be significant in fast charging batteries operating under high currents [51]. Here, the net electrical energy losses ΔE_e (in J) between the electrical energy provided during charging and that recovered during discharging was illustrated in the hysteric voltage $V(x,t)$ and expressed as [48]

$$\Delta E_e = \oint_{cycle} V(x,t)dq \tag{3.3}$$

where q is the charge transferred upon electrochemical reaction. The total thermal energy dissipated Q_T (in J) as well as the heat dissipated in the form of Joule heating Q_J and

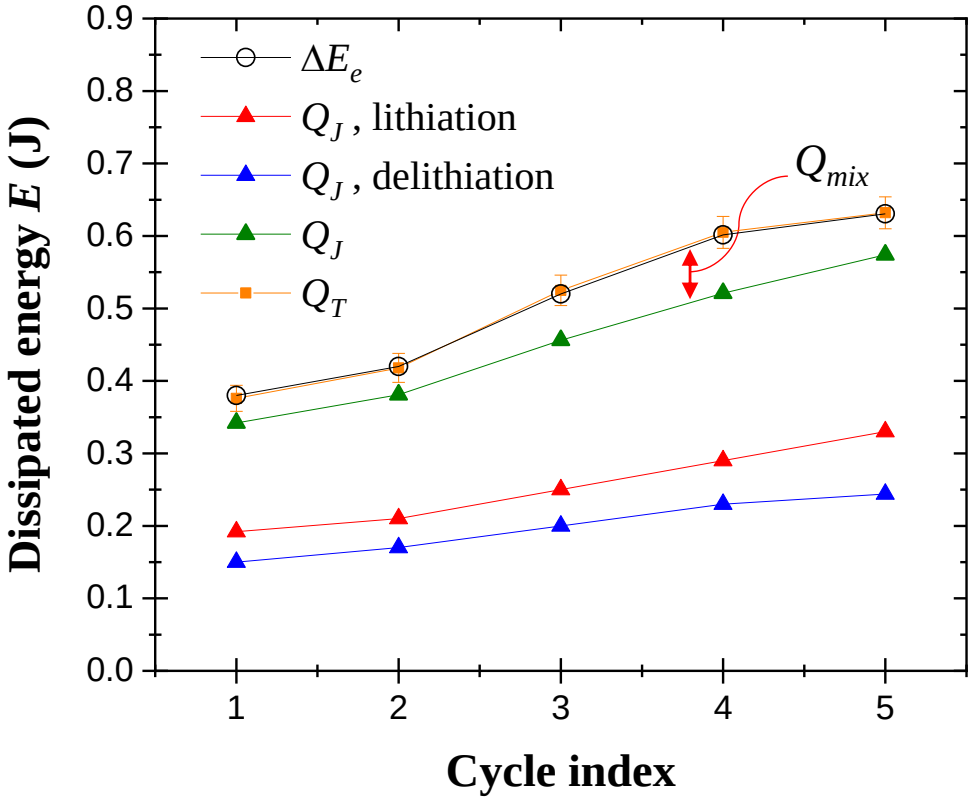

Figure 3.7: Net electrical energy losses ΔE_e and total thermal energy dissipated Q_T for the first five charging-discharging cycles as well as that due to Joule heating Q_J during lithiation and delithiation. The enthalpy of mixing corresponds to $Q_{mix} = Q_T - Q_J = \Delta E_e - Q_J$.

enthalpy of mixing Q_{mix} were calculated according to [48]

$$Q_i = \oint_{cycle} \dot{Q}_i(x,t)dt \quad \text{with } i = \ T,\ J,\ rev, \text{or } mix \tag{3.4}$$

Figure 3.7 presents the electrical energy losses ΔE_e over the first five cycles and the total thermal energy dissipated Q_T along with that due to Joule heating Q_J during lithiation and delithiation. The experimental error associated with Q_T was calculated based on the sensitivity of the heat flux sensor and on the precision of the data acquisition system (DAQ). Figure 3.7 indicates that ΔE_e increased upon cycling possibly due to the associated increase in the internal resistance [122, 123]. More importantly, ΔE_e fell within 2 % of the measured total thermal energy Q_T generated per cycle, i.e., the electrical energy losses were dissipated entirely in the form of heat, i.e., $\Delta E_e = Q_T$. In addition, the irreversible Joule

heating during lithiation was larger than that during delithiation due to the slower kinetics of lithiation characterized by a smaller apparent diffusion coefficient compared to delithiation resulting in a larger overpotential [124]. Since $Q_{rev} \simeq 0$, the difference between Q_T and Q_J represented the heat dissipated as enthalpy of mixing Q_{mix}. Over the first five cycles, thermal losses Q_T and Q_J increased as cycling proceeded. This can be attributed to the increase in the internal resistance with cycling possibly due to the mechanical degradation and growth of the SEI layer on the $TiNb_2O_7$ electrode [122, 123]. Nevertheless, the enthalpy of mixing remained nearly constant regardless of the cycle number and contributed only 15 % of the total energy dissipated. By contrast, calculations based on isothermal calorimetry on $LiAl_{0.2}Mn_{1.8}O_{4-\delta}F_{0.2}$ showed that the energy dissipated in the form of enthalpy of mixing was 52 % of total dissipated heat at the same rate with the same electrolyte and counter electrode [51]. The present results indicate that the heat dissipation due to the enthalpy of mixing remained small in the calorimeter cell even at a C-rate of 2C which is very promising for fast charging battery applications.

3.3 Conclusion

This paper reports a fast, simple, and inexpensive synthesis method of small $TiNb_2O_7$ particles, requiring a mere 7 to 8 minutes in a microwave oven under an ambient atmosphere. This preparation method presents new opportunities for reducing the production costs and synthesis times of promising LIB anode with excellent performance at high C-rates. The synthesized $TiNb_2O_7$ particles were smaller than those synthesized with conventional solid state methods. Entropy measurements combined with previous *in situ* XRD measurements [31, 117] established the occurrence of intralayer lithium ordering enabling the fast charging of $TiNb_2O_7$. In addition, the heat generation rate due to Joule heating varied widely during lithiation and delithiation and dominated the energy losses during cycling at C-rate of 2C. Such calorimetric measurements can further provide insight into changes in the electrical conductivity of batteries for different SOC upon cycling. Furthermore, the enthalpy of mixing remained small even at high C-rates and correlated with changes in the measured apparent diffusion

coefficient of Li^+ in the $Li_xTiNb_2O_7$ electrode upon lithiation/delithiation. These results establish that $TiNb_2O_7$ constitutes an excellent anode material for fast charging battery applications.

CHAPTER 4

Potentiometric Entropy and *Operando* Calorimetric Measurements Reveal Fast Charging Mechanisms in PNb_9O_{25}

This chapter aims to identify the entropic and calorimetric signatures of the different physicochemical phenomena taking place during charging/discharging at the PNb_9O_{25} working electrode and at the lithium metal counter electrode. Potentiometric entropy and calorimetry measurements were combined with XRD measurements to understand the structural changes in the PNb_9O_{25} upon lithiation/delithiation. Furthermore, the instantaneous heat generation rate measurements at each electrodes during cycling was used to deepen our understanding of electrochemical phenomena resulting in heat dissipation.

4.1 Materials and methods

4.1.1 Synthesis of PNb_9O_{25} powder

Stoichiometric ratios of Nb_2O_5 (Materion, 99.95%) and $(NH_4)_3PO_4$ (Sigma Aldrich, 98%) were ground using an agate mortar and pestle for 20 minutes to achieve a well-ground mixture. Then, 3 grams of powder was pressed into a 13 mm diameter pellet under 2 tons of force. The pellet was placed into an alumina crucible on a bed of sacrificial powder mixture and heated in air in two steps. First, the material was heated to 623 K for 20 hours. Second, the temperature was increased to 1523 K for 18 hours and the samples were slowly cooled to room temperature. The average particle size of the synthesized PNb_9O_{25} powder was 5 μm and decreased to 1 μm after 30 minutes of ball-milling.

4.1.2 Electrode and device fabrication

The synthesized PNb_9O_{25} pellet was ground with SuperP (TIMCAL) using an agate mortar and pestle for 5 minutes until visibly combined. The mixture was transferred to a stainless-steel ball mill canister (5 mL, one ball), and mechanically milled for a total of 20 minutes in order to achieve thorough mixture of the carbon and active materials. A slurry was prepared by first suspending polyvinylidene fluoride (PVDF) in N-Methyl-2-pyrrolidone (NMP) and speedmixing at 2000 rpm for 10 minutes. The PNb_9O_{25}/carbon mixture was added to the PVDF and speedmixed at 2000 rpm for another 10 minutes. The resulting slurry had mass ratio 1:0.15:0.05 of PNb_9O_{25}:conductive carbon:binder. A doctor blade was used to cast the slurry onto a copper foil current collector. The resulting 200 μm thick film was dried at 90 °C under vacuum for 18 hours. Then, electrodes were punched into a 10 mm diameter disc. The mass loading of active material on the electrode was 6.2 mg/cm^2.

Cyclic voltammetry and galvanostatic cycling were conducted using a coin cell configuration (MTI parts, 2032 SS casings). All coin cells were fabricated in an Ar-filled glove box and consisted of a 200 μm thick PNb_9O_{25} electrode with 1 M of $LiPF_6$ in EC:DMC 1:1 v/v (Sigma Aldrich) as the electrolyte, a 10×10×1 mm thick polished metallic lithium (Sigma Aldrich) ribbon as the counter electrode, and a 200 μm thick glass microfiber filter separator (Whatman, Grade GF/C). The coin cells were cycled using a high accuracy potentiostat (Biologic, VSP-300) in the voltage range of 1.0−3.0 V.

4.1.3 Material characterization

In order to confirm the formation of the desired composition and phase, X-ray diffraction spectra were collected using a Panalytical Empyrean powder diffractometer equipped with Cu K-α radiation (λ = 1.5406 Å). The PNb_9O_{25} powder was distributed onto a Si zero-background plate and the data were collected in Bragg-Brentano geometry. Rietveld refinement was performed using TOPAS (Academic v.6) and fit to the previously solved space group for PNb_9O_{25} *I4/m* [125].

4.1.4 Potentiometric entropy measurements

The open circuit voltage $U_{ocv}(x,T)$ and the entropic potential $\partial U_{ocv}(x,T)/\partial T$ of the coin cells with the PNb_9O_{25} anode and lithium metal counter electrode were measured as functions of lithium composition x with a potentiometric entropy measurement technique using the appartus described previously [50]. The potentiometric entropy measurements procedure consists of imposing a series of constant current pulses each followed by a relaxation period. Here, the constant current pulse lasted 30 minutes with a current of 130 μA corresponding to a C-rate of C/10. After each current pulse, the cells were allowed to relax for 90 minutes. During the relaxation period, the temperature of the coin cell was varied from 15 °C to 25 °C in 5 °C increments by imposing a step-like temperature profile using a thermoelectric cold plate (TE technology, CP-121). The temporal evaluation of the cell voltage was recorded with a high accuracy potentiostat (Biologic, VSP-300). Likewise, $U^{avg}(x,T)$ and $\partial U^{avg}(x,T)/\partial T$ were measured using the same procedure as that used for measuring $U_{ocv}(x,T)$, including the same relaxation time, but at different C-rates. The duration of the current pulses also changed with C-rates. For instance, at C-rate of 1C, each current pulse lasted 3 minutes, while it lasted 2 minutes for C-rate of 2C, and 1 minute for 3C. Before imposing the next temperature step and recording $U_{ocv}(x,T)$ or $U^{avg}(x,T)$, two conditions needed to be satisfied to ensure that the cell had reached thermodynamic equilibrium namely (i) the temperature difference between the cold plate and the top of the coin cell was less than 0.1 °C, and (ii) the time rate of change of the open circuit voltage $\partial U_{ocv}(x,T)/\partial t$ or $\partial U^{avg}(x,T)/\partial t$ was less than 1 mV/h.

4.1.5 *Operando* isothermal calorimetry

The instantaneous heat generation rates at the PNb_9O_{25} and lithium metal electrodes were measured separately under galvanostatic cycling using a custom-made isothermal calorimeter described previously [109]. Similar to the coin cell assembly, the calorimetric cell consisted of (i) a 1 x 1 cm^2 square shaped PNb_9O_{25} electrode, (ii) two 50 μm thick Celgard C380 polypropylene/polyethylene separator sheets, (iii) 1 M $LiPF_6$ in EC:DMC 1:1 v/v (Sigma

Aldrich) as the electrolyte, and (iv) polished metallic lithium (Sigma Aldrich) as the counter electrode.

Based on the thermal analysis of a single electrode described in Supplementary Materials of Ref. [109], the heat generation rate $\dot{Q}_i(t)$ (in mW) at each electrode was equal to the heat transfer rate $q_i''(t)$ passing through the 1×1 cm^2 thermoelectric heat flux sensor (greenTEG, gSKIN-XP) placed in thermal contact with the back of each electrode such that [109],

$$\dot{Q}_i(t) = q_i''(t)A_i = \frac{\Delta V_i(t)}{S_i}A_i \quad \text{with } i = PNO \text{ or } Li. \tag{4.1}$$

Here, ΔV_i is the voltage difference measured in each heat flux sensor, A_i denotes the footprint area of the electrode (in cm^2), and S_i is the temperature-dependent sensitivity of the heat flux sensor provided by the manufacturer (in μV/(W/cm^2)). The total instantaneous heat generation rate in the entire cell can be expressed as the sum of the heat generation rate measured at each electrode, i.e., $\dot{Q}_T(t) = \dot{Q}_{\mathrm{Li}}(t) + \dot{Q}_{\mathrm{PNO}}(t)$.

Moreover, the instantaneous heat generation rate $\dot{Q}_i(t)$ at electrode "i" can be divided into an irreversible $\dot{Q}_{irr,i}(t)$, and a reversible $\dot{Q}_{rev,i}(t)$ heat generation rate so that $\dot{Q}_i(t)$=$\dot{Q}_{irr,i}(t)$+$\dot{Q}_{rev,i}(t)$. Obtaining $\dot{Q}_{irr,i}(t)$ for a battery electrode is rendered difficult by the fact that the electrical conductivity of the electrode may change upon lithiation/delithiation. However, it is convenient to note that, time-averaging $\dot{Q}_{rev,i}(t)$ at each electrode over an entire cycle should yield zero. Thus, the time-averaged irreversible heat generation rate $\bar{\dot{Q}}_{irr,i}(t)$ at electrode "i" can be expressed as

$$\bar{\dot{Q}}_{irr,i} = \frac{1}{t_c + t_d}\oint_{cycle} \dot{Q}_i(t)\mathrm{d}t \quad \text{with } i = \ PNO \text{ or } Li \tag{4.2}$$

where t_c and t_d are the duration of the charging (delithiation), and the discharging (lithiation) steps, respectively. The time-averaged heat generation rates during either the lithiation (subscript 'd") or the delithiation (subscript 'c") step can also be calculated as

$$\bar{\dot{Q}}_{i,j} = \frac{1}{t_j}\int_0^{t_j} \dot{Q}_i(t)\mathrm{d}t \quad \text{with } i = \ PNO \text{ or } Li \quad \text{and} \quad j = \ c \text{ or } d. \tag{4.3}$$

Thus, the time-averaged reversible heat generation rate during charging or discharging is given by

$$\bar{\dot{Q}}_{rev,i} = \bar{\dot{Q}}_{i,j} - \bar{\dot{Q}}_{irr,i} \quad \text{with } i = \ PNO \text{ or } Li \quad \text{and} \quad j = \ c \text{ or } d. \tag{4.4}$$

Furthermore, under galvanostatic cycling, the time t (in sec) can be converted into the lithium composition x in $Li_xPNb_9O_{25}$ such that

$$x = \frac{It}{3600MC_{theo}}. \tag{4.5}$$

Here, M is the mass loading of the active material and C_{theo} is the theoretical capacity of PNb_9O_{25} estimated as C_{theo}=190.3 mAh/g based on one electron per transition metal.

4.2 Results and discussion

4.2.1 Material and Electrochemical characterization

Figure 4.1(a) shows the XRD pattern of the pristine PNb_9O_{25} particles synthesized in this study. The lattice parameters and the atomic positions were refined. Here, the weighted profile R-factor R_{wp} was 18.736, which is slightly high because the peak shape asymmetry was captured. However, all peaks observed in the pattern were assigned to a single phase consistent with PNb_9O_{25} in the space group I4/m with a = 15.62054(7) Å, c = 3.82920(7) Å, and unit cell volume of 934.33(2) $Å^3$. These peaks were in a good agreement with previous studies [125].

Figure 4.1(b) shows the cyclic voltammograms of the PNb_9O_{25} half-cell at different scan rates between 1.0 V and 3.0 V vs. Li/Li^+. It features four distinct pairs of cathodic and anodic peaks, revealing the reversibility of lithiation/delithiation in PNb_9O_{25}. In addition, all four pairs of redox peaks occured at potential above 1.0 V vs. Li/Li^+, confirming that PNb_9O_{25} is a high voltage anode material for LIBs. The pair of cathodic and anodic peaks with the highest potential observed at 1.63/1.78 V vs. Li/Li^+ (blue dots), was attributed to Nb^{5+}/Nb^{4+} redox reactions [125–127]. Likewise, the pair of cathodic and anodic peaks with the lowest potential observed at 1.12/1.28 V vs. Li/Li^+ (orange dots), was attributed to Nb^{4+}/Nb^{3+} redox reactions [125–127]. The b-value associated with each cathodic and anodic peak was obtained by fitting the peak current I_{peak} vs. scan rate ν with a power law such that $I_{peak} = a\nu^b$ (see Appendix C). The b-values of these four cathodic and anodic peaks were around 0.6 suggesting that charging and discharging might be limited by diffusion of

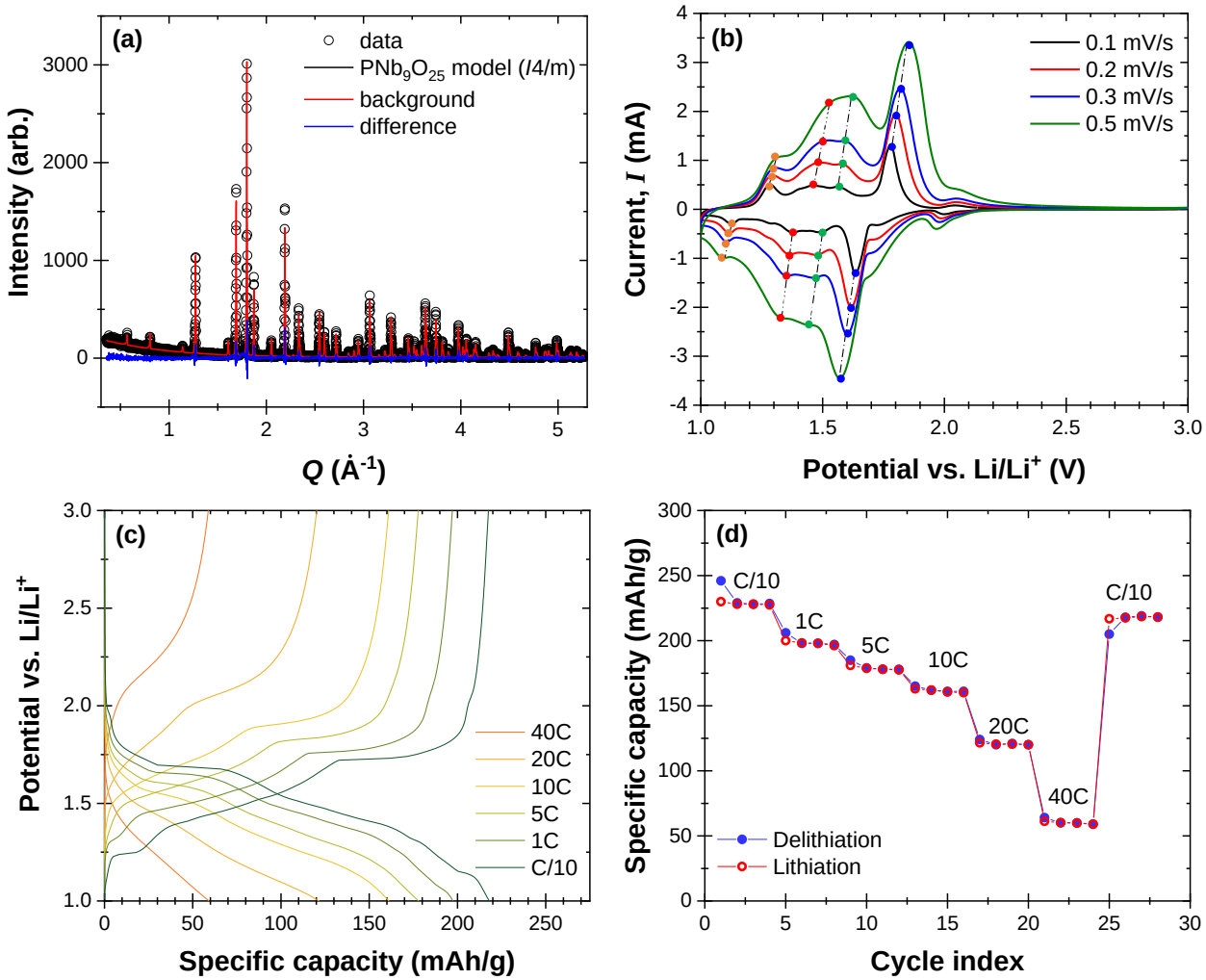

Figure 4.1: (a) X-ray diffraction pattern of the pristine PNb_9O_{25} particles synthesized, (b) cyclic voltammogram of PNb_9O_{25} half-cell cycled with potential window ranging from 1.0 to 3.0 V vs. Li/Li^+ at different scan rates ν, (c) galvanostatic charge-discharge potential profile, and (d) specific capacity retention of the PNb_9O_{25} half-cell cycled between 1.0 and 3.0 V vs. Li/Li^+ at C-rates between C/10 and 40C.

lithium in the PNb_9O_{25} electrode [128]. Furthermore, two more pairs of cathodic and anodic peaks were observed at 1.37/1.45 V (red dots) and 1.49/1.56 V (green dots) vs. Li/Li^+. The b-values associated with these peaks were found to be around 0.95 corresponding to fast and reversible redox reactions [128]. Such large b-values illustrate the potential of PNb_9O_{25} anodes for high power density batteries despite undergoing phase transitions upon

lithiation [128].

Figure 4.1(c) shows galvanostatic charge and discharge profiles of PNb_9O_{25} half-cell cycled between 1.0 and 3.0 V (vs. Li/Li^+) at different C-rates. At C-rate of C/10, the specific capacity was measured to be 225 mAh/g. The latter was larger than the theoretical capacity calculated as $C_{theo} = 190$ mAh/g based on the assumption of 1 electron per transition metal. Measurements by X-ray photoelectron spectroscopy showed that more than 1 electron was stored per transition metal confirming multi-electron redox reaction [129]. Two voltage plateaus were observed around 1.7 V and 1.1 V corresponding to the redox peaks with low b-values of 0.6 observed in Figure 4.1(b).

Figure 4.1(d) shows the specific capacity retention of the PNb_9O_{25} electrode as a function of cycle number for C-rates ranging from C/10 to 40C. The capacity of the PNb_9O_{25} electrode was around 200 mAh/g at C-rate of 1C. Furthermore, even at C-rate of 10 C, the PNb_9O_{25} electrode showed impressive fast charging ability and maintained 75 % of its capacity at C/10. In addition, after 30 cycles, it maintained its capacity and demonstrated excellent reversibility. By comparison, $TiNb_2O_7$, one of the commercially accepted fast charging type lithium-ion battery anode materials, maintained 40 % of its C/10 capacity at C-rate of 10 C [50].

4.2.2 Entropic potential of PNb_9O_{25}

Figure 4.2 plots the open circuit voltage $U_{ocv}(x,T)$ and the entropic potential $\partial U_{ocv}(x,T)/\partial T$ at 20 °C as functions of x composition in $Li_xPNb_9O_{25}$ at C-rate of C/10 during lithiation. The trend of both measured $U_{ocv}(x,T)$ and $\partial U_{ocv}(x,T)/\partial T$ were repeatable during lithiation and subsequent delithiation at C-rate of C/10. It features six distinct regions based on the slope of $U_{ocv}(x,T)$ and $\partial U_{ocv}(x,T)/\partial T$. In Region I, corresponding to $x < 2$, both the open circuit voltage $U_{ocv}(x,T)$ and the entropic potential $\partial U_{ocv}(x,T)/\partial T$ feature sharp drop and sloped curve indicative of lithium insertion in a homogeneous solid solution [125, 129]. Here, $\partial U_{ocv}(x,T)/\partial T$ decreased sharply upon lithiation in the homogeneous solid solution resulting in a more ordered structure. In Region II, for $2 \leq x \leq 3.5$, both $U_{ocv}(x,T)$ and $\partial U_{ocv}(x,T)/\partial T$

were constant and independent of x confirming a two-phase coexistence region also observed previously in XRD measurements [125]. Note that $U_{ocv}(x,T)$ associated with this two-phase coexistence region was 1.7 V (vs Li/Li^+) and corresponded to the potential of the redox peak observed in the CV curve [Figure 4.1(a)]. In addition, *in situ* X-ray powder diffraction of PNb_9O_{25} revealed that the structure goes through both solid solution regions and two-phase coexistence regions [129]. However, the two coexisting phases belong to the original refined space group with two different lattice parameters [129]. First, a solid solution of the original I4/m space group was formed upon lithiation from PNb_9O_{25} to $Li_2PNb_9O_{25}$. Second, between $Li_2PNb_9O_{25}$ and $Li_{3.5}PNb_9O_{25}$ the second I4/m phase emerged with a larger unit cell volume confirming the two-phase coexistence region identified from the analysis of $U_{ocv}(x,T)$ and $\partial U_{ocv}(x,T)/\partial T$.

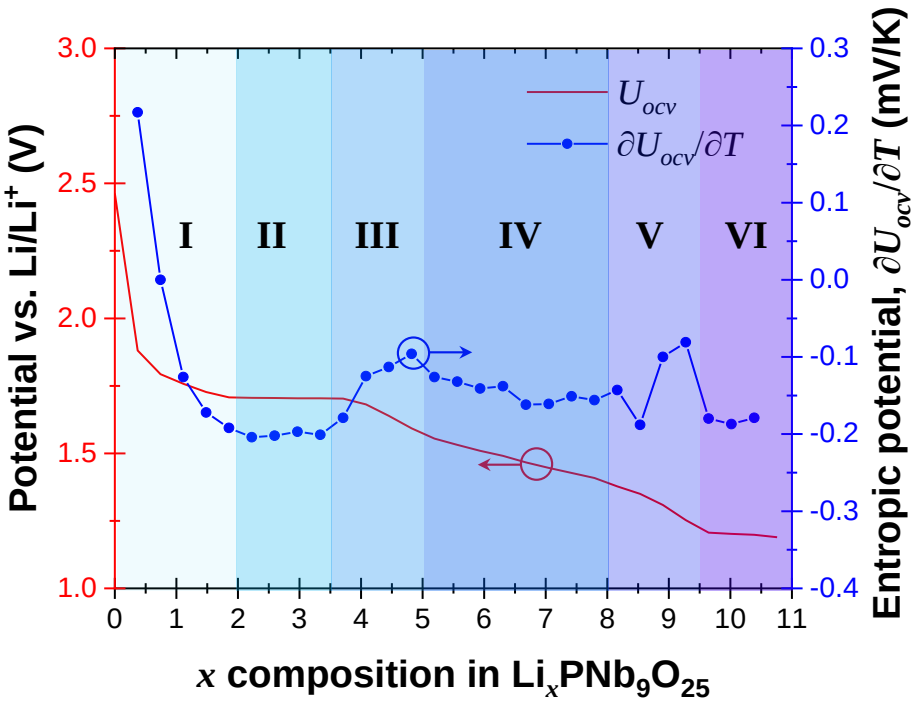

Figure 4.2: Open circuit voltage $U_{ocv}(x,T)$ and entropic potential $\partial U_{ocv}(x,T)/\partial T$ of PNb_9O_{25} half cell as functions of lithium composition x in $Li_xPNb_9O_{25}$ during lithiation at C-rate of C/10.

For $3.5 \leq x \leq 9.5$, $U_{ocv}(x,T)$ shows a sloped potential suggesting a homogeneous solid

solution. *In situ* XRD measurements also confirmed a monophasic lithiation process [126]. However, based on $\partial U_{ocv}(x,T)/\partial T$, this composition range can be further divided into three distinct regions. First, in Region III, defined by $3.5 \leq x \leq 5$, $\partial U_{ocv}(x,T)/\partial T$ increased first then decreased at higher x composition resulting in a local maxima. This behavior could be attributed to an semiconductor-to-metal transition known to occur in this region, based on magnetic susceptibility and solid-state nuclear magnetic resonance measurements, electrochemical impedance spectroscopy data, and density functional theory calculations [129]. The electronic entropy of insulating oxide is nearly zero due to the zero density of state at the Fermi level [89]. However, when the oxide becomes metallic, it exhibits high electronic entropy. Thus, $\partial U_{ocv}(x,T)/\partial T$, which corresponds essentially the partial molar entropy of the PNb_9O_{25} electrode, featured a peak at the semiconductor-to-metal transition (see Appendix C). In Region IV, such that $5 \leq x \leq 8$, $\partial U_{ocv}(x,T)/\partial T$ presents a small negative slope from -0.12 mV/K to -0.16 mV/K indicating the intercalation of lithium ion in a homogeneous solid solution. Furthermore, in Region V corresponding to $8 \leq x \leq 9.5$, $\partial U_{ocv}(x,T)/\partial T$ displays a tilde shape fluctuation. These observations were attributed to intralayer lithium ordering similar to that observed in TiS_2 [118] and $LiCoO_2$ [81]. Such ordering occurs when it is energetically advantageous for the intercalated lithium ions to arrange themselves in the vacant sites in a more ordered manner instead of being randomly inserted [50,59]. Furthermore, numerical simulations based on statistical mechanical modeling and validated experimentally with Li-ions in graphite suggest that the interatomic forces can caused ion ordering and result in tilde shape fluctuation in the partial molar entropy [130]. This intralayer lithium ordering possibly corresponds to fast lithium transport within type-α edge sites with low kinetic barriers [129]. It is interesting to note that the XRD measurements suggest no crystallographic phase change in this region. Lastly, in Region VI with $x \geq 9.5$, both $U_{ocv}(x,T)$ and $\partial U_{ocv}(x,T)/\partial T$ were constant suggesting another two-phase coexistence of $Li_{9.5}PNb_9O_{25}$ and $Li_{10.5}PNb_9O_{25}$ phases.

Overall, the entropic potential measurements confirm the existence of two two-phase coexistence regions also identified from electrochemical testing and XRD measurements [125, 129]. Most notably, the present analysis of both $U_{ocv}(x,T)$ and $\partial U_{ocv}(x,T)/\partial T$ also captured

the entropic signature of semiconductor-to-metal transition (Region III) and intralayer ion ordering (region IV) which could not be identified from other characterization methods.

4.2.3 Heat generation rates

4.2.3.1 Instantaneous heat generation rates

Figures 4.3(a)-4.3(c) plot the instantaneous heat generation rates $\dot{Q}_{PNO}(t)$ measured at the PNb_9O_{25} electrode and $\dot{Q}_{Li}(t)$ at the lithium metal electrode as well as the total instantaneous heat generation rate $\dot{Q}_T(t) = \dot{Q}_{PNO}(t) + \dot{Q}_{Li}(t)$, as functions of dimensionless time t/t_{cd}, with t_{cd} being the charging/discharging cycle period, for three consecutive cycles at temperature of 20 °C and at C-rate of 1C, 2C, and 3C, respectively. First, the measurements at each electrode were repeatable cycle after cycle. In addition, the magnitude of $\dot{Q}_{Li}(t)$ at the lithium metal electrode was relatively constant over the charging or discharging step for any given C-rates unlike $\dot{Q}_{PNO}(t)$ at the PNb_9O_{25} electrode which varied significantly with time.

Figures 4.4(a) and 4.4(b) plot the instantaneous heat generation rates $\dot{Q}_{PNO}(x)$ measured at the PNb_9O_{25} electrode during lithiation and delithiation at 20 °C as a function of composition x in $Li_xPNb_9O_{25}$ for C-rate of 1C, 2C, and 3C. At the onset of lithiation for $x \lesssim 2.0$, $\dot{Q}_{PNO}(x)$ featured an endothermic dip resulting in $\dot{Q}_{PNO}(x) \leq 0$. This can be attributed to the reversible entropic heat generation $\dot{Q}_{rev}(x)$ [eq.4(10)] characterized by a positive $\partial U_{ocv}(x,T)/\partial T$ and featuring a sharp drop as the lithium composition increased (Figure 4.2). This dip was enhanced by the decrease in Joule heating $\dot{Q}_J(x) \geq 0$ due to the drop in electrical resistance of PNb_9O_{25} associated with the insulator to semiconductor phase transition upon lithiation [129]. Indeed, the pristine PNb_9O_{25} was white and electrically insulating but became black as it underwent an insulator-to-semiconductor and semiconductor to metal transitions sequentially upon lithiation [129]. This transition was observed as a peak in the entropic potential measurements (Figure 4.2). Beyond $x \simeq 2$, $\dot{Q}_{PNO}(x)$ was positive and increased with increasing C-rate due to the associated increase in Joule heating. Conversely, $\dot{Q}_{PNO}(x)$ increased sharply during delithiation at low lithium composition due to the

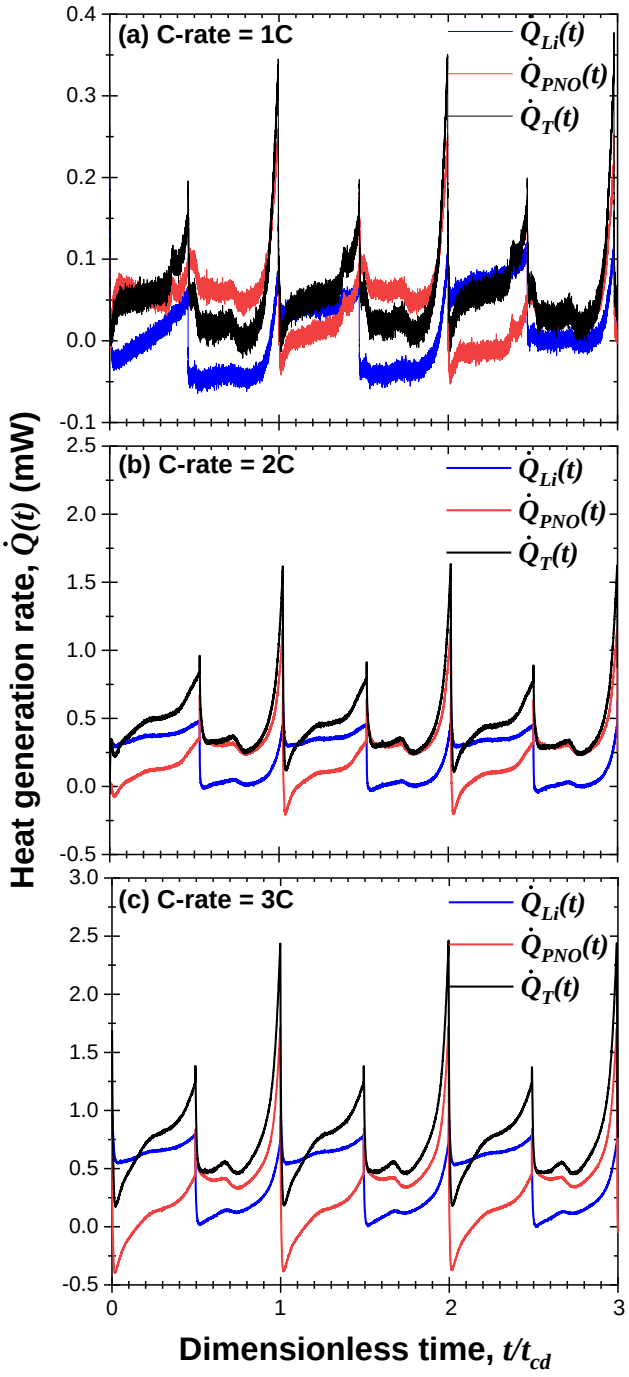

Figure 4.3: Measured instantaneous heat generation rates $\dot{Q}_{PNO}(t)$ at the PNb_9O_{25} electrode, $\dot{Q}_{Li}(t)$ at the lithium metal electrode, and $\dot{Q}_T(t) = \dot{Q}_{PNO}(t) + \dot{Q}_{Li}(t)$ in the cell as functions of dimensionless time t/t_{cd} for three consecutive cycles with potential window ranging from 1.0 V to 3.0 V vs Li/Li^+ at C-rates of (a) 1C, (b) 2C, and (c) 3C.

exothermic reversible entropic heat generation and the increase in the electrical resistance of $Li_xPNb_9O_{25}$. Likewise, it also increased with increasing current or C-rate accompanied by the associated increase in Joule heating. In addition, Figure 4.4(b) shows a local maxima for $x \simeq 5$ corresponding to the semiconductor-to-metal transition observed in the entropic potential $\partial U_{ocv}(x,T)/\partial T$ (Figure 4.2).

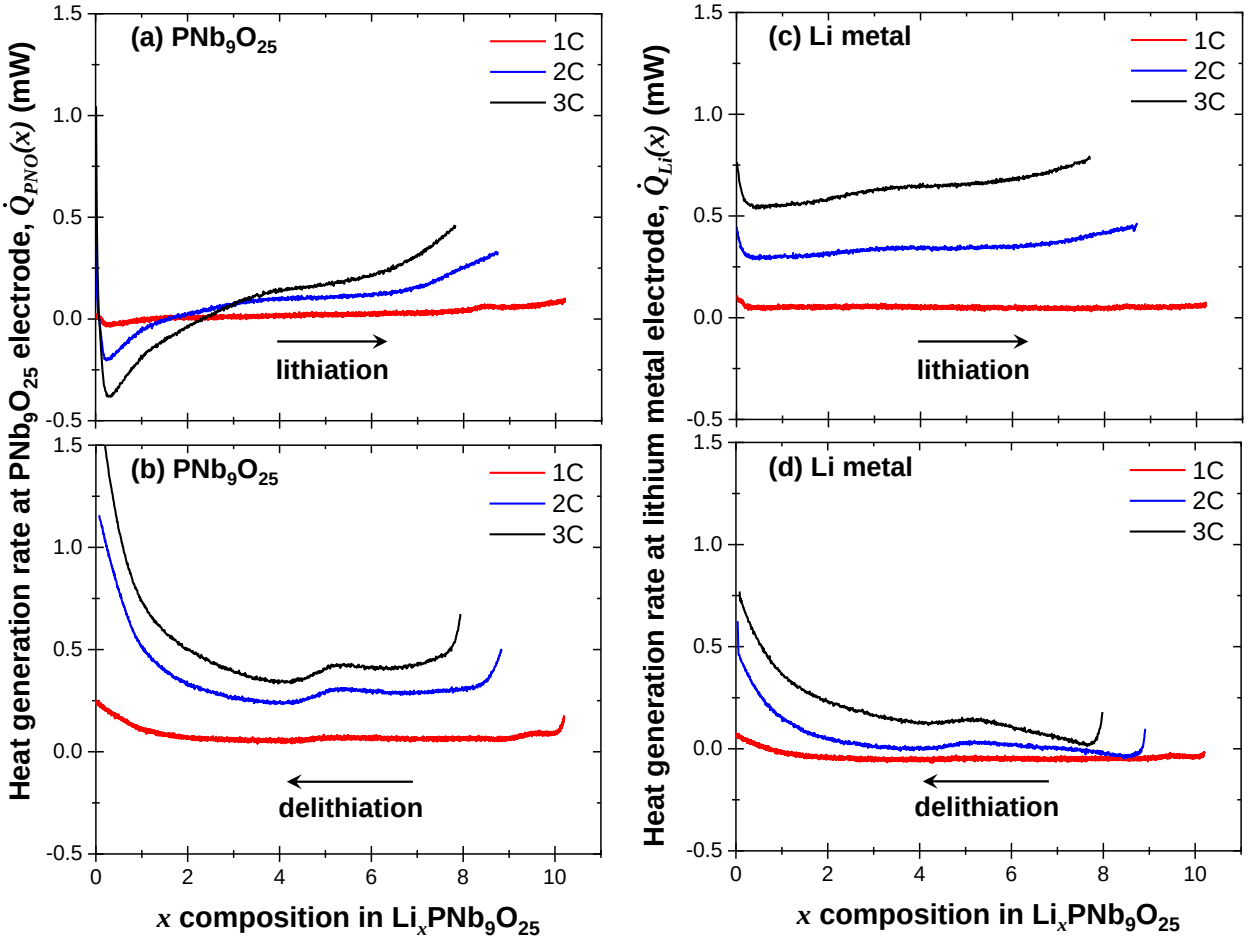

Figure 4.4: Instantaneous heat generation rates $\dot{Q}_{PNO}(x)$ at the PNb_9O_{25} electrode during (a) lithiation, (b) delithiation, and $\dot{Q}_{Li}(x)$ at the lithium metal electrode during (c) lithiation, (d) delithiation in the calorimetric cell cycled between 1.0 and 3.0 V vs. Li/Li^+ at C-rates of 1C, 2C, and 3C as functions of x in $Li_xPNb_9O_{25}$.

Furthermore, Figures 4.4(c) and 4.4(d) plot the instantaneous heat generation rate $\dot{Q}_{Li}(x)$ measured at the lithium metal electrode at 20 °C as a function of lithium composition x for C-rate ranging from 1C to 3C during lithiation and delithiation, respectively. Figure 4.4(c)

indicates that the magnitude of the heat generation rate at the lithium metal electrode $\dot{Q}_{Li}(x)$ was relatively constant throughout the lithiation process. This was attributed to the continuous Li^+ ion stripping and exothermic Li^+ ion solvation accompanied by ion-pairing in the EC:DMC electrolyte at constant current [131]. Then, $\dot{Q}_{Li}(x)$ increased with increasing current I. By contrast, Figure 4.4(d) shows that $\dot{Q}_{Li}(x)$ increased during delithiation due to the plating of Li^+ on the lithium metal counter electrode accompanied by endothermic ion dissociation and exothermic dendrite formation on the surface of lithium metal counter electrode [132]. Indeed, during delithiation, Li^+ ions deintercalated from the PNb_9O_{25} electrode, got solvated in EC:DMC and transported across the device until they reached the Li metal counter electrode where they lost their solvation shells before being deposited on the lithium metal electrode surface in the form of dendrites [133].

4.2.3.2 Time-averaged heat generation rates

Figure 4.5(a) plots the time-averaged irreversible heat generation rates $\bar{\dot{Q}}_{irr,PNO}$ and $\bar{\dot{Q}}_{irr,Li}$ over a cycle at the PNb_9O_{25} and the lithium metal electrodes as functions of imposed current I. Here, the square data points correspond to the time averaged $\bar{\dot{Q}}_{irr,j}$ performed over 5 consecutive cycles at at give C-rate. In addition, the error bars correspond to two standard deviations or 95 % confidence interval. Fitting of $\bar{\dot{Q}}_{irr,Li}(I)$ at the lithium metal electrode indicates that it increased quadratically with respect to I, i.e., $\bar{\dot{Q}}_{irr,Li}(I) \propto I^2$. In other words, the irreversible heat generation was dominated by Joule heating as the electrode resistance of the Li electrode was constant and independent of the state of charge. In addition, $\bar{\dot{Q}}_{irr,PNO}$ at the PNb_9O_{25} electrode was similar to that of the lithium metal electrode $\bar{\dot{Q}}_{irr,Li}$ at low current. However, $\bar{\dot{Q}}_{irr,PNO}$ was smaller than $\bar{\dot{Q}}_{irr,Li}$ at higher current. This can also be attributed to the increasing magnitude of the endothermic peak with increasing current (or C-rate) which resulted in negative $\dot{Q}_{PNO}(x)$ early in the lithiation process [Figure 4.4(a)]. In addition, Joule heating in the PNb_9O_{25} electrode did not vary as I^2 due to the important changes in its electrical resistivity upon lithium intercalation/deintercalation. Moreover, as the C-rate increased, the capacity of the battery decreased indicating that the amount of lithium intercalating/deintercalating also decreased. In fact, at C-rate of 1C, PNb_9O_{25} was

lithiated up to $Li_{10.5}PNb_9O_{25}$ while it was only lithiated up to $Li_8PNb_9O_{25}$ at C-rate of 3C for the same potential window. Thus, at high C-rate, the material underwent a narrower change in composition so that the average electical resistivity also varied with C-rate.

Figure 4.5(b) plots the time-averaged reversible heat generation rate $|\bar{\dot{Q}}_{rev,PNO,j}|$ at the PNb_9O_{25} working electrode and $|\bar{\dot{Q}}_{rev,Li,j}|$ at the lithium metal counter electrode computed according to eqs.4(16)-(18) during lithiation (j=d) and delithiation (j=c) for different currents I. It establishes that both $|\bar{\dot{Q}}_{rev,PNO,j}|$ and $|\bar{\dot{Q}}_{rev,Li,j}|$ at each electrode were identical during lithiation and delithiation, confirming their reversible nature. Furthermore, both $|\bar{\dot{Q}}_{rev,PNO,j}|$ and $|\bar{\dot{Q}}_{rev,Li,j}|$ were linearly proportional to the current I. Combining eqs.4(7) and (10) yields the time averaged reversible heat generation rate $\bar{\dot{Q}}_{rev,i}$ due to the entropic change at each electrode during galvanostatic cycling, i.e.,

$$\bar{\dot{Q}}_{rev,Li} = -\frac{IT}{e} s^o_{Li} \quad \text{and} \quad \bar{\dot{Q}}_{rev,PNO} = \frac{IT}{e} \frac{\partial \bar{s}_{PNO}}{\partial x}. \tag{4.6}$$

Thus, $\bar{\dot{Q}}_{rev,Li}$ is exothermic (> 0) during discharging and endothermic (< 0) during charging whereas $\bar{\dot{Q}}_{rev,PNO}$ is endothermic during discharging and exothermic during charging. In addition, eq.4(20) suggests that $\bar{\dot{Q}}_{rev,i}$ is linearly proportional to current I in qualitative agreement with experimental data plotted in Figure 4.5(b). The formation entropy s^o_{Li} of lithium metal is equal to 0.29 meV/K [41]. Based on the measured entropic pontential $\partial U_{ocv}/\partial T$, the averaged $\partial \bar{s}_{PNO}/\partial x$ over all compositions x achieved during a cycle was estimated as 0.21 meV/K [eq.4(7)]. Thus, the ratio $|\bar{\dot{Q}}_{rev,i,j}/(I/e)|$ should be equal to Ts^o_{Li}=85 meV for the lithium metal electrode and $T\partial \bar{s}_{PNO}/\partial x$=63 meV for the PNb_9O_{25} electrode at 20 °C [eq.4(20)]. Figure 4.5(c) plots $|\bar{\dot{Q}}_{rev,PNO,j}/(I/e)|$ vs. current I at the PNb_9O_{25} ($i = PNO$) and at the Li metal ($i = Li$) electrode. It establishes that the ratios $|\bar{\dot{Q}}_{rev,PNO,c/d}/(I/e)|$ and $|\bar{\dot{Q}}_{rev,Li,c/d}/(I/e)|$ were independent of I for both lithiation and delithiation. Furthermore, $|\bar{\dot{Q}}_{rev,Li,c/d}/(I/e)|$ was larger than $|\bar{\dot{Q}}_{rev,PNO,c/d}/(I/e)|$ as predicted from the entropic potential measurements. Here, $|\bar{\dot{Q}}_{rev,Li,c/d}/(I/e)|$ was measured to be 41 meV while $|\bar{\dot{Q}}_{rev,PNO,c/d}/(I/e)|$ was 34 meV. These values were smaller than the calculated Ts^o_{Li} and $T\partial \bar{s}_{PNO}/\partial x$, thus implying the occurrence of other physicochemical phenomena contributing to the reversible heat generation rate at each electrode.

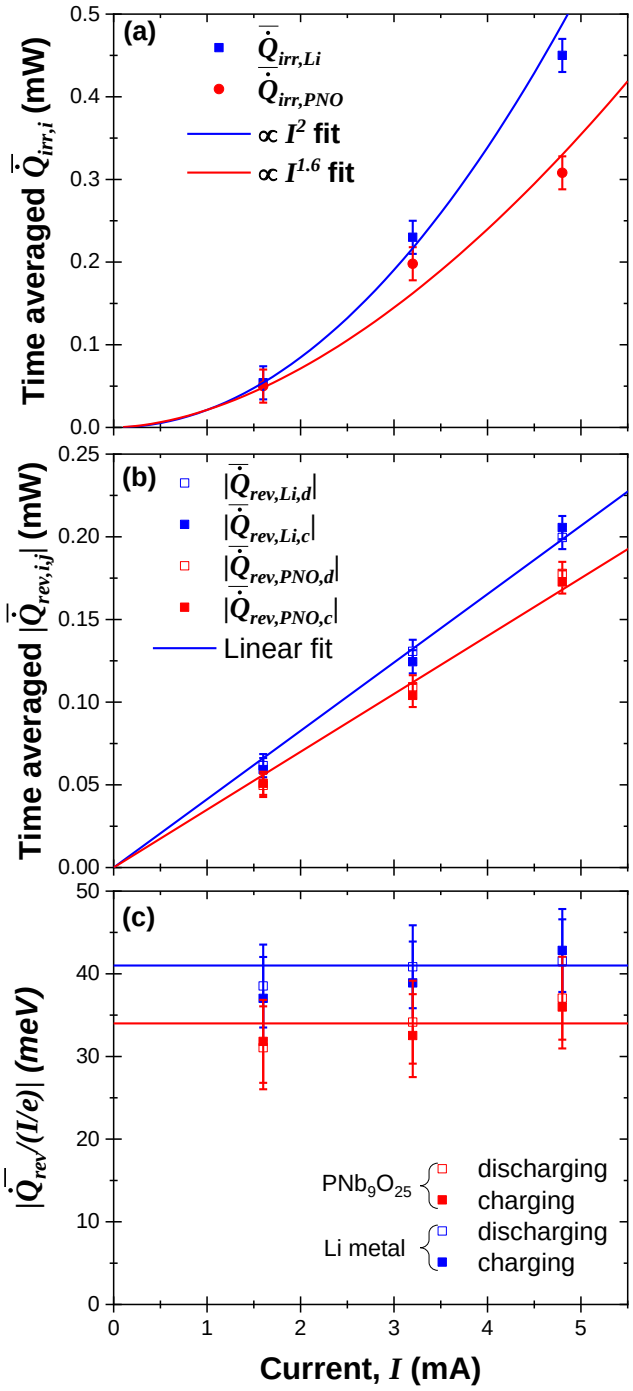

Figure 4.5: Time-averaged (a) irreversible heat generation rates $\bar{\dot{Q}}_{irr,PNO}$ and $\bar{\dot{Q}}_{irr,Li}$, and (b) reversible heat generation rates $|\bar{\dot{Q}}_{rev,PNO,j}|$ and $|\bar{\dot{Q}}_{rev,Li,j}|$ during charging ($j = c$) and discharging ($j = d$), and (c) ratio of $|\bar{\dot{Q}}_{rev,i,c}/(I/e)|$, as functions of current I, based on the isothermal *operando* calorimetry measurements at 20 °C.

The reversible heat generation rate at each electrode could be attributed not only to the entropic change [eq.4(10)] [47–49] but also to ion solvation/desolvation accompanied with ion-pairing [131,134–137], and to ion adsorption/desorption at the electrode surface [68–71]. Solvation or desolvation of Li^+ ions in carbonate takes place alternatively at the anode and cathode during charging and discharging. Thermochemistry calculations revealed that the enthalpy of solvation ΔH_{sol} of Li^+ ion in EC:DMC is negative so that the complexation of the Li^+ ion-carbonate is spontaneous and exothermic [134–136]. Conversely, desolvation is endothermic. Moreover, upon solvation, the solvated Li^+ ions may form ion-pairs with solvated PF_6^- [137]. The electric energy is released when two oppositely charged ions are brought together so that forming an ion pair is an exothermic process, i.e., $\Delta H_{el} < 0$ [131]. The enthalpy associated with ion-pairing ΔH_{ip} is the sum of the change in electric enthalpy ΔH_{el} due to ion association and the enthalpy of desolvation ΔH_{desol}, i.e., $\Delta H_{ip} = \Delta H_{el} + \Delta H_{desol} = \Delta H_{el} - \Delta H_{sol}$ [131]. More specifically, ΔH_{ip} for 1M of $LiPF_6$ in 1:1 v/v EC:DMC electrolyte was estimated using molecular dynamic simulations to be -0.8 kJ/mol at 20 °C [131]. Thus, forming an ion-pairs is an exothermic process while dissociation of ion-pairs is endothermic. During charging, ion-pairing takes place at the PNb_9O_{25} electrode while the reverse process occurs at the lithium metal counter electrode.

Finally, ion adsorption and desorption may also contribute to the reversible heat generation rate in battery electrodes. The heat generation rate associated with ion adsorption and desorption was found to be significant in electric double layer capacitor and was also proportional to the applied current I [68–71]. During charging, PF_6^- adsorbed to the PNb_9O_{25} electrode while, simultaneously, Li^+ desorbed from it. Previous numerical simulations have established that the reversible heat generation rate decreased with increasing ion diameter [138]. Thus, the endothermic contribution of Li^+ desorption is more significant than the exothermic contribution of PF_6^- adsorption. In brief, reversible heat generation rates due to ion adsorption/desorption have opposite sign compared with those associated with reversible entropic change. Overall, calorimetric measurements established that the reversible heat generation rate at each electrode was dominated by the entropic changes with some contributions from ion solvation/desolvation accompanied with ion-pairing as well as ion

adsorption/desorption.

4.2.3.3 Heat generation rate of a full cell

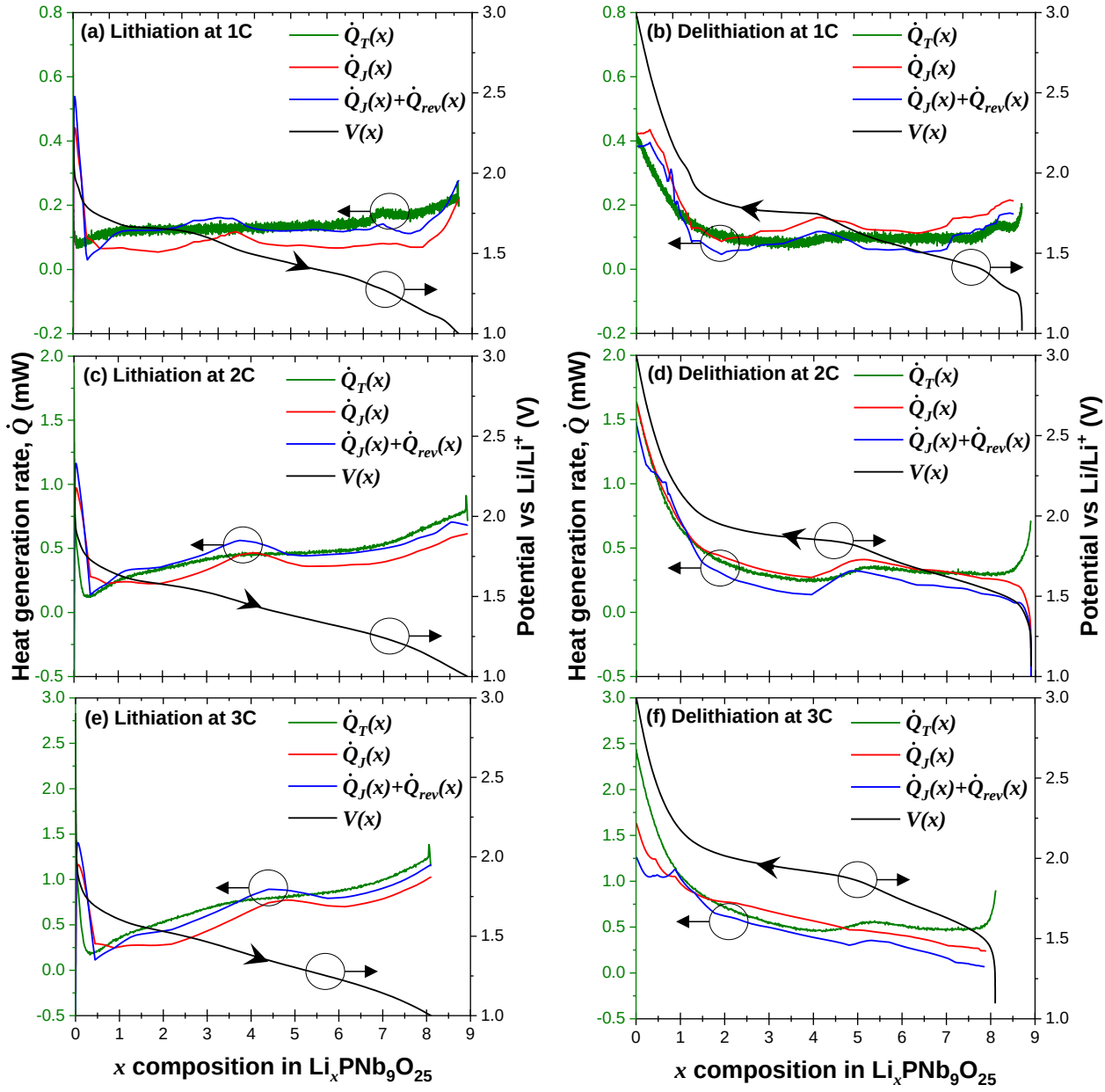

Figure 4.6: Measured total heat generation rate $\dot{Q}_T(x)$ and heat generation rates $\dot{Q}_J(x)$, $\dot{Q}_J(x)+\dot{Q}_{rev}(x)$ calculated according to eqs.4(9) and (10) along with operating voltage $V(x)$ of a cell upon (a) lithiation, (b) delithiation at C-rate of 1C, (c) lithiation, (d) delithiation at C-rate of 2C, and (e) lithiation, (f) delithiation at C-rate of 3C at 20 °C.

Figures 4.6(a)-4.6(f) plot the total instantaneous heat generation rate $\dot{Q}_T(x) = \dot{Q}_{PNO}(x) + \dot{Q}_{Li}(x)$ as a functions of x in $Li_xPNb_9O_{25}$ measured in the entire cell at 20 °C during lithiation and delithiation for C-rate of 1C, 2C, and 3C. It also shows the contributions from Joule heating $\dot{Q}_J(x)$ and entropic reversible heat generation $\dot{Q}_{rev}(x)$, respectively calculated using eqs.4(9) and (10) based on the measured open circuit voltage $U_{ocv}(x)$, operating voltage $V(x)$, and entropic potential $\partial U_{ocv}(x)/\partial T$ of the device. Here, for all C-rates considered, $\dot{Q}_J(x)$ decreased sharply for $x < 2$ during lithiation due to the transition of PNb_9O_{25} from insulator to semiconductor upon lithiation. Conversely, $\dot{Q}_J(x)$ increased sharply for $x < 2$ during delithiation. It is interesting to note that the trends of the calculated Joule heating $\dot{Q}_J(x)$ was similar to those observed in the reported resistivity of the PNb_9O_{25} electrode based on the electrochemical impedance spectroscopy measurements [129]. Moreover, predictions of the sum $\dot{Q}_J(x) + \dot{Q}_{rev}(x)$ agreed relatively well with the measured total heat generation rate $\dot{Q}_T(x)$ for both lithiation and delithiation. neglecting the heat generation rate due to side reactions $\dot{Q}_{sr}(x)$ leads to expressing the enthalpy of mixing $\dot{Q}_{mix}(x)$ as the difference between $\dot{Q}_T(x)$ and the sum $\dot{Q}_J(x) + \dot{Q}_{rev}(x)$, i.e., $\dot{Q}_{mix}(x) = \dot{Q}_T(x) - \dot{Q}_J(x) - \dot{Q}_{rev}(x)$[eq.4(8)] [47–49]. Then, Figure 4.6 indicates that $\dot{Q}_{mix}(x)$ increased with increasing C-rate. This can be attributed to larger Li^+ concentration gradients developed within the electrode due to diffusion limitation as the imposed current I increased [53].

4.2.3.4 Energy balance

Figure 4.7 presents the electrical energy losses ΔE_e measured from the hysteresis in the cell potential $V(x,T)$ [eq.4(14)] at C-rates of 1C, 2C, and 3C. It also plots the measured total thermal energy Q_T dissipated in the entire cell along with the contributions from Joule heating Q_J [eq.4(13)] during lithiation and delithiation. Figure 4.7 indicates that ΔE_e increased with increasing C-rates due to the associated increase in the overpotential $[V(x,T) - U^{avg}(x,T)]$ [122, 123]. The values $U^{avg}(x,T)$ and $\partial U^{avg}(x,T)/\partial T$ measured by GITT at different C-rates used in the calculation of $\dot{Q}_J(x,T)$ and $\dot{Q}_{rev}(x,T)$. Furthermore, the electrical energy losses ΔE_e fell within 4 % of the measured total thermal energy Q_T dissipated over cycle. In other words, the electrical energy losses were dissipated in the

form of heat and the electrochemical measurements were in excellent agreement with the calorimetric measurements so that $\Delta E_e = Q_T$. Additionally, the irreversible Joule heating during delithiation was smaller than that during lithiation due to relatively fast kinetics of delithiation compared to that of lithiation as observed in the apparent diffusion coefficient of Li^+ ion in the PNb_9O_{25} electrode (see Appendix C).

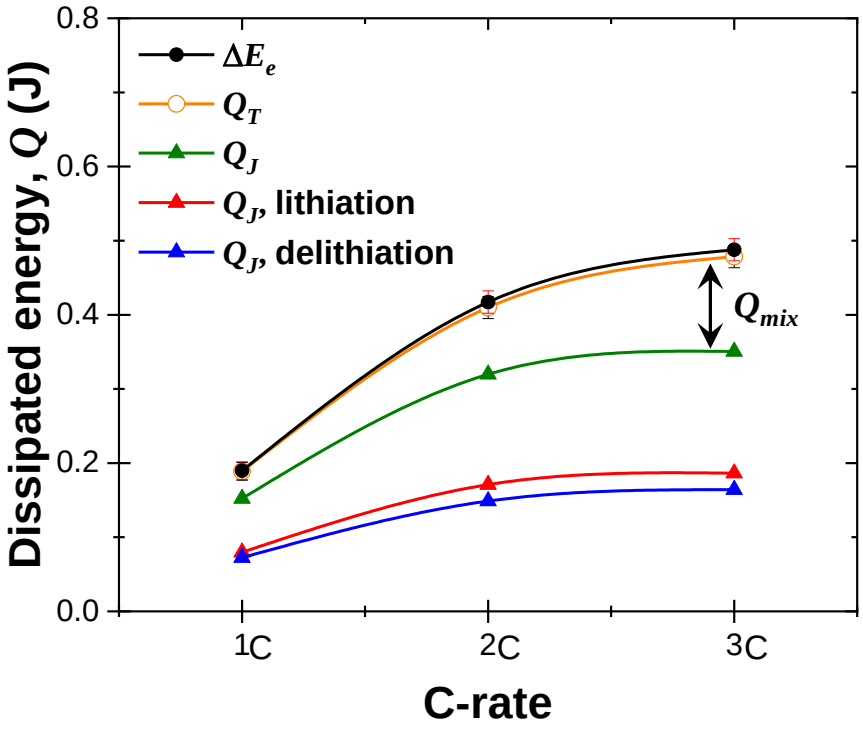

Figure 4.7: Net electrical energy losses ΔE_e and total thermal energy dissipated Q_T averaged over the first five charging-discharging cycles as well as contributions from Joule heating Q_J during lithiation and delithiation. The enthalpy of mixing corresponds to $Q_{mix} = Q_T - Q_J = \Delta E_e - Q_J$.

Moreover, since $Q_{rev} \simeq 0$, the difference between Q_T and Q_J corresponded to the heat dissipated as enthalpy of mixing, i.e., Q_{mix}=Q_T - Q_J. At C-rate of 1C, the irreversible Joule heating was responsible for 89 % of the total energy dissipated while the enthalpy of mixing contributed only 11 %. However, the contribution of the enthalpy of mixing to the total energy dissipated increased with increasing C-rate to reach 33 % at C-rate of 3C. The present results suggest that the contribution of the enthalpy of mixing in the heat generation

of PNb_9O_{25} was relatively small compared with other battery electrode materials even at high C-rate [51]. These new results confirm that PNb_9O_{25} is a very promising anode material for fast charging LIB applications.

4.3 Conclusion

This study investigated the charging mechanisms responsible for the fast charging of PNb_9O_{25} electrode in lithium ion batteries. The cyclic voltammetry and galvanostatic cycling confirmed the impressive rate performance of PNb_9O_{25} with cathodic and anodic peaks above 1 V (vs. Li/Li^+) thus avoiding SEI formation. Entropy measurements not only confirmed the phase transitions identified from XRD measurements but also identified semiconductor-to-metal transition and intralayer lithium ordering which could not be identified from other characterization methods. Moreover, this study reports, for the first time, the individual heat generation rates at the PNb_9O_{25} working electrode and at the Li metal counter electrode in a battery cell during cycling. The heat generation rate due to Joule heating dominated the energy losses. The time-averaged irreversible heat generation rate indicated that the electrical resistance of the lithium metal electrode was constant and independent of the state of charge while the electrical resistance of the PNb_9O_{25} changed significantly with the state of charge. Furthermore, the time-averaged reversible heat generation rates over the charging or discharging steps were equal and linearly proportional to the imposed current at both electrodes. In addition, entropic changes dominated the reversible heat generation rate at each electrode. The enthalpy of mixing increased with the increasing C-rate but remained relatively small even at high C-rates compared to other LIB electrode materials. These results establish that PNb_9O_{25} constitutes an excellent anode material undergoing insulator-to-metal transition and intralayer ion ordering during lithiation, two attractive features of fast charging battery applications.

CHAPTER 5

Probing the effect of particle size in the heat generation of Wadsley-Roth Shear Phase $(W_{0.2}V_{0.8})_3O_7$ with Operando Calorimetry

This chapter aims to use potentiometric entropy and calorimetric measurement techniques to understand structural changes and different physicochemical phenomena occurring in $(W_{0.2}V_{0.8})_3O_7$ working electrodes made of particles with different sizes during charging/discharging. To do so, potentiometric entropy measurements at low C-rates were combined with other electrochemical characterization techniques as well as with *in situ* X-ray diffraction (XRD) measurements to investigate the phase transition occurring in the $(W_{0.2}V_{0.8})_3O_7$ electrode. Furthermore, the instantaneous heat generation rates were measured by *operando* isothermal calorimeter at high C-rate at the electrode made of $(W_{0.2}V_{0.8})_3O_7$ *microparticles* or *nanoparticles* and the lithium metal counter electrode in 1 M of $LiPF_6$ in EC:DMC 1:1 v/v during cycling. These measurements were used to gain insight into the dynamic interfacial and transport phenomena responsible for any energy dissipation upon cycling.

5.1 Materials and methods

5.1.1 Synthesis of $(W_{0.2}V_{0.8})_3O_7$ powders

The solid-state preparation of $(W_{0.2}V_{0.8})_3O_7$ microparticles followed the synthesis described in Ref. [139]. In brief, the material was prepared by heating a stoichiometric mixture of precursor oxide powders of WO_3, V_2O_5, and V_2O_3 to 700 °C for 24 hours in a sealed vitreous silica tube back-filled with a partial pressure of argon. After annealing, the tube was water

quenched to room temperature to obtain $(W_{0.2}V_{0.8})_3O_7$ microparticles.

The $(W_{0.2}V_{0.8})_3O_7$ nanoparticles were prepared by combining sol-gel synthesis with a freeze-drying method. First, 200 mg of NH_4VO_3 and 105 mg of $(NH_4)_{10}(H_2W_{12}O_{42})$ were added to 4 mL of distilled water and heated while stirring until the solids were fully dissolved. The resulting yellow solution was added dropwise to liquid nitrogen. After the removal of the remaining liquid nitrogen, the frozen solution was subjected to vacuum (<100 mTorr) on a Schlenk line for 10 – 20 hours to remove water. The dried powder was calcined in a tube furnace with flowing Ar with a heat ramp of 30 °C/min followed by a one hour hold at 700 °C. The furnace was then cooled down to room temperature. The synthesized nanoparticles were stored under an inert atmosphere to prevent unwanted surface oxidation.

Finally, the $(W_{0.2}V_{0.8})_3O_7$ particles, synthesized by solid-state or sol-gel synthesis with freeze-drying methods, were characterized with FEI Apreo C scanning electron microscope (SEM) with a voltage of 15 kV and a current of 0.8 nA.

5.1.2 Electrode and device fabrication

The same procedure was followed to fabricate working electrodes made of the $(W_{0.2}V_{0.8})_3O_7$ powders synthesized by either solid-state or freeze-drying methods, as described previously. First, the synthesized $(W_{0.2}V_{0.8})_3O_7$ powder was ball-milled using a vortex mixer (Genie, Vortex-Genine) for 20 minutes in a 2 cm^3 canister with SuperP (TIMCAL) and carbon nanotubes (CNT). Then, the mixture was combined with polyvinylidene fluoride (PVDF) dissolved in N-methyl-2-pyrrolidone (NMP) to form a slurry with a mass ratio 8:0.5:0.5:1 of $(W_{0.2}V_{0.8})_3O_7$:Super P:CNT:PVDF. The slurry was thoroughly mixed using the vortex mixer for 30 minutes before casting. A doctor blade set to 250 μm was used to cast the slurry onto a copper foil current collector. The electrode was dried in a vacuum oven at 110 °C overnight. Then, electrodes were punched into a 10 mm diameter disc for coin cell fabrication. For calorimetry, the electrode were cut into 1×1 cm^2 square shape with 4 cm × 0.25 cm strip current collector, as described previously [109]. The mass loading of the active material in electrodes made of $(W_{0.2}V_{0.8})_3O_7$ microparticles and nanoparticles was in

the range of 6-7 mg/cm^2

All coin cells were fabricated in an Ar-filled glove box using 2032 SS casings (MTI parts). They consisted of $(W_{0.2}V_{0.8})_3O_7$ electrode with 1 M of $LiPF_6$ in EC:DMC 1:1 v/v (Sigma Aldrich) as the electrolyte, polished metallic lithium (Sigma Aldrich) ribbon as the counter electrode, and a 50 μm thick Celgard C380 polypropylene/polyethylene separator. Cyclic voltammetry, galvanostatic cycling, and potentiometric entropy measurements were performed on the coin cells using a high accuracy potentiostat (Biologic, VSP-300) in the voltage range of 1.0−3.0 V.

5.1.3 Potentiometric entropy measurements

The open circuit voltage $U_{ocv}(x,T)$ and the entropic potential $\partial U_{ocv}(x,T)/\partial T$ of the coin cells were measured as functions of lithium composition x using the potentiometric entropy measurement technique and the apparatus previously described in Ref. [50]. In brief, the measurements consisting of imposing a series of constant current pulses at a C-rate of C/10 at 20 °C. Each current pulse lasted for 30 minutes followed by a relaxation period of 90 minutes. During the relaxation period, the temperature of the coin cell was varied from 15 °C to 25 °C in 5 °C increments using a thermoelectric cold plate (TE technology, CP-121) in contact with the coin cell. The corresponding coin cell voltage evolution was recorded with a high accuracy potentiostat (Biologic, VSP-300). The lithium composition x in $Li_x(W_{0.2}V_{0.8})_3O_7$ can be estimated based on the charging/discharging time t (in sec), i.e.,

$$x = \frac{It}{3600MC_{theo}} \tag{5.1}$$

where M is the mass loading of the active material in the electrode and C_{theo} is the theoretical capacity of $(W_{0.2}V_{0.8})_3O_7$ calculated as C_{theo}=230 mAh/g based on one electron per transition metal.

Moreover, $U^{avg}(x,T)$ and $\partial U^{avg}(x,T)/\partial T$ were also measured using the same procedure and the same relaxation time as that used for measuring $U_{ocv}(x,T)$, but with current pulses corresponding to different C-rates. In addition, the duration of the current pulses changed with C-rates such that, at C-rate of 1C, each current pulse lasted 3 minutes, while it lasted

2 minutes at 2C, and 1 minute at 3C. Regardless of the C-rate, we verified that the coin cell had reached thermodynamic equilibrium before imposing the next temperature step during the relaxation period. To do so, we verified that (i) the temperature difference between the cold plate and the top of the coin cell surface was less than 0.1 °C and (ii) the time rate of change of the open circuit voltage $\partial U_{ocv}(x,T)/\partial t$ or $\partial U^{avg}(x,T)/\partial t$ was less than 5 mV/h.

5.1.4 *Operando* isothermal calorimetry

The instantaneous heat generation rates at the $(W_{0.2}V_{0.8})_3O_7$ working electrode and at the metallic lithium counter electrode were measured separately under galvanostatic cycling using a custom-made isothermal calorimeter described previously [109]. The calorimetric cell consisting of (i) a 1 x 1 cm^2 $(W_{0.2}V_{0.8})_3O_7$-based electrode, (ii) two 50 μm thick Celgard C380 polypropylene/polyethylene separator sheets, (iii) 1 M $LiPF_6$ in EC:DMC 1:1 v/v (Sigma Aldrich) as the electrolyte, and (iv) polished metallic lithium (Sigma Aldrich) as the counter electrode. Here, the mass loading of the active material in the electrode made of $(W_{0.2}V_{0.8})_3O_7$ microparticles and nanoparticles was 6.5 mg/cm^2 and 6.9 mg/cm^2, respectively. As discussed in Ref. [109], the heat generation rate $\dot{Q}_i(t)$ (in mW) at each electrode was equal to the heat transfer rate $q_i''(t)$ measured at the 1×1 cm^2 thermoelectric heat flux sensor (greenTEG, gSKIN-XP) placed in thermal contact with the back of each electrode, i.e., [109],

$$\dot{Q}_i(t) = q_i''(t)A_i = \frac{\Delta V_i(t)}{S_i}A_i \quad \text{with } i = WVO \text{ or } Li. \tag{5.2}$$

Here, A_i is the footprint area of the electrode (in cm^2), ΔV_i is the voltage difference measured at each heat flux sensor, and S_i is the sensitivity of the heat flux sensor (in μV/(W/cm^2)). The total instantaneous heat generation rate in the entire calorimetric cell can be expressed as the sum of the heat generation rate measured at each electrode, i.e., $\dot{Q}_T(t) = \dot{Q}_{\mathrm{Li}}(t) + \dot{Q}_{\mathrm{WVO}}(t)$.

The instantaneous heat generation rate $\dot{Q}_i(t)$ at electrode "i" can be divided into an irreversible $\dot{Q}_{irr,i}(t)$ and a reversible $\dot{Q}_{rev,i}(t)$ contribution, i.e.,

$$\dot{Q}_i(t) = \dot{Q}_{irr,i}(t) + \dot{Q}_{rev,i}(t) \quad \text{with } i = \ WVO \text{ or } Li. \tag{5.3}$$

Here, $\dot{Q}_{irr,i}(t)$ may vary with time as the electrical and/or ionic conductivities of the electrode may change upon charging/discharging, for example [50]. However, $\dot{Q}_{rev,i}(t)$ averaged over an entire cycle should yield zero due to its reversible nature. Therefore, the time-averaged irreversible heat generation rate $\bar{\dot{Q}}_{irr,i}(t)$ at electrode "i" can be calculated according to,

$$\bar{\dot{Q}}_{irr,i} = \frac{1}{t_{cd}} \oint_{cycle} \dot{Q}_i(t)\mathrm{d}t \quad \text{with } i = \ WVO \text{ or } Li \tag{5.4}$$

where t_{cd} is the cycle period.

5.2 Results and discussion

5.2.1 Material and Electrochemical characterization

Figure 5.1 shows the SEM images of the two types of $(W_{0.2}V_{0.8})_3O_7$ particles synthesized in this study. Both types of particles featured a rod-like morphology consistent with earlier observations [140]. Figure 5.1(a) indicates that the average particle size of $(W_{0.2}V_{0.8})_3O_7$ particles synthesized by solid-state method was around 1-2 μm. On the other hand, Figure 5.1(b) shows that the average length of the shorter side of the rod synthesized by freeze-drying method was about 100 nm, and that of the longer side was about 1-2 μm.

Consistent with our previous work, Figures 5.2(a) and 5.2(b) show cyclic voltammograms at scan rates ν between 0.1 and 0.5 mV/s for a potential window between 1.0 and 3.0 V vs. Li/Li^+ for electrodes made of $(W_{0.2}V_{0.8})_3O_7$ microparticles and nanoparticles, respectively. Both $(W_{0.2}V_{0.8})_3O_7$-based electrodes showed 4 redox peaks at similar potentials at the relatively low scan rate $\nu = 0.1$ mV/s. As the scan rate increased, the redox peaks for the electrode made of $(W_{0.2}V_{0.8})_3O_7$ microparticles shifted significantly compared to that of nanoparticles and were not as sharp. This can be attributed to the fact that the redox reactions were more kinetically-limited in the microparticles than in the nanoparticles.

The b-values associated with each cathodic and anodic peaks were obtained by fitting the peak current I_{peak} vs. scan rate ν with the power law $I_{peak} = a\nu^b$ (see Appendix) [141]. Table 5.1 reports the potential and the associated b-value corresponding to each redox peak for electrodes made of $(W_{0.2}V_{0.8})_3O_7$ microparticles and nanoparticles. For both types of

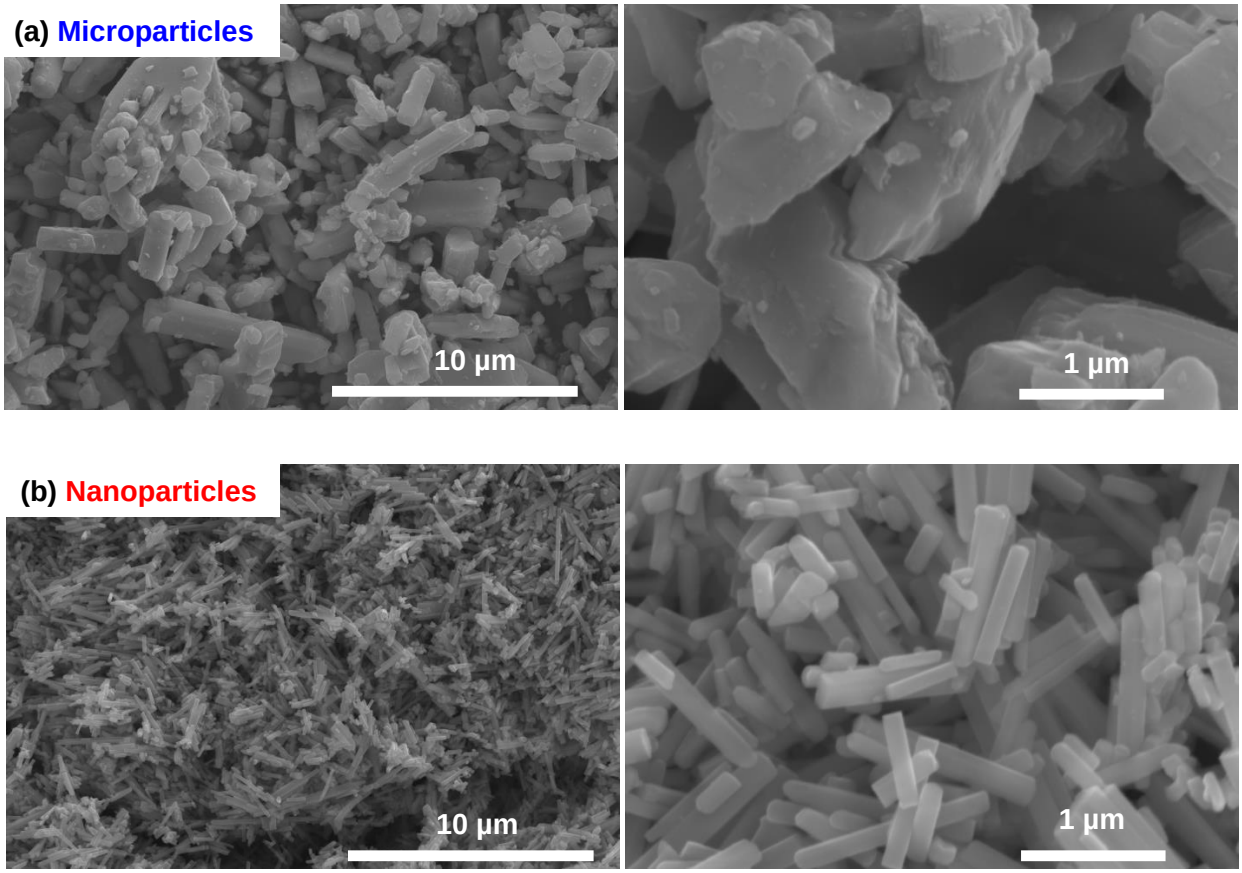

Figure 5.1: Scanning electron microscope images of (a) $(W_{0.2}V_{0.8})_3O_7$ microparticles synthesized by solid-state method and (b) nanoparticles made by sol-gel synthesis combined with freeze-drying method.

electrodes, all cathodic and anodic peaks featured a b-value close to 0.5, suggesting that charging and discharging were limited by diffusion. As such, $(W_{0.2}V_{0.8})_3O_7$ behaved as a traditional battery material [128]. Interestingly, the calculated b-values for the electrode made of $(W_{0.2}V_{0.8})_3O_7$ nanoparticles were systemically larger, albeit only slightly, than those of the electrode made of microparticles suggesting that redox reactions were slightly less diffusion limited in nanoparticles than microparticles [128].

Figure 5.2(c) shows the galvanostatic charge-discharge potential profile at a C-rate of C/5 of coin cells containing electrodes composed of $(W_{0.2}V_{0.8})_3O_7$ microparticles or nanoparticles between 1.0 and 3.0 V vs. Li/Li^+. The trends in the voltage curves of both coin cells were

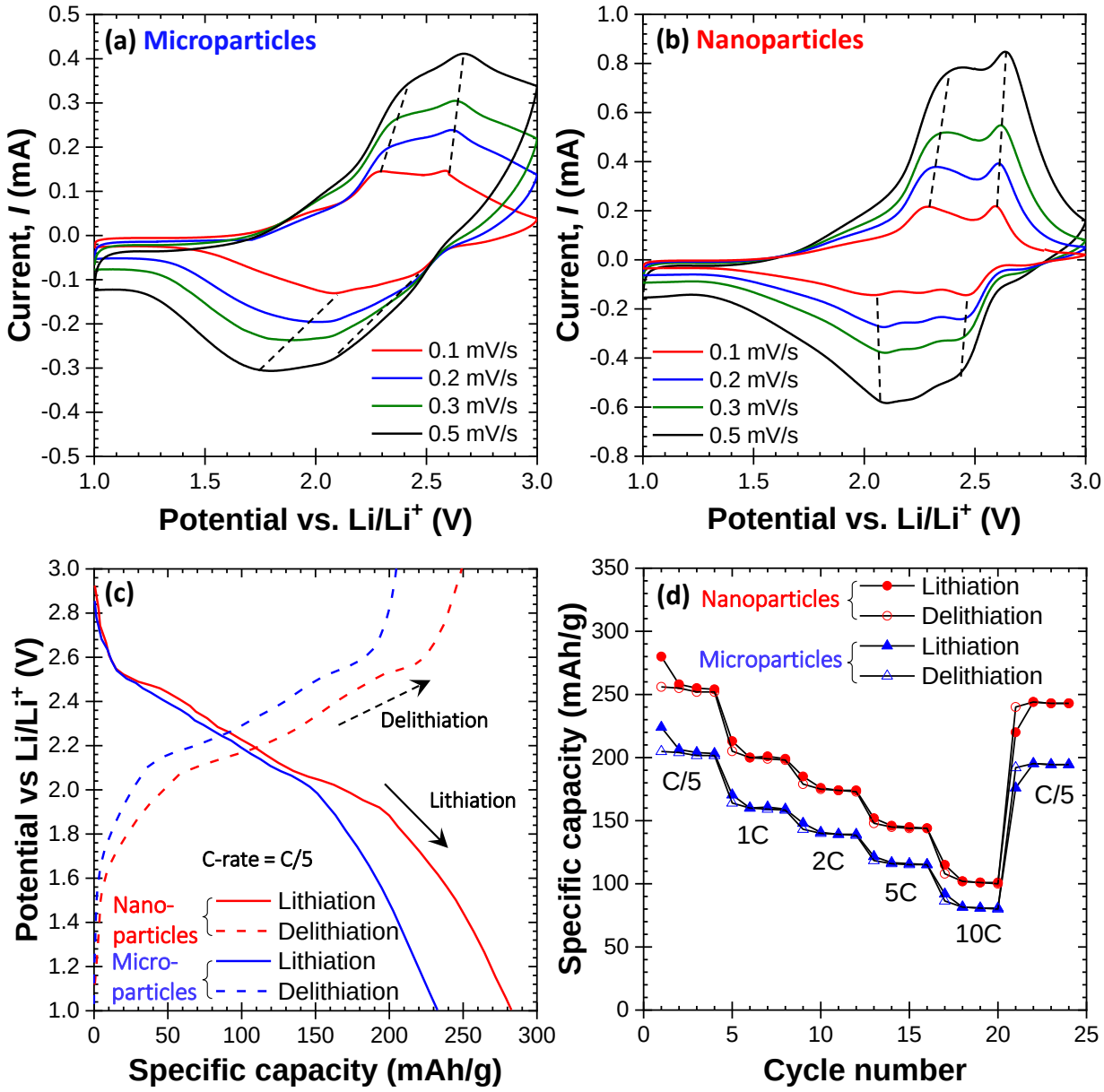

Figure 5.2: Cyclic voltammogram of the cell containing electrode made of $(W_{0.2}V_{0.8})_3O_7$ in the form of (a) microparticles synthesized by solid-state method and of (b) nanoparticles from freeze-drying method cycled with potential window ranging from 1.0 to 3.0 V vs. Li/Li^+ at different scan rates ν, (c) galvanostatic charge-discharge potential profile at C-rate of C/5, and (d) specific capacity retention of the cell cycled between 1.0 and 3.0 V vs. Li/Li^+ at C-rates between C/5 and 10C.

Table 5.1: Potential and b-values of redox peaks in the cyclic voltammetry curve for electrodes made of $(W_{0.2}V_{0.8})_3O_7$ microparticles and nanoparticles.

	Microparticles		Nanoparticles	
	Potential (V)	b-value	Potential (V)	b-value
Oxidation peaks	2.26	0.55	2.19	0.62
	2.58	0.56	2.52	0.64
Reduction peaks	2.08	0.57	2.01	0.63
	2.46	0.52	2.47	0.58

similar during lithiation and delithiation. However, as observed in our previous work on this system [139] the specific capacity of the cell with the electrode made of $(W_{0.2}V_{0.8})_3O_7$ nanoparticles was 280 mAh/g compared with 230 mAh/g for that made of microparticles. Note also that, in both cases, the capacity was larger than the theoretical capacity calculated based on one electron per transition metal. These results demonstrate the ability of $(W_{0.2}V_{0.8})_3O_7$ to engage in multielectron redox reactions, as confirmed previously by X-ray photoelectron spectrosccopy (XPS) measurements [139].

Figure 5.2(d) shows the specific capacity as a function of cycle number for coin cells with electrodes made of $(W_{0.2}V_{0.8})_3O_7$ microparticles and nanoparticles at different C-rates between C/5 and 10C for the same potential window. Here also, the cell made with an electrode consisting of $(W_{0.2}V_{0.8})_3O_7$ nanoparticles featured a larger capacity than that consisting of $(W_{0.2}V_{0.8})_3O_7$ microparticles at any C-rate. Moreover, both electrodes showed impressive fast-charging ability. In fact, at C-rate of 10C, both types of electrodes maintained about 50% of their specific capacity at C/5. In addition, after 20 cycles, they maintained their specific capacity and showed reversibility. Overall, the electrochemical testing was consistent with that reported in our previous study [139]. It is presented here for the sake of completeness and confirm that the samples used in this work show the fast-charging abilities and to demonstrate the superior performance of electrodes made of nanoparticles compared to those made of microparticles.

5.2.2 $U_{ocv}(x,T)$ and $\partial U_{ocv}(x,T)/\partial T$ measurements

Figure 5.3 plots the open circuit voltage $U_{ocv}(x,T)$ and entropic potential $\partial U_{ocv}(x,T)/\partial T$ measured at 20 °C as functions of x composition in $Li_x(W_{0.2}V_{0.8})_3O_7$ at a C-rate of C/10 during lithiation [Figures 5.3(a,b)] and delithiation [Figures 5.3(c,d)] for coin cells with electrodes consisting of $(W_{0.2}V_{0.8})_3O_7$ microparticles [Figures 5.3(a,c)] and nanoparticles [Figures 5.3(b,d)]. The trends of both $U_{ocv}(x,T)$ and $\partial U_{ocv}(x,T)/\partial T$ were very similar for both types of electrodes and were almost identical during lithiation and delithiation. These results confirmed that the physicochemical phenomena occurring at the $(W_{0.2}V_{0.8})_3O_7$ electrodes were reversible. However, the electrode made of $(W_{0.2}V_{0.8})_3O_7$ nanoparticles was able to accommodate more lithium and featured a larger range of x composition compared to that with microparticles, as also observed in Figure 5.2(c).

Three different regions corresponding to different physicochemical phenomena could be identified in Figure 5.3. In Region I, $U_{ocv}(x,T)$ decreased monotonically indicating lithium insertion in a homogeneous solid solution, as confirmed by *in situ* XRD measurements [139]. This regime was observed for $x < 1.5$ in coin cell with the electrode made of $(W_{0.2}V_{0.8})_3O_7$ microparticles and for $x < 1.7$ in that with the electrode made of nanoparticles. Here, in Region I, $\partial U_{ocv}(x,T)/\partial T$ increased first and then decreased with increasing x resulting in a local maximum. This behavior could be attributed to the semiconductor to metal transition occurring in $(W_{0.2}V_{0.8})_3O_7$ resulting in large change in the partial molar electronic entropy. Assuming $(W_{0.2}V_{0.8})_3O_7$ as an ideal intercalation compound, the total entropy $s_{WVO}(x,T)$ of the $(W_{0.2}V_{0.8})_3O_7$ can be expressed as the sum of individual contributions according to [142]

$$s_{WVO}(x,T) = s^{conf}_{WVO}(x,T) + s^{vib}_{WVO}(x,T) + s^{elec}(x,T) \tag{5.5}$$

where $s^{conf}_{WVO}(x,T)$, $s^{vib}_{WVO}(x,T)$ and $s^{elec}_{WVO}(x,T)$ are the configurational, vibrational, and electronic entropy of the $(W_{0.2}V_{0.8})_3O_7$ compound, respectively. Therefore, eq.5(2) can also be expressed as

$$\frac{\partial U_{ocv}(x,T)}{\partial T} = \frac{1}{e}\left[\frac{\partial s^{conf}_{WVO}(x,T)}{\partial x} + \frac{\partial s^{vib}_{WVO}(x,T)}{\partial x} + \frac{\partial s^{elec}_{WVO}(x,T)}{\partial x} - s^{\circ}_{Li}(T)\right]. \tag{5.6}$$

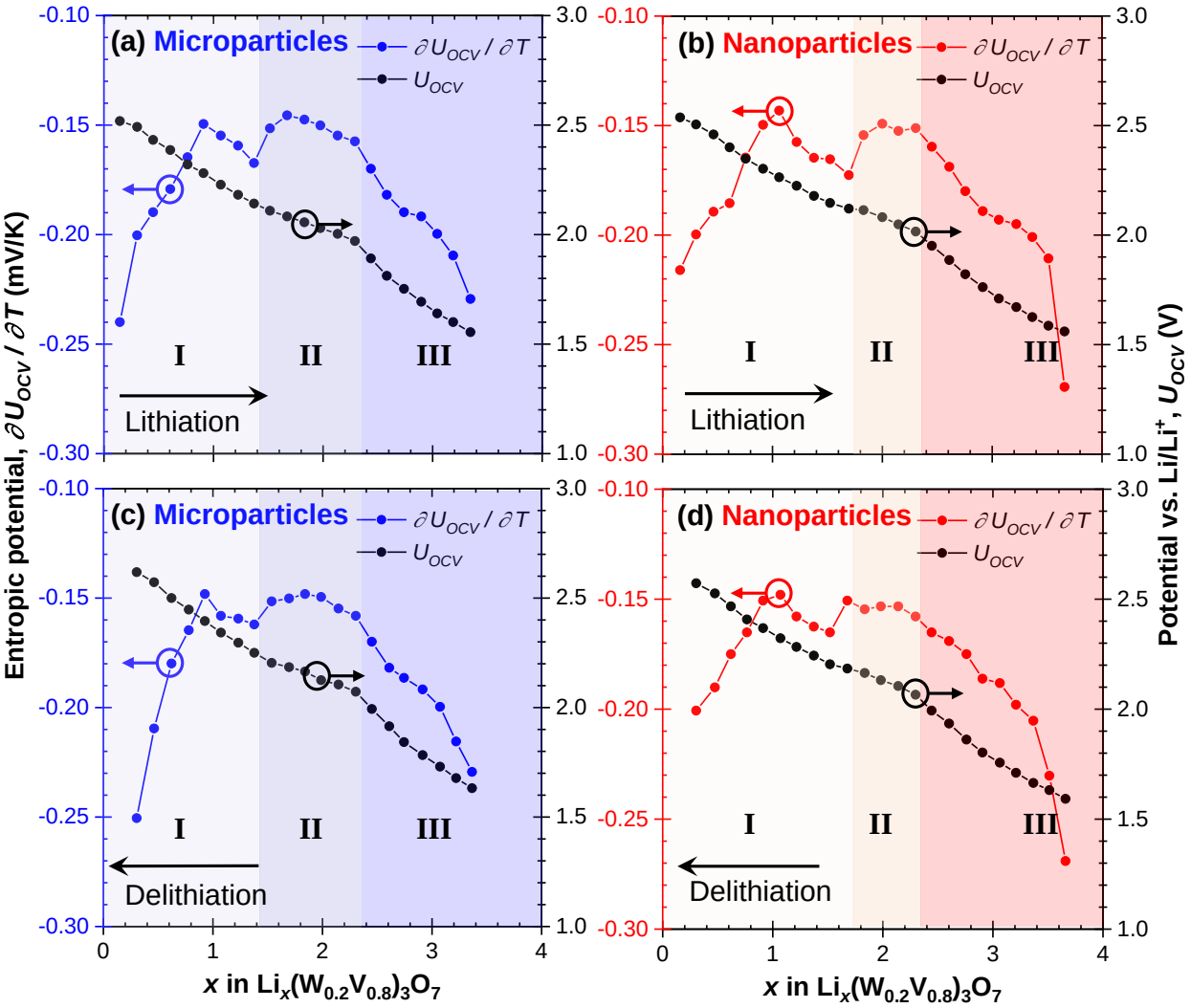

Figure 5.3: Open circuit voltage $U_{ocv}(x,T)$ and entropic potential $\partial U_{ocv}(x,T)/\partial T$ of the cell containing electrodes made of $(W_{0.2}V_{0.8})_3O_7$ (a,c) microparticles and (b,d) nanoparticles during (a,b) lithiation and (c,d) delithiation as functions of lithium composition x in $Li_x(W_{0.2}V_{0.8})_3O_7$ at temperature T = 20 °C.

Previous study has demonstrated that $\partial s^{conf}_{WVO}(x,T)/\partial x$ decreased monotonically with increasing x [142]. In addition, $\partial s^{vib}_{WVO}(x,T)/\partial x$ was independent of x based on vibrational spectrum of the Li ions approximated by the Einstein model [142]. Thus, the trend of $\partial U_{ocv}(x,T)/\partial T$ leading to a local maximum in Region I was attributed to change in partial molar electronic entropy $\partial s^{elec}_{WVO}(x,T)/\partial x$. For itinerant electrons, the electronic entropy can

be expressed as [83]

$$s^{elec}(x,T) = -k_B \int \left[\mathcal{F}(\epsilon)\ln\left[\mathcal{F}(\epsilon)\right] + \left[1-\mathcal{F}(\epsilon)\right]\ln\left[1-\mathcal{F}(\epsilon)\right]\right]\mathcal{D}^{elec}(\epsilon)d\epsilon \tag{5.7}$$

where $\mathcal{F}(\epsilon)$ is the Fermi-Dirac distribution and $\mathcal{D}^{elec}(\epsilon)$ is the electronic density of states per unit cell. The electronic entropy depends on the shape of the electronic density of states $\mathcal{D}^{elec}(\epsilon)$ and the position of the Fermi level ϵ_F. The majority of Wadsley-Roth materials begin as fully oxidized d^0 oxides. Lithiation of these materials effectively serves to dope the material by reducing the transition metals and putting electrons into the d bands, lifting the Fermi level. With sufficient lithiation, this is seen to manifest as an insulator to metal transition in PNb_9O_{25}, supported with both experimental and computational results [55, 129]. Here, $(W_{0.2}V_{0.8})_3O_7$ is unique in that it does not begin fully oxidized and instead contains a small amount of partially reduced V^{4+}. However, the material is not metallic, and can be characterized as a type of semiconductor. The electronic structure of unlithiated $(W_{0.2}V_{0.8})_3O_7$ is analogous to that of low lithiation levels in PNb_9O_{25}, with the charge density localized on the central corner-connected octahedron [139]. In both cases, more doping, or lithiation, is required to instigate a transition to a metallic state, with electron delocalization along the edge-sharing features in both structures. Because of this localization, $s^{elec}_{WVO}(x,T)$ was small initially at low x composition when the material is semiconductor due to the small density of state at the Fermi level [89]. However, it increased sharply upon lithiation as the material became a metal and exhibited large density of state at the Fermi level. Therefore, the peak in $\partial U_{ocv}(x,T)/\partial T$ observed in Region I could be attributed to the change in partial molar electronic entropy $\partial s^{elec}_{WVO}(x,T)/\partial x$ due to the semiconductor to metal transition known to occur in this regime(see Appendix).

We next consider Region II. Here, both $U_{ocv}(x,T)$ and $\partial U_{ocv}(x,T)/\partial T$ were approximately constant confirming a two-phase coexistence region observed previously in *in situ* XRD measurements [139]. The range of x composition in this region ranges for $1.5 \leq x \leq 2.3$ for the electrode composed of microparticles and $1.7 \leq x \leq 2.3$ for that made of nanoparticles. The shorter two-phase coexistence region for the electrode made of nanoparticles can be attributed to the fact that nucleation of a first order phase transition is often inhibited

in smaller particles, and many of these systems are observed to have suppressed phase transition [143–145]. Moreover, upon two-phase coexistence, lattice mismatch occurs within the particle due to the different lattice parameters associated with two different phases. For a small particle, the lattice mismatch accompanied with two-phase coexistence cannot be compensated internally, thus inhibiting the two phase coexistence [146]. For example, $LiFePO_4$ experiences large volume expansion during two-phase coexistence leading to notable lattice mismatch within the particle. Therefore, $LiFePO_4$ particles with mean size less than 140 nm significantly shorten the two-phase coexistence region by avoiding substantial lattice mismatch accompanied with two-phase coexistence within the particle [147].

Finally, in Region III, both $U_{ocv}(x,T)$ and $\partial U_{ocv}(x,T)/\partial T$ decreased monotonically indicating lithium insertion in a homogeneous solid solution. This was consistent with observations from *in situ* XRD measurements [139]. Region III prevails for $x \geq 2.3$ for both types of electrodes consisting of $(W_{0.2}V_{0.8})_3O_7$ microparticles or nanoparticles.

5.2.3 *Operando* isothermal calorimetry

5.2.3.1 Instantaneous heat generation rates

Figures 5.4(a)-4(c) show the instantaneous heat generation rates $\dot{Q}_{WVO}(t)$ measured at the electrode made of $(W_{0.2}V_{0.8})_3O_7$ microparticles and $\dot{Q}_{Li}(t)$ measured at the lithium metal counter electrode and averaged over 5 consecutive cycles as functions of lithium composition x in $Li_x(W_{0.2}V_{0.8})_3O_7$ at 20 °C and at C-rate of (a) 1C, (b) 2C, and (c) 3C, respectively. Similarly, Figures 5.4(d)-4(f) plot $\dot{Q}_{WVO}(t)$ measured at the electrode consisting of $(W_{0.2}V_{0.8})_3O_7$ nanoparticles and $\dot{Q}_{Li}(t)$ at the lithium metal counter electrode averaged over 5 consecutive cycles as functions of x composition at C-rate of (d) 1C, (e) 2C, and (f) 3C, respectively under the same conditions. The measurements at each electrode were repeatable over many cycles (see Appendix). In addition, the trend and magnitude of $\dot{Q}_{WVO}(t)$ for both electrodes made of $(W_{0.2}V_{0.8})_3O_7$ microparticles and nanoparticles were very similar. In both cases, $\dot{Q}_{WVO}(t)$ was small at the beginning of discharging at low x composition when $(W_{0.2}V_{0.8})_3O_7$ particles were electrically conductive [139]. However, $\dot{Q}_{WVO}(t)$ increased

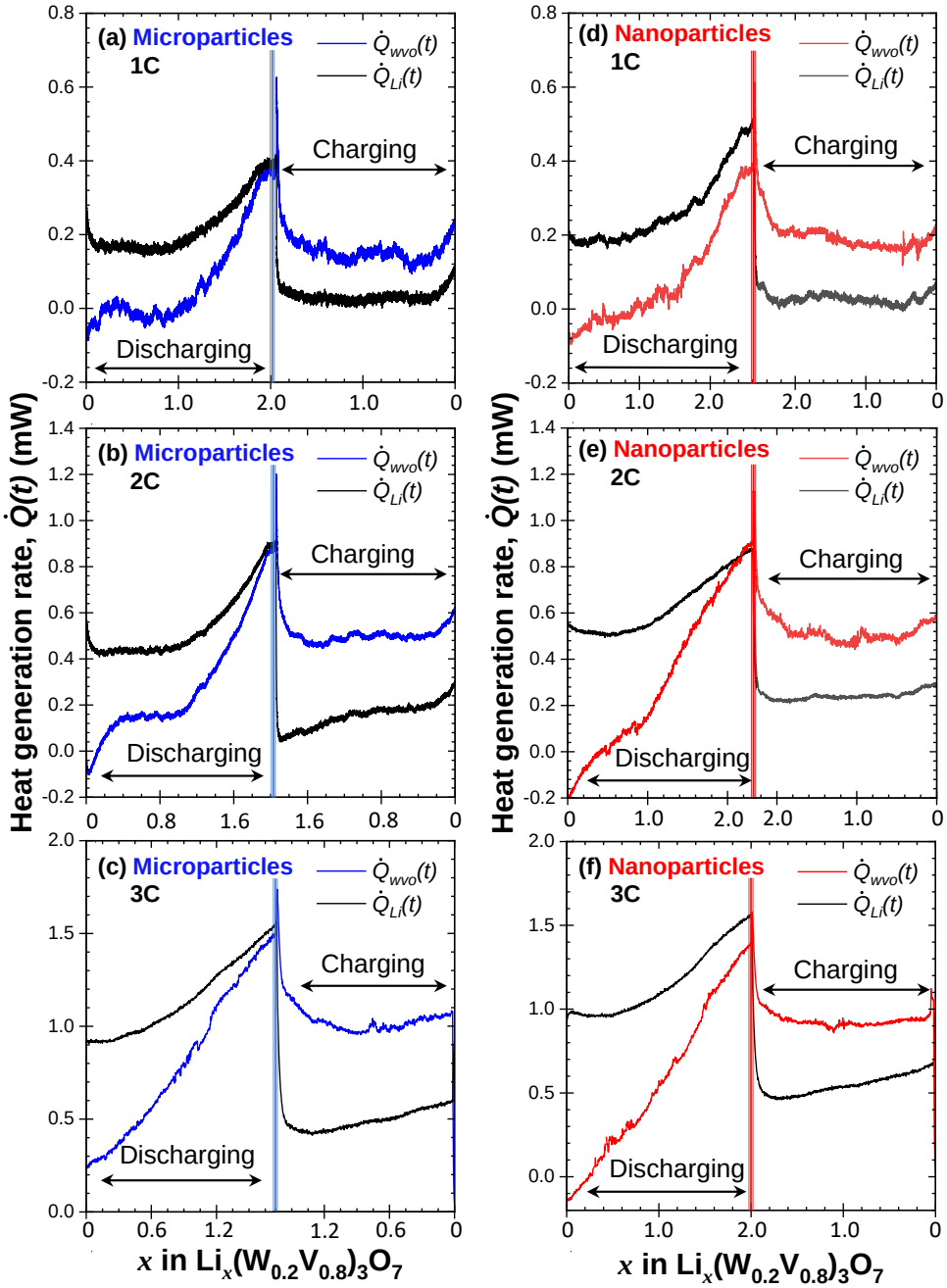

Figure 5.4: Measured instantaneous heat generation rates $\dot{Q}_{WVO}(t)$ at the $(W_{0.2}V_{0.8})_3O_7$-based electrodes and $\dot{Q}_{Li}(t)$ at the lithium metal electrode averaged over 5 consecutive cycles as functions of lithium composition x in $Li_x(W_{0.2}V_{0.8})_3O_7$ with potential window ranging from 1.0 V to 3.0 V vs. Li/Li^+ at C-rates of (a,d) 1C, (b,e) 2C, and (c,f) 3C for $(W_{0.2}V_{0.8})_3O_7$ (a,b,c) microparticles and (d,e,f) nanoparticles.

rapidly due to the increase in charge transfer resistance with increasing x composition in $Li_x(W_{0.2}V_{0.8})_3O_7$ upon discharging (lithiation) [139]. In addition, $\dot{Q}_{WVO}(t)$ for electrode composed of $(W_{0.2}V_{0.8})_3O_7$ nanoparticles and microparticles featured a small plateau-like region upon discharging at C-rate of 1C and 2C. Interestingly, the x composition of the plateau region in the $\dot{Q}_{WVO}(t)$ was ranged between 0.5 and 1.2 corresponding to the end of Region I where $\partial U_{ocv}(x,T)/\partial T$ decreased with increasing x identified in Figure 5.3. As previously discussed, $\partial U_{ocv}(x,T)/\partial T$ is directly related to the reversible heat generation rate [eq.5(5)]. In fact, decreasing $\partial U_{ocv}(x,T)/\partial T$ observed in this x composition could diminish the reversible heat generation rate, thus resulting in a plateau in $\dot{Q}_{WVO}(t)$. However, at C-rates of 3C, this feature was not apparent possibly due to the fact that the irreversible heat generation was much larger than the reversible heat generation and dominated the total heat generation rate.

5.2.3.2 Time-averaged heat generation rates

Figure 5.5 shows the time-averaged irreversible heat generation rates $\bar{\dot{Q}}_{irr,WVO}$ and $\bar{\dot{Q}}_{irr,Li}$ [eq.5(13)] averaged over 5 consecutive cycles. The error bars represent two standard deviations or 95 % confidence interval. Fitting of $\bar{\dot{Q}}_{irr,Li}$ with respect to current I at the metallic Li electrode yields $\bar{\dot{Q}}_{irr,Li} \propto I^2$. In other words, the irreversible heat generation was dominated by Joule heating since the resistance of the metallic Li electrode was constant. Importantly, $\bar{\dot{Q}}_{irr,WVO}$ in the electrode made of $(W_{0.2}V_{0.8})_3O_7$ microparticles became slightly but systematically larger than that in the electrode made of nanoparticles at C-rates of 2C and 3C, despite the fact that the applied current was larger for the nanoparticle based electrode. This behavior could be attributed to the fact that an electrode with larger particles generally features larger electrical resistivity thus increasing Joule heating [148].

The enthalpy of mixing also contributed to the irreversible heat generation and increased with increasing particle size due to diffusion limitation, particularly at high C-rates [49, 55]. Decreasing the particle size reduced the lithium concentration gradient formed within the particles and thus reduced the irreversible heat of mixing [eq.5(6)] [51, 53]. Here, $\bar{\dot{Q}}_{irr,WVO}$ at

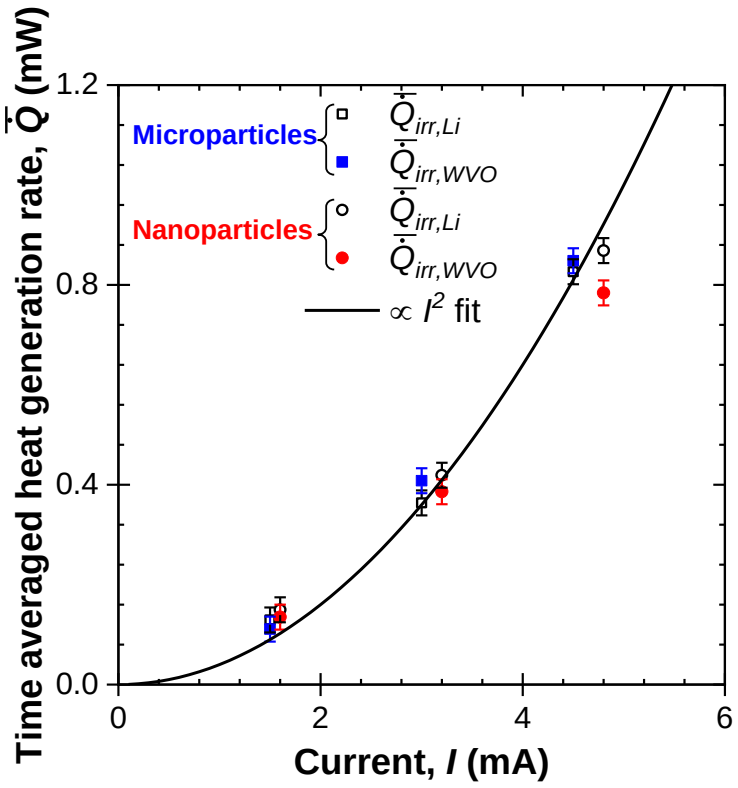

Figure 5.5: Time-averaged irreversible heat generation rates $\bar{\dot{Q}}_{irr,WVO}$ and $\bar{\dot{Q}}_{irr,Li}$, as functions of applied current I based on the isothermal *operando* calorimetry measurements at temperature $T = 20$ °C.

the $(W_{0.2}V_{0.8})_3O_7$-based electrodes made of microparticles and nanoparticles were similar at C-rate of 1C. This observation could possibly be attributed to the fact that the contribution of enthalpy of mixing to the irreversible heat generation rate is small at relatively low C-rates. Furthermore, the mass loading of $(W_{0.2}V_{0.8})_3O_7$ nanoparticles was larger than that of microparticles. Thus, the applied current was also larger for the electrode consisting of nanoparticles.

5.2.3.3 Heat generation rate of a full cell

Figure 5.6 plots the total instantaneous heat generation rate given by $\dot{Q}_T(x) = \dot{Q}_{Li}(x) + \dot{Q}_{WVO}(x)$ in the entire cell containing electrode made of $(W_{0.2}V_{0.8})_3O_7$ in the form of (a,b) microparticles and (c,d) nanoparticles as functions of lithium composition x at C-rate of 1C

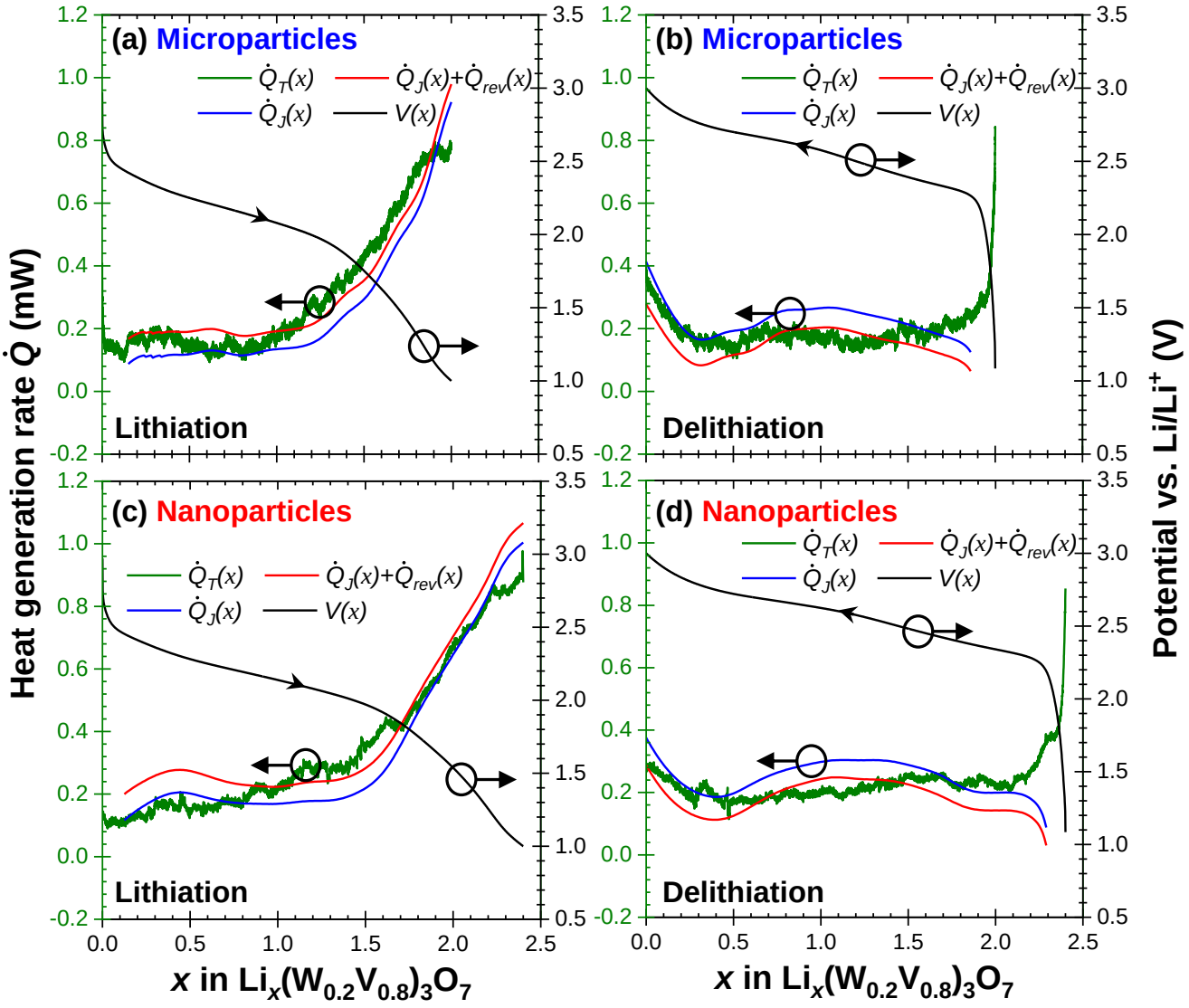

Figure 5.6: Measured total heat generation rate $\dot{Q}_T(x)$=$\dot{Q}_{Li}(x)$+$\dot{Q}_{WVO}(x)$ and predictions of the heat generation rates $\dot{Q}_J(x)$ and $\dot{Q}_J(x)$+$\dot{Q}_{rev}(x)$ calculated based on eqs.5(4) and (5) along with the measured voltage $V(x)$ upon (a,c) lithiation, (b,d) delithiation at C-rate of 1C for a cell containing electrode consisting of (a,b) $(W_{0.2}V_{0.8})_3O_7$ microparticles synthesized by solid-state method and (c,d) $(W_{0.2}V_{0.8})_3O_7$ nanoparticles synthesized by freeze-drying method at temperature T = 20 °C.

during (a,c) lithiation and (b,d) delithiation, respectively. It also shows the contributions from Joule heating $\dot{Q}_J(x)$ and the reversible entropic heat generation $\dot{Q}_{rev}(x)$ predicted by eqs.5(4) and (5), respectively [47–50]. Here, $\dot{Q}_{rev}(x)$ was exothermic during lithiation and

endothermic during delithiation, as expected from the sign of $\partial U_{ocv}(x,T)/\partial T$ shown in Figure 5.3. The predictions of $\dot{Q}_J(x) + \dot{Q}_{rev}(x)$ from the measured current and voltage agreed well with the measured total heat generation rate $\dot{Q}_T(x)$ for lithiation. The differences between the predictions of $\dot{Q}_J(x) + \dot{Q}_{rev}(x)$ and the measured $\dot{Q}_T(x)$ were larger during delithiation than lithiation possibly due to relatively slow kinetics of delithiation compared to that of lithiation, as observed in the apparent diffusion coefficient of Li^+ ions in the $(W_{0.2}V_{0.8})_3O_7$ electrode (see Appendix).

To understand what happens when the cell is cycled faster, Figure 5.7 plots the total instantaneous heat generation $\dot{Q}_T(x)$ in the entire cell containing electrode consisting of $(W_{0.2}V_{0.8})_3O_7$ in the form of (a,b) microparticles and (c,d) nanoparticles as functions of lithium composition x at a C-rate of 3C during (a,c) lithiation and (b,d) delithiation, respectively. Again, at 3C the difference between the predictions of $\dot{Q}_J(x) + \dot{Q}_{rev}(x)$ and the measured $\dot{Q}_T(x)$ was larger during delithiation than lithiation at C-rate of 3C. Moreover, the differences between the predictions of $\dot{Q}_J(x) + \dot{Q}_{rev}(x)$ and the measurements of $\dot{Q}_T(x)$ was larger at a C-rate of 3C than at 1C (Figure 5.6). This can be attributed to the enthalpy of mixing $\dot{Q}_{mix}$, according to eq.5(3). The heat generation rate $\dot{Q}_{mix}(x)$ should increase with increasing C-rates due to an increase in the lithium concentration gradients developed within the electrode due to diffusion limitations [51, 53].

5.2.3.4 Energy balance

Figure 5.8 presents the electrical energy losses per unit of specific capacity $\Delta E_e/C_m$ [eq.5(9)] at C-rates of 1C, 2C, and 3C along with the predicted Joule heating Q_J [eq.5(8)] and the total thermal energy Q_T per specific capacity C_m dissipated in the entire cell measured experimentally for electrodes made of (a) $(W_{0.2}V_{0.8})_3O_7$ microparticles and (b) nanoparticles, respectively. It is worth noting that the cell specific capacity was larger with the electrodes made of $(W_{0.2}V_{0.8})_3O_7$ nanoparticles than that made of microparticles. Indeed, specific capacity C_m was measured to be 155 mAh/g at C-rate of 1C, 140 mAh/g at 2C, and 130 mAh/g at 3C for the electrodes made of microparticles and 200 mAh/g at C-rate of 1C, 175

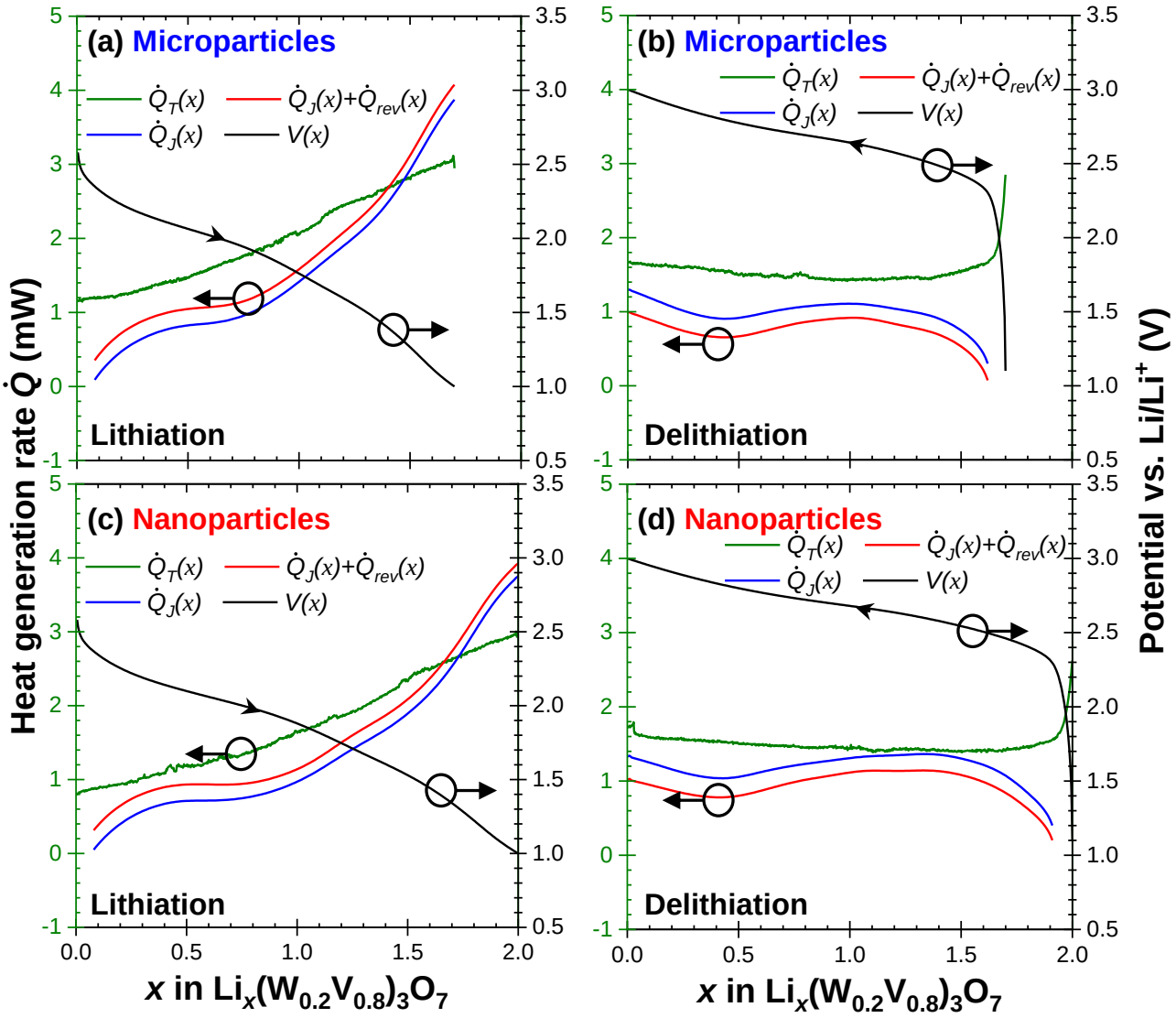

Figure 5.7: Measured total heat generation rate $\dot{Q}_T(x)$=$\dot{Q}_{Li}(x)$+$\dot{Q}_{WVO}(x)$ and predictions of the heat generation rates $\dot{Q}_J(x)$ and $\dot{Q}_J(x)$+$\dot{Q}_{rev}(x)$ calculated based on eqs.5(4) and (5) along with the measured voltage $V(x)$ upon (a,c) lithiation, (b,d) delithiation at C-rate of 3C for a cell containing electrode consisting of (a,b) $(W_{0.2}V_{0.8})_3O_7$ microparticles synthesized by solid-state method and (c,d) $(W_{0.2}V_{0.8})_3O_7$ nanoparticles synthesized by freeze-drying method at temperature $T = 20$ °C.

mAh/g at 2C, and 160 mAh/g at 3C for the electrodes made of nanoparticles. In both cells, $\Delta E_e/C_m$ increased with increasing C-rate due to the associated increase in the overpotential $[V(x,T) - U^{avg}(x,T)]$ [122, 123]. Moreover, the specific electrical energy losses $\Delta E_e/C_m$

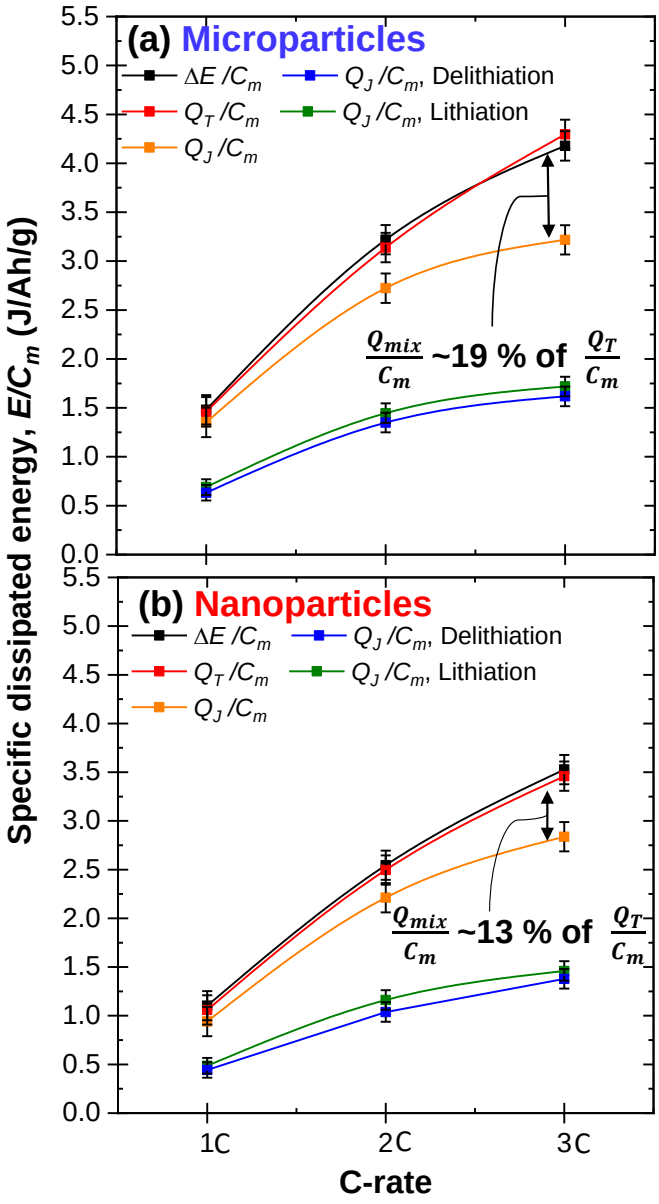

Figure 5.8: Measured specific net electrical energy losses $\Delta E_e/C_m$ and total specific thermal energy dissipated Q_T/C_m averaged over the first five charging-discharging cycles as well as predicted contributions from Joule heating Q_J/C_m during lithiation and delithiation for a cell made of an electrode consisting of $(W_{0.2}V_{0.8})_3O_7$ (a) microparticles synthesized by solid-state method and (b) nanoparticles synthesized by freeze-drying method. The enthalpy of mixing corresponds to $Q_{mix}/C_m = Q_T/C_m - Q_J/C_m = \Delta E_e/C_m - Q_J/C_m$.

due to the hysteretic voltage profile was within 5 % of the independently measured total specific thermal energy, Q_T/C_m dissipated over a cycle. In other words, the electrical energy losses were dissipated entirely in the form of heat so that $\Delta E_e/C_m = Q_T/C_m$. Furthermore, dissipated energy per unit of specific capacity was smaller for a cell with electrode consisting of $(W_{0.2}V_{0.8})_3O_7$ nanoparticles than that of microparticles suggesting that the electrode made of nanoparticles was energetically more efficient and lost less electrical energy per energy stored.

When averaged over a cycle $Q_{rev}/C_m \simeq 0$; this means that the difference between Q_T/C_m and Q_J/C_m corresponded to the heat dissipated in the form of enthalpy of mixing, i.e., $Q_{mix}/C_m = Q_T/C_m$ - Q_J/C_m. In both cells, the contribution of the enthalpy of mixing to the total energy dissipated increased with increasing C-rate. For a cell with electrode consisting of $(W_{0.2}V_{0.8})_3O_7$ microparticles, Q_{mix}/C_m reached 19 % at C-rate of 3C compared with 13 % for an electrode made of $(W_{0.2}V_{0.8})_3O_7$ nanoparticles. These calorimetry measurements thus demonstrated that using nanoparticles instead of microparticles make it kinetically more favorable for lithium-ions to intercalate, and results in smaller enthalpy of mixing and overall heat dissipation. These two systems show nearly identical behavior in almost all other respects, making this an ideal system for isolating the effects of particle size on enthalpy of mixing and heat dissipation.

5.3 Conclusion

This study investigated the effect of particle size of Wadsley-Roth compound $(W_{0.2}V_{0.8})_3O_7$ on the thermodynamic properties and heat generation of battery cells. Galvanostatic cycling confirmed that the electrode made of $(W_{0.2}V_{0.8})_3O_7$ nanoparticles synthesized by sol-gel method combined with freeze-drying featured larger capacity and better capacity retention at high C-rates than that made of the $(W_{0.2}V_{0.8})_3O_7$ microparticles synthesized by solid-state method. Entropic potential measurements confirmed the phase transition identified previously from *in situ* XRD measurements and identified the semiconductor to metal transition occurring at low lithium composition [139]. Furthermore, entropic potential measurements

showed that the $(W_{0.2}V_{0.8})_3O_7$ nanoparticle underwent a two-phase coexistence region over a narrower range of x compositions possibly due to inhibition of the phase transition caused by their nanoscale size. Isothermal *operando* calorimetry measurements demonstrated that the heat generation rate increased at the $(W_{0.2}V_{0.8})_3O_7$-based electrode upon lithiation due to an increase in charge transfer resistance. Moreover, the time-averaged irreversible heat generation rate and the enthalpy of mixing were smaller at the electrode made of nanoparticles than at that made of the microparticles particularly at high C-rates. Finally, dissipated electrical energy per unit of specific capacity was smaller for a cell with electrodes made of $(W_{0.2}V_{0.8})_3O_7$ nanoparticles than that made of microparticles due to reduced concentration gradients and thus reduced enthalpy of mixing. These results demonstrate that using electrodes consisting of nanoparticles is energetically more efficient thanks to more kinetically favorable lithium ion intercalation.

CHAPTER 6

Conclusions and future work

6.1 Conclusions

The objectives of this study were (i) to develop an interpretative guide of the open circuit voltage U_{ocv} and the entropic potential $\partial U_{ocv}(x,T)/\partial T$ measurements for different charging/discharging mechanisms, (ii) to investigate the thermal signatures associated with electrochemical and transport phenomena occurring in LIBs during cycling, and (iii) to investigate the effect of particle size of active on the heat generation in LIB systems.

A general interpretative guide of the open circuit voltage U_{ocv} and the entropic potential $\partial U_{ocv}(x,T)/\partial T$ measurements was developed by numerically calculating different contributions from configurational, vibrational, and electronic excitations to the entropy of an ideal intercalation compound. The analysis suggests that general trends of $\partial U_{ocv}(x,T)/\partial T$ of a homogeneous solid solution are dominated by configurational entropy, which leads to a monotonically decreasing $U_{ocv}(x,T)$ and $\partial U_{ocv}(x,T)/\partial T$ with increasing lithium composition x. Ion ordering over a subset of energetically favorable interstitial sites is characterized by a tilde-shaped fluctuation in $\partial U_{ocv}(x,T)/\partial T$ versus x. Furthermore, a first order phase transition accompanied by two-phase coexistence manifests itself as a constant $U_{ocv}(x,T)$ and $\partial U_{ocv}(x,T)/\partial T$. Finally, a two-phase coexistence with a stable intermediate phase leads to a monotonically decreasing $U_{ocv}(x,T)$ curve upon lithiation that is characterized by two plateaus separated by a step. The $\partial U_{ocv}(x,T)/\partial T$ curve for this scenario also exhibits two plateaus. However, depending on the entropy of the intermediate phase, the second plateau can either be higher or lower than the first plateau. These interpretations were systematically illustrated using experimental data for various electrode materials, such as TiS_2, $LiCoO_2$,

$Li_{4/3}Ti_{5/3}O_4$, $LiFePO_4$, and graphite.

Thermal signatures associated with electrochemical and transport phenomena occurring in LIB systems were investigated by performing potentiometric entropy measurement on LIB systems and measuring separately the instantaneous heat generation rate at each electrode. Here, LIB system consisting of electrodes made of Wadsley-Roth shear phase compounds $TiNb_2O_7$ and PNb_9O_{25} were investigated. Potentiometric entropy measurements not only confirmed the phase transitions identified from XRD measurements but also identified intralayer lithium ion ordering occurring in $TiNb_2O_7$ and PNb_9O_{25} which could not be identified from other characterization methods. Furthermore, entropy measurements also confirmed the semiconductor to metal transition taking place at PNb_9O_{25} upon lithiation. The heat generation rate due to Joule heating varied widely during lithiation and delithiation and dominated the energy losses during cycling. In addition, the time-averaged irreversible heat generation rate indicated that the electrical resistance of the lithium metal electrode was constant and independent of the state of charge while the electrical resistance of the PNb_9O_{25} changed significantly with the state of charge. These results illustrate that calorimetric measurements can provide insight into changes in the electrical conductivity of batteries for different SOC upon cycling. Moreover, calorimetry measurements have demonstrated that the electrical energy losses were dissipated entirely in the form of heat. Furthermore, the enthalpy of mixing increased with increasing C-rate. However, the enthalpy of mixing remained relatively small even at high C-rates for both electrodes made of $TiNb_2O_7$ and PNb_9O_{25} compared to other LIB electrode materials. These results establish that both $TiNb_2O_7$ and PNb_9O_{25} constitute an excellent anode material for fast charging battery applications.

Moreover, the effect of particle size on the electrochemical performance and heat generation in LIB systems were investigated using two LIBs consisting of electrodes made of another Wadsley-Roth shear phase compound namely $(W_{0.2}V_{0.8})_3O_7$ in the form of either *nanoparticles* synthesized by sol-gel method combined with freeze-drying or $(W_{0.2}V_{0.8})_3O_7$ *microparticles* synthesized by solid-state method. Galvanostatic cycling confirmed that the electrode made of $(W_{0.2}V_{0.8})_3O_7$ *nanoparticles* featured larger capacity and better retention

at high C-rates than that made of $(W_{0.2}V_{0.8})_3O_7$ *microparticles*. Entropic potential measurements confirmed the phase transition observed previously from *in situ* XRD measurements and identified a semiconductor to metal transition occurring at low lithium composition. Furthermore, entropic potential measurements showed that the $(W_{0.2}V_{0.8})_3O_7$ nanoparticles underwent a two-phase coexistence region over a narrower range of x compositions possibly due to inhibition of the phase transition caused by their nanoscale size. Isothermal *operando* calorimetry measurements demonstrated that the heat generation rate increased at the $(W_{0.2}V_{0.8})_3O_7$-based electrode upon lithiation due to an increase in charge transfer resistance. Moreover, the time-averaged irreversible heat generation rate and the enthalpy of mixing were smaller at the electrode made of *nanoparticles* than at that made of the *microparticles* particularly at high C-rates. Finally, dissipated electrical energy per unit of specific capacity was smaller for a cell with electrodes made of $(W_{0.2}V_{0.8})_3O_7$ *nanoparticles* than that made of *microparticles*. These results demonstrate that using electrodes consisting of *nanoparticles* is energetically more efficient thanks to more kinetically favorable lithium ion intercalation.

6.2 Future work

Entropic characterization of chalcogenides

Most of the Wadsley-Roth shear phase compounds are transition metal containing oxides. These oxides cannot be used for cathode in LIBs since they can undergo irreversible O_2 evolution upon oxidation at high voltage [149,150]. To address the challenges associated with oxides, chalcogenides, such as Li_2FeS_2, Li_2FeSSe, and Li_2FeSe_2, have been developed as new cathode materials for LIBs by Prof See's group at CalTech. Even though these chalcogenides are isostructural with each other, the charging/discharging curves are not identical indicating that different charging/discharging mechanisms occur for different chalcogenides. Thus, potentiometric entropy measurements of the chalcogenides can offer more insight into not only the effect of different chalcogens on selected chalcogenides, but also of the different

physicochemical phenomena occurring upon intercalation/deintercalation of lithium ions into the host material.

Table 6.1: Mass loading of Li_2FeS_2, Li_2FeSSe, and Li_2FeSe_2 used in the working electrode.

Chalcogenides	Mass loading (mg)
Li_2FeS_2	10.2
Li_2FeSSe	14.16
Li_2FeSe_2	12.66

Potentiometric entropy measurements were performed on the cells consisting of working electrodes made of chalcogenides and the lithium metal counter electrode in 1 M of $LiPF_6$ in EC:PC:DMC 1:1:3. Here, the working electrode had mass ratio 6:2:2 of active material: conductive carbon: polytetrafluoroethylene (PTFE) binder. Table 6.1 reports the mass loading of the active material used in the working electrode.

Figure 6.1 presents the open circuit voltage $U_{ocv}(x,T)$ of the cell containing electrodes made Li_2FeS_2, Li_2FeSSe, and Li_2FeSe_2 during the first (a) charging and (b) discharging steps at temperature T = 20 °C. Here, the chalcogenides were charged by delithiation and discharged by lithiation. It is interesting to note that all three chalcogenides shared two distinct regions in $U_{ocv}(x,T)$ during charging namely a sloping region with multiple inflections followed by a long plateau. Previous Fe, S, and Se K-edge X-ray absorption spectroscopy indicated that the sloping region corresponded to $Fe^{2+/3+}$ redox and the long plateau was related to the redox of chalcogens such as S^{2-}/S_2^{2-} or Se^{2-}/Se_2^{2-} [151, 152]. In addition, the voltage plateau at high states of charge consistently shifted to lower voltages as the Se content increased. In fact, the electron orbital of selenides is higher than that of sulfides resulting in anionic electronic states at higher energy, which are then oxidized at a lower voltage [152]. Likewise, the voltage plateau in $U_{ocv}(x,T)$ during discharging also shifted down as the Se content increased. This shift may be derived from the increased metallic character of the materials, as would be expected for a selenide over a sulfide due to the less

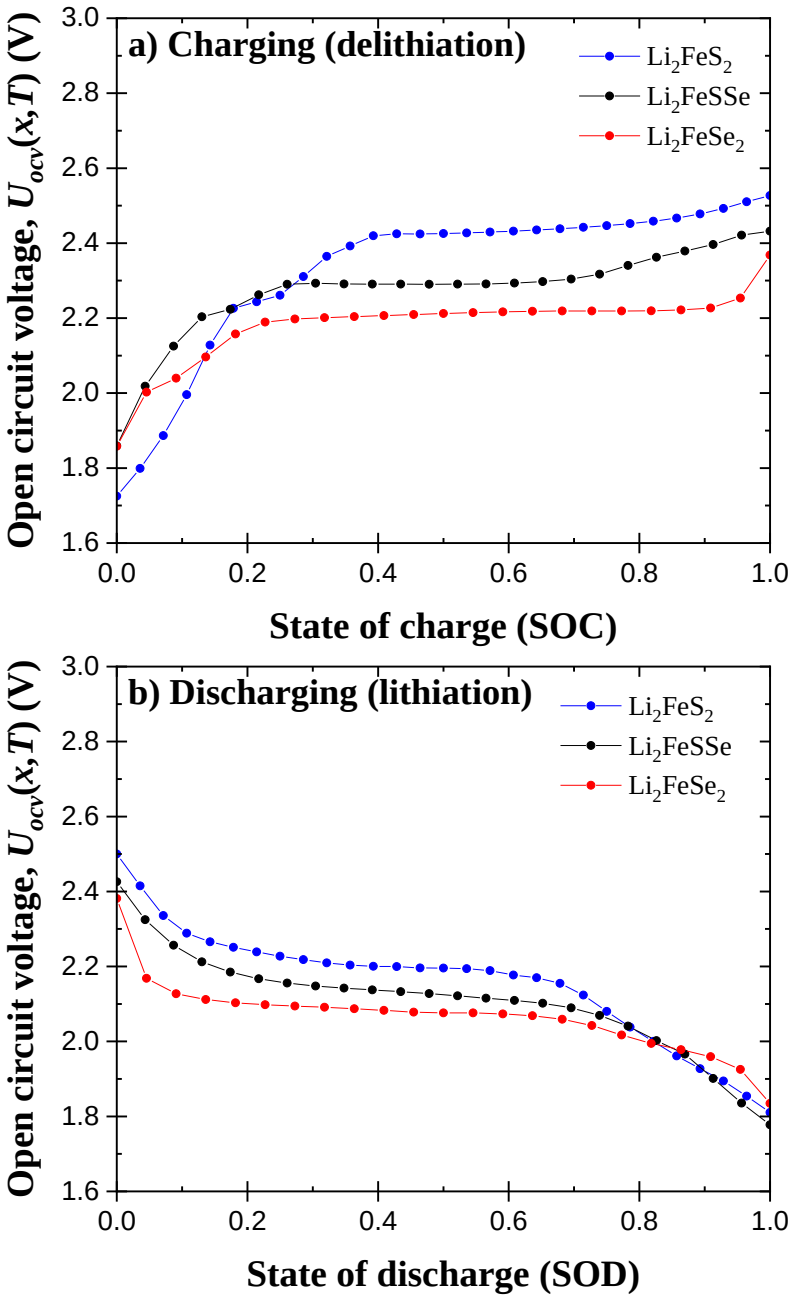

Figure 6.1: Open circuit voltage $U_{ocv}(x,T)$ of cells containing electrodes made of Li_2FeS_2, Li_2FeSSe, and Li_2FeSe_2 during (a) charging (delithiation) as functions of state of charge and (b) discharging (lithiation) as functions of state of discharge at temperature T = 20 °C.

localized bands and greater orbital overlap [152]. The systematic shift of the voltage plateau in $U_{ocv}(x,T)$ measurements indicated that anion redox can be directly manipulated through anion substitution.

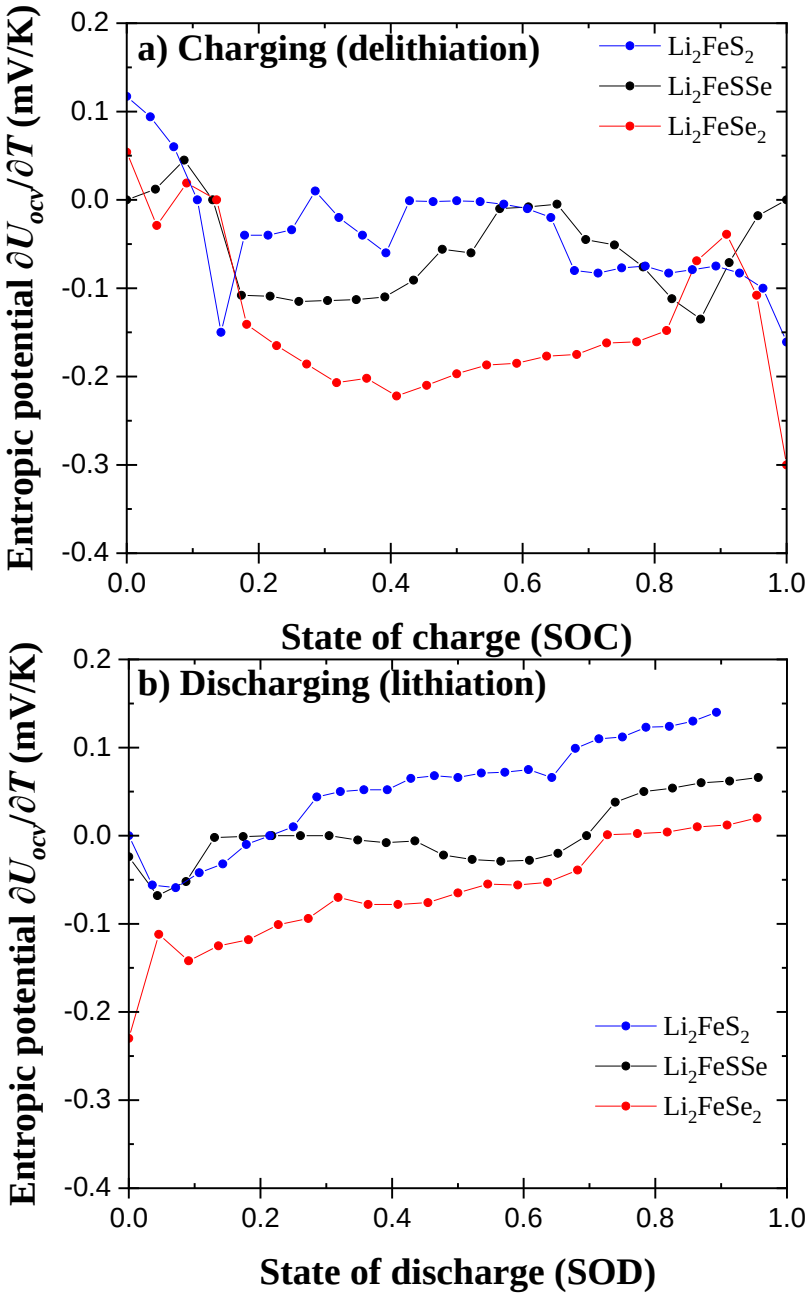

Figure 6.2: Entropic potential $\partial U_{ocv}(x,T)/\partial T$ of the cells with electrodes made of Li_2FeS_2, Li_2FeSSe, and Li_2FeSe_2 during (a) charging (delithiation) as functions of state of charge and (b) discharging (lithiation) as functions of state of discharge at temperature T = 20 °C.

Furthermore, Figure 6.2 plots the entropic potential $\partial U_{ocv}(x,T)/\partial T$ of the cell containing electrodes made of Li_2FeS_2, Li_2FeSSe, and Li_2FeSe_2 during the first (a) charging and (b)

discharging steps at temperature T = 20 °C. Interestingly, the magnitude of $\partial U_{ocv}(x,T)/\partial T$ also shifted down as the Se content increased during both charging and discharging. These shifts in $\partial U_{ocv}(x,T)/\partial T$ could be attributed to the difference in configurational entropy. Previous XRD measurements indicated that the sulfides underwent more significant structural change compared to selenides [152]. Therefore, sulfides would exhibit larger configurational entropy resulting in larger $\partial U_{ocv}(x,T)/\partial T$ compared to selenides. Moreover, there are distinctive fluctuations in $\partial U_{ocv}(x,T)/\partial T$ during charging but not during discharging. This observation could be attributed to the fact that these chalcogenides undergo apparent crystallographic structure changes upon charging but undergo an amorphous phase change upon discharging [152]. However, exact crystallographic structures are not investigated to fully analyze the $\partial U_{ocv}(x,T)/\partial T$ measurements. Thus, further high-resolution synchrotron X-ray measurements and Raman spectroscopy would be beneficial to further analyze the entropic potential measurements.

Entropic characterization of conversion materials

While chalcogendies such as Li_2FeS_2, undergo intercalation/deintercalation upon charging/discharging, iron disulfide FeS_2 undergoes conversion reaction upon charging/discharging. Conversion materials represent a viable route to improve specific capacity of LIBS, but their products and reaction pathway were unclear. Furthermore, recent study demonstrated that the products and reaction pathway of FeS_2 depends on the temperature [153]. Thus, performing potentiometric entropy measurements of such materials can deepen our understanding of conversion materials and observe the effect of temperature in the entropic potential measurements.

Potentiometric entropy measurements were performed on the cell consisted of working electode made of FeS_2 and lithium metal counter electrode in 1 M of lithium bis(fluorosulfonyl)imide (LiFSI) in 1-butyl-1-methylpyrrolidinium bis(trifluoromethanesulfonyl)imide ($PYR_{14}TFSI$) electrolyte. Here, the working electrode had mass ratio 8:1:1 of active material: conductive carbon: polyvinylidene fluoride (PVDF) binder. The mass loadings of active material were

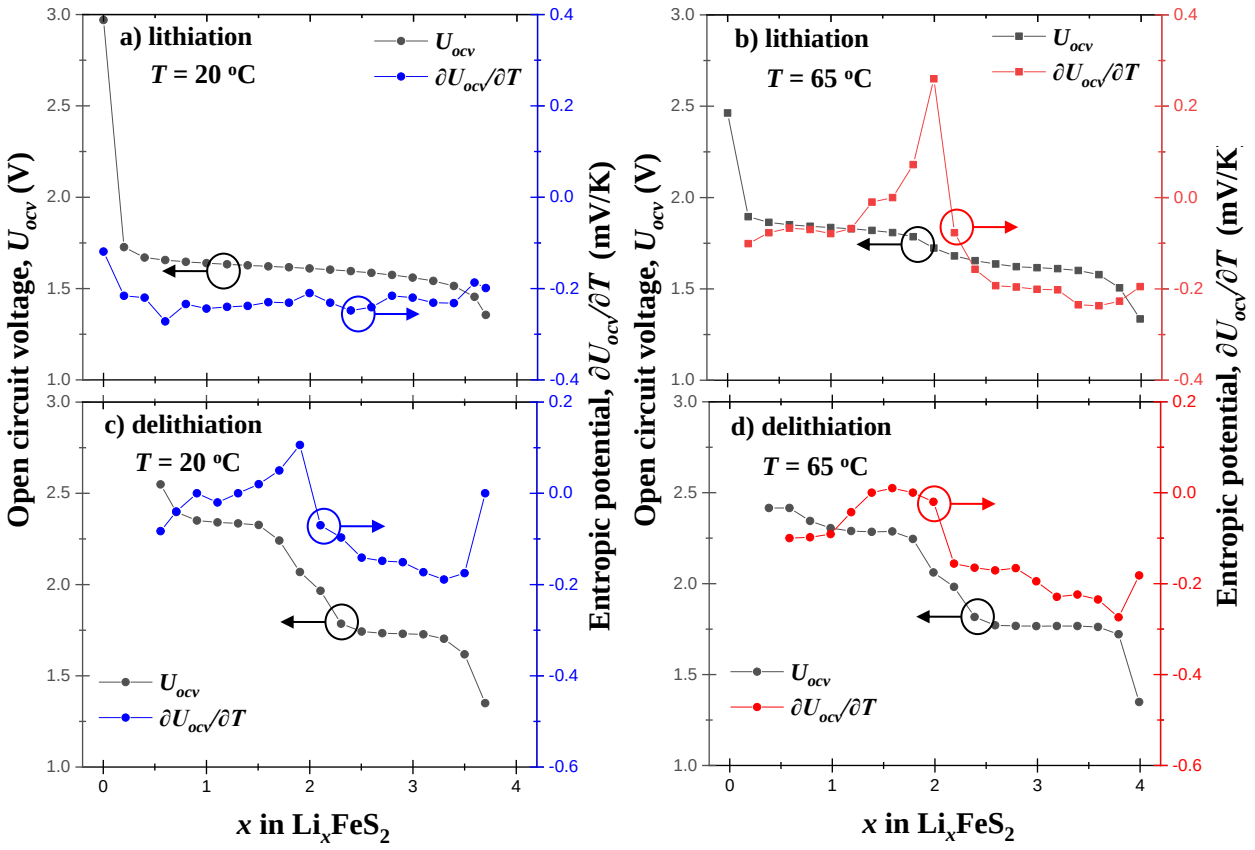

Figure 6.3: Open circuit voltage $U_{ocv}(x,T)$ and entropic potential $\partial U_{ocv}(x,T)/\partial T$ of the cell containing electrodes made of FeS_2 during (a,b) lithiation and (c,d) delithiation as functions of lithium composition x in Li_xFeS_2 at temperature (a,c) $T = 20$ °C and (b,d) $T = 65$ °C.

1.03 mg for the electrode cycled at temperature $T = 20$ °C and 1.21 mg for $T = 65$ °C.

Figure 6.3 presents $U_{ocv}(x,T)$ and $\partial U_{ocv}(x,T)/\partial T$ of the cell containing electrodes made of FeS_2 during (a,b) lithiation and (c,d) delithiation as functions of lithium composition x in Li_xFeS_2 at temperature (a,c) $T = 20$ °C and (b,d) $T = 65$ °C. First of all, only one plateau was observed in $U_{ocv}(x,T)$ at $T = 20$ °C (Figure 6.3a), while two distinctive plateaus of $U_{ocv}(x,T)$ were observed at $T = 65$ °C during lithiation (Figure 6.3b). This behavior could be attributed to the fact that FeS_2 undergoes either a one-step or a two-step reaction upon lithiation depending on the temperature [154, 155]. At room temperature, FeS_2 undergoes a one-step reaction upon lithiation, i.e. [154],

$$FeS_2 + 4Li \rightarrow 2Li_2S + Fe. \tag{6.1}$$

On the other hand, at higher temperatures, FeS_2 undergoes a two-step reaction during lithiation, such that [154, 155]

$$FeS_2 + 2Li \rightarrow Li_2S + FeS \quad \text{(at 1.9 V)} \quad \text{and} \quad FeS + 2Li \rightarrow Li_2S + Fe \quad \text{(at 1.7 V)}. \tag{6.2}$$

Moreover, $\partial U_{ocv}(x,T)/\partial T$ was relatively constant upon lithiation at $T = 20$ °C, while $\partial U_{ocv}(x,T)/\partial T$ featured a peak around $x = 2$ upon lithiation at $T = 65$ °C. This peak could be due to the formation of FeS resulting from a two-step reaction.

Unlike lithiation, behaviors of both $U_{ocv}(x,T)$ and $\partial U_{ocv}(x,T)/\partial T$ curves were similar at two different temperatures indicating that FeS_2 underwent the same reaction. In fact, FeS_2 undergoes the following two-step reaction upon delithiation, regardless of the temperature [154]

$$Li_2S + Fe \rightarrow FeS + 2Li \quad \text{(at 1.7 V)} \quad \text{and} \quad Li_2S \rightarrow 2Li + S \quad \text{(at 2.3 V)}. \tag{6.3}$$

In addition, a local maxima in $\partial U_{ocv}(x,T)/\partial T$ curve was observed around $x = 2$ at $T = 20$ °C. This peak could be attributed to the fact that FeS_2 loses its sulfur much more abruptly at lower temperatures that at higher temperature resulting in larger entropic change [153].

Effect of binders on the heat generation

In the process of fabricating electrodes, binders are used to hold the active materials together, and often it takes about 10 % of the total mass of the electrode. Previous study showed that dihexyl-substituted poly(3,4-propylenedioxythiophene) (PProDOT-Hx_2), conductive polymer binder, exhibited excellent performance as a cathode binder for $LiNi_{0.8}Co_{0.15}Al_{0.05}O_2$ (NCA) [156]. Furthermore, hexyl (Hex) oligoether (OE) PProDOTs (Hex:OE), copolymers based on PProDOT-Hx_2 where the hexyl side chains are replaced to varying extents with oligoether side chains can further enhance the ionic conductivity [157]. Here, *operando* isothermal calorimetric measurements were performed on cells consisting of working electrodes made of NCA with PVDF, PProDOT-Hx_2, and Hex:OE binders and the lithium metal counter electrode in 1 M of $LiPF_6$ in EC:DMC 1:1 v/v. The working electrodes had mass ratio 90:3:3:4 of NCA: super P: carbon nano tube (CNT): binder. Table 6.2 summarizes

the mass loadings of active material in each working electrode.

Table 6.2: Mass loading of $LiNi_{0.8}Co_{0.15}Al_{0.05}O_2$ (NCA) used in the working electrode with different binders for calorimetry measurements.

Binder	Mass loading of NCA (mg)
PVDF	13.4
Hex:OE	14.1
PProDOT-Hx_2	10.2

Figures 6.4 (a,b,c) plot the open circuit voltage $U_{ocv}(x,T)$ and entropic potential $\partial U_{ocv}(x,T)/\partial T$ of the cells containing electrodes made of NCA with (a) PVDF, (b) Hex:OE, and (c) PProDOT-Hx_2 measured at 20 °C as functions of specific capacity at C-rate of C/10 during the first delithiation. First of all, the NCA electrode with Hex:OE was able to accommodate more lithium than other electrodes and featured the largest specific capacity while that with PVDF exhibited the lowest specific capacity. In fact, the electronic conductivity of both PProDOT-Hx_2 and Hex:OE are orders of magnitude larger than that of PVDF thus enhancing the electrochemical performance of the electrode [156–158]. Furthermore, the trends of both $U_{ocv}(x,T)$ and $\partial U_{ocv}(x,T)/\partial T$ were very similar for different types of electrodes and increased monotonically with increasing specific capacity indicating deintercalation in solid solution. However, there were discrepancies in $\partial U_{ocv}(x,T)/\partial T$ for $U_{ocv}(x,T)$ $\leq$ 3.5 V vs. Li/Li^+ [Figure 6.4(d)]. This behavior could be attributed to the fact that Hex:OE and PProDOT-Hx_2 are redox active in that potential range while PVDF is not redox active [156, 157]. Thus, the redox reaction occurring at the binder could facilitate deintercalation in faster and more ordered manner resulting in smaller $\partial U_{ocv}(x,T)/\partial T$.

Moreover, Figures 6.5 (a,b,c) plot the open circuit voltage $U_{ocv}(x,T)$ and entropic potential $\partial U_{ocv}(x,T)/\partial T$ of the cells containing electrodes made of NCA with (a) PVDF, (b) Hex:OE, and (c) PProDOT-Hx_2 measured at 20 °C as functions of specific capacity at C-rate of C/10 during the first lithiation. Again, the NCA electrode with PVDF featured the

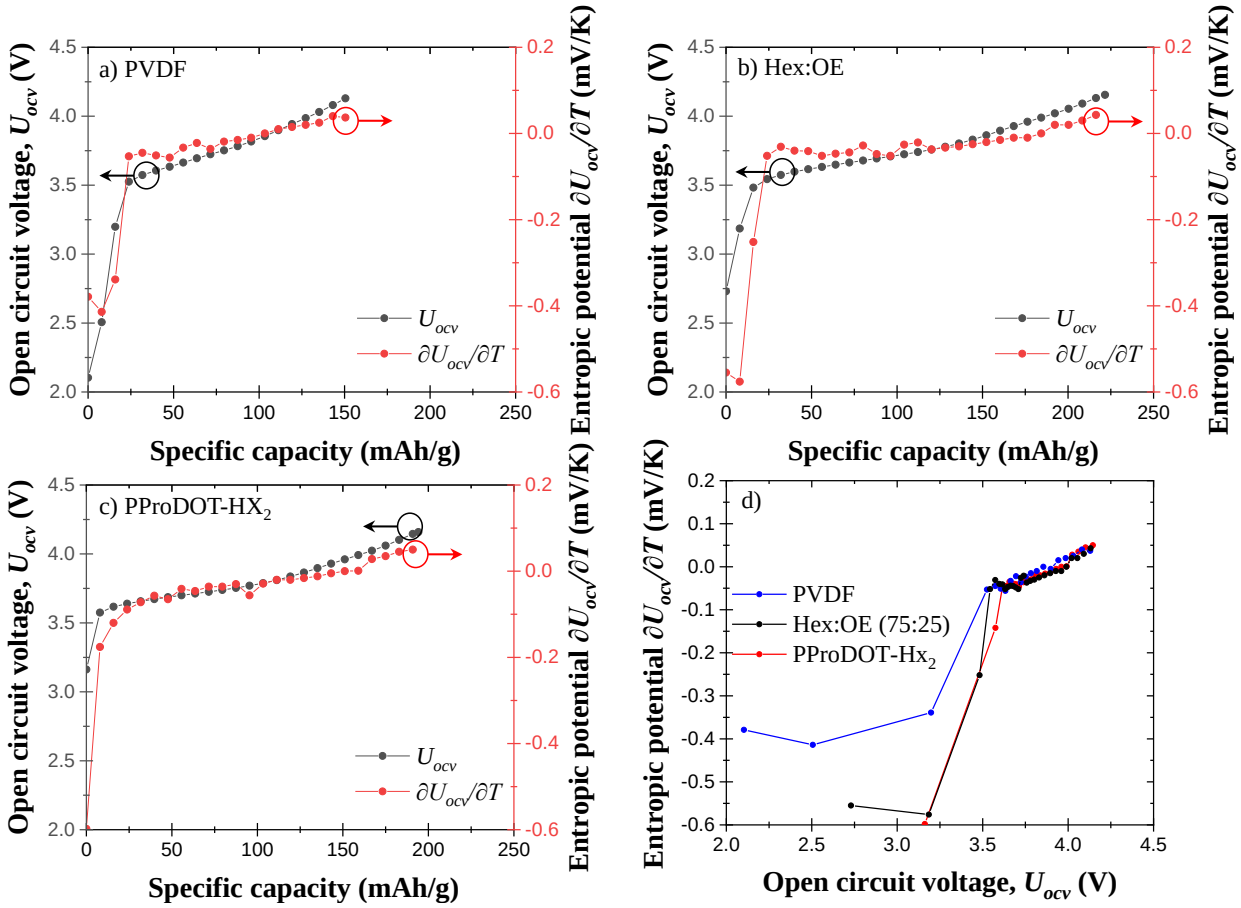

Figure 6.4: Open circuit voltage $U_{ocv}(x,T)$ and entropic potential $\partial U_{ocv}(x,T)/\partial T$ of the cell containing electrodes made of NCA with (a) PVDF, (b) Hex:OE, and (c) PProDOT-Hx$_2$; (d) entropic potential $\partial U_{ocv}(x,T)/\partial T$ of all three cells as functions of open circuit voltage $U_{ocv}(x,T)$ during delithiation as functions of specific capacity at temperature $T = 20$ °C.

lowest specific capacity confirming that the lower electronic conductivity diminished the electrochemical performance of the electrode. Figure 6.5(d) presents that $\partial U_{ocv}(x,T)/\partial T$ for all three NCA electrodes with different binders were identical unlike the first delithiation [Figure 6.4(d)]. Therefore, this results confirm that the discrepancies in $\partial U_{ocv}(x,T)/\partial T$ for $U_{ocv}(x,T)$ during the first delithiation could be attributed to initial specific capacity loss from trapped lithium ions and/or activating the conductive binder through redox reaction [156, 157].

Figure 6.6 shows the instantaneous heat generation rates $\dot{Q}_{NCA}(t)$ measured at the electrode made of NCA with (a,b) PVDF, (c,d) Hex:OE, and (e,f) PProDOT-Hx$_2$. and $\dot{Q}_{Li}(t)$

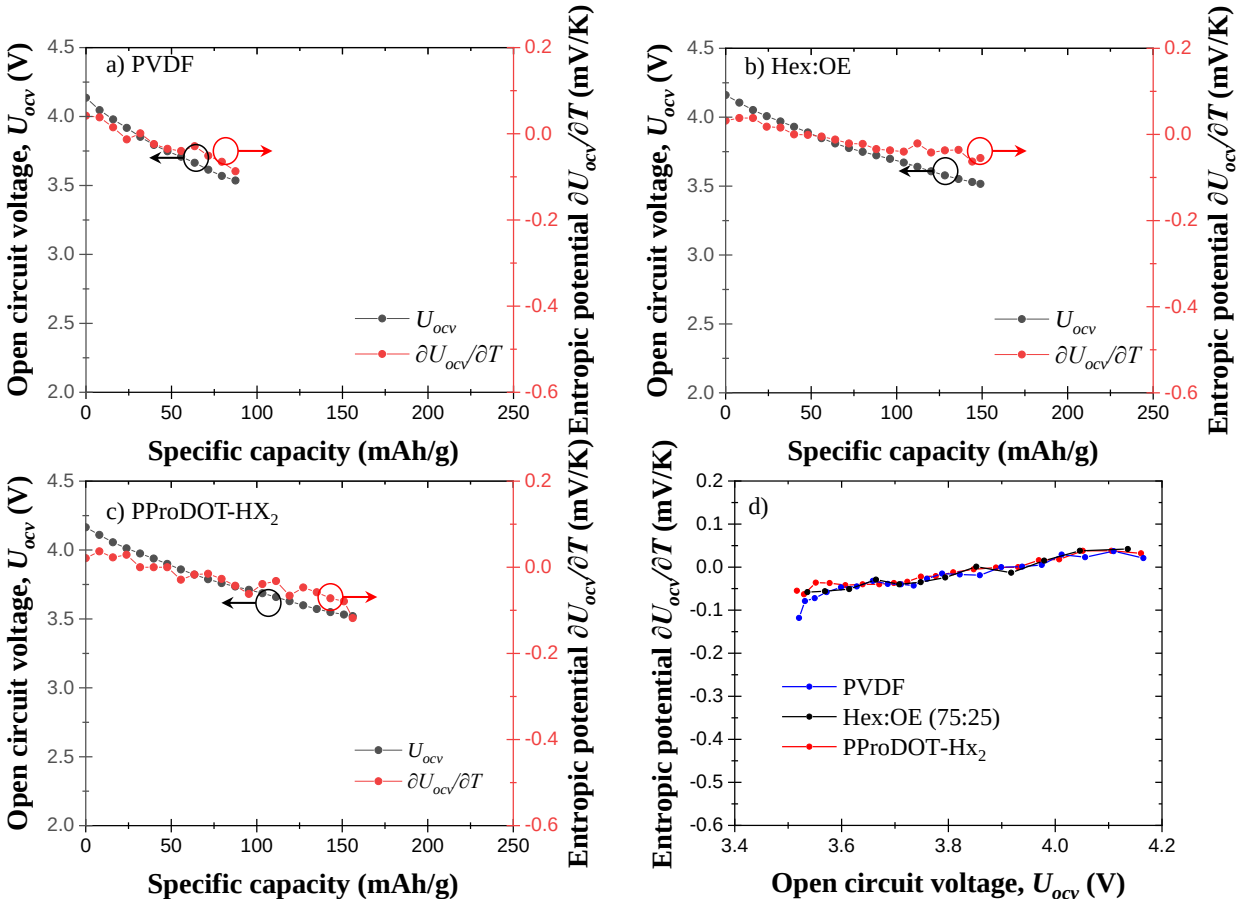

Figure 6.5: Open circuit voltage $U_{ocv}(x,T)$ and entropic potential $\partial U_{ocv}(x,T)/\partial T$ of the cell containing electrodes made of NCA with (a) PVDF, (b) Hex:OE, and (c) PProDOT-Hx$_2$; (d) entropic potential $\partial U_{ocv}(x,T)/\partial T$ of all three cells as functions of open circuit voltage $U_{ocv}(x,T)$ during lithiation as functions of specific capacity at temperature $T = 20$ °C.

measured at the lithium metal counter electrode and averaged over 5 consecutive cycles as functions of dimensionless time t_{cd} at 20 °C and at C-rate of (a,c,e) 1C and (b,d,f) 3C. Here, t_{cd} is the cycling period starting with charging (delithiation) followed by dicharging (lithiation). First of all, the magnitude of $\dot{Q}_{NCA}(t)$ at the NCA electrode with PProDOT-Hx$_2$ was smaller than those at the NCA electrodes with PVDF and Hex:OE due to the smaller mass loading compared to those of other electrodes (Table 6.2). Moreover, the trend of $\dot{Q}_{NCA}(t)$ for all three electrodes were very similar. However, $\dot{Q}_{NCA}(t)$ at the NCA electrode with PVDF was large and featured a sharp drop at the beginning of the charging process while $\dot{Q}_{NCA}(t)$ at the NCA electrode with Hex:OE and PProDOT-Hx$_2$ were relatively small and

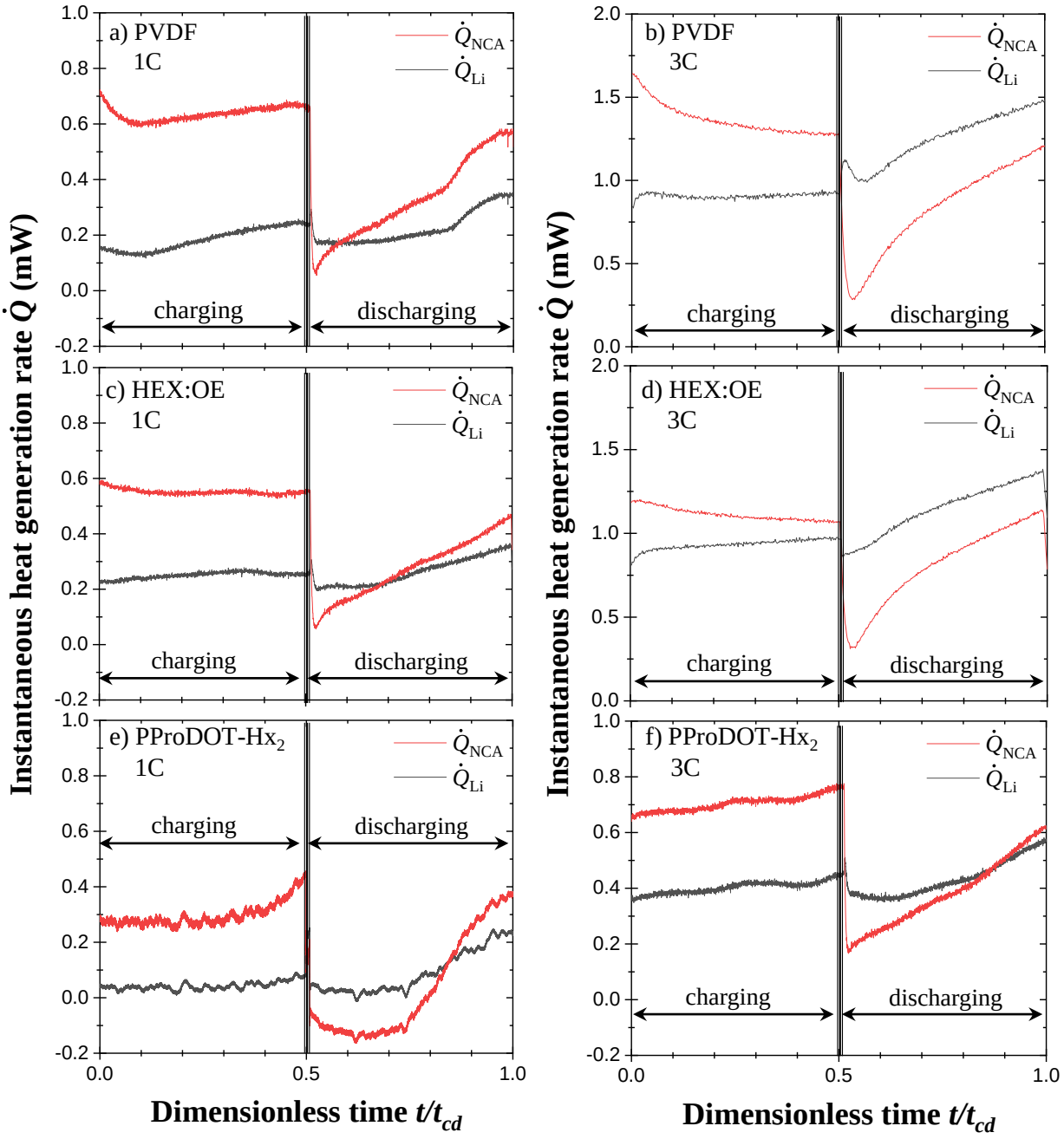

Figure 6.6: Measured instantaneous heat generation rates $\dot{Q}_{NCA}(t)$ at the NCA electrodes and $\dot{Q}_{Li}(t)$ at the lithium metal electrode averaged over 5 consecutive cycles as functions of dimensionless time t_{cd} with potential window ranging from 2.7 V to 4.2 V vs. Li/Li^+ at C-rates of (a,c,e) 1C and (b,d,f) 3C for NCA with (a,b) PVDF, (c,d) Hex:OE, and (e,f) PProDOT-Hx_2.

flat. This behavior could be attributed to the fact that Hex:OE and PProDOT-Hx$_2$ feature relatively high electronic conductivity thus reducing the Joule heating [156, 157].

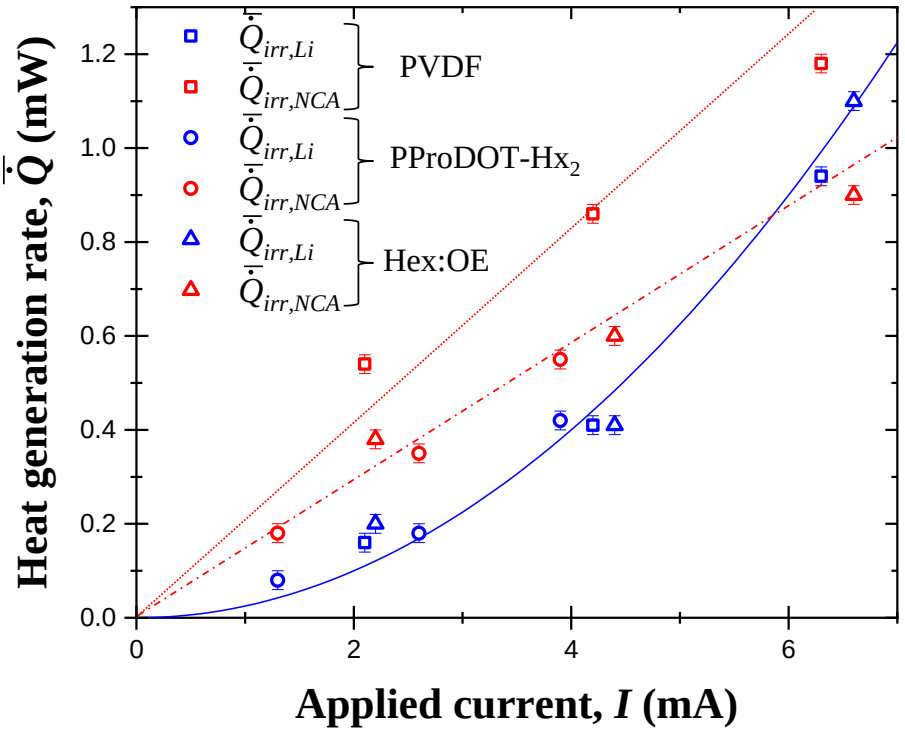

Figure 6.7: Time-averaged irreversible heat generation rates $\bar{\dot{Q}}_{irr,NCA}$ and $\bar{\dot{Q}}_{irr,Li}$, as functions of applied current I based on the isothermal *operando* calorimetry measurements at temperature $T = 20$ °C.

Figure 6.7 shows the time-averaged irreversible heat generation rates $\bar{\dot{Q}}_{irr,NCA}$ and $\bar{\dot{Q}}_{irr,Li}$ averaged over 5 consecutive cycles. The error bars represent two standard deviations or 95 % confidence interval. Fitting of $\bar{\dot{Q}}_{irr,Li}$ with respect to current I at the metallic Li electrode yields $\bar{\dot{Q}}_{irr,Li} \propto I^2$. In other words, the irreversible heat generation was dominated by Joule heating since the resistance of the metallic Li electrode was constant. By contrast, $\bar{\dot{Q}}_{irr,NCA}$ increased linearly with respect to the applied current I for all three different binders. This could be due, in part, to the fact that the electrical resistivity of NCA changes upon lithium intercalation/deintercalation. Moreover, as the C-rate increased, the capacity of the cells containing electrodes consisting of NCA with different binders decreased indicating that

the amount of lithium intercalating/deintercalating also decreased. Thus, at a high C-rate, the material underwent a narrower change in composition so that the average electrical resistivity also varied with C-rate. Furthermore, there was no significant difference between $\bar{\dot{Q}}_{irr,NCA}$ in the electrode consisting of NCA with PProDOT-Hx_2 and NCA with Hex:OE. In fact, the electrical conductivity of PProDOT-Hx_2 and Hex:OE are almost the same [157]. However, $\bar{\dot{Q}}_{irr,NCA}$ in the electrode consisting of NCA with PVDF was larger than those in the electrodes consisting of NCA with PProDOT-Hx_2 and NCA with Hex:OE at any C-rate. This behavior could be attributed to the fact that both PProDOT-Hx_2 and Hex:OE are conductive binders that enhanced the electrical conductivity of the electrodes [156, 157]. These results indicate that using electrodes consisting of conductive binders is energetically more efficient and results in less Joule heating.

Figure 6.8 plots the net electrical energy loss ΔE_e and the total thermal energy dissipated Q_T over a charging/discharging cycle for calorimetric cells with NCA electrodes with (a) PVDF, (b) Hex:OE, and (c) PProDOT-Hx_2 as functions of C-rate. First of all, Q_T measured for the calorimetric cell with the NCA electrode with PProDOT-Hx_2 was smaller than those at the NCA electrodes with PVDF and Hex:OE for any given C-rate due to the smaller mass loading compared to those of other electrodes (Table 6.2). For the cell with PVDF, the total thermal energy Q_T increased first then decreased for C-rate $\geq$ 2C while those for the cells with Hex:OE and PProDOT-Hx_2 increased with C-rate. This behavior could be attributed to the fact that cycle period t_{cd} decreased more significantly with increasing C-rate for the cell consisting of NCA electrode with PVDF compared to those consisting of NCA electrodes with Hex:OE and PProDOT-Hx_2. Finally, for both cells at any C-rate, the total dissipated thermal energy Q_T measured by *operando* isothermal calorimeter fell within 10 % of the net electrical energy loss ΔE_e measured by the potentiostat. In other words, the net electrical energy loss was entirely dissipated in the form of heat.

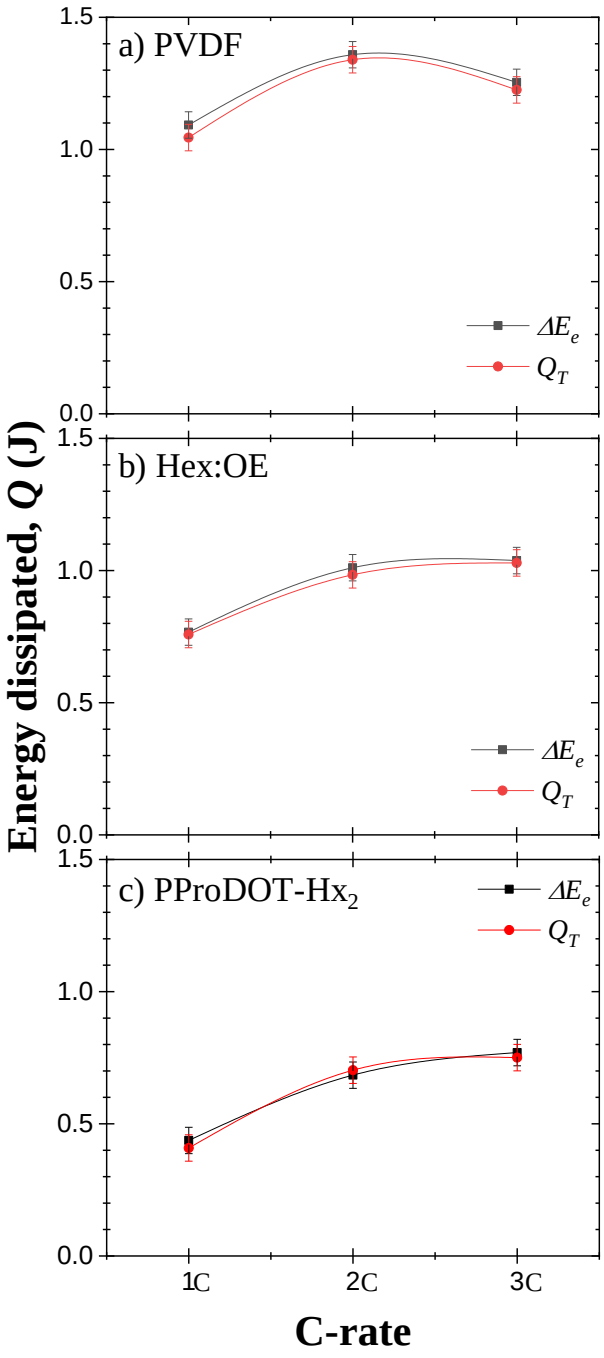

Figure 6.8: Net electrical energy loss ΔE_e and total thermal energy dissipated Q_T over a charging/discharging cycle for calorimetric cells with NCA electrodes with (a) PVDF, (b) Hex:OE, and (c) PProDOT-Hx_2 as functions of C-rate.

Appendix A

Supplementary materials for Chapter 2

A.1 Experimental procedures

A.1.1 Coincell fabrication

Three separate slurries were prepared for each active material using an 80:10:10 (wt%) ratio of active material [TiS_2 (Sigma Aldrich), $LiCoO_2$ (Sigma Aldrich), graphite (Sigma Aldrich)], conductive carbon (TIMCAL SuperP), and polyvinylidene fluoride (Sigma Aldrich). First, each active material was ball-milled for 30 minutes in a 2 cm^3 canister with SuperP. The mixtures were added to PVDF dissolved in 1-methyl-2-pyrrolidinone (Sigma Aldrich) to form a slurry and were mixed in a FlackTek speed mixer at 2000 rpm for 30 minutes. The prepared TiS_2 and graphite slurries were cast onto a copper foil while $LiCoO_2$ slurry was cast onto an aluminum foil using a doctor blade set for 150 μm. Then, the film was dried overnight at 110 °C in a vacuum oven. The fabricated electrodes were then punched into 10 mm diameter discs and assembled into a coin cell configuration (MTI parts, 2032 SS casings) with 1 M of $LiPF_6$ in EC:DMC 1:1 v/v (Sigma Aldrich) as electrolyte and polished lithium metal (Sigma Aldrich) as the counter electrode with a 50 μm thick polypropylene/polyethylene separator (Celgard C380).

A.1.2 Potentiometric entropy measurements

The potentiometric entropy measurements consisted of imposing a series of constant current pulses at a C-rate of C/10 for 30 minutes at 20 °C each followed by a relaxation period lasting 4 hours for TiS_2 and $LiCoO_2$, and 1 hour for graphite. During the relaxation, a step-like temperature profile was applied to the coin cell from 15 °C to 25 °C in 5 °C increments. The resulting voltage profile was recorded with the potentiostat (Biologic, VSP-300). Before recording the open circuit voltage $U_{ocv}(x, T)$ and imposing the next temperature step, we verified that the cell was in thermodynamic equilibrium by making sure that (i)

the temperature difference between the cold plate and the top of the coin cell was less than 0.1 °C and (ii) the time rate of change of the open circuit voltage $\partial U_{ocv}/\partial t$ was less than 5 mV/h.

A.2 Vibrational entropy derivation

For an *ideal* intercalation compound MA, the lithium composition x is defined as the fraction of the number of intercalated lithium N_{Li} per number of host MA units N_{MA}, i.e.,

$$x = \frac{N_{\mathrm{Li}}}{N_{\mathrm{MA}}}. \tag{6.4}$$

Assuming the vibrational spectrum of the Li ions can be approximated by the Einstein model with a characteristic frequency ω_{Li} independent of the overall lithium composition and volume of the host, each Li contributes a vibrational energy according to $\hbar\omega_{Li}(n_x + n_y + n_z + 3/2)$ where n_x, n_y, and n_z are quantum numbers, i.e., n_x, n_y, and $n_z = 0, 1, 2, \cdots$. Thus, the total energy of the Li_xMA compound can be expressed as

$$E_{\mathrm{Li}_x\mathrm{MA}} = E_{\mathrm{MA}} + N_{Li}\epsilon_{Li} + \sum_{i=1}^{N_{Li}} \hbar\omega_{Li}\left(n_x^i + n_y^i + n_z^i + \frac{3}{2}\right) \tag{6.5}$$

where E_{MA} is the energy of the host MA in the absence of Li and ϵ_{Li} is the energy of taking a Li from metallic Li to a vacant site in MA. For a canonical ensemble that is classical and discrete, the partition function can be written as

$$Z = \sum_{\delta} e^{-\beta E_\delta} \tag{6.6}$$

where δ is the index of configurational and vibrational microstates of the system, β is $1/k_bT$, and E_δ is the total energy of the system in the respective microstate. Thus, at fixed lithium composition x, the partition function of Li_xMA can be written as

$$Z_{\mathrm{Li}_x\mathrm{MA}} = \frac{N_{\mathrm{MA}}!}{N_{\mathrm{Li}}!(N_{\mathrm{MA}} - N_{\mathrm{Li}})!} e^{-\beta N_{\mathrm{Li}}\epsilon_{\mathrm{Li}}} \sum_{n_x^1=0}^{\infty}\sum_{n_y^1=0}^{\infty}\cdots\sum_{n_x^i=0}^{\infty}\cdots\sum_{n_z^{N_{\mathrm{Li}}}=0}^{\infty} e^{-\beta\hbar\omega_{\mathrm{Li}}\sum_{i=1}^{N_{Li}}\hbar\omega_{Li}\left(n_x^i+n_y^i+n_z^i+\frac{3}{2}\right)}. \tag{6.7}$$

Here, the factorial coefficient term represents the number of the configuration while the summation term accounts all vibrational microstates for each configuration. Furthermore,

Eq.(4) can be mathematically simplified as

$$Z_{\mathrm{Li}_x\mathrm{MA}} = \frac{N_{\mathrm{MA}}!}{N_{\mathrm{Li}}!(N_{\mathrm{MA}} - N_{\mathrm{Li}})!} e^{-\beta N_{\mathrm{Li}} \epsilon_{\mathrm{Li}}} \left(\frac{e^{\frac{-\beta\hbar\omega_{\mathrm{Li}}}{2}}}{1 - e^{\frac{-\beta\hbar\omega_{\mathrm{Li}}}{2}}} \right)^{3N_{\mathrm{Li}}} . \tag{6.8}$$

Finally, the molar Helmholtz free energy $f_{\mathrm{Li}_x\mathrm{MA}}$ of $\mathrm{Li}_x\mathrm{MA}$ can be expressed in terms of partition function, i.e.,

$$f_{\mathrm{Li}_x\mathrm{MA}} = \frac{F_{\mathrm{Li}_x\mathrm{MA}}}{N_{\mathrm{MA}}} = \frac{-k_B T ln Z}{N_{\mathrm{MA}}} \tag{6.9}$$

Combining Eqs.(5) and (6) results

$$f_{\mathrm{Li}_x\mathrm{MA}} = -\frac{k_b T}{N_{\mathrm{MA}}} ln \frac{N_{\mathrm{MA}}!}{N_{\mathrm{Li}}!(N_{\mathrm{MA}} - N_{\mathrm{Li}})!} + \frac{N_{\mathrm{Li}} \epsilon_{\mathrm{Li}}}{N_{\mathrm{MA}}} - \frac{3 N_{\mathrm{Li}} k_b T}{N_{\mathrm{MA}}} ln \left(\frac{e^{\frac{-\beta\hbar\omega_{\mathrm{Li}}}{2}}}{1 - e^{\frac{-\beta\hbar\omega_{\mathrm{Li}}}{2}}} \right). \tag{6.10}$$

Based on the Stirling's approximation, Eq.(7) can be simplified as

$$f_{\mathrm{Li}_x\mathrm{MA}} = k_b T[x ln x + (1-x) ln(1-x)] + \epsilon_{\mathrm{Li}} x + 3 \left[\frac{\hbar\omega_{\mathrm{Li}}}{2} + k_B T \ln\left(1 - e^{-\hbar\omega_{\mathrm{Li}}/k_B T}\right) \right] x \tag{6.11}$$

Here, the last term represents the vibrational free energy imposing the approximations of ideality in the evaluation of the vibrational partition function.

A.3 Density functional theory calculation for lithium metal counter electrode

Density functional theory (DFT) calculations were performed with the Vienna *ab initio* simulation package (VASP) [159–162] using the generalized gradient approximation (GGA) as formulated by Perdew, Burke, and Ernzerhoff (PBE) [163]. The projector augmented wave (PAW) [164, 165] method was utilized with a plane-wave energy cutoff of 650 eV. A fully automatic k-point mesh setting that corresponded to a 21 × 21 × 21 Monkhorst–Pack grid was used.

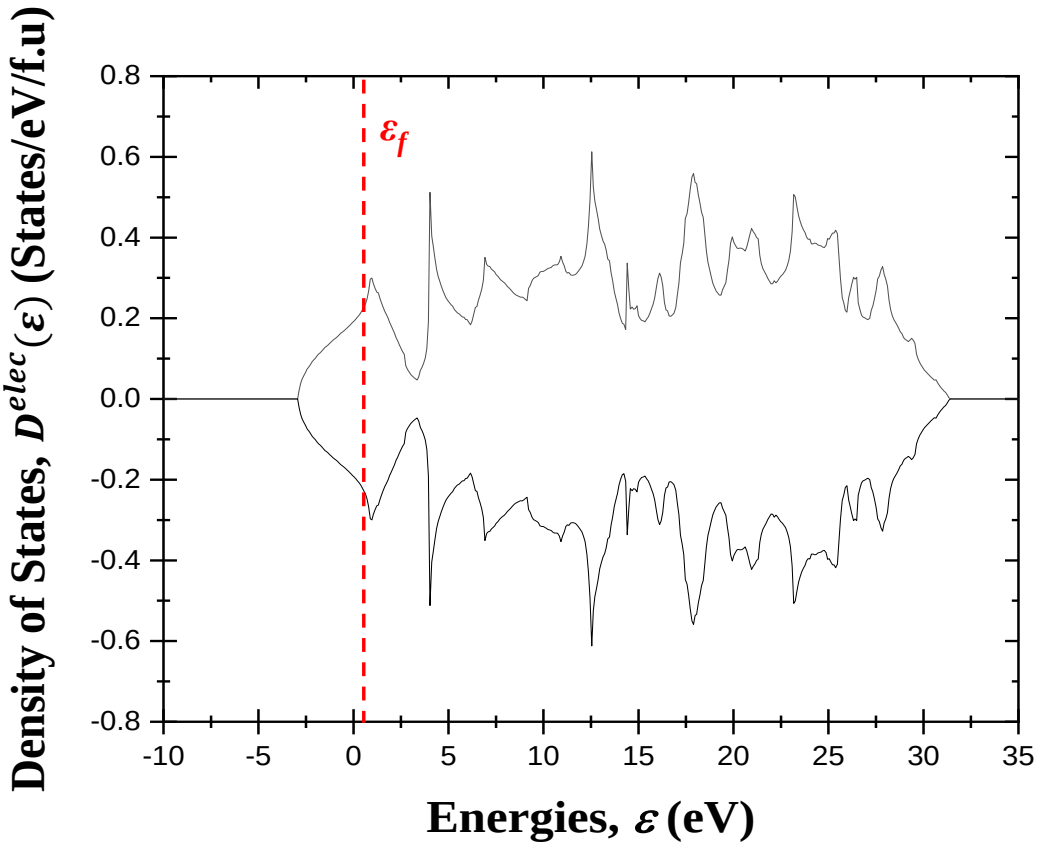

Figure A9: Calculated electronic density of states of body centered cubic (BCC) lithium metal as a function of energy based on density functional theory (DFT) calculations.

A.4 Electronic entropy of constant electronic density of state

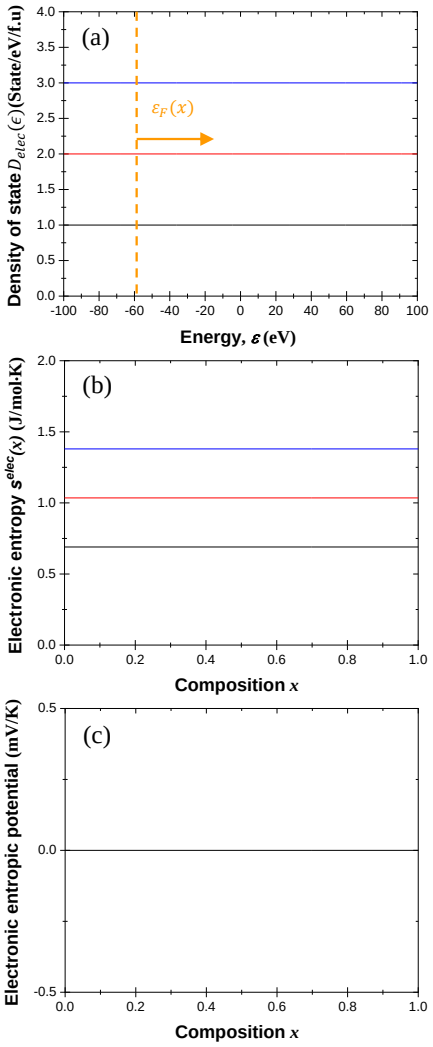

Figure A10: (a) Constant electronic density of state $\mathcal{D}^{elec}_{\mathrm{Li}_x\mathrm{MA}}(\epsilon)$ of $\mathrm{Li}_x\mathrm{MA}$ as functions of electric energy ϵ. (b) Electronic entropy $s^{elec}_{\mathrm{Li}_x\mathrm{MA}}(x,T)$ of $\mathrm{Li}_x\mathrm{MA}$, and (c) electronic entropic potential $\partial U^{elec}_{ocv}(x,T)/\partial T$ of a battery cell for constant electronic density of state as functions of lithium composition x.

A.5 Free energy calculation for ion ordering from a homogeneous solid solution

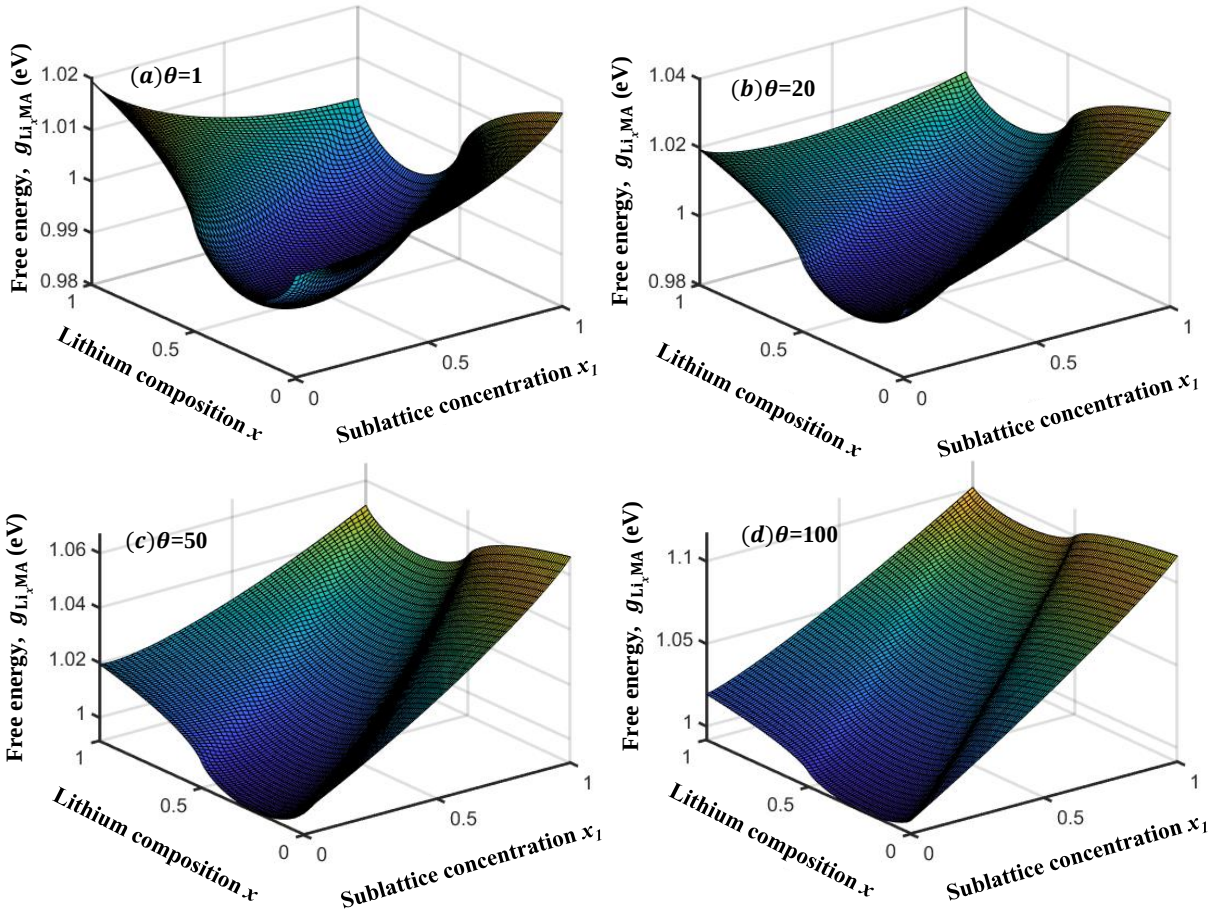

Figure A11: The Gibbs free energy $g_{\mathrm{Li}_x\mathrm{MA}}(x,T)$ of $\mathrm{Li}_x\mathrm{MA}$ as functions of lithium composition x and sublattice concentration x_1 for (a) $\theta=\epsilon_1/\epsilon_2$=1, (b) θ=20, (c) θ=50, and (d) θ=100.

Appendix B

Supplementary materials for Chapter 3

B.6 Synthesized materials

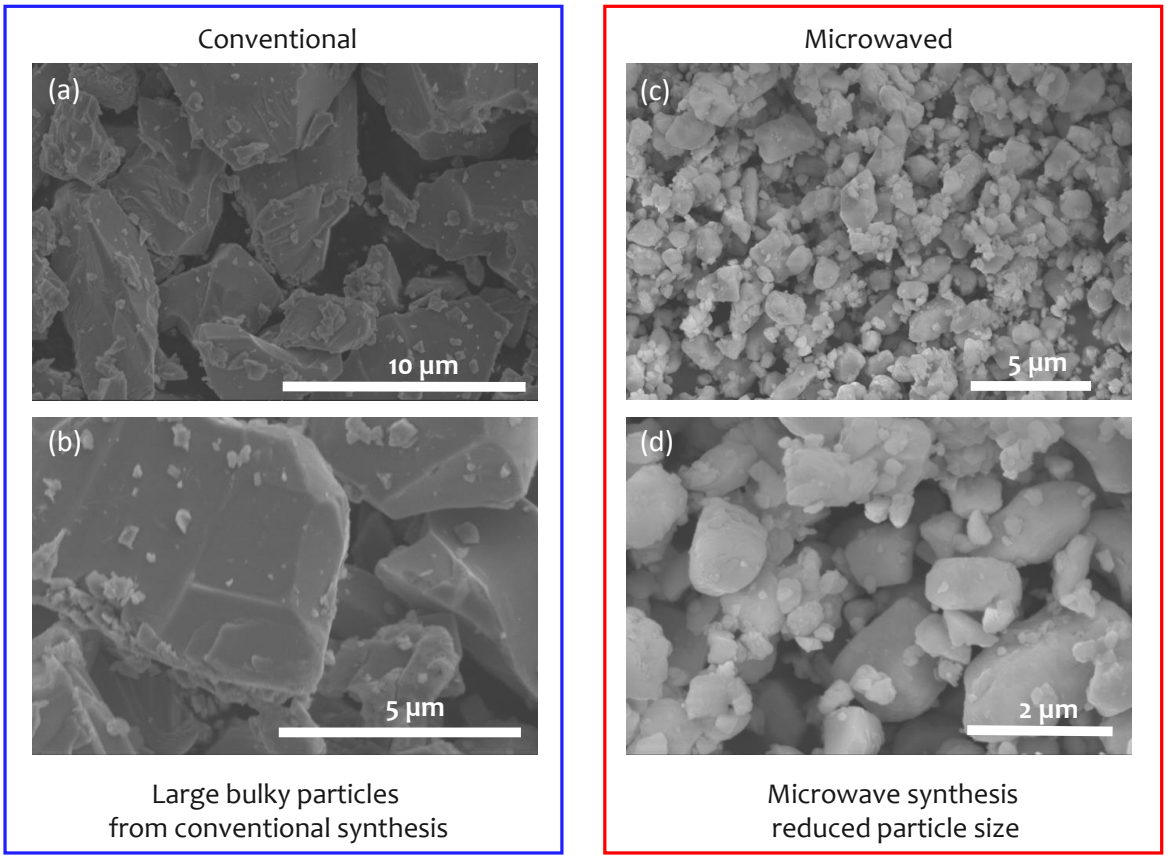

Figure B12: SEM images of the $TiNb_2O_7$ particles synthesized (a),(b) by the conventional solid state synthesis method, (c),(d) by the microwave synthesis method.

B.7 Potentiometric entropy measurement

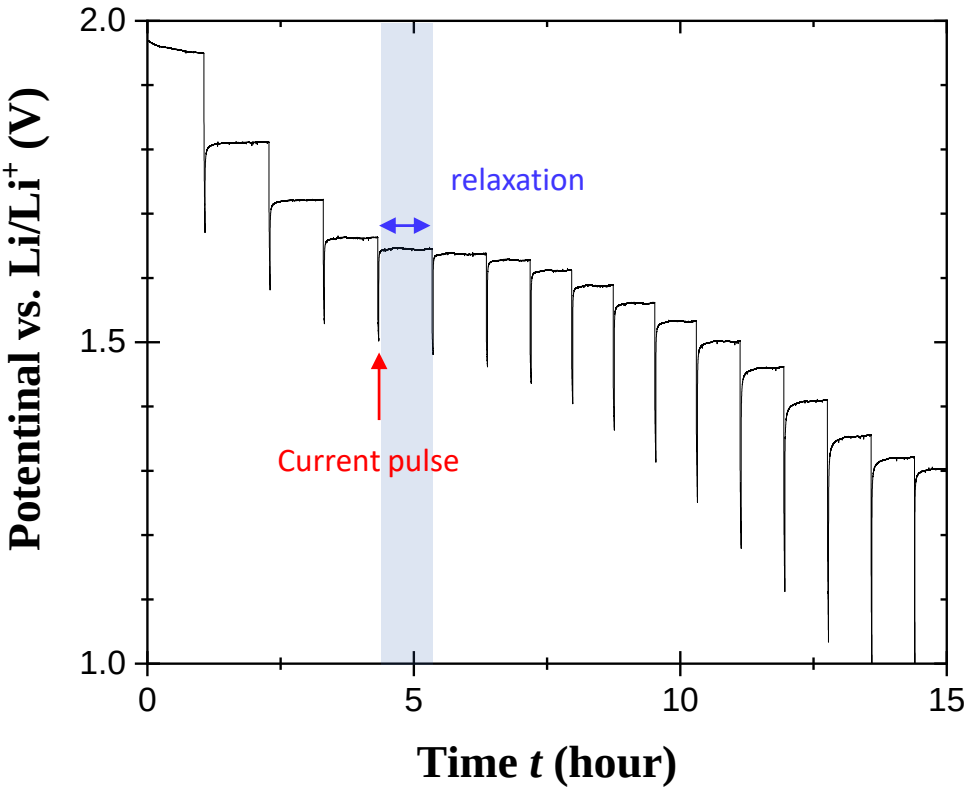

Figure B13: Measured voltage $V(x,t)$ during potentiometric entropy measurement as a function of time t at C-rate of 2C.

Figure B2 shows the measured voltage $V(x,t)$ as a function of time t during the potentiometric entropy measurement technique. In addition, Figure B3(a) shows enlarged $V(x,t)$ during the 4^{th} current pulse and the following relaxation period as a function of t highlighted in the Figure B2. Moreover, Figure B3(b) shows the enlarged potential curve circled in Figure B3(a) to clarify the voltage change upon step-like temperature change. The open circuit voltage $U_{ocv}(x,T)$ was measured to be the potential value right before the temperature change was imposed.

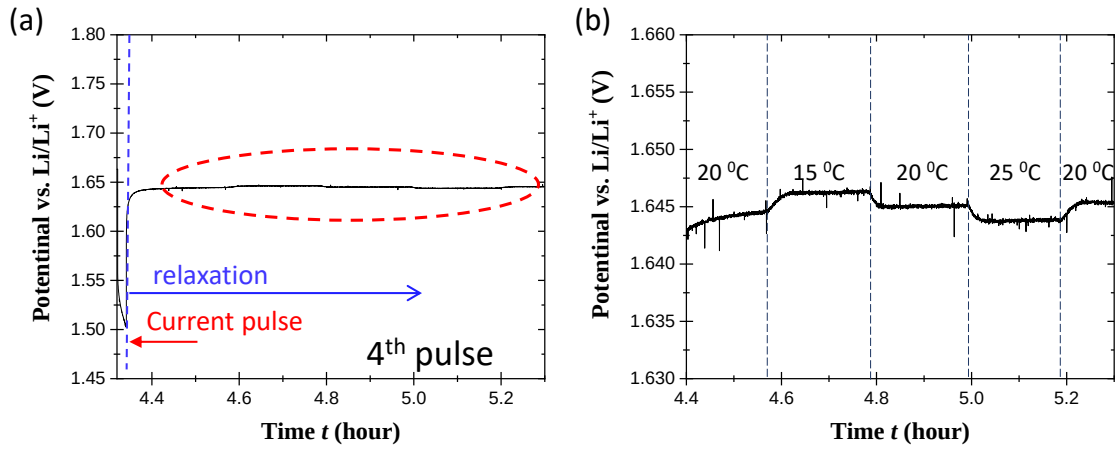

Figure B14: (a) Measured voltage $V(x,t)$ during 4^{th} current pule and relaxation period as a function of time t, and (b) the enlarged measured voltage $V(x,t)$ during relaxation time circled in Figure B5 (a).

Table B1 compares the measured $U_{ocv}(x,T)$ for different temperatures after the 4^{th} current pulse corresponding to $x = 0.71$. The midpoint numerical differentiation for three point was used to calculate $\partial U_{ocv}(x,T)/\partial T$ from the measured $U_{ocv}(x,T)$ values at three different temperatures.

Table B3: The measured $U_{ocv}(x,T)$ for three different temperature at $x = 0.71$.

Temperature (°C)	15	20	25
Measured U_{ocv} (V)	1.646	1.645	1.643

Appendix C

Supplementary materials for Chapter 4

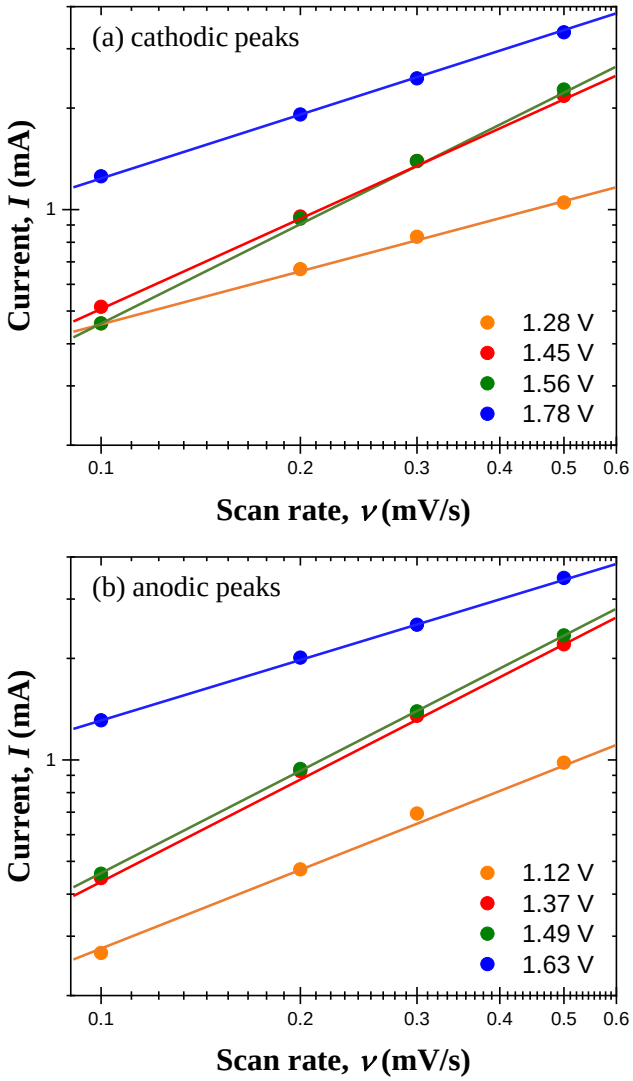

Figure C15: Measured peak current I_{peak} as a function of scan rate ν for the (a) cathodic peaks, and (b) for the anodic peaks.

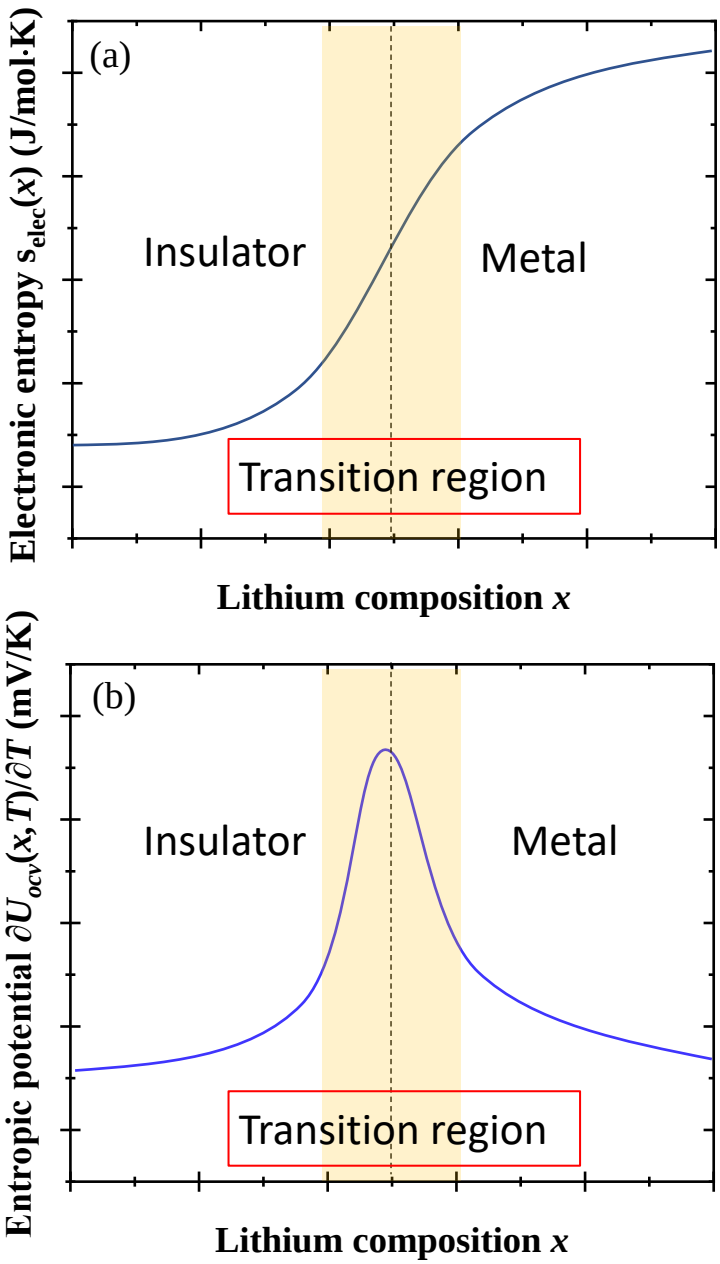

Figure C16: Schematic illustration of (a) electronic entropy $s^{elec}(x,T)$ and (b) Entropic potential $\partial U_{ocv}(x,T)/\partial T$ upon insulator to metal transition as functions of lithium composition x.

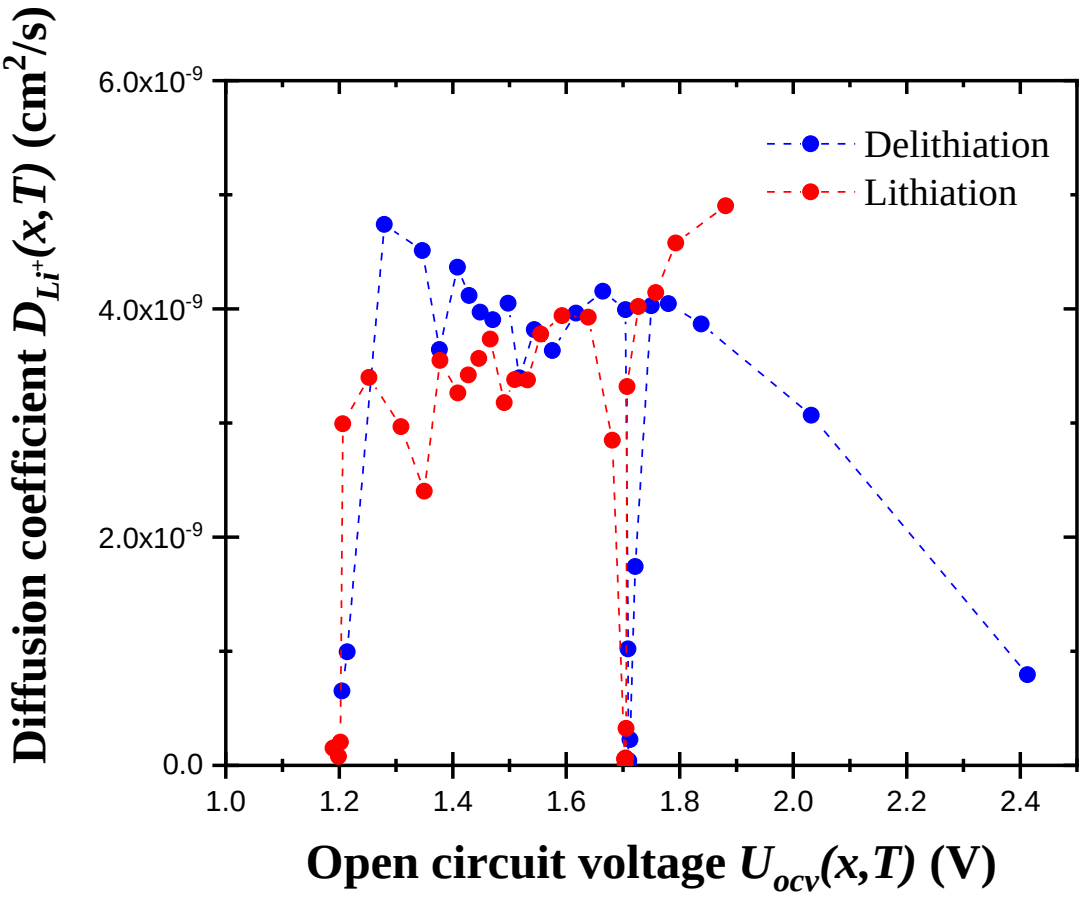

Figure C17: Apparent diffusion coefficient $D_{Li^+}(x,T)$ of lithium ion in PNb_9O_{25} as a function of open circuit voltage $U_{ocv}(x,T)$.

Appendix D

Supplementary materials for Chapter 5

D.8 b-value analysis

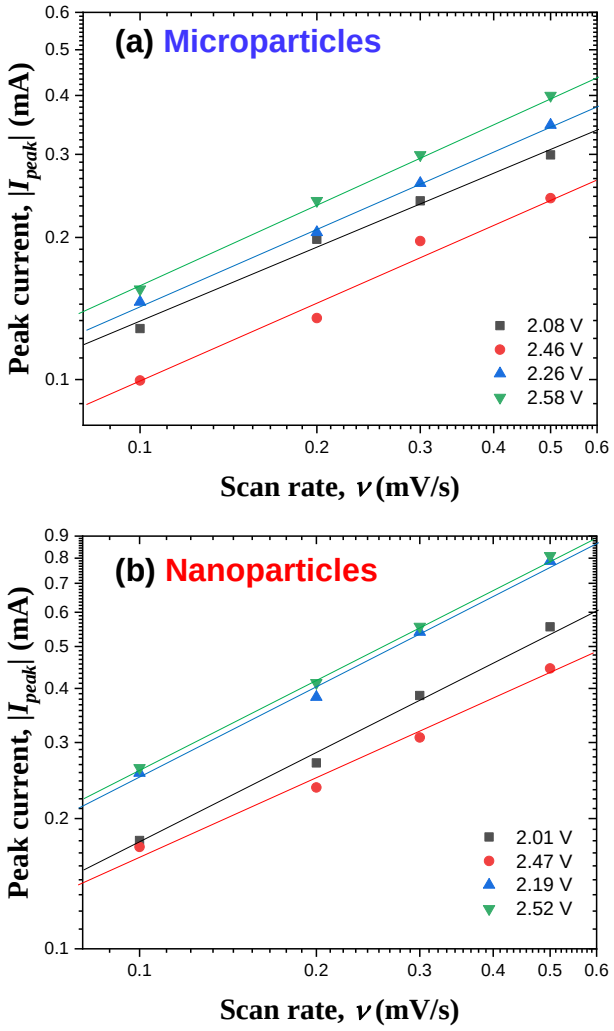

Figure D18: Measured peak current I_{peak} as a function of scan rate ν for the electrode consisting of a) *microparticles* and that consisting of b) *nanoparticles*.

D.9 Insulator to metal transition

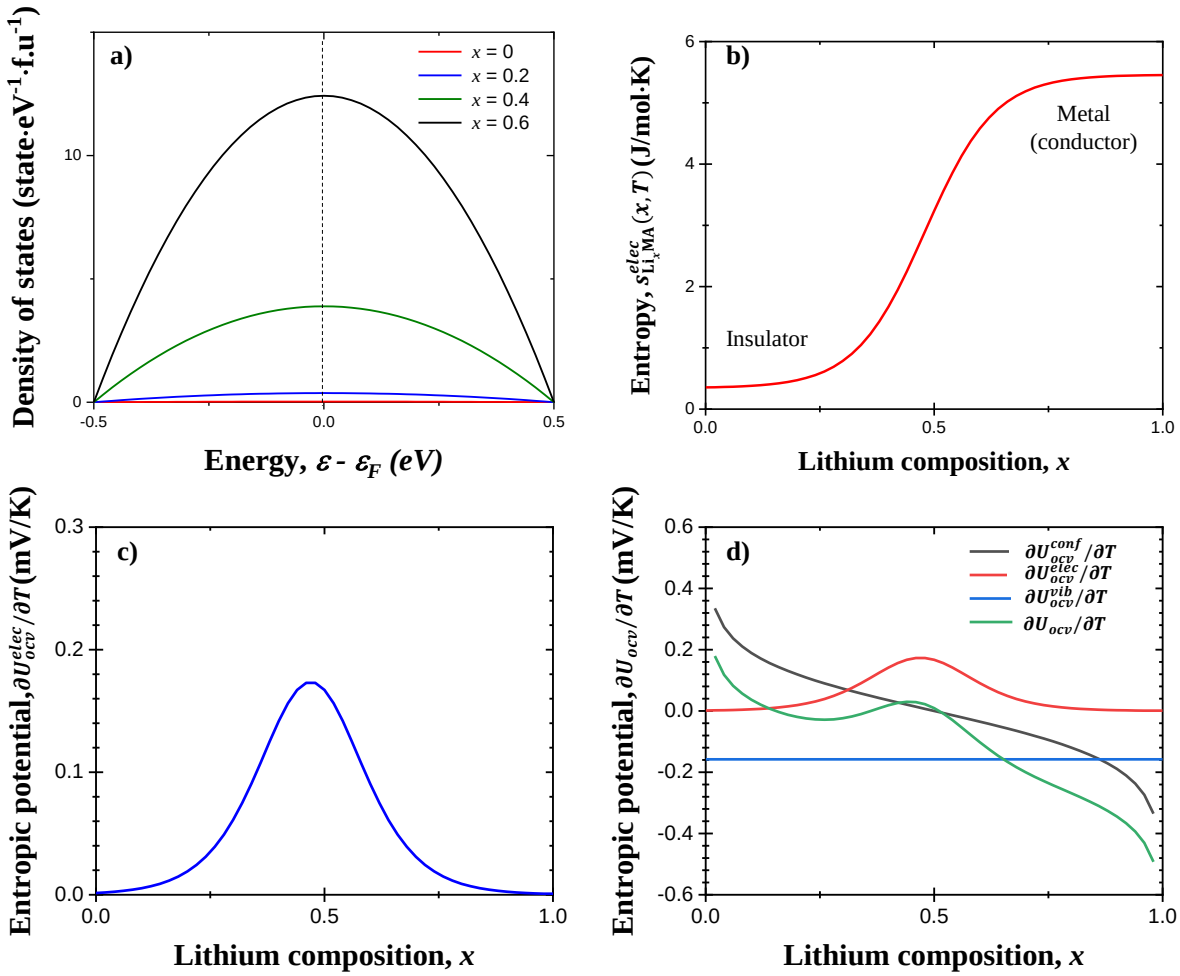

Figure D19: (a) Density of state $\mathcal{D}^{elec}_{\mathrm{Li}_x\mathrm{MA}}(\epsilon)$ of Li_xMA as functions of electric energy ϵ-ϵ_f for $x = 0$, 0.2, 0.4, and 0.6. b) Corresponding electronic entropy $s^{elec}_{\mathrm{Li}_x\mathrm{MA}}(x,T)$ of Li_xMA and c) electronic entropic potential $\partial U^{elec}_{ocv}(x,T)/\partial T$ as functions of lithium composition x. d) (b) Entropic potential associated with configurational $\partial U^{conf}_{ocv}(x,T)/\partial T$, vibrational $\partial U^{vib}_{ocv}(x,T)/\partial T$, and electronic $\partial U^{elec}_{ocv}(x,T)/\partial T$ excitations as well as the entropic potential of the battery, i.e., $\partial U_{ocv}(x,T)/\partial T = \partial U^{conf}_{ocv}(x,T)/\partial T + \partial U^{vib}_{ocv}(x,T)/\partial T + \partial U^{elec}_{ocv}(x,T)/\partial T$.

D.10 Instantaneous heat generation rate

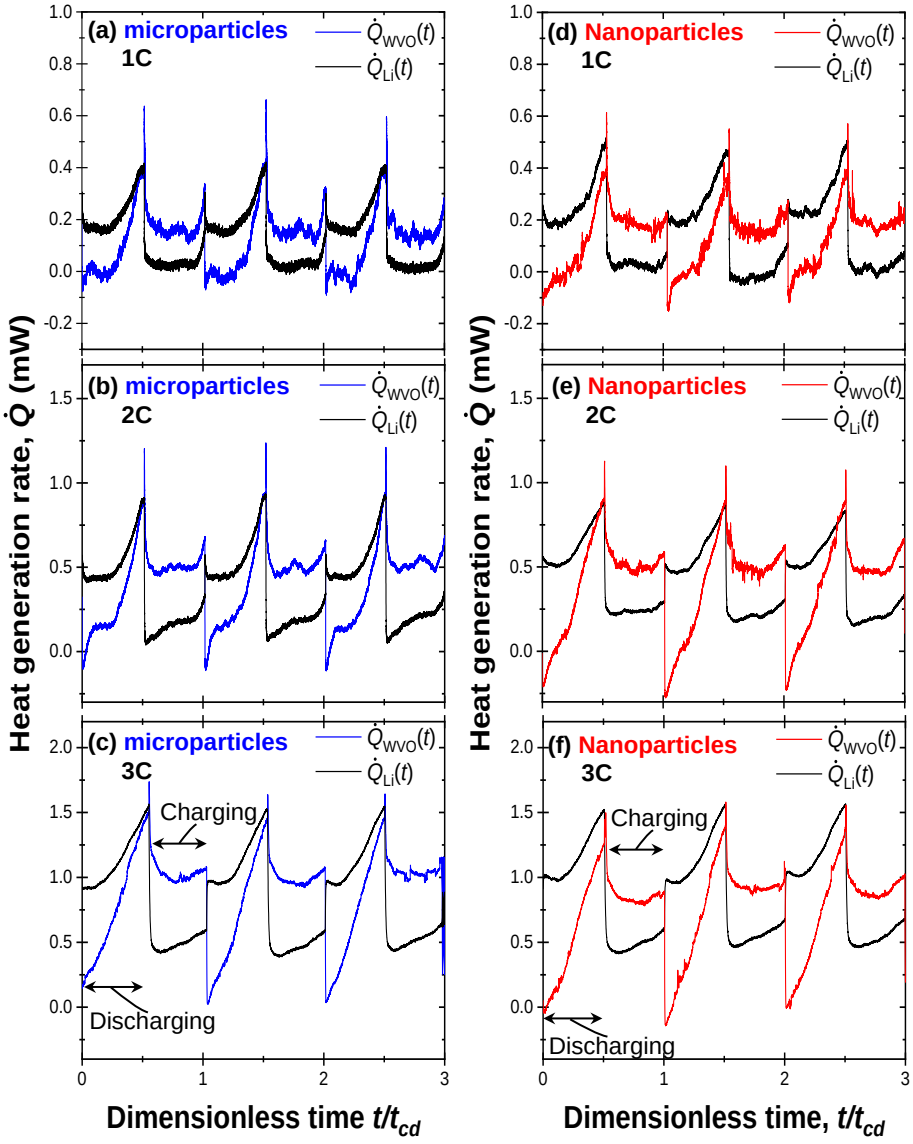

Figure D20: Measured instantaneous heat generation rates $\dot{Q}_{WVO}(t)$ at the $(W_{0.2}V_{0.8})_3O_7$-based electrodes and $\dot{Q}_{Li}(t)$ at the lithium metal electrode as functions of diemsionless time t/t_{cd} for 3 consecutive cycles with potential window ranging from 1.0 V to 3.0 V vs. Li/Li^+ at C-rates of (a,d) 1C, (b,e) 2C, and (c,f) 3C for $(W_{0.2}V_{0.8})_3O_7$ (a,b,c) *microparticles* and (d,e,f) *nanoparticles*.

D.11 Apparent diffusion coefficient

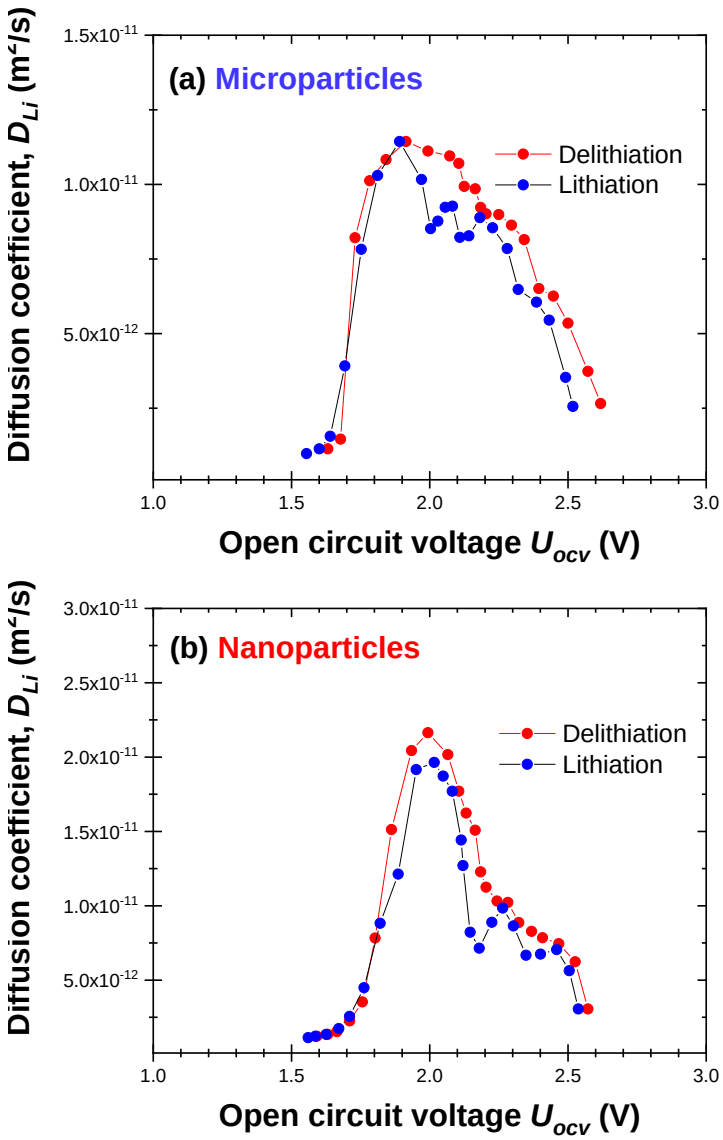

Figure D21: Apparent diffusion coefficient D_{Li^+} calculated from GITT for the electrode consisting of a) *microparticles* and that consisting of b) *nanoparticles*.

References

[1] W. Lu, I. Belharouak, J. Liu, and K. Amine, "Thermal properties of $Li_{4/3}Ti_{5/3}O_4/LiMn_2O_4$ cell", *Journal of Power Sources*, vol. 174, no. 2, pp. 673–677, 2007.

[2] J. Jiang, W. Shi, J. Zheng, P. Zuo, J. Xiao, X. Chen, W. Xu, and J.-G. Zhang, "Optimized operating range for large-format $LiFePO_4$/graphite batteries", *Journal of The Electrochemical Society*, vol. 161, no. 3, pp. A336–A341, 2013.

[3] J. A. Rogers, "Electronics for the human body", *JAMA Journal of American Medical Association*, vol. 313, no. 6, pp. 561–562, 2015.

[4] M. Walter, M. V. Kovalenko, and K. V. Kravchyk, "Challenges and benefits of post-lithium-ion batteries", *New Journal of Chemistry*, vol. 44, no. 5, pp. 1677–1683, 2020.

[5] H. Nishide and K. Oyaizu, "Toward flexible batteries", *Science*, vol. 319, no. 5864, pp. 737–738, 2008.

[6] H. Guo, M.-H Yeh, Y. Zi, Z. Wen, J. Chen, G. Liu, C. Hu, and Z.L. Wang, "Ultralight cut-paper-based self-charging power unit for self-powered portable electronic and medical systems", *ACS Nano*, vol. 11, no. 5, pp. 4475–4482, 2017.

[7] A. Meintz, J. Zhang, R. Vijayagopal, C. Kreutzer, S. Ahmed, I. Bloom, A. Burnham, R. B. Carlson, F. Dias, and E. J. Dufek, "Enabling fast charging–vehicle considerations", *Journal of Power Sources*, vol. 367, pp. 216–227, 2017.

[8] P. Cotti, "The discovery of the electric current", *Physica B: Condensed Matter*, vol. 204, no. 1-4, pp. 367–369, 1995.

[9] M. Piccolino, "The bicentennial of the voltaic battery (1800–2000): the artificial electric organ", *Trends in Neurosciences*, vol. 23, no. 4, pp. 147–151, 2000.

[10] A. C. Marschilok, Y. J. Kim, K. J. Takeuchi, and E. S. Takeuchi, "Silver vanadium phosphorous oxide, $Ag_{0.48}VOPO_4$: exploration as a cathode material in primary and secondary battery applications", *Journal of The Electrochemical Society*, vol. 159, no. 10, pp. A1690–A1695, 2012.

[11] X. Hu, W. Zhang, X. Liu, Y. Mei, and Y. Huang, "Nanostructured mo-based electrode materials for electrochemical energy storage", *Chemical Society Reviews*, vol. 44, no. 8, pp. 2376–2404, 2015.

[12] D. Linden and T. Reddy, "Handbook of batteries, mcgraw-hill companies inc", 2002.

[13] M. Selvam, S. R. Srither, K. Saminathan, and V. Rajendran, "Chemically and electrochemically prepared graphene/MnO_2 nanocomposite electrodes for zinc primary cells: a comparative study", *Ionics*, vol. 21, no. 3, pp. 791–799, 2015.

[14] T. Sakai, H. Ishikawa, K. Oguro, C. Iwakura, and H. Yoneyama, "Effects of microencapsulation of hydrogen storage alloy on the performances of sealed nickel/metal hydride batteries", *Journal of The Electrochemical Society*, vol. 134, no. 3, pp. 558–562, 1987.

[15] S. R. Ovshinsky, M. A. Fetcenko, and J. Ross, "A nickel metal hydride battery for electric vehicles", *Science*, vol. 260, no. 5105, pp. 176–181, 1993.

[16] E.-J. Yoo, J. Kim, E. Hosono, H.-S. Zhou, T. Kudo, and I. Honma, "Large reversible li storage of graphene nanosheet families for use in rechargeable lithium ion batteries", *Nano Letters*, vol. 8, no. 8, pp. 2277–2282, 2008.

[17] J.-M. Tarascon, N. Recham, M. Armand, J.-N. Chotard, P. Barpanda, W. Walker, and L. Dupont, "Hunting for better li-based electrode materials via low temperature inorganic synthesis", *Chemistry of Materials*, vol. 22, no. 3, pp. 724–739, 2010.

[18] M. D. Slater, D. Kim, E. Lee, and C. S. Johnson, "Sodium-ion batteries", *Advanced Functional Materials*, vol. 23, no. 8, pp. 947–958, 2013.

[19] L.-X. Yuan, Z.-H. Wang, W.-X. Zhang, X.-L. Hu, J.-T. Chen, Y.-H. Huang, and J. B. Goodenough, "Development and challenges of $LiFePO_4$ cathode material for lithium-ion batteries", *Energy & Environmental Science*, vol. 4, no. 2, pp. 269–284, 2011.

[20] Y. Wang and G. Cao, "Developments in nanostructured cathode materials for high-performance lithium-ion batteries", *Advanced materials*, vol. 20, no. 12, pp. 2251–2269, 2008.

[21] A. J. Bard and L. R. Faulkner, "Fundamentals and applications", *Electrochemical Methods*, vol. 2, no. 482, pp. 580–632, 2001.

[22] H. Panda, "Handbook on electroplating with manufacture of electrochemicals", 2017.

[23] M. S. Whittingham, "Electrical energy storage and intercalation chemistry", *Science*, vol. 192, no. 4244, pp. 1126–1127, 1976.

[24] K. Mizushima, P. C. Jones, P. J. Wiseman, and J. B. Goodenough, "Li_xCoO_2 (0<x<-1): A new cathode material for batteries of high energy density", *Materials Research Bulletin*, vol. 15, no. 6, pp. 783 – 789, 1980.

[25] M. Noel and R. Santhanam, "Electrochemistry of graphite intercalation compounds", *Journal of Power Sources*, vol. 72, no. 1, pp. 53–65, 1998.

[26] D. Allart, M. Montaru, and H. Gualous, "Model of lithium intercalation into graphite by potentiometric analysis with equilibrium and entropy change curves of graphite electrode", *Journal of The Electrochemical Society*, vol. 165, no. 2, pp. A380, 2018.

[27] H. Liu, W. Li, D. Shen, D. Zhao, and G. Wang, "Graphitic carbon conformal coating of mesoporous TiO_2 hollow spheres for high-performance lithium ion battery anodes", *Journal of the American Chemical Society*, vol. 137, no. 40, pp. 13161–13166, 2015.

[28] V. Aravindan, W. Chuiling, and S. Madhavi, "High power lithium-ion hybrid electrochemical capacitors using spinel $LiCrTiO_4$ as insertion electrode", *Journal of Materials Chemistry*, vol. 22, no. 31, pp. 16026–16031, 2012.

[29] K.-S. Park, A. Benayad, D.-J. Kang, and S.-G. Doo, "Nitridation-driven conductive $Li_4Ti_5O_{12}$ for lithium ion batteries", *Journal of the American Chemical Society*, vol. 130, no. 45, pp. 14930–14931, 2008.

[30] K. Amine, I. Belharouak, Z. Chen, T. Tran, H. Yumoto, N. Ota, S.-T. Myung, and Y.-K. Sun, "Nanostructured anode material for high-power battery system in electric vehicles", *Advanced Materials*, vol. 22, no. 28, pp. 3052–3057, 2010.

[31] B. Guo, X. Yu, X.-G. Sun, M. Chi, Z.-A. Qiao, J. Liu, Y.-S. Hu, X.-Q. Yang, J. B. Goodenough, and S. Dai, "A long-life lithium-ion battery with a highly porous $TiNb_2O_7$ anode for large-scale electrical energy storage", *Energy & Environmental Science*, vol. 7, no. 7, pp. 2220–2226, 2014.

[32] K. Ise, S. Morimoto, Y. Harada, and N. Takami, "Large lithium storage in highly crystalline $TiNb_2O_7$ nanoparticles synthesized by a hydrothermal method as anodes for lithium-ion batteries", *Solid State Ionics*, vol. 320, pp. 7–15, 2018.

[33] H.-Y. Wang, H.-N. He, Z. Nan, G.-H. Jin, and Y.-G. Tang, "Electrochemical behavior and cyclic fading mechanism of $LiNi_{0.5}Mn_{0.5}O_2$ electrode in $LiNO_3$ electrolyte", *Transactions of Nonferrous Metals Society of China*, vol. 24, no. 2, pp. 415–422, 2014.

[34] E. P. Roth and C. J. Orendorff, "How electrolytes influence battery safety", *Electrochemical Society Interface*, vol. 21, no. 2, pp. 45, 2012.

[35] C. Fasciani, S. Panero, J. Hassoun, and B. Scrosati, "Novel configuration of poly (vinylidenedifluoride)-based gel polymer electrolyte for application in lithium-ion batteries", *Journal of Power Sources*, vol. 294, pp. 180–186, 2015.

[36] S. Choudhury, "A highly reversible room-temperature lithium metal battery based on cross-linked hairy nanoparticles", in *Rational Design of Nanostructured Polymer Electrolytes and Solid–Liquid Interphases for Lithium Batteries*, pp. 35–57. Springer, 2019.

[37] Z. Zhang and S.S. Zhang, *Rechargeable Batteries*, Springer, New York, NY, USA, 2015.

[38] A. Van der Ven, J. Bhattacharya, and A. A. Belak, "Understanding li diffusion in li-intercalation compounds", *Accounts of chemical research*, vol. 46, no. 5, pp. 1216–1225, 2013.

[39] A. Van der Ven and M. Wagemaker, "Effect of surface energies and nano-particle size distribution on open circuit voltage of Li-electrodes", *Electrochemistry communications*, vol. 11, no. 4, pp. 881–884, 2009.

[40] M. J. Moran, M. B. Bailey, D. D. Boettner, and H. N. Shapiro, *Fundamentals of engineering thermodynamics*, Wiley, 2018.

[41] M. W. Chase Jr, "NIST-JANAF thermochemical tables", *J. Phys. Chem. Ref. Data, Monograph*, vol. 9, 1998.

[42] B. P. Kai, *Modern Battery Engineering: A Comprehensive Introduction*, World Scientific, 2019.

[43] K. Ventura, M. B. Smith, J. R. Prat, L. E. Echegoyen, and D. Villagran, "Introducing students to inner sphere electron transfer concepts through electrochemistry studies in diferrocene mixed-valence systems", *Journal of Chemical Education*, vol. 94, no. 4, pp. 526–529, 2017.

[44] N. Elgrishi, K. J. Rountree, B. D. McCarthy, E. S. Rountree, T. T. Eisenhart, and J. L. Dempsey, "A practical beginner's guide to cyclic voltammetry", *Journal of Chemical Education*, vol. 95, no. 2, pp. 197–206, 2018.

[45] E. Deiss, "Spurious chemical diffusion coefficients of Li^+ in electrode materials evaluated with gitt", *Electrochimica Acta*, vol. 50, no. 14, pp. 2927–2932, 2005.

[46] D. W. Dees, S. Kawauchi, D. P Abraham, and J. Prakash, "Analysis of the galvanostatic intermittent titration technique (GITT) as applied to a lithium-ion porous electrode", *Journal of Power Sources*, vol. 189, no. 1, pp. 263–268, 2009.

[47] G. Liu, M. Ouyang, L. Lu, J. Li, and X. Han, "Analysis of the heat generation of lithium-ion battery during charging and discharging considering different influencing factors", *Journal of Thermal Analysis and Calorimetry*, vol. 116, no. 2, pp. 1001–1010, 2014.

[48] G. Assat, S. L. Glazier, C. Delacourt, and J.-M. Tarascon, "Probing the thermal effects of voltage hysteresis in anionic redox-based lithium-rich cathodes using isothermal calorimetry", *Nature Energy*, vol. 4, no. 8, pp. 647–656, 2019.

[49] J. Newman, K. E. Thomas, H. Hafezi, and D. R. Wheeler, "Modeling of lithium-ion batteries", *Journal of power sources*, vol. 119, pp. 838–843, 2003.

[50] S.W. Baek, K.E. Wyckoff, D.M. Butts, J. Bienz, A. Likitchatchawankun, M.B. Preefer, M. Frajnkovič, B.S. Dunn, R. Seshadri, and L. Pilon, "*Operando* calorimetry informs the origin of rapid rate performance in microwave-prepared $TiNb_2O_7$ electrodes", *Journal of Power Sources*, vol. 490, 2021.

[51] K. E. Thomas and J. Newman, "Thermal modeling of porous insertion electrodes", *Journal of The Electrochemical Society*, vol. 150, no. 2, pp. A176, 2003.

[52] W Lu and J Prakash, "*In situ* measurements of heat generation in a Li/mesocarbon microbead half-cell", *Journal of the Electrochemical Society*, vol. 150, no. 3, pp. A262, 2003.

[53] K. E. Thomas and J. Newman, "Heats of mixing and of entropy in porous insertion electrodes", *Journal of Power Sources*, vol. 119, pp. 844–849, 2003.

[54] Kandler Smith and Chao-Yang Wang, "Power and thermal characterization of a lithium-ion battery pack for hybrid-electric vehicles", *Journal of power sources*, vol. 160, no. 1, pp. 662–673, 2006.

[55] Sun Woong Baek, Molleigh B Preefer, Muna Saber, Kuan Zhai, Matevž Frajnkovič, Yucheng Zhou, Bruce S Dunn, Anton Van der Ven, Ram Seshadri, and Laurent Pilon, "Potentiometric entropy and *operando* calorimetric measurements reveal fast charging mechanisms in PNb_9O_{25}", *Journal of Power Sources*, vol. 520, pp. 230776, 2022.

[56] Yucheng Zhou, Etienne Le Calvez, Sun Woong Baek, Matevž Frajnkovič, Camille Douard, Eric Gautron, Olivier Crosnier, Thierry Brousse, and Laurent Pilon, "Effect of particle size on thermodynamics and lithium ion transport in electrodes made of ti2nb2o9 microparticles or nanoparticles", 2022.

[57] A.H. Thompson, "Thermodynamics of Li intercalation batteries: Entropy measurements on Li_xTiS_2", *Physica B + C*, vol. 105, no. 1-3, pp. 461–465, 1981.

[58] M.P. Mercer, S. Finnigan, D. Kramer, D. Richards, and H.E. Hoster, "The influence of point defects on the entropy profiles of lithium ion battery cathodes: a lattice-gas Monte Carlo study", *Electrochimica Acta*, vol. 241, pp. 141–152, 2017.

[59] N. S. Hudak, L. E. Davis, and G. Nagasubramanian, "Cycling-induced changes in the entropy profiles of lithium cobalt oxide electrodes", *Journal of the Electrochemical Society*, vol. 162, no. 3, pp. A315, 2014.

[60] X.-F. Zhang, Y. Zhao, Y. Patel, T. Zhang, W.-M. Liu, M. Chen, G. J. Offer, and Y. Yan, "Potentiometric measurement of entropy change for lithium batteries", *Physical Chemistry Chemical Physics*, vol. 19, no. 15, pp. 9833–9842, 2017.

[61] J.P. Schmidt, A. Weber, and E. Ivers-Tiffée, "A novel and precise measuring method for the entropy of lithium-ion cells: δS via electrothermal impedance spectroscopy", *Electrochimica Acta*, vol. 137, pp. 311–319, 2014.

[62] K. Jalkanen, T. Aho, and K. Vuorilehto, "Entropy change effects on the thermal behavior of a $LiFePO_4$/graphite lithium-ion cell at different states of charge", *Journal of Power Sources*, vol. 243, pp. 354–360, 2013.

[63] S. Wang, "Entropy and heat generation of lithium cells/batteries", *Chinese Physics B*, vol. 25, no. 1, 2015.

[64] G. Ceder, "A derivation of the ising model for the computation of phase diagrams", *Computational Materials Science*, vol. 1, no. 2, pp. 144–150, 1993.

[65] A. Van der Ven, J. C. Thomas, B. Puchala, and A. R. Natarajan, "First-principles statistical mechanics of multicomponent crystals", *Annual Review of Materials Research*, vol. 48, pp. 27–55, 2018.

[66] A. Van der Ven, Z. Deng, S. Banerjee, and S. P. Ong, "Rechargeable alkali-ion battery materials: theory and computation", *Chemical Reviews*, vol. 120, no. 14, pp. 6977–7019, 2020.

[67] A. Van De Walle and G. Ceder, "The effect of lattice vibrations on substitutional alloy thermodynamics", *Reviews of Modern Physics*, vol. 74, no. 1, pp. 11–45, 2002.

[68] Ampol Likitchatchawankun, Grace Whang, Jonathan Lau, Obaidallah Munteshari, Bruce S Dunn, and Laurent Pilon, "Effect of temperature on irreversible and reversible heat generation rates in ionic liquid-based electric double layer capacitors", *Electrochimica Acta*, vol. 338, pp. 135802, 2020.

[69] Obaidallah Munteshari, Arie Borenstein, Ryan H DeBlock, Jonathan Lau, Grace Whang, Yucheng Zhou, Ampol Likitchatchawankun, Richard B Kaner, Bruce S Dunn, and Laurent Pilon, "In operando calorimetric measurements for activated carbon electrodes in ionic liquid electrolytes under large potential windows", *ChemSusChem*, vol. 13, no. 5, pp. 1013–1026, 2020.

[70] Ampol Likitchatchawankun, Arpan Kundu, Obaidallah Munteshari, Timothy S Fisher, and Laurent Pilon, "Heat generation in all-solid-state supercapacitors with graphene electrodes and gel electrolytes", *Electrochimica Acta*, vol. 303, pp. 341–353, 2019.

[71] Obaidallah Munteshari, Jonathan Lau, Ampol Likitchatchawankun, Bing-Ang Mei, Christopher S Choi, Danielle Butts, Bruce S Dunn, and Laurent Pilon, "Thermal signature of ion intercalation and surface redox reactions mechanisms in model pseudocapacitive electrodes", *Electrochimica Acta*, vol. 307, pp. 512–524, 2019.

[72] Ampol Likitchatchawankun, Ryan H DeBlock, Grace Whang, Obaidallah Munteshari, Matevž Frajnkovič, Bruce S Dunn, and Laurent Pilon, "Heat generation in electric double layer capacitors with neat and diluted ionic liquid electrolytes under large potential window between 5 and 80 °C", *Journal of Power Sources*, vol. 488, pp. 229368, 2021.

[73] Obaidallah Munteshari, Jonathan Lau, David S Ashby, Bruce S Dunn, and Laurent Pilon, "Effects of constituent materials on heat generation in individual EDLC electrodes", *Journal of The Electrochemical Society*, vol. 165, no. 7, pp. A1547, 2018.

[74] S. Ma, M. Jiang, P. Tao, C. Song, J. Wu, J. Wang, T. Deng, and W. Shang, "Temperature effect and thermal impact in lithium-ion batteries: A review", *Progress in Natural Science: Materials International*, vol. 28, no. 6, pp. 653–666, 2018.

[75] F. Leng, C. M. Tan, and M. Pecht, "Effect of temperature on the aging rate of li ion battery operating above room temperature", *Scientific Reports*, vol. 5, pp. 12967, 2015.

[76] J.R. Dahn and R.R. Haering, "Entropy measurements on Li_xTiS_2", *Canadian Journal of Physics*, vol. 61, no. 7, pp. 1093–1098, 1983.

[77] J.N. Reimers and J.R. Dahn, "Electrochemical and in situ X-ray diffraction studies of lithium intercalation in Li_xCoO_2", *Journal of the Electrochemical Society*, vol. 139, no. 8, pp. 2091–2097, 1992.

[78] T. Ohzuku and A. Ueda, "Solid-state redox reactions of $LiCoO_2$ (R3m) for 4 Volt secondary lithium cells", *Journal of The Electrochemical Society*, vol. 141, no. 11, pp. 2972–2977, 1994.

[79] J.C. Wang, "Model for lithium intercalation into TiS_2", *Solid State Ionics*, vol. 40, pp. 548–552, 1990.

[80] M.S. Whittingham, "Ultimate limits to intercalation reactions for lithium batteries", *Chemical Reviews*, vol. 114, no. 23, pp. 11414–11443, 2014.

[81] Y. Reynier, J. Graetz, T. Swan-Wood, P. Rez, R. Yazami, and B. Fultz, "Entropy of li intercalation in Li_xCoO_2", *Physical Review B*, vol. 70, no. 17, pp. 174304, 2004.

[82] A.R. Natarajan, J.C. Thomas, B. Puchala, and A. Van der Ven, "Symmetry-adapted order parameters and free energies for solids undergoing order-disorder phase transitions", *Physical Review B*, vol. 96, no. 13, pp. 134204, 2017.

[83] D.C. Wallace, *Thermodynamics of Crystals*, Dover, Mineola, NY, USA, 1998.

[84] A. Van der Ven, M.K. Aydinol, G. Ceder, G. Kresse, and J. Hafner, "First-principles investigation of phase stability in Li_xCoO_2", *Physical Review B*, vol. 58, no. 6, pp. 2975, 1998.

[85] J. L. Kaufman, J. Vinckevičiūtė, S.K. Kolli, J.G. Goiri, and A. Van der Ven, "Understanding intercalation compounds for sodium-ion batteries and beyond", *Philosophical Transactions of the Royal Society A*, vol. 377, no. 2152, pp. 20190020, 2019.

[86] S. Pal, "Phonon dispersion in lithium", *Physical Review B*, vol. 2, no. 12, pp. 4741–4742, 1970.

[87] M.-H. Chen, B. Puchala, and A. Van der Ven, "High-temperature stability of δ'-ZrO", *Calphad*, vol. 51, pp. 292–298, 2015.

[88] R. K. Rhein, P. C. Dodge, M.-H. Chen, M. S. Titus, T. M. Pollock, and A. Van der Ven, "Role of vibrational and configurational excitations in stabilizing the $L1_2$ structure in Co-rich Co-Al-W alloys", *Physical Review B*, vol. 92, no. 17, pp. 174117, 2015.

[89] F. Zhou, T. Maxisch, and G. Ceder, "Configurational electronic entropy and the phase diagram of mixed-valence oxides: the case of Li_xFePO_4", *Physical Review Letters*, vol. 97, no. 15, 2006.

[90] E. Decolvenaere, E. Levin, R. Seshadri, and A. Van der Ven, "Modeling magnetic evolution and exchange hardening in disordered magnets: The example of $Mn_{1-x}Fe_xRu_2Sn$ Heusler alloys", *Physical Review Materials*, vol. 3, no. 10, 2019.

[91] D. A. Kitchaev, E. C. Schueller, and A. Van der Ven, "Mapping skyrmion stability in uniaxial lacunar spinel magnets from first principles", *Physical Review B*, vol. 101, no. 5, 2020.

[92] J. L. Zuo, D. Kitchaev, E. C. Schueller, J. D. Bocarsly, R. Seshadri, A. Van der Ven, and S. D. Wilson, "Magnetoentropic mapping and computational modeling of cycloids and skyrmions in the lacunar spinels GaV_4S_8 and GaV_4Se_8", *Physical Review Materials*, vol. 5, no. 5, 2021.

[93] Edward A Stern, "Rigid-band model of alloys", *Physical Review*, vol. 157, no. 3, pp. 544–551, 1967.

[94] J. L. Kaufman and A. Van der Ven, "Na_xCoO_2 phase stability and hierarchical orderings in the O3/P3 structure family", *Physical Review Materials*, vol. 3, no. 1, pp. 015402, 2019.

[95] A. Van der Ven, J. C. Thomas, Q. Xu, B. Swoboda, and D. Morgan, "Nondilute diffusion from first principles: Li diffusion in Li_xTiS_2", *Physical Review B*, vol. 78, no. 10, 2008.

[96] M.S. Whittingham, "Lithium batteries and cathode materials", *Chemical Reviews*, vol. 104, no. 10, pp. 4271–4302, 2004.

[97] M.G. Verde, L. Baggetto, N. Balke, G.M. Veith, J.K. Seo, Z. Wang, and Y.S. Meng, "Elucidating the phase transformation of $Li_4Ti_5O_{12}$ lithiation at the nanoscale", *ACS Nano*, vol. 10, no. 4, pp. 4312–4321, 2016.

[98] M. Kitta, T. Akita, S. Tanaka, and M. Kohyama, "Characterization of two phase distribution in electrochemically-lithiated spinel $Li_4Ti_5O_{12}$ secondary particles by electron energy-loss spectroscopy", *Journal of Power Sources*, vol. 237, pp. 26–32, 2013.

[99] L. Laffont, C. Delacourt, P. Gibot, M.Y. Wu, P. Kooyman, C. Masquelier, and J.M. Tarascon, "Study of the $LiFePO_4/FePO_4$ two-phase system by high-resolution electron energy loss spectroscopy", *Chemistry of Materials*, vol. 18, no. 23, pp. 5520–5529, 2006.

[100] R. Dedryvere, M. Maccario, L. Croguennec, F. Le Cras, C. Delmas, and D. Gonbeau, "X-ray photoelectron spectroscopy investigations of carbon-coated Li_xFePO_4 materials", *Chemistry of Materials*, vol. 20, no. 22, pp. 7164–7170, 2008.

[101] L. Castro, R. Dedryvere, M. El Khalifi, P.-E. Lippens, J. Bréger, C. Tessier, and D. Gonbeau, "The spin-polarized electronic structure of $LiFePO_4$ and $FePO_4$ evidenced by in-lab XPS", *The Journal of Physical Chemistry C*, vol. 114, no. 41, pp. 17995–18000, 2010.

[102] M. D. Levi, E. A. Levi, and D. Aurbach, "The mechanism of lithium intercalation in graphite film electrodes in aprotic media. part 2. potentiostatic intermittent titration and in situ XRD studies of the solid-state ionic diffusion", *Journal of Electroanalytical Chemistry*, vol. 421, no. 1-2, pp. 89–97, 1997.

[103] J. Park, S. S. Park, and Y. S. Won, "In situ XRD study of the structural changes of graphite anodes mixed with SiO_x during lithium insertion and extraction in lithium ion batteries", *Electrochimica Acta*, vol. 107, pp. 467–472, 2013.

[104] Emily E Levin, Jason H Grebenkemper, Tresa M Pollock, and Ram Seshadri, "Protocols for high temperature assisted-microwave preparation of inorganic compounds", *Chemistry of Materials*, vol. 31, no. 18, pp. 7151–7159, 2019.

[105] A. A. Coelho, "TOPAS and TOPAS-academic: an optimization program integrating computer algebra and crystallographic objects written in C^{++}", *Journal of Applied Crystallography*, vol. 51, no. 1, pp. 210–218, 2018.

[106] K. Momma and F. Izumi, "VESTA 3 for three-dimensional visualization of crystal, volumetric and morphology data", *Journal of Applied Crystallography*, vol. 44, no. 6, pp. 1272–1276, 2011.

[107] V. V. Viswanathan, D. Choi, D. Wang, W. Xu, S. Towne, R. E. Williford, J.-G. Zhang, J. Liu, and Z. Yang, "Effect of entropy change of lithium intercalation in cathodes and anodes on Li^+ion battery thermal management", *Journal of Power Sources*, vol. 195, no. 11, pp. 3720–3729, 2010.

[108] S. Schlueter, R. Genieser, D. Richards, H. E. Hoster, and M. P. Mercer, "Quantifying structure dependent responses in Li-ion cells with excess li spinel cathodes: matching voltage and entropy profiles through mean field models", *Physical Chemistry Chemical Physics*, vol. 20, no. 33, pp. 21417–21429, 2018.

[109] O. Munteshari, J. Lau, A. Krishnan, B. Dunn, and L. Pilon, "Isothermal calorimeter for measurements of time-dependent heat generation rate in individual supercapacitor electrodes", *Journal of Power Sources*, vol. 374, pp. 257–268, 2018.

[110] X. Lu, Z. Jian, Z. Fang, L. Gu, Y.-S. Hu, W. Chen, Z. Wang, and L. Chen, "Atomic-scale investigation on lithium storage mechanism in $TiNb_2O_7$", *Energy & Environmental Science*, vol. 4, no. 8, pp. 2638–2644, 2011.

[111] K. J. Griffith, I. D. Seymour, M. A. Hope, M. M. Butala, L. K. Lamontagne, M. B. Preefer, C. P. Kocer, G. Henkelman, A. J. Morris, and M. J. Cliffe, "Ionic and electronic conduction in $TiNb_2O_7$", *Journal of the American Chemical Society*, vol. 141, no. 42, pp. 16706–16725, 2019.

[112] J.-T. Han, Y.-H. Huang, and J. B. Goodenough, "New anode framework for rechargeable lithium batteries", *Chemistry of Materials*, vol. 23, no. 8, pp. 2027–2029, 2011.

[113] H. Li, L. Shen, G. Pang, S. Fang, H. Luo, K. Yang, and X. Zhang, "$TiNb_2O_7$ nanoparticles assembled into hierarchical microspheres as high-rate capability and long-cycle-life anode materials for lithium ion batteries", *Nanoscale*, vol. 7, no. 2, pp. 619–624, 2015.

[114] X. Wang and G. Shen, "Intercalation pseudo-capacitive $TiNb_2O_7$@ carbon electrode for high-performance lithium ion hybrid electrochemical supercapacitors with ultrahigh energy density", *Nano Energy*, vol. 15, pp. 104–115, 2015.

[115] H.-T. Kwon, J.-H. Kim, K.-J. Jeon, and C.-M. Park, "Co_xP compounds: electrochemical conversion/partial recombination reaction and partially disproportionated nanocomposite for li-ion battery anodes", *RSC Advances*, vol. 4, no. 81, pp. 43227–43234, 2014.

[116] N. Takami, K. Ise, Y. Harada, T. Iwasaki, T. Kishi, and K. Hoshina, "High-energy, fast-charging, long-life lithium-ion batteries using $TiNb_2O_7$ anodes for automotive applications", *Journal of Power Sources*, vol. 396, pp. 429–436, 2018.

[117] H. Yu, H. Lan, L. Yan, S. Qian, X. Cheng, H. Zhu, N. Long, M. Shui, and J. Shu, "$TiNb_2O_7$ hollow nanofiber anode with superior electrochemical performance in rechargeable lithium ion batteries", *Nano Energy*, vol. 38, pp. 109–117, 2017.

[118] J. Dahn and R. R. Haering, "Lithium intercalation in TiS_2", *Materials Research Bulletin*, vol. 14, no. 10, pp. 1259–1262, 1979.

[119] W. Xing, L.-E. Kalland, Z. Li, and R. Haugsrud, "Defects and transport properties in $TiNb_2O_7$", *Journal of the American Ceramic Society*, vol. 96, no. 12, pp. 3775–3781, 2013.

[120] W. Weppner and R. A. Huggins, "Determination of the kinetic parameters of mixed-conducting electrodes and application to the system Li_3Sb", *Journal of The Electrochemical Society*, vol. 124, no. 10, pp. 1569, 1977.

[121] R. Inada, R. Kumasaka, S. Inabe, T. Tojo, and Y. Sakurai, "Li^+ insertion/extraction properties for $TiNb_2O_7$ single particle characterized by a particle-current collector integrated microelectrode", *Journal of The Electrochemical Society*, vol. 166, no. 3, pp. A5157, 2018.

[122] M. Ecker, J. B. Gerschler, J. Vogel, S. Käbitz, F. Hust, P. Dechent, and D. U. Sauer, "Development of a lifetime prediction model for lithium-ion batteries based on extended accelerated aging test data", *Journal of Power Sources*, vol. 215, pp. 248–257, 2012.

[123] D. Andre, M. Meiler, K. Steiner, C. Wimmer, T. Soczka-Guth, and D. U. Sauer, "Characterization of high-power lithium-ion batteries by electrochemical impedance spectroscopy. I. experimental investigation", *Journal of Power Sources*, vol. 196, no. 12, pp. 5334–5341, 2011.

[124] B. Babu and M. M. Shaijumon, "Studies on kinetics and diffusion characteristics of lithium ions in $TiNb_2O_7$", *Electrochimica Acta*, p. 136208, 2020.

[125] Sebastien Patoux, Mickael Dolle, Gwenaëlle Rousse, and Christian Masquelier, "A reversible lithium intercalation process in an ReO_3 type structure PNb_9O_{25}", *Journal of the Electrochemical Society*, vol. 149, no. 4, pp. A391–A400, 2002.

[126] Haoxiang Yu, Jundong Zhang, Runtian Zheng, Tingting Liu, Na Peng, Yu Yuan, Yufei Liu, Jie Shu, and Zhen-Bo Wang, "The journey of lithium ions in the lattice of PNb_9O_{25}", *Materials Chemistry Frontiers*, vol. 4, no. 2, pp. 631–637, 2020.

[127] Haoxiang Yu, Jundong Zhang, Maoting Xia, Chenchen Deng, Xikun Zhang, Runtian Zheng, Shi Chen, Jie Shu, and Zhen-Bo Wang, "PNb_9O_{25} nanofiber as a high-voltage anode material for advanced lithium ions batteries", *Journal of Materiomics*, vol. 6, no. 4, pp. 781–787, 2020.

[128] T. Kim, W. Choi, H.-C. Shin, J.-Y. Choi, J.M. Kim, M.-S. Park, and W.-S. Yoon, "Applications of voltammetry in lithium ion battery research", *Journal of Electrochemical Science and Technology*, vol. 11, no. 1, pp. 14–25, 2020.

[129] Molleigh B. Preefer, Muna Saber, Qiulong Wei, Nicholas H. Bashian, Joshua D. Bocarsly, William Zhang, Glenn Lee, JoAnna Milam-Guerrero, Erica S. Howard, Rebecca C. Vincent, Brent C. Melot, Anton Van der Ven, Ram Seshadri, and Bruce S. Dunn, "Multielectron redox and insulator-to-metal transition upon lithium insertion in the fast-charging, Wadsley-Roth phase PNb_9O_{25}", *Chemistry of Materials*, vol. 32, no. 11, pp. 4553–4563, 2020.

[130] M. Otero, A. Sigal, E.M. Perassi, D. Barraco, and E.P.M. Leiva, "Statistical mechanical modeling of the transition stage II→ stage I of Li-ion storage in graphite. A priori vs induced heterogeneity", *Electrochimica Acta*, vol. 245, pp. 569–574, 2017.

[131] Christopher L Berhaut, Daniel Lemordant, Patrice Porion, Laure Timperman, Grégory Schmidt, and Mériem Anouti, "Ionic association analysis of LiTDI, LiFSI and $LiPF_6$ in EC/DMC for better Li-ion battery performances", *RSC advances*, vol. 9, no. 8, pp. 4599–4608, 2019.

[132] Umamaheswari Janakiraman, Taylor R Garrick, and Mary E Fortier, "Lithium plating detection methods in Li-ion batteries", *Journal of the Electrochemical Society*, vol. 167, no. 16, pp. 160552, 2020.

[133] Feng Hao, Ankit Verma, and Partha P Mukherjee, "Mechanistic insight into dendrite–SEI interactions for lithium metal electrodes", *Journal of Materials Chemistry A*, vol. 6, no. 40, pp. 19664–19671, 2018.

[134] Mehdi Shakourian-Fard, Ganesh Kamath, and Subramanian KRS Sankaranarayanan, "Evaluating the free energies of solvation and electronic structures of lithium-ion battery electrolytes", *ChemPhysChem*, vol. 17, no. 18, pp. 2916–2930, 2016.

[135] Wei Cui, Yves Lansac, Hochun Lee, Seung-Tae Hong, and Yun Hee Jang, "Lithium ion solvation by ethylene carbonates in lithium-ion battery electrolytes, revisited by density functional theory with the hybrid solvation model and free energy correction in solution", *Physical Chemistry Chemical Physics*, vol. 18, no. 34, pp. 23607–23612, 2016.

[136] Oleg Borodin, Marco Olguin, P Ganesh, Paul RC Kent, Joshua L Allen, and Wesley A Henderson, "Competitive lithium solvation of linear and cyclic carbonates from quantum chemistry", *Physical Chemistry Chemical Physics*, vol. 18, no. 1, pp. 164–175, 2016.

[137] Daniel M Seo, Stefanie Reininger, Mary Kutcher, Kaitlin Redmond, William B Euler, and Brett L Lucht, "Role of mixed solvation and ion pairing in the solution structure of lithium ion battery electrolytes", *The Journal of Physical Chemistry C*, vol. 119, no. 25, pp. 14038–14046, 2015.

[138] Anna L d'Entremont and Laurent Pilon, "Thermal effects of asymmetric electrolytes in electric double layer capacitors", *Journal of Power Sources*, vol. 273, pp. 196–209, 2015.

[139] Kira E Wyckoff, Daniel D Robertson, Molleigh B Preefer, Samuel ML Teicher, Jadon Bienz, Linus Kautzsch, Thomas E Mates, Joya A Cooley, Sarah H Tolbert, and Ram Seshadri, "High-capacity Li^+ storage through multielectron redox in the fast-charging Wadsley–Roth phase $(W_{0.2}V_{0.8})_3O_7$", *Chemistry of Materials*, vol. 32, no. 21, pp. 9415–9424, 2020.

[140] G Heurung and R Gruehn, "High-resolution transmission electron microscopy—investigation of vanadium-tungsten oxides prepared by chemical transport reactions", *Journal of Solid State Chemistry*, vol. 55, no. 3, pp. 337–343, 1984.

[141] Jesse S Ko, Chun-Han Lai, Jeffrey W Long, Debra R Rolison, Bruce Dunn, and Johanna Nelson Weker, "Differentiating double-layer, psuedocapacitance, and battery-like mechanisms by analyzing impedance measurements in three dimensions", *ACS applied materials & interfaces*, vol. 12, no. 12, pp. 14071–14078, 2020.

[142] Sun Woong Baek, Muna Saber, Anton Van der Ven, and Laurent Pilon, "Thermodynamic analysis and interpretative guide to entropic potential measurements of lithium-ion battery electrodes", *The Journal of Physical Chemistry C*, vol. 126, no. 14, pp. 6096–6110, 2022.

[143] Dong-Han Kim and Jaekook Kim, "Synthesis of $LiFePO_4$ nanoparticles in polyol medium and their electrochemical properties", *Electrochemical and Solid-State Letters*, vol. 9, no. 9, pp. A439–A442, 2006.

[144] Zhenguo Yang, Daiwon Choi, Sebastien Kerisit, Kevin M Rosso, Donghai Wang, Jason Zhang, Gordon Graff, and Jun Liu, "Nanostructures and lithium electrochemical reactivity of lithium titanites and titanium oxides: A review", *Journal of Power Sources*, vol. 192, no. 2, pp. 588–598, 2009.

[145] John B Cook, Terri C Lin, Hyung-Seok Kim, Andrew Siordia, Bruce S Dunn, and Sarah H Tolbert, "Suppression of electrochemically driven phase transitions in nanostructured MoS_2 pseudocapacitors probed using *operando* X-ray diffraction", *ACS nano*, vol. 13, no. 2, pp. 1223–1231, 2019.

[146] Ying Zhao, Luis R De Jesus, Peter Stein, Gregory A Horrocks, Sarbajit Banerjee, and Bai-Xiang Xu, "Modeling of phase separation across interconnected electrode particles in lithium-ion batteries", *RSC advances*, vol. 7, no. 65, pp. 41254–41264, 2017.

[147] D. Li and H. Zhou, "Two-phase transition of Li-intercalation compounds in Li-ion batteries", *Materials Today*, vol. 17, no. 9, pp. 451–463, 2014.

[148] Kazuya Nagata, Hitoshi Iwabuki, and Hideyuki Nigo, "Effect of particle size of graphites on electrical conductivity of graphite/polymer composite", *Composite Interfaces*, vol. 6, no. 5, pp. 483–495, 1998.

[149] Joke Hadermann and Artem M Abakumov, "Structure solution and refinement of metal-ion battery cathode materials using electron diffraction tomography", *Acta Crystallographica Section B: Structural Science, Crystal Engineering and Materials*, vol. 75, no. 4, pp. 485–494, 2019.

[150] A Robert Armstrong, Michael Holzapfel, Petr Novák, Christopher S Johnson, Sun-Ho Kang, Michael M Thackeray, and Peter G Bruce, "Demonstrating oxygen loss and associated structural reorganization in the lithium battery cathode li [ni0. 2li0. 2mn0. 6] o2", *Journal of the American Chemical Society*, vol. 128, no. 26, pp. 8694–8698, 2006.

[151] Charles J Hansen, Joshua J Zak, Andrew J Martinolich, Jesse S Ko, Nicholas H Bashian, Farnaz Kaboudvand, Anton Van der Ven, Brent C Melot, Johanna Nelson Weker, and Kimberly A See, "Multielectron, cation and anion redox in lithium-rich iron sulfide cathodes", *Journal of the American Chemical Society*, vol. 142, no. 14, pp. 6737–6749, 2020.

[152] Andrew J Martinolich, Joshua J Zak, David N Agyeman-Budu, Seong Shik Kim, Nicholas H Bashian, Ahamed Irshad, Sri R Narayan, Brent C Melot, Johanna Nelson Weker, and Kimberly A See, "Controlling covalency and anion redox potentials through anion substitution in li-rich chalcogenides", *Chemistry of Materials*, vol. 33, no. 1, pp. 378–391, 2020.

[153] Grace Whang, David S Ashby, Aliya S Lapp, Yi-Chieh Hsieh, Danielle M Butts, Igor V Kolesnichenko, Pu-Wei Wu, Timothy N Lambert, A Alec Talin, and Bruce S Dunn, "Temperature-dependent reaction pathways in fes2: Reversibility and the electrochemical formation of fe3s4", *Chemistry of Materials*, 2022.

[154] Jian Zou, Jun Zhao, Bojun Wang, Shulin Chen, Pengyu Chen, Qiwen Ran, Li Li, Xin Wang, Jingming Yao, Hong Li, et al., "Unraveling the reaction mechanism of fes2 as a li-ion battery cathode", *ACS Applied Materials & Interfaces*, vol. 12, no. 40, pp. 44850–44857, 2020.

[155] David S Ashby, Jeffrey S Horner, Grace Whang, Aliya S Lapp, Scott A Roberts, Bruce Dunn, Igor V Kolesnichenko, Timothy N Lambert, and A Alec Talin, "Understanding the electrochemical performance of fes2 conversion cathodes", *ACS Applied Materials & Interfaces*, 2022.

[156] Pratyusha Das, Billal Zayat, Qiulong Wei, Charlene Z Salamat, Ioan-Bogdan Magdau, Rodrigo Elizalde-Segovia, Dakota Rawlings, Dongwook Lee, Gordon Pace, Ahamed Irshad, et al., "Dihexyl-substituted poly (3, 4-propylenedioxythiophene) as a dual ionic and electronic conductive cathode binder for lithium-ion batteries", *Chemistry of Materials*, vol. 32, no. 21, pp. 9176–9189, 2020.

[157] Pratyusha Das, Rodrigo Elizalde-Segovia, Billal Zayat, Charlene Z Salamat, Gordon Pace, Kuan Zhai, Rebecca C Vincent, Bruce S Dunn, Rachel A Segalman, Sarah H Tolbert, et al., "Enhancing the ionic conductivity of poly (3, 4-propylenedioxythiophenes) with oligoether side chains for use as conductive cathode binders in lithium-ion batteries", *Chemistry of Materials*, vol. 34, no. 6, pp. 2672–2686, 2022.

[158] Johnny N Martins, Michaela Kersch, Volker Altstädt, and Ricardo VB Oliveira, "Electrical conductivity of poly (vinylidene fluoride)/polyaniline blends under oscillatory and steady shear conditions", *Polymer testing*, vol. 32, no. 5, pp. 862–869, 2013.

[159] G. Kresse and J. Hafner, "*Ab initio* molecular dynamics for liquid metals", *Physical review B*, vol. 47, no. 1, pp. 558, 1993.

[160] G. Kresse and J. Hafner, "*Ab initio* molecular-dynamics simulation of the liquid-metal–amorphous-semiconductor transition in germanium", *Physical Review B*, vol. 49, no. 20, pp. 14251, 1994.

[161] Georg Kresse and Jürgen Furthmüller, "Efficiency of ab-initio total energy calculations for metals and semiconductors using a plane-wave basis set", *Computational Materials Science*, vol. 6, no. 1, pp. 15–50, 1996.

[162] Georg Kresse and Jürgen Furthmüller, "Efficient iterative schemes for ab initio total-energy calculations using a plane-wave basis set", *Physical Review B*, vol. 54, no. 16, pp. 11169, 1996.

[163] John P Perdew, Kieron Burke, and Matthias Ernzerhof, "Generalized gradient approximation made simple", *Physical Review Letters*, vol. 77, no. 18, pp. 3865, 1996.

[164] Peter E Blöchl, "Projector augmented-wave method", *Physical Review B*, vol. 50, no. 24, pp. 17953, 1994.

[165] Georg Kresse and Daniel Joubert, "From ultrasoft pseudopotentials to the projector augmented-wave method", *Physical Review B*, vol. 59, no. 3, pp. 1758, 1999.